MAGNETOM Flash

Issue Number 71 · 2/2018
RSNA Edition

Contents

The MAGNETOM World is the community of
Siemens Healthineers MR users worldwide,
providing you with relevant clinical information.
Here you will find application tips and proto-
cols to optimize your daily work. Lectures and
presentations from experts in the field will allow
you to be exposed to new ideas and alternative
clinical approaches.

Put the advantages of the MAGNETOM World
to work for you!

Dr. Sunshine is Professor of Radiology, Neurology and Neurosurgery at Case Western Reserve University recognized for his efforts to promote and advance the use of technology to improve patient outcomes. His research work covers now decades of effort in developing, demonstrating and deploying novel imaging tools for use in particular with acute stroke patients. This work has been long supported by both industry and government, including the National Institute of Health (NIH). Concurrently clinical domains include active practice in both diagnostic and interventional Neuroradiology. His efforts have encompassed many NIH funded trials across the use of functional MRI, imaging changes in chronic

Dr. Jeffrey Sunshine

Dear readers and colleagues,

I'm extremely honored to serve as editor for this year's RSNA edition of Siemens Healthineers MAGNETOM Flash journal. This opportunity allows me to share my perspective so fortunately gained from participating in MR developments applied to healthcare for nearly three decades.

My career began as the discovery and availability of MR Diffusion imaging dawned. We were able to pursue its use in the earliest identification of hyper-acute ischemic stroke first in pre-clinical models, and then within just a couple of years into clinical care [1]. The power of rapid diffusion-weighted images to reveal earliest cerebral infarct in a manner never seen before generated enormous enthusiasm, crowded lecture halls, numerous publications by many of you, and most importantly dramatically altered how we can and should care for patients when they face these impactful challenges. For certain, MR diffusion newly showed critical physiology necessary to judge acute intervention, yet additionally it heralded another dimension in MRI, which brings innovation from lab to bedside even today: the power of advanced imaging created with ultra-fast methodologies to confirm health or reveal disease. The likes of simultaneous multi-slice acquisitions, sparse image space acquisitions and high powered novel reconstructions have been developed, made readily available and can be read about today throughout this edition of MAGNETOM Flash – we discuss key examples below.

Simultaneous multi-slice acquisition techniques arose as the demand for image generation over less acquisition time grew considerably beyond initial parallel imaging, whether for greater spatial resolution, greater number of sequences per subject, or larger coverage.

These advancing methods took advantage of special RF pulses that excite multiple slices, encoding mechanisms to distribute signal from simultaneously acquired slices, and reconstruction methods to resolve images from multiple slices [2]. RF encoding and gradient encoding both introduce phase modulation during acquisition in k-space, and thus introduce a slice shift in the image domain to shift multiple slices with respect to each other. Subsequent reconstruction methods can separate them and take advantage of the information from the shifted images. Specifically CAIPIRINHA (Controlled Aliasing in Parallel Imaging Results in Higher Acceleration) can use controlled slice shifts and different coil sensitivity from multiple receiver coils to improve artifact reduction and allow higher acceleration factors [3]. A great advantage of these techniques has been mainly in preserving clinical image quality over relatively still anatomic targets, while still supporting important gains in acquisition time efficiency.

Next compressed sensing represents a prime example of high-speed acquisition techniques providing unique clinical advantages most notably under dynamic scans as best represented by cardiac imaging even with irregular or fast rhythms. Compressed sensing reconstructs images from significantly fewer measurements thus reducing scan time by exploiting the sparsity of the images. In this sense sparsity refers to the relatively few meaningful nonzero pixels in an image compared with the many noise pixels. There may also be sparsity in a transfer domain with wavelet transforms exploiting spatial sparsity or Fourier transform exploiting temporal sparsity in dynamic images. Sparse images can be recovered through random under-sampling and non-linear

disease cohorts, and evaluating tools and methods for triage and treatment of hyper-acute and acute cerebral ischemia. Dr. Sunshine has more than 80 peer-reviewed publications including those in the journals Radiology, Science and Nature; he has delivered more than 85 national or international invited talks.

At University Hospitals (UH) in Cleveland, he is the Chief Medical Information Officer (CMIO) serving as the primary liaison between clinical and IT staff, helping to facilitate the integrated use of their UHCare electronic medical record and many clinical applications across UH. In his tenure as CMIO, Dr. Sunshine has partnered with IT to optimize and connect electronic medical records (EMRs) and other key clinical systems, advance digital health capabilities and elevate the patient experience through technology. Dr. Sunshine has been named "Best Doctor" by Castle Connolly since 2006 through 2018, "One of 25 Leading CMIOs" by Health Data Management in 2016 and 2017, "Who's Who of Medicine and Health-care" over many years by Marquis. Having contributed to many advances in MRI technology and clinical use, he remains in practice of Diagnostic and Interventional Neuroradiology, and continues service as Professor and Vice Chair of Informatics in Radiology for CWRU & UH.

reconstruction, where the random sampling makes the under-sampling artifacts incoherent so they appear like background noise. The non-linear reconstruction can then recover the sparse coefficients to effectively recover the image. For the clinician, all this translates to rapid acquisition of key information from very dynamic subject tissue, with then heavy additional processing regenerating the entire image. In addition to cardiac applications, compressed sensing advantages 3D Angiography as it typically requires large FOV and high spatial resolution, while the blood vessel information is intrinsically sparse. For example, vessel information can be preserved using only 5% of the transform coefficients, representing a 20-fold acceleration for the scan time [4].

A combination of fast imaging techniques has improved imaging across other motion laden anatomy, as used within abdominal imaging obtained with the patient breathing freely. A key example in this domain, GRASP (Golden-angle Radial Sparse Parallel MRI) combines radial sampling, compressed sensing and parallel imaging methods to support fast volumetric MR imaging. Radial sampling provides incoherent artifacts from under-sampling closely matching an essential requirement from compressed sensing. Sensitivity to motion is diminished as the radii keep sampling the center of *k*-space with every spoke. The technique then includes parallel imaging recon-struction to recover the under-sampled data and maintain image quality using the different spatial sensitivity information provided from multiple receiver coils. GRASP has been applied to free-breathing 3D abdominal imaging, cardiac cine imaging and 3D DCE imaging of the liver [5]. Techniques such as these permit imaging across a much wider number of patients including the more infirm or elderly who otherwise could not hold breathes sufficient to support consistent diagnostic image quality.

I believe that now as I write to you we witness the dawn of another age beyond fast advanced imaging alone, we enter excitedly the time of quantitative image output, with all its potential to provide specificity of tissue, diagnoses and importantly broad data linkage to machine assisted analyses. In this wave of ongoing innovation, we have reported the ideas and prototypical implementations of MR Fingerprinting (MRF)[1] [6]. The MRF framework has three main components: data acquisition, dictionary generation and pattern recognition. MRF uses a pseudorandomized acquisition that makes the signal from different tissues have a unique signal evolution, simultaneously a function of multiple parameters of interest. This is accomplished by varying parameters such as flip angle and phase of RF pulses, TR, TE and sampling patterns during the acquisition to generate spatial and temporal incoherence. For this technique, one constructs a dictionary that contains signal evolutions from all foreseeable combi-nation of relaxation and system-related parameters. Then one uses a pattern recognition algorithm to match the acquired signal to the dictionary, the results of which identifies the parameter combination in each of the voxels, and can then be translated to quantitative maps.

---

[1] *WIP, the product is currently under development and is not for sale in the US and in other countries. Its future availability cannot be ensured.*

As MRF arises it can achieve the requisite burdens of proof that its quantitative output is indeed efficient and reproducible across time, subjects and machines. These characteristics remain fundamental. We have had measurement of T1, T2 and other parameters for some time, but we haven't had them with sufficient rigor to allow wide consistency across the varying circumstances of acquisition across time, place and subject. Such consistency to standards of measurement, i.e. precision, will allow us to generate broad, deep data domains through which we expect to find parameter patterns

with true specificity to the underlying human situations. We can envision our future where the end result of our imaging experiments evolve beyond the image and radiologist's necessarily loose consideration of tissue diagnoses currently framed as a differential diagnosis, perhaps including terms like moderate or severe, or descriptions of intensity. We begin to see a world where images become more complete with specific reproducible parameters of the tissue under study, where those same data permit us to create the very same weighted images as derived necessarily from the core physical

Figure 1:
ISMRM/NIST Phantom.
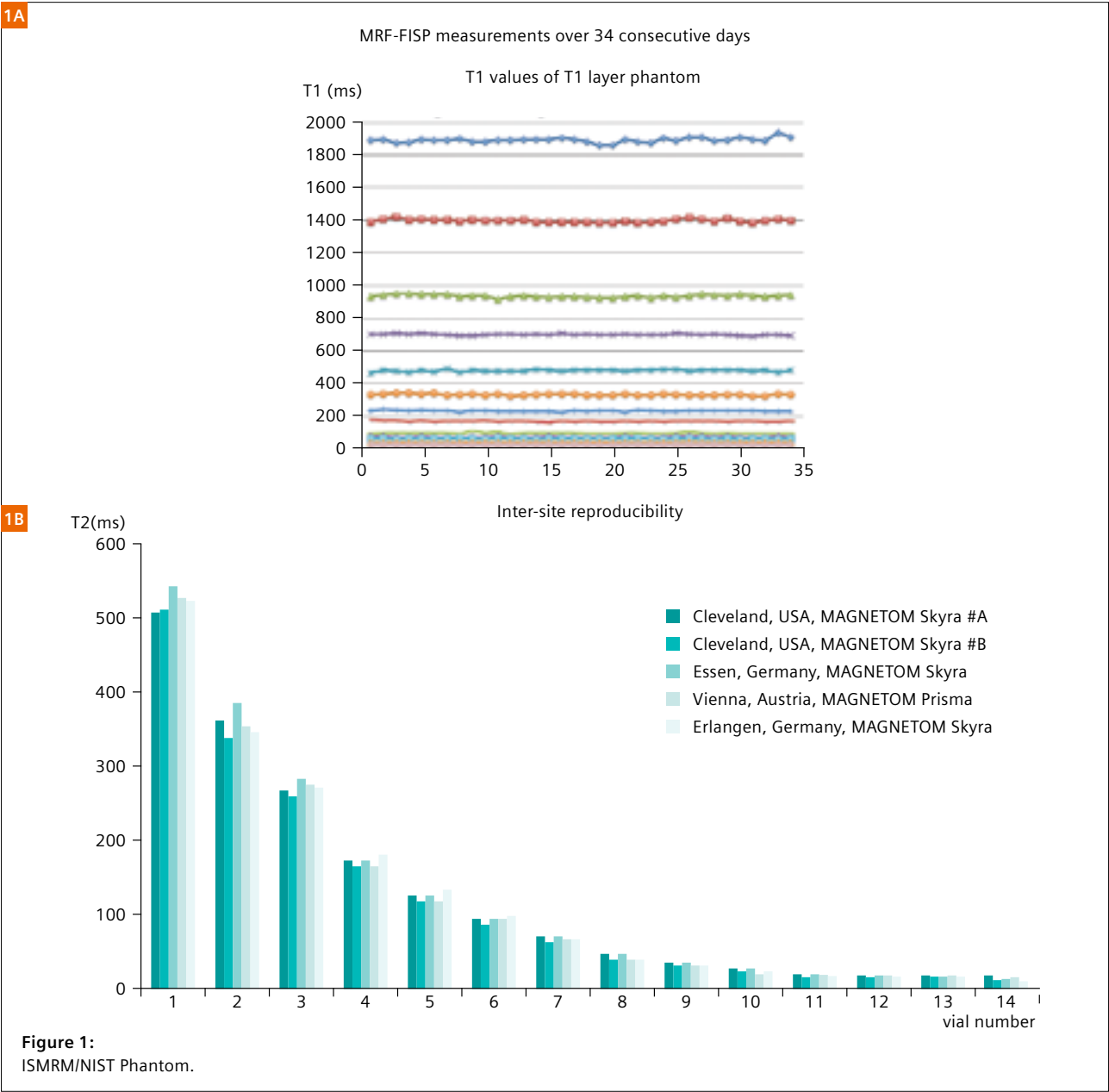
parameters. Most anticipated of all by me, we will allow the radiologist's conclusions to morph to newly enabled forms such as "the tissue in question represents tumor A with calculated probability X, and if not that then B with probability significantly lower of Y" or "the organ reveals diffuse changes compatible with normal aging of the matched age and gender in our population within two standard deviations, and this pattern has been seen in a disease C but only with significantly lower probability of Z." What a new world we create together to see ever better what's happening, what may be wrong and how we might intervene to adjust the health of our patients.

Inherent to MR Fingerprinting design then remains the focus on generation of measurements from rapid acquisition centered on the early time courses of parameter curves richest in distinguishing among tissues. The output of MRF then isn't initially targeting image quality, rather the numerical distinctions needed for specific characterization. These data must be vigorously reproducible with at least great precision to support broad implementation and comparable utilization. Some early examples of this necessary groundwork are shown in Figure 1A, where the consistency of measured T1 from the ISMRM/NIST standard phantom (NIST – US National Institute for Standards and Technology – those who bring us time from the atomic clock) is demonstrated [7]. Note that these measurements show the consistency across a month of days with all the environmental variations

of a single scanner and room. In Figure 1B we see the reliability of measured T2 from those standard phantoms across a range of T2 values with inter-site reproducibility from 5 sites, 2 machine types, and 4 cities in 3 countries. This need for consistent precision extends naturally across physiologic variations for example in heart rate. My colleagues have shown no parameter value changes through simulations across heart rates from as low as 40 bpm to as many as 120 bpm [8].

Once the quality of the quantified imaging output has been established, then the now known measured parameter values can be used to create the predicted companion T1 or T2 weighted images given the base data. Indeed we have identified a color mapping standard that allows visual distinction of T1 from T2 maps and allows our visual spectrum to better align with the apparent progression of the numeric scale as shown for MRF calculated brain images in Figure 2. Necessary data can be acquired with rapidity in as few as 15 or 16 heartbeats, then constructing images comparable to previous techniques permitting comparison of images and parameter values. As consistency holds, images can now come with additional quantified output of normal myocardial tissue prior to or following intravenous gadolinium based contrast injections. The technique has been applied preliminarily to hypertrophic cardiac myopathy where the muscle walls show typical thickening, and we receive the additional data of muscle T1 and T2 values. As we expect true change of muscle
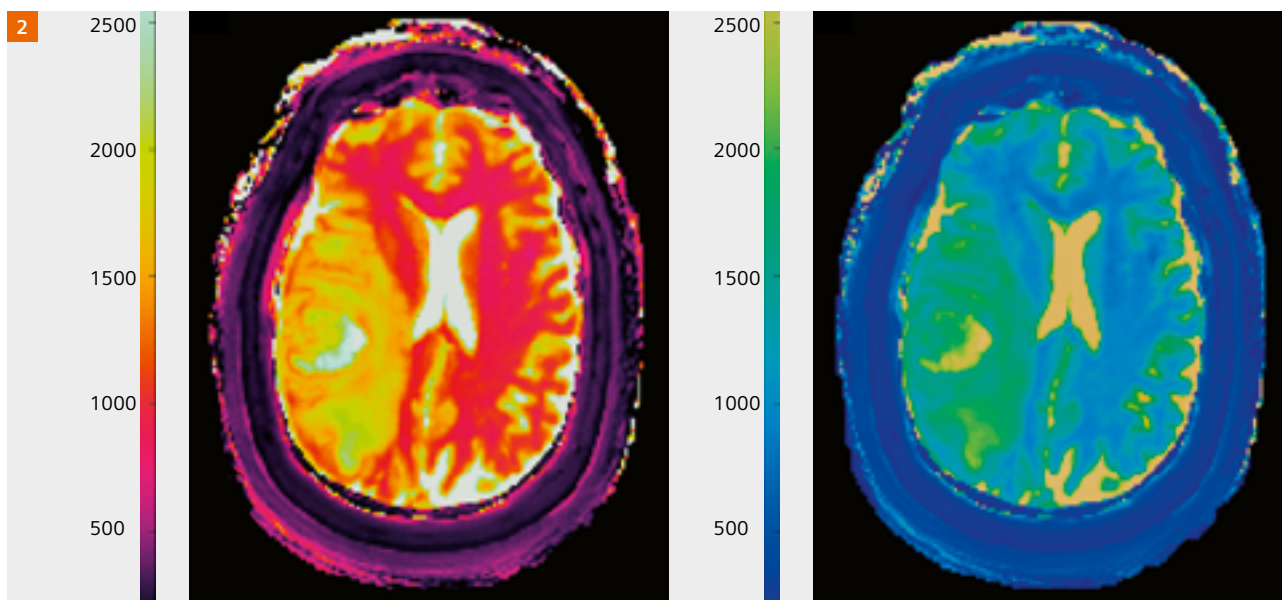

Figure 2:
Quantitative T1 and T2 maps with distinct colors.

tissue has occurred with this myopathy, we aren't surprised to learn these parameters have shifted and are distinct from those measured in dilated cardiac myopathy. Our future will reveal whether we can detect such diseases ever earlier than the thickening or dysfunction to allow intervention to slow down or avoid harmful progressions.

Combinations of MRF measured parameters and accompanying derived images allow characterization of other normal and specific disease tissues, and colleagues have published results from MRF generated over patient abdominal tissues [9]. Specific T1 and T2 normal ranges have been measured and as expected vary by tissue types across renal cortex, renal medulla, spleen, skeletal muscle, fat and liver, yet stay consistent in different organ's parenchyma. When further compared in a single tissue such as liver, a clear, significant numerical distinction with metastatic adenocarcinoma can be revealed. We look to the wider analyses needed to show how well and reliably different tumor types can be mapped between one another.

Quantitative relaxometry results can also allow us to identify changes in tissue which otherwise appears unchanged through conventional MR image acquisition, in other words increasing the dimensionality of output from MRI. Colleagues with me have used MRF to measure the T1 and T2 parameters of brain gray and white matter that has no visible lesions across changing ages and between genders [10]. This exposed a generally rising T1 value of certain brain tissues, with concomitant generally decreasing T2 value in other brain regions. There is an initial age related decrease in T2 values of frontal white matter that then increases in the later years, and this pattern is higher in males compared to females.

Given that specific quantified values have been obtained, we can combine them for analytical distinctions among otherwise conventionally similar abnormal tissues. By using both T1 and T2 values and plotting them simultaneously, valuable groupings become apparent, as when evaluating brain tumor lesions from metastases, low grade gliomas or glioblastomas [11]. The tissues may align such that only tumors display parameters above lower thresholds. Similarly when the peritumoral tissue surrounding the tumor is measured we can clearly distinguish areas with overlap to normal white matter from those that have tissue with parameters aligned to tumors. The initial analysis proceeds further and from T2 a threshold allows separation of low grade glioma from metastasis, and from T1 a separation in peri-tumoral tissue between low grade glioma and glioblastoma. Once the measures are complete they enable even further evaluations, for example textural analysis which suggests that with derived factors such

Figure 3:
Distinction of tissue type through quantification.
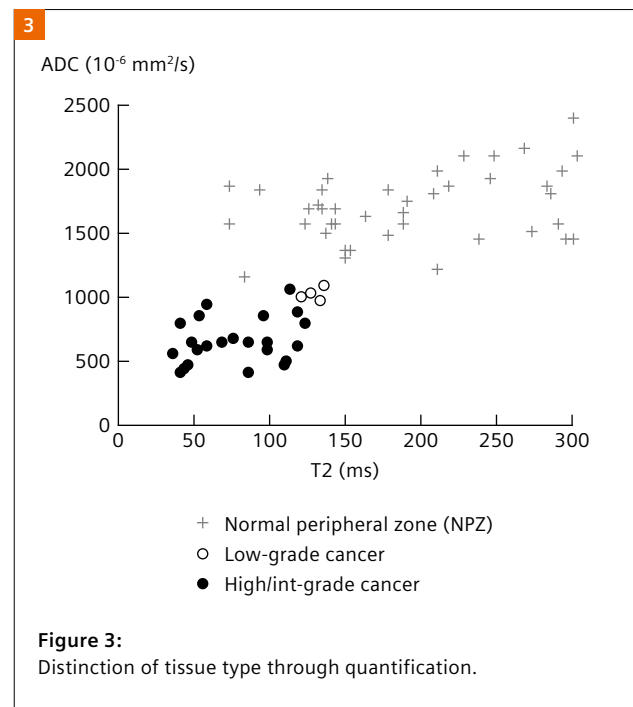
as T1 correlation or T2 homogeneity, low grade glioma tumors can be distinguished from glioblastoma.

Combining measurements across sources can provide other pathways to identify disease. Colleagues' work has shown in prostate cancer that combining T2 values determined from MRF acquisition with ADC values from typical MR diffusion studies generate high significant difference between normal tissue and cancer in prostate peripheral zone disease [12]. Using the combination of parameters also remarkably drives the diagnostic area under the ROC curve in separating low grade from grouped intermediate and high grade lesions (the grouping reflecting need for treatment) above 0.9. When these data are used in conjunction with conventional ADC maps and calculated MRF images, biopsy can be guided, and the resultant tissue falls into distinct clusters across ADC and T2 (Fig. 3).

The power from quantified image output again provides synergies as one considers additional diagnostic complexities. After all patients don't present as simply as normal versus tumor, they may have symptoms possibly related to any of the multitude of disorders. So within the example of prostate analyses one may consider normal findings, tumor or commonly prostatitis. Separation among these appears best combining measures: a higher ADC value can sensitively select the group which excludes all worrisome cancer, while a lower value can specifically identify those which are almost always cancer needing treatment. That then leaves a middle group,

Figure 4:
Potential of image quantification in diagnosis.
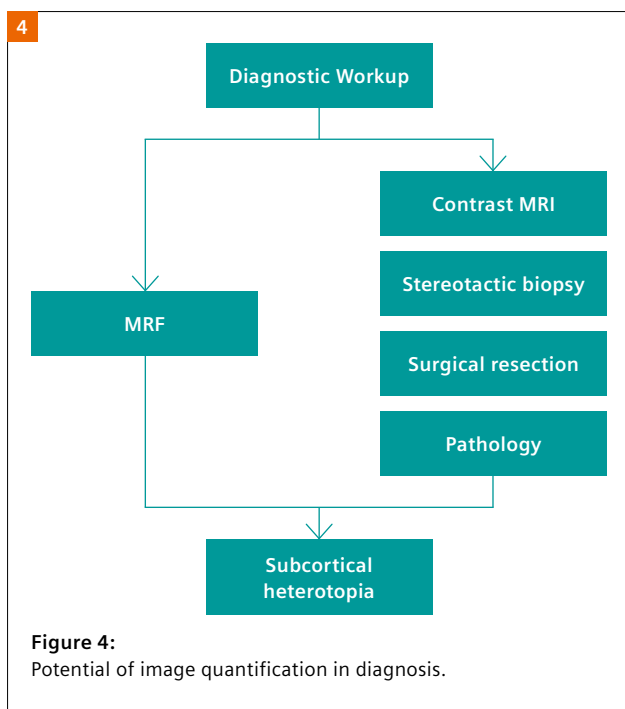
which can still be any of the lesions. First let's note that's not all bad – we've reduced the unknowns as the high values need treatment for benign conditions, and the low more aggressive care – the middle group is much smaller than the initial cohort. Further when colleagues introduce a second parameter, T2 value, another threshold appears that can stratify even this middle cohort between prostatitis and more aggressive tumors. Availability of additional quantification may also add to our ability to evaluate early response to therapy, lack of response or disease progression. Preliminary evidence from my colleagues suggests that although early decrease in breast cancer tumor volume may signify response, confirmation by change in T1 and T2 values provides clearer distinction of true responders among all those with some early shrinkage.

Specificity of tissue typing through rapid precise measurement of tissue physical characteristics including T1 and T2 offer high efficiency in healthcare. Consider a brain lesion that has appearance under conventional MRI that could represent congenitally displaced gray matter heterotopia, or less likely low grade glioma, which if so ought best be resected. Colleagues have such an example in which an initial biopsy returned consistent with a tumor, leading to full open resection. Of interest here, MRF acquisition obtained during the initial imaging generated T1 and T2 numerical values aligned only with gray matter and quite distinct from the range found in low grade gliomas. Full pathologic evaluation

of tissue after resection revealed only heterotopic gray matter with no evidence of neoplasm. Diagnostic workup of today (Figure 4, right column) included three resource intensive steps of i) enhanced conventional MRI ii) stereotactic biopsy and iii) surgical resection to learn the true diagnosis, which of itself needs no surgery. The workup of tomorrow enabled by quantitative imaging output ought well engage only the single step of MR Fingerprinting or similar to confirm the sole tissue present and forego any need of intervention.

I couldn't conclude my discussions here without acknowledging the extraordinary privileges afforded to me at Case Western Reserve University and University Hospitals in Cleveland, Ohio, USA. In particular as a long active clinician here, my partners from the science of MR Physics sequentially moved along the lines here connecting Mark Haacke, Jeffrey Duerk, Mark Griswold and Nicole Seiberlich, Ph.D.s all; few indeed have been impacted so deeply over such a continuum of gifted MR minds. There remain many other collaborators here gifted in their own right that stand too numerous to mention all, yet our MR Fingerprinting work could not have succeeded as it has without the vision and leading contributions from Vikas Gulani M.D. and Dan Ma Ph.D. (with special acknowledgement for their exceptional efforts shaping our clinical vision with MRF, and assisting in preparation of this editorial respectively). I'd also note, again representing my extraordinary opportunities, the decades long partnership with Siemens Healthineers Magnetic Resonance group and its many individual contributors.

Finally, I conclude again with excitement around the expansion of quantified image output occurring now, which will provide rich data already aligned to computational analysis, pattern recognition, and machine assisted learning of many varieties. These growing quantifications can unlock the vast repository of information derived from ongoing patient imaging in healthcare to analysis under 'artificial intelligence' (perhaps which may ultimately prove neither artificial nor intuitively intelligent in the human representation of that word). So relish all going on about the MR field as represented here, join in the wonder of the age of quantitative image output with all it may do to alter how we create images, and explore what we learn through the additional content, and define further how we will use these standardized data to augment our care through advanced machine processing across many domains.

Jeff Sunshine

Editorial

References

1 Sunshine JL, Tarr RW, Lanzieri CF, Landis DM, Selman WR, Lewin JS: Hyperacute stroke: ultrafast MR imaging to triage patients prior to therapy. Radiology. 1999 Aug;212(2):325-32.

2 Barth M, Breuer F, Koopmans PJ, Norris DG, Poser BA: Simultaneous multislice (SMS) imaging techniques. Magn Reson Med 2016; 75:63–81.

3 Breuer F a, Blaimer M, Heidemann RM, Mueller MF, Griswold MA, Jakob PM: Controlled Aliasing in Parallel Imaging Results in Higher Acceleration (CAIPIRINHA) for Multi-Slice Imaging. Magn Reson Med 2005; 53:684–91.

4 Lustig M, Donoho DL, Pauly JM: Sparse MRI: The Application of Compressed Sensing for Rapid MR Imaging. Magn Reson Med 2007; 58:1182–95.

5 Feng L, Axel L, Chandarana H, Block KT, Sodickson DK, Otazo R: XD-GRASP: Golden-angle radial MRI with reconstruction of extra motion-state dimensions using compressed sensing. Magn Reson Med 2016; 75:775–788.

6 Ma D, Gulani V, Seiberlich N, et al.: Magnetic Resonance Fingerprinting. Nature 2013; 495:187–192.

7 Jiang Y, Ma D, Keenan KE, Stupic KF, Gulani V, Griswold MA: Repeatability of magnetic resonance fingerprinting T1 and T2 estimates assessed using the ISMRM/NIST MRI system phantom. Magn Reson Med 2017 Oct;78(4):1452-1457.

8 Hamilton JI, Jiang Y, Chen Y, Ma D, Lo WC, Griswold M, Seiberlich N: MR fingerprinting for rapid quantification of myocardial T1 , T2 , and proton spin density. Magn Reson Med. 2017 Apr;77(4):1446-1458.

9 Chen Y, Jiang Y, Pahwa S, Ma D, Lu L, Twieg MD, Wright KL, Seiberlich N, Griswold MA, Gulani V. MR Fingerprinting for Rapid Quantitative Abdominal Imaging. Radiology. 2016 Apr;279(1):278-86.

10 Badve C, Yu A, Rogers M, et al.: Simultaneous T1 and T2 Brain Relaxometry in Asymptomatic Volunteers Using Magnetic Resonance Fingerprinting. Tomography 2015 Dec;1(2):136-144.

11 Badve C, Yu A, Dastmalchian S, et al.: MR Fingerprinting of Adult Brain Tumors: Initial Experience. Am J Neuroradiol 2017 Mar;38(3):492-499.

12 Yu AC, Badve C, Ponsky LE, Pahwa S, Dastmalchian S, Rogers M, Jiang Y, Margevicius S, Schluchter M, Tabayoyong W, Abouassaly R, McGivney D, Griswold MA, Gulani V.: Development of a Combined MR Fingerprinting and Diffusion Examination for Prostate Cancer. Radiology. 2017 Jun;283(3):729-738.

The statements by Siemens' customers presented here are based on results that were achieved in the customer's unique setting. Since there is no 'typical' hospital and many variables exist (e.g., hospital size, case mix, level of IT adoption), there can be no guarantee that other customers will achieve the same results.

We appreciate your comments.
Please contact us at magnetomworld.team@siemens-healthineers.com

Editorial Board

Rebecca Ramb Ph.D.
Head of Global MR Collaborations

Dr. Sunil Kumar. S. L.
Clinical & Product Specialist MRI Dubai, UAE

Wellesley Were
MR Business Development Manager Australia and New Zealand

Gary R. McNeal, MS (BME)
Advanced Application Specialist, Cardiovascular MR Imaging Hoffman Estates, IL, USA

Review Board

Fast, Standardized, and Robust Imaging with ⬛⬛⬛⬛⬛ and ⬛⬛⬛

Johan Dehem, M.D.

VZW Jan Yperman, Ypres, Belgium

When high-tech applications leave the shelter of the lab and come to the hospital to face real clinical challenges, the question arises: Does it work? Spoiler alert: The answer can be found in the images.

Upon arrival of the 1.5T MAGNETOM Sola, the first thing you notice is the small bump in the back. Since the magnet is such a short bore system, which I can literally hold in my arms, this rear extension is a quite logical way to support table movement beyond the bore.

Indeed, patient friendly magnets should be as short as possible. Speaking of patient comfort, listen when you move the table; you can't hear it. It's smooth and slides silently in place, in sharp contrast to the high-pitched shrieking on older systems. The acoustic isolation from gradient power has also improved. Many patients in follow-up studies spontaneously mention a more quiet noise level throughout the exam.

Another innocuous, innocent looking, but much appreciated change is the head coil. For the first time ever, it's tiltable! Slight tilting of the head is preferred by many patients and helps them to relax. It's also very much appreciated by sick and older patients or those with kyphosis or other malformations, since we no longer need to tilt the patient until the head fits but simply tilt the head coil. Together with the standard leg support, every patient fits. It's a small tilt for the coil, but a giant leap for patient comfort.

Patient comfort is one thing, how about operator comfort? Well, MAGNETOM Sola has some appealing tricks up its sleeve to charm the technologists. Patient positioning, for example, is done automatically; you just acknowledge by pressing the Go button and you're done. Using the laser beam to position suddenly seems so last century. Moreover, this automatic positioning avoids suboptimal positioning or even errors by eliminating interoperator variability, regardless of your patient's body type. As a result, scanning is always in local mode, which is less shim-dependent and hence faster (except for large FOV exams). Together with AutoAlign and AutoCoverage in the Dot engines, a highly standardized and robust examination quality results. DotGO and Dot engines are a match made in heaven! (Actually, a match made in Germany).
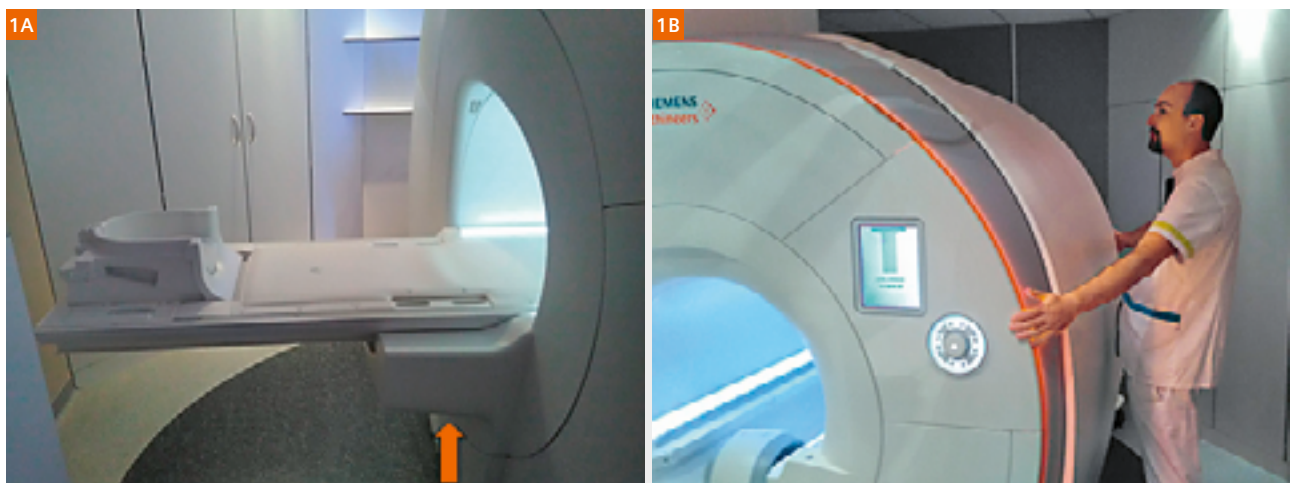
Figure 1:
The support in the back is needed since the magnet is so short that a person can easily hold the magnet in their arms. It may be quite an unusual feature; however it is a reliable parameter to determine if your magnet is patient friendly.

The user interface has changed quite a bit – dramatically in fact; however, we didn't complain about the transformation at all because it has changed for the better! For example, you can actually scroll through the images in the graphic segments, speeding up and improving the accuracy of planning. Or double click and have your planning stack in full screen. The dual screen setup at the console is efficient at separating scanning workflow from viewing, postprocessing, and archiving. Another benefit is the distribution of images where complex multiphase, multiseries studies are neatly presented in a graphic overview, guiding you to send only the relevant series to the PACS system instead of blindly dumping images.

The built-in respiratory sensor is helping us in different ways. First, if you ask your patient to hold their breath, you get a direct view if the breath-hold is properly done. If your patient is sick, you keep an eye on the respiration frequency together with the ECG. Second, the BioMatrix Sensor is robust and reliable for triggering T2 TSE, HASTE, or DWI acquisitions of the liver. There is no need to put on a respiratory belt and no scanning time is lost with the navigator. A kinetic sensor and beat sensor are in the development pipeline and I am eager to see if they perform just as well.
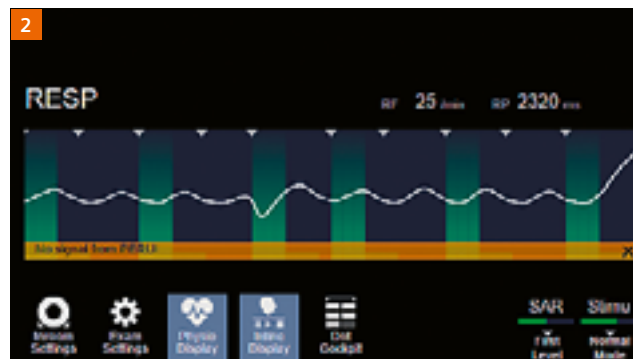
Now that we have touched on the subject of breath-holding, it seems a good time to mention that not every patient is very good at holding their breath, especially on command. On the Aera, we used StarVIBE to minimize respiratory movement artifacts (at the cost of dynamic contrast enhancement information), the Sola with GRASP-VIBE excels at getting rid of these artifacts while maintaining all the dynamic information over time. It turns out image quality that is surprisingly good, giving pristine images in not-so-compliant patients.
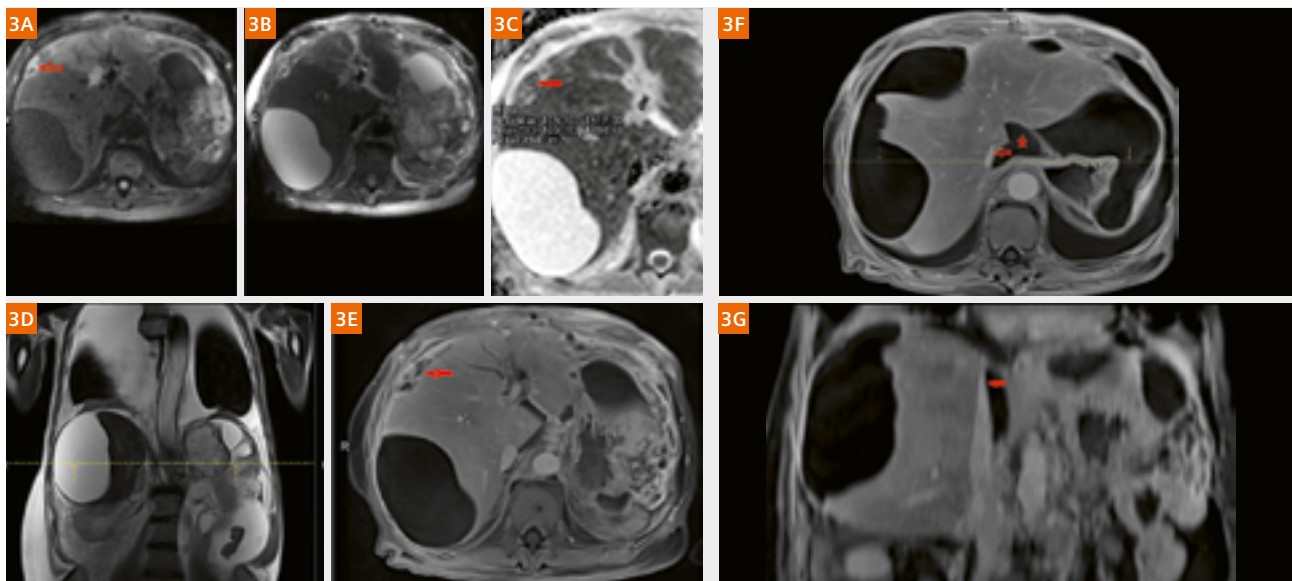

Figure 3: This 73-year-old male presented with shortness of breath and leg swelling. History of pancreatectomy and duodenectomy for pancreas cancer
DWI with high b-value **(3A)**, low b-value **(3B)**, and ADC map **(3C)**. Coronal HASTE **(3D, E)**. Note the coverage was head to feet with GRASP-VIBE for artifact-free free-breathing T1 imaging, demonstrating peritoneal implant (red arrow). Ascites (dielectrical effect) and massive pleural fluid are challenging image quality. Shortness of breath is immediately explained by the massive pleural effusion and compression atelectasis.
GRASP-VIBE free-breathing aquisition in the venous phase **(3F)** depicts the severe extrinsic compression of the inferior vena cava (red arrow) in diaphragmatic hiatus explaining edema and swelling of the lower limbs. Since slice thickness is 2.5 mm, you can reconstruct coronal images to better delineate anatomical landmarks.

To be honest, the gold standard breath-holding acquisition itself is quite limited in temporal resolution (it takes time for the patient to breathe in and out between different phases) and you need to time your acquisition very well to have a crisp arterial phase; whereas in GRASP-VIBE, the acquisition simply keeps going while the patient is quietly breathing; hence, GRASP-VIBE does not simply maintain dynamic information, but actually enhances time resolution giving you, for example, three arterial phases in liver imaging. Here, the time resolution was just 7 seconds.
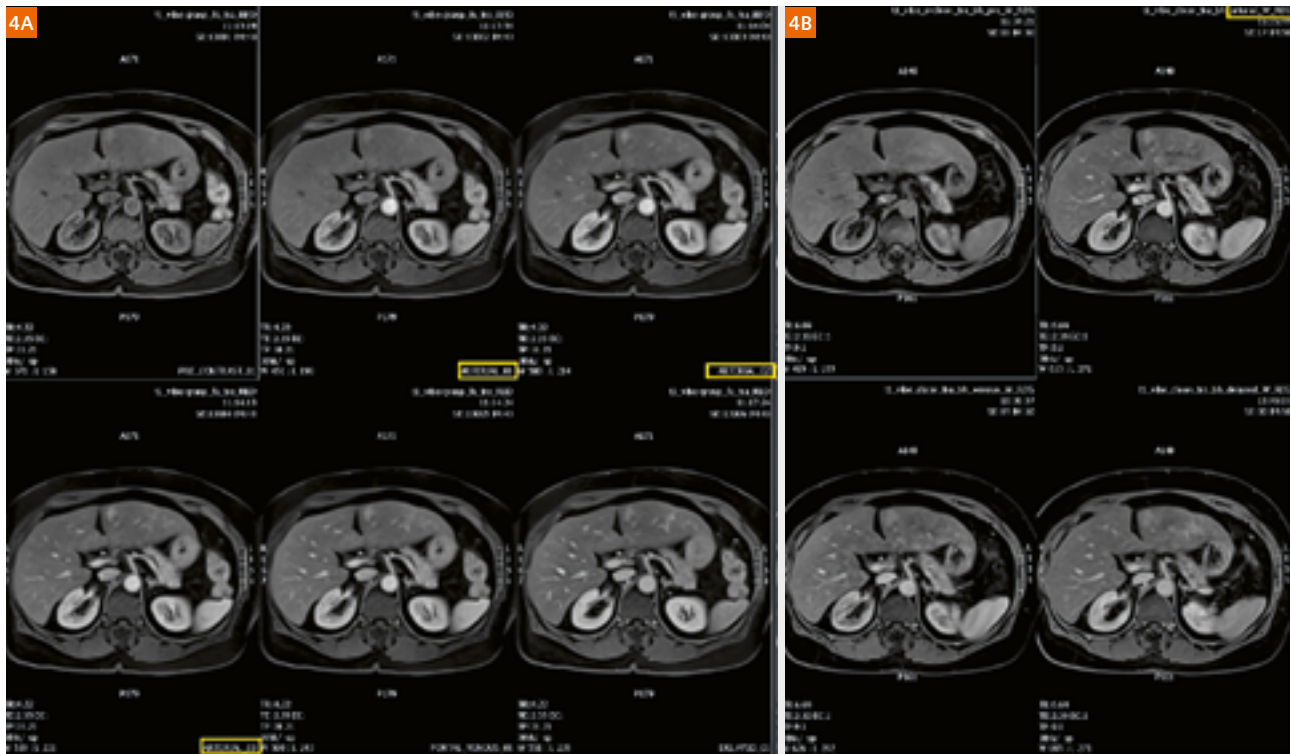
Figure 4:
(4A) Three columns showing reduced reconstruction sets of GRASP-VIBE with three arterial phases (yellow box); **(4B)** two columns showing previous exam using CAIPIRINHA 4 VIBE on the Aera with standard single arterial phase (yellow box).
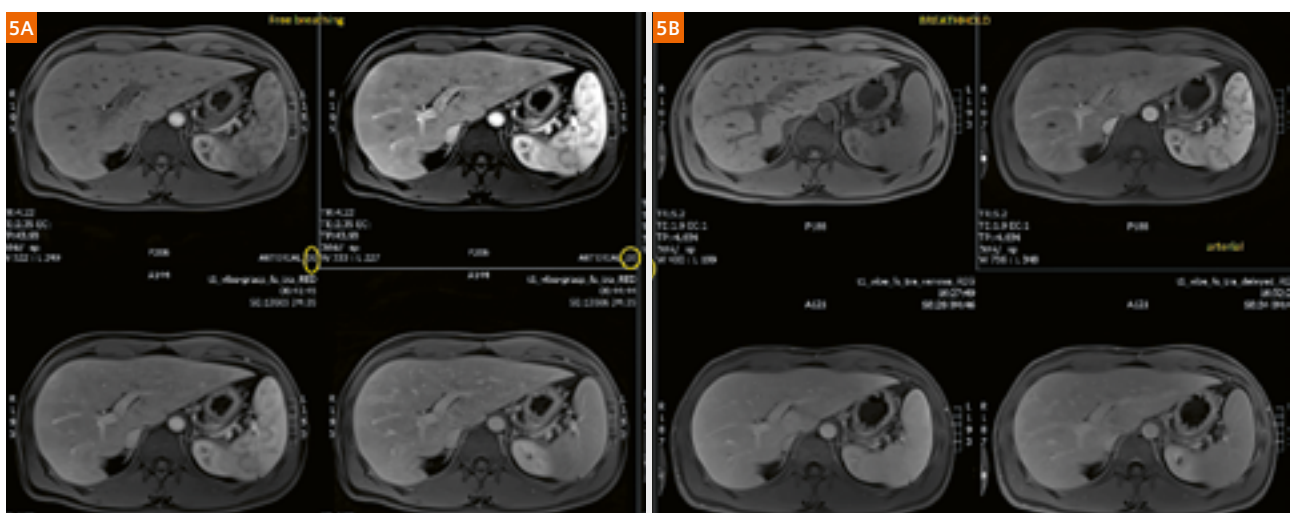

Figure 5:
(5A) When comparing this free-breathing GRASP acquisition in this young and cooperative patient, the quality of the free-breathing series equals that of the best CAIPIRINHA 4 VIBE technique **(5B)** we had available last year; however, you have much higher temporal resolution with more phases, e.g., three consecutive arterial phases (arterial 01 and 03 are depicted, phase 02 is left out for sake of comparison).

For older and sick patients, free breathing makes an even bigger difference with better image quality in addition to higher temporal resolution.
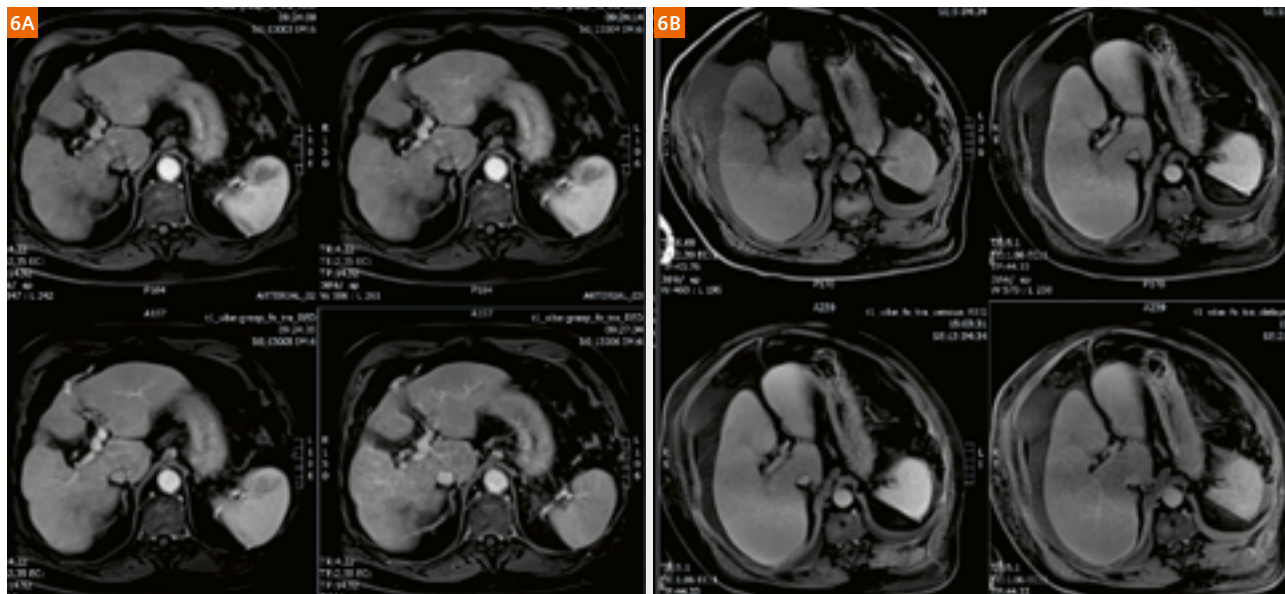
Figure 6:
In this 76-year-old patient with advanced liver cirrhosis, the GRASP-VIBE exam **(6A)** compared side-by-side with previous exam **(6B**; at 70 years) shows the portal vessels and the recanalized umbilical vein to a far better extent. This improved image quality is achieved despite the fact that patient is 6 years older and, worse, at an more advanced stage of cirrhosis. In addition to the image quality improvement, instead of one weak arterial phase, we have three confident arterial phases!

GRASPing dynamic inflow information is actually new and makes GRASP a new tool to help differentiate liver lesions.
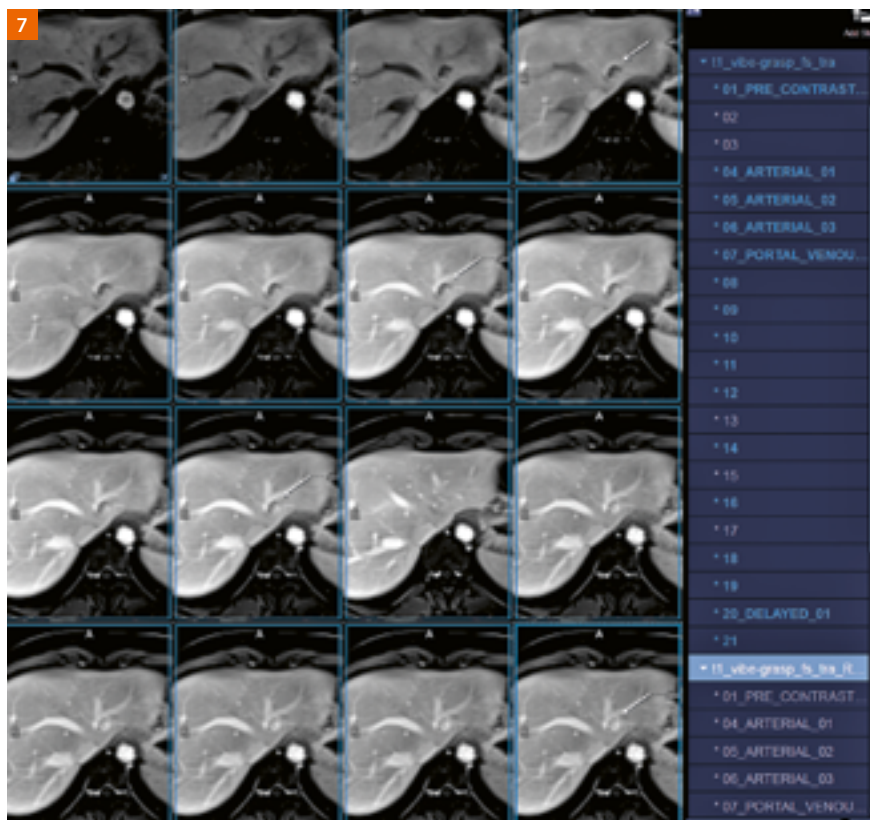

Figure 7:
Classic filling of liver hemangioma (arrow); however, with no breath-holding, time resolution 7 seconds, 3 mm slice thickness. The system automatically detects contrast bolus arrival and labels the phases accordingly. For convenience, a reduced dataset containing only the relevant, labelled phases (scroll down menu on the right side of the image series) is prepared, which can be sent separately to the PACS.
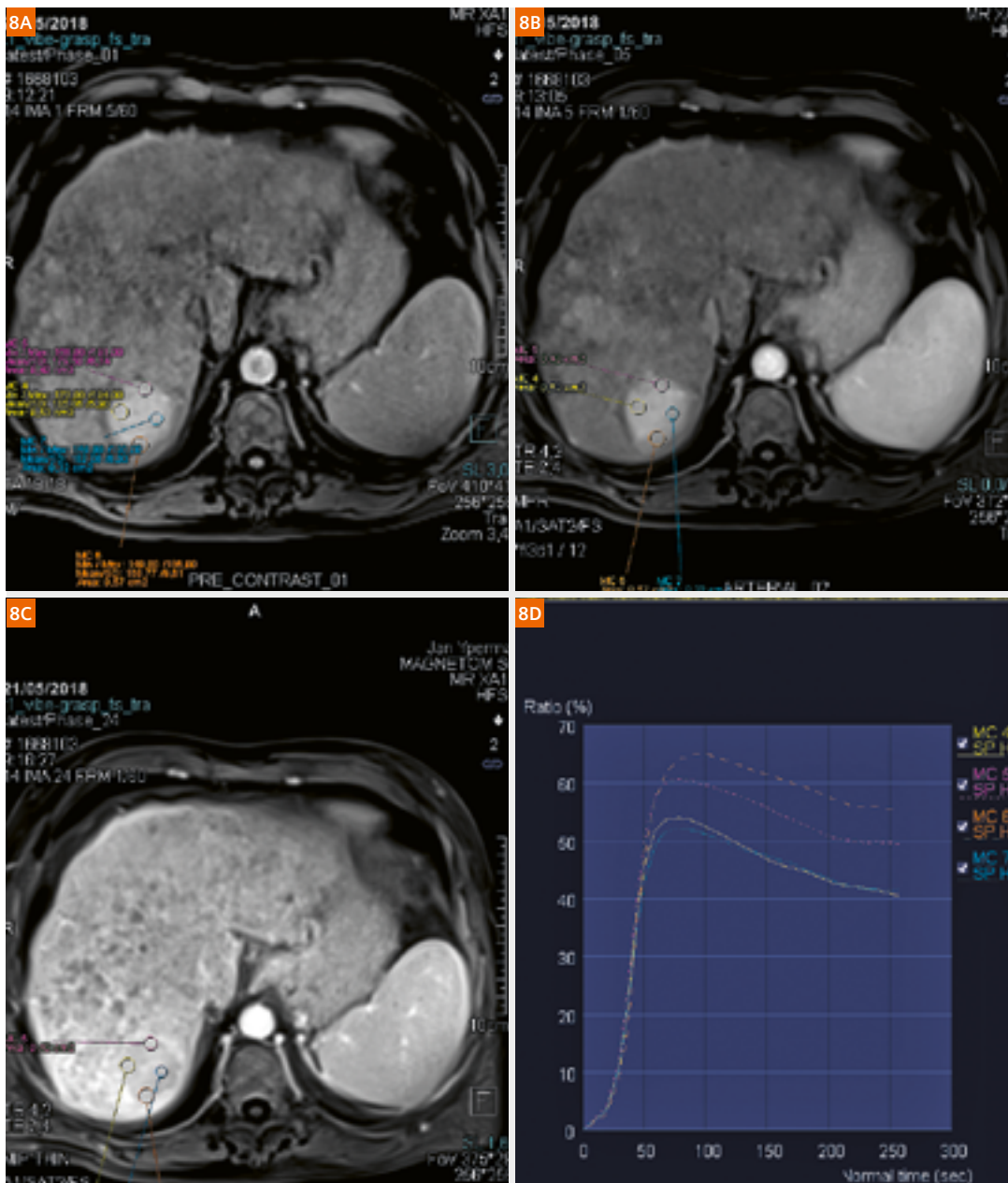
Figure 8:
Large HCC with selected images T1 fatsat precontrast **(8A)**, arterial enhancing **(8B)**, and washout on delayed phase **(8C)** with the corresponding high quality contrast enhancement curve over time resulting from the high temporal resolution sampling in 4D GRASP. One can actually see the washin in the upper row and the washout in **8D**.

4D GRASP can also showcase dynamic filling, for example, of the mesenteric vessels, or even give an impression as to how organs are moving or are restricted in movement. In GRASP liver imaging, the reconstructor receives a respiration-dependent fluctuating signal. This respiratory information in the dataset is actually used to gate the reconstructions in expiratory phases only when wanted (our standard approach in liver imaging). This is convenient when reading/reporting the GRASP-VIBE dynamic series side-by-side with T2 and diffusion-weighted imaging, where having the same position in slices facilitates lesion recognition and characterization. GRASP-VIBE is also outperforming breath-hold imaging in this practical reading aspect.
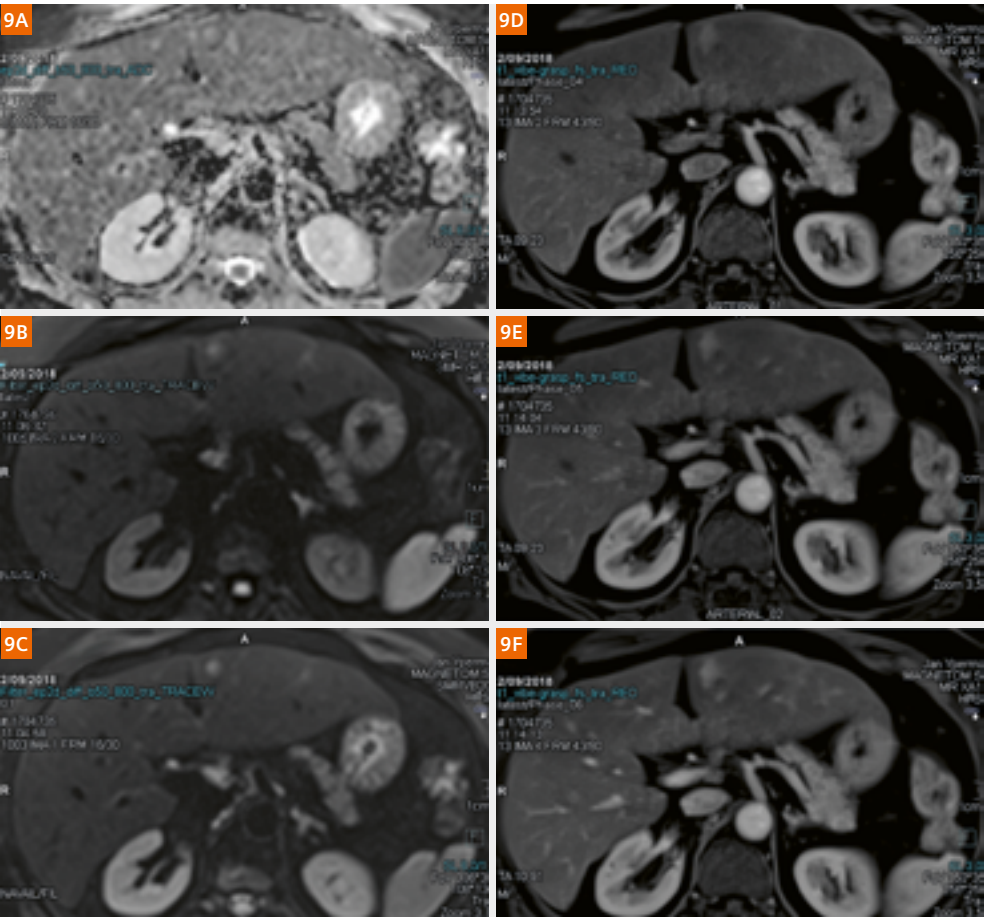
Figure 9:
The DWI **(9A–C)** nicely match the three arterial phases in a row **(9D–F)** making lesion detection and characterization easier and more reliable.
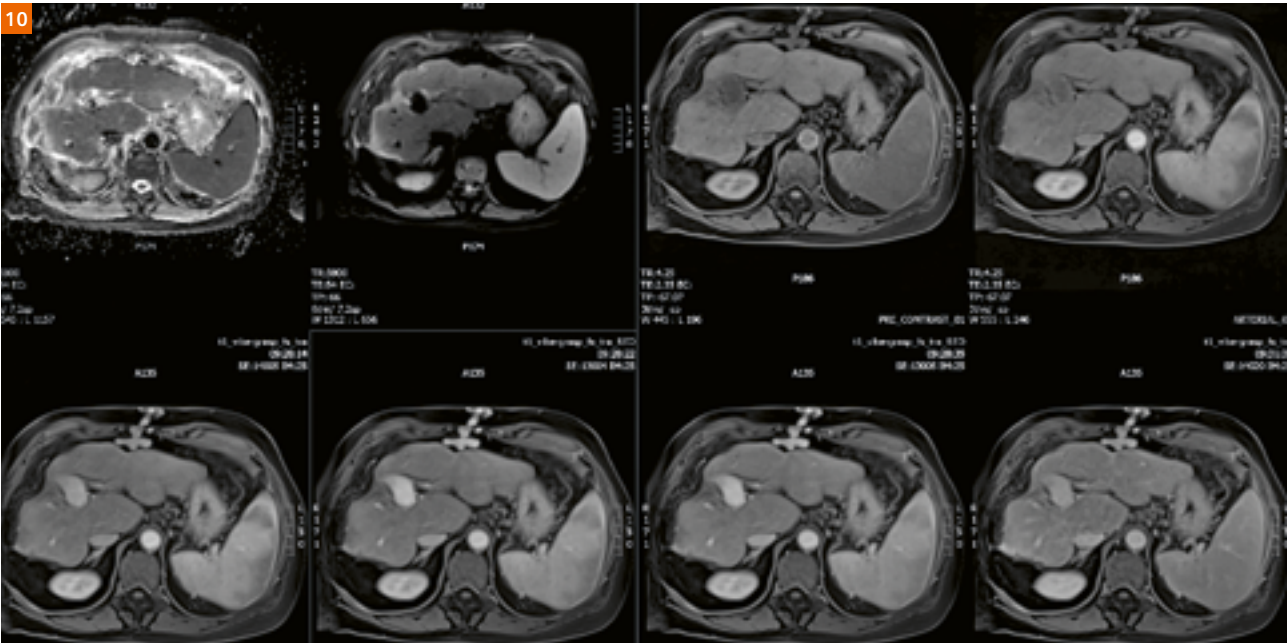

Figure 10:
Macronodular liver cirrhosis with recanalized umbilical vein; effortless dynamic imaging is perfectly aligned with the DWI thanks to the reconstruction in the expiratory phase.

Without respiratory gating in reconstruction, we can take temporal and spatial resolution even higher – as high as 28 slices x 1 mm in-plane, 3 mm thick every 3 seconds as in this case of fibromuscular stroma carcinoma of the prostate extending in the transition zone. Just as in liver imaging, side-by-side comparison with DWI is able to "resolve" prostate issues with amazing simplicity and accuracy.
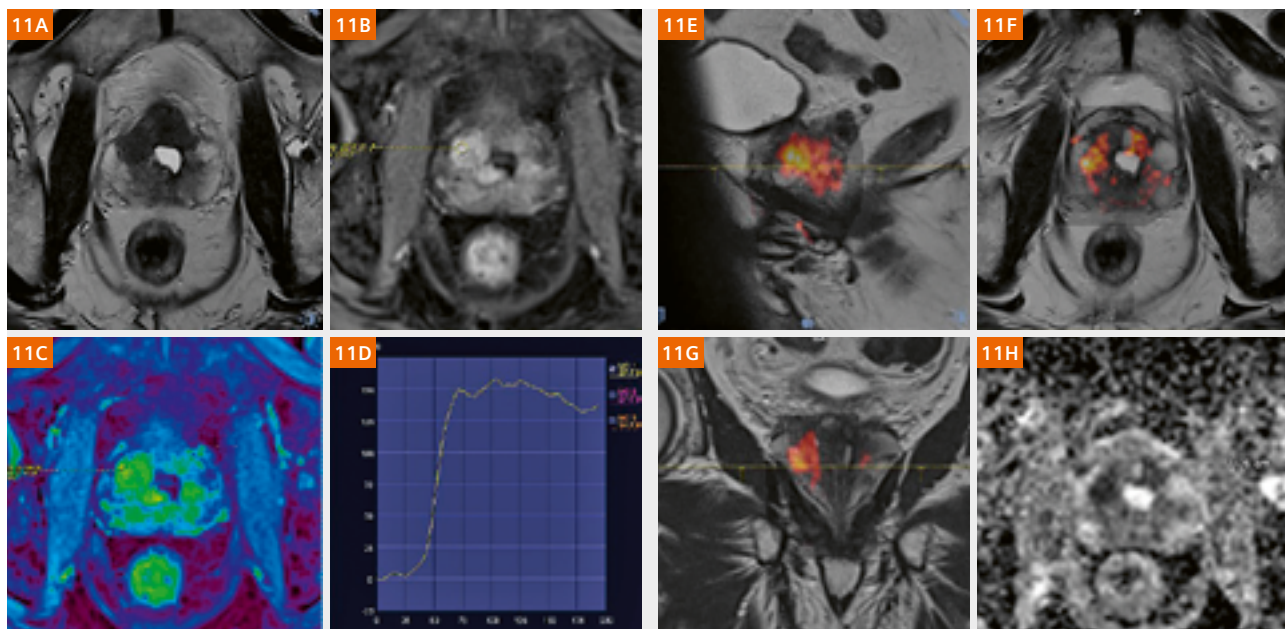

Figure 11:
Axial T2 **(11A)** demonstrating charcoal-like dark mass, capsule retraction. Fusion images of high b-value and T2 demonstrating diffusion restriction in the T2 dark zones Ax 4D GRASP **(11F)**; wash in-wash out pattern depicted on the graph. ADC map **(11H)** with restricted diffusion.
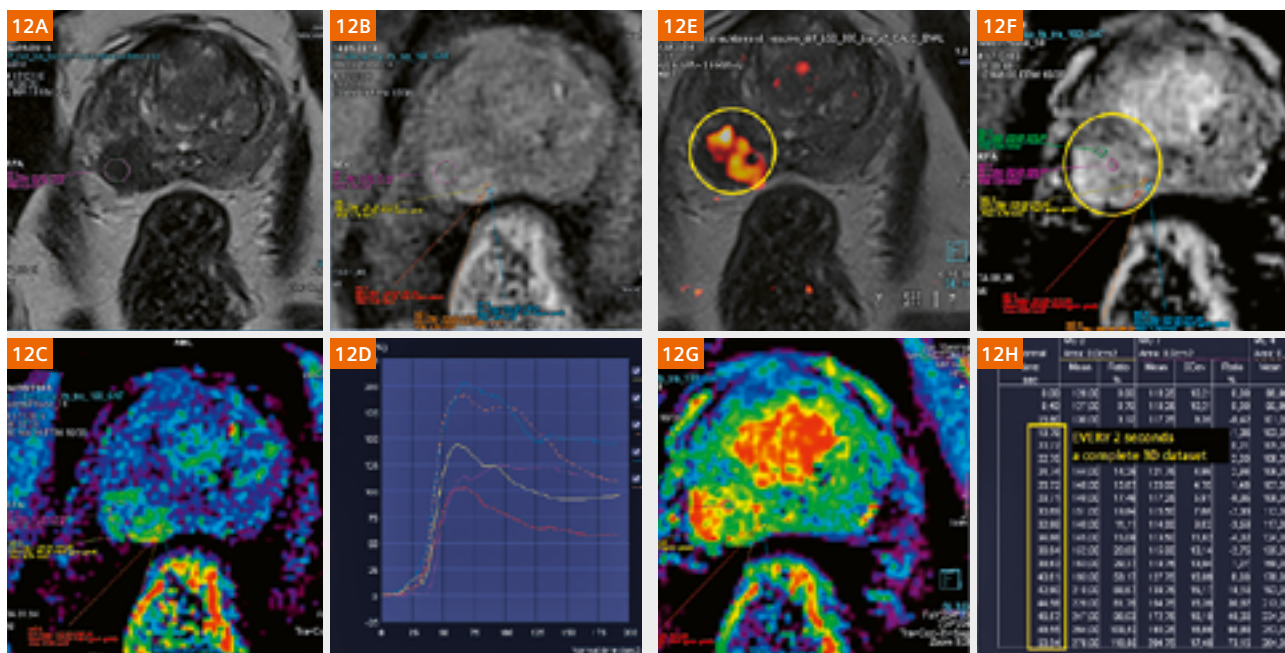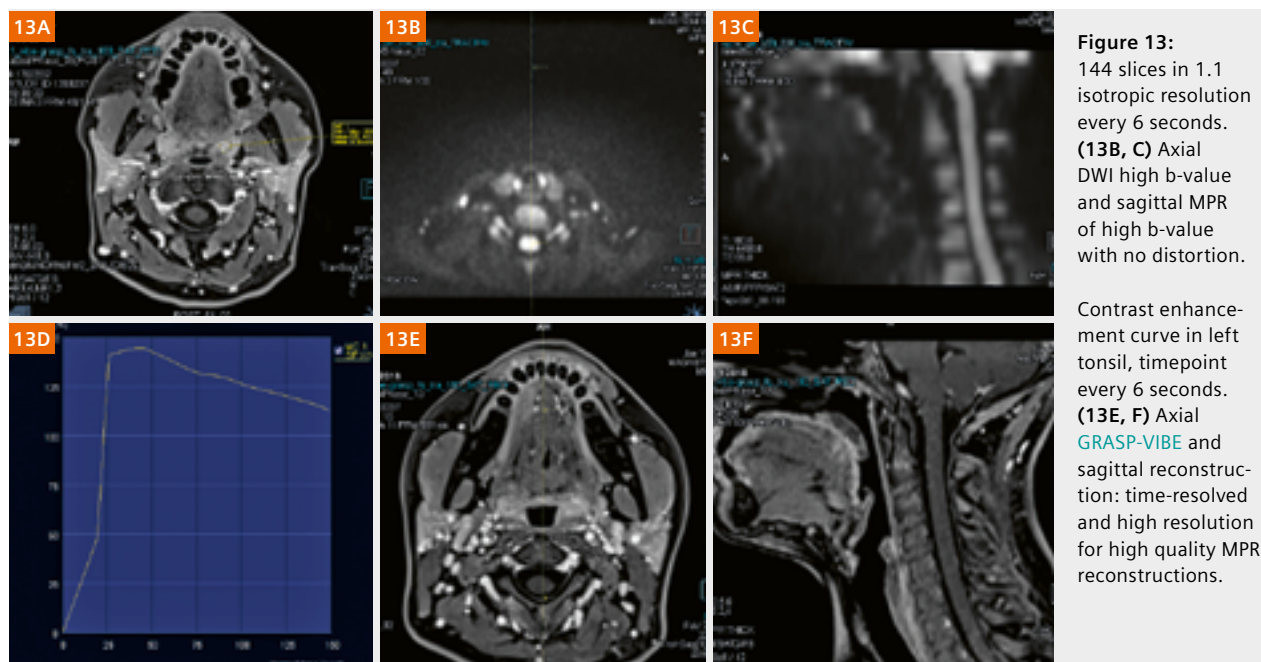
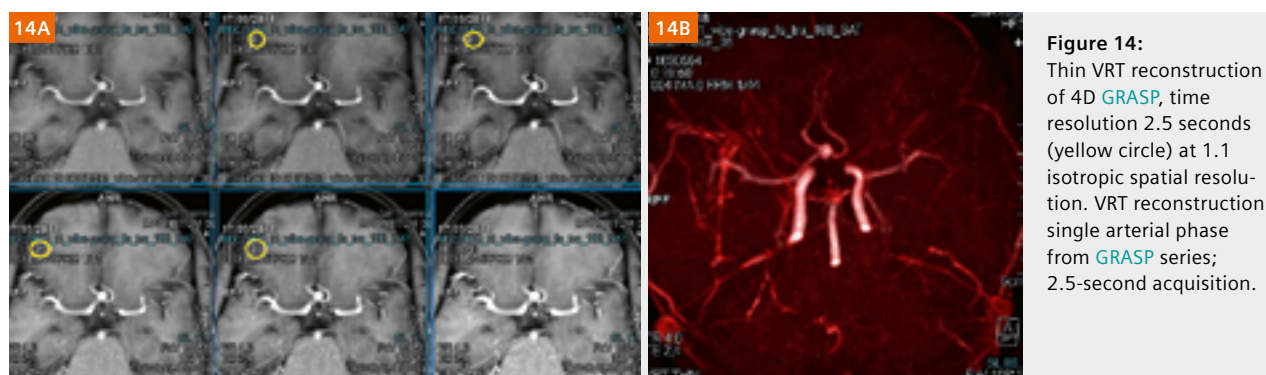

Figure 12:
Besides the contrast enhancement curve, one can see the wash in **(12B)** in addition to seeing the wash out **(12F)** (yellow circle).
Also note the T2 hypointense nodule **(12A)** and corresponding DWI fusion image with high b-value hyperintensity **(12E)** (yellow circle).
Note time resolution in the mean curve table: 2 seconds for 36 x 3 mm slices; 1 mm in-plane resolution.

GRASP-VIBE is an excellent solution to counter motion artifacts, on the one hand, and for resolving contrast enhancement dynamics, on the other hand, making it ideal for neck imaging[1]. In radiology, the neck is also known as the "Great Swallowing Region".

1 mm in-plane resolution and slice thickness of 1.1 mm, 144 slices covered every 6 seconds artifact-free. This means not only no swallowing artifacts, but also robust fatsat thanks to the CoilShim. This same CoilShim allows perfect DWI in the neck, which was previously difficult to achieve.

Figure 13:
144 slices in 1.1 isotropic resolution every 6 seconds. **(13B, C)** Axial DWI high b-value and sagittal MPR of high b-value with no distortion.

Contrast enhancement curve in left tonsil, timepoint every 6 seconds. **(13E, F)** Axial GRASP-VIBE and sagittal reconstruction: time-resolved and high resolution for high quality MPR reconstructions.

We can push the speed of GRASP acquisition even further; fast enough to grasp the filling of an aneurysm. 1.1 isotropic acquisition matrix and 2.5 seconds temporal resolution.

Figure 14:
Thin VRT reconstruction of 4D GRASP, time resolution 2.5 seconds (yellow circle) at 1.1 isotropic spatial resolution. VRT reconstruction single arterial phase from GRASP series; 2.5-second acquisition.

[1]Compressed Sensing GRASP-VIBE for other regions than liver is not for sale in the U.S. Intended Use: Compressed Sensing GRASP-VIBE (GRASP = Golden-angle Radial Sparse Parallel MRI) is intended to be used in dynamic and/or non-contrast liver examinations to support patients who cannot reliably hold their breath for a conventional breath-hold measurement.

Introduction

Obesity is one of the most common lifestyle diseases in many countries and has led to a dramatic increase in patients diagnosed with non-alcoholic fatty liver disease (NAFLD). Within just half a decade, prevalence of NAFLD among a general population in the United States increased from 15% in 2005 to 25% in 2010 [1]. The picture is even more dramatic in the obese population with the reported prevalence ranging from 30–37% [2].

The clinical appearance of NAFLD encompasses a broad spectrum ranging from mild fatty liver disease, steatosis, inflammation, fibrosis, cirrhosis, and, finally,

Figure 1:
Sequence scheme for conventional GRE MRE **(1A)** and rapid fractional MRE **(1B)**.

to hepatocellular carcinoma. Early detection and grading of fibrosis, therefore, has important implications for the management of patients with NAFLD to retard the progression to more severe stages of liver disease.

Percutaneous liver biopsy and histopathological analysis used to be the standard method to confirm and classify nonalcoholic steatohepatitis (NASH). This has now been widely replaced by noninvasive tests such as Ultrasound Elastography and MR Elastography (MRE) of the liver. In several comparison studies of MRE with different Ultrasound Elastography techniques, and MRE with functional MR imaging, MRE has been shown to exceed all other techniques in terms of diagnostic accuracy, sensitivity, specificity, and organ coverage [3–5].

Commercially available solutions for MRE allow the assessment of liver stiffness to be seamlessly integrated into a normal MR examination, including automated processing of the data[1].

How does MRE work? MRE depicts motion of mechanical shear waves in tissue using motion-sensitized sequences, followed by 'inverting' the wave pattern to deduce tissue stiffness. External motion is induced by an acoustic driver system (Resoundant Inc., Rochester, MN, USA). MRE requires additional hardware, and mechanical wave propagation varies inter-individually, so in practical application MRE does have some pitfalls, which if ignored, may lead to e.g., improper tissue actuation, offset slice positioning, and, ultimately, suboptimal results. Another challenge is posed by patients with marked iron deposits in the liver: In these cases, T2*-mediated signal loss can make it impossible to sufficiently capture the shear wave propagation through tissue using MRI. According to the literature, the technical failure rate is about 10% for conventional GRE-based MRE [6].

Alternative ways to overcome this problem include the use of fractional encoding [7] to allow a shorter echo time (TE) and the use of spin-echo-based MRE sequences [8].

Therefore, it is essential to set up the MRE equipment carefully, prepare patients properly, and choose the right MRE sequence for the given case. And ensure that the evaluation of stiffness values follows established procedures. This article provides some practical guidance and tips on how to perform MRE successfully in daily clinical practice.
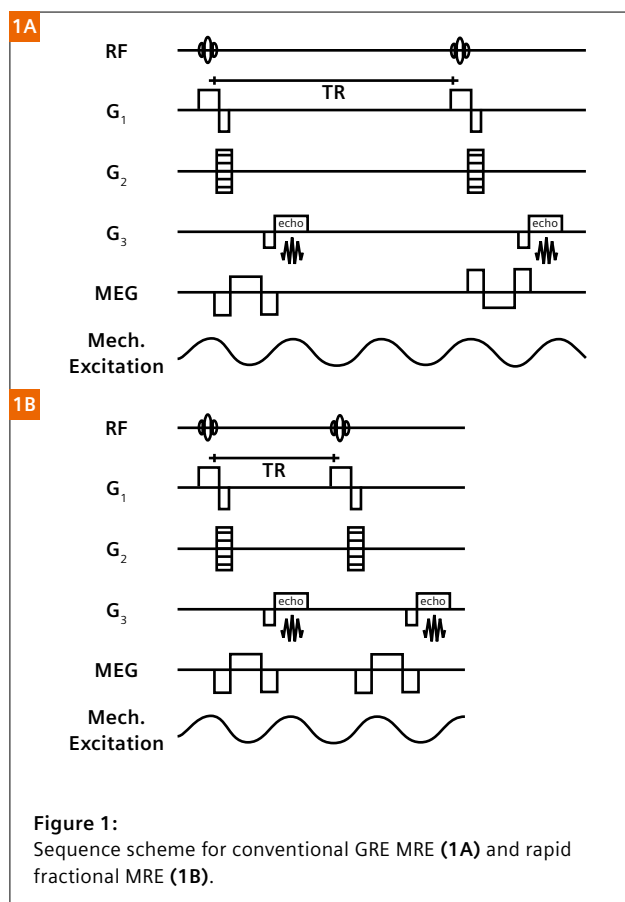
MRE sequence improvements tailored to different use cases

Rapid MRE[2]

In the original version, MRE is performed with a phase-contrast gradient recalled echo (GRE) sequence, which applies motion-encoding gradients (MEGs) in synchronization with a 60 Hz external shear wave induced to the abdomen (Fig. 1A). This scheme is repeated every 50 ms with alternating polarity of the MEGs, resulting in a total acquisition time of about 20 seconds per slice, depending on the spatial resolution [9].

With rapid GRE (RF-GRE, [9]) this scheme is optimized as follows: Instead of applying MEGs with different polarity every 50 ms in the same phase of the mechanical excitation, the MEGs are played out with the same polarity every 25 ms, matching with opposite phases of the mechanical excitation (Fig. 1B).

The 50% shorter TRs dramatically reduce the required breath-hold duration. This means that patients have to hold their breath for just ~10 seconds rather than ~20 seconds, positively impacting the robustness of the method.

Fractional MRE encoding[3]

Motion encoding is normally done with a gradient waveform matching the mechanical wave period, i.e. a "1-2-1" MEG of 16.6 ms duration at 60 Hz driver frequency. This puts a lower limit on the achievable minimum TE, wh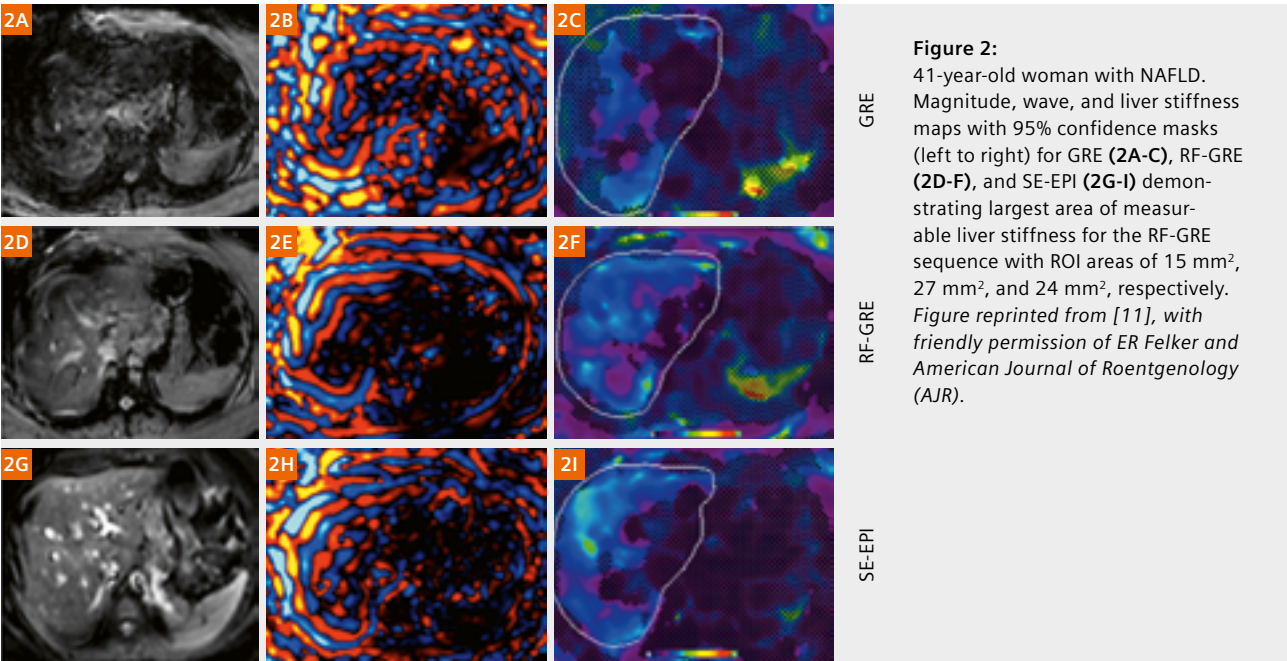ich may be too long for livers with iron overload, or at 3T. Alternatively, shortened, 'fractional' MEGs can be used. These have a lower motion-encoding strength, but the resulting shorter TE makes the GRE sequence less prone to T2*-induced signal loss, giving a net benefit for the final MRE result [10].

Spin Echo EPI MRE[4]

As an alternative to a GRE-type sequence for MRE, a Spin Echo (SE) sequence with a fast Echo-planar imaging (EPI) readout can also be used for MRE [8]. Due to the rapid readout, all required *k*-space data for several slices can typically be acquired within a 10–12 second breath-hold. Other advantages of the SE-EPI based approach are a higher robustness in patients with iron overload and a higher signal-to-noise ratio of the wave images compared with GRE-based MRE. SE-EPI MRE can also be combined with fractional encoding.

	Conventional GRE	RF-GRE	SE-EPI
Breath-hold duration	~20 sec	~10 sec	~10 sec
Measureable area of liver stiffness		+	+
Robustness against iron overload		+	++

[2]Rapid MRE is available with the syngo MR E11C software version.
[3]Rapid and fractional gre-MRE are available with syngo MR E11C. (There are no new protocols in the Siemens tree, but recommended protocols are available from application support.)
[4]Spin Echo MRE is available with the syngo MR E11E software version. The product is still under development and not commercially available yet. Its future availability cannot be ensured.

Figure 2:
41-year-old woman with NAFLD. Magnitude, wave, and liver stiffness maps with 95% confidence masks (left to right) for GRE **(2A-C)**, RF-GRE **(2D-F)**, and SE-EPI **(2G-I)** demonstrating largest area of measurable liver stiffness for the RF-GRE sequence with ROI areas of 15 mm², 27 mm², and 24 mm², respectively. *Figure reprinted from [11], with friendly permission of ER Felker and American Journal of Roentgenology (AJR).*
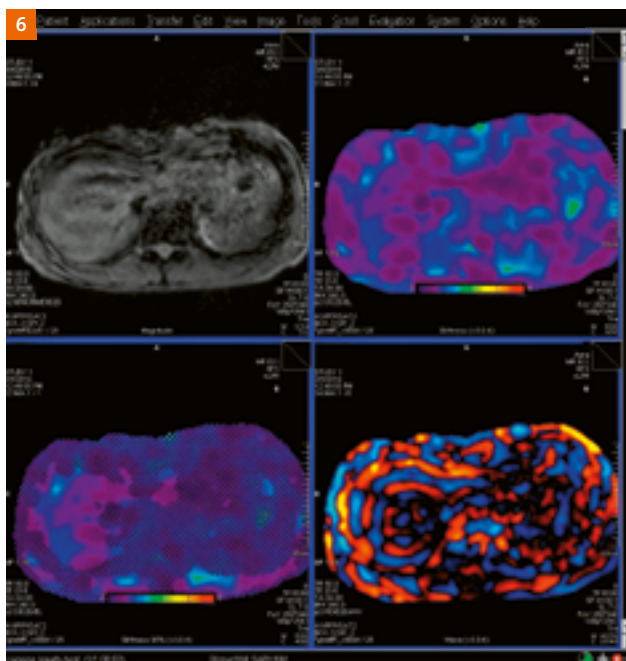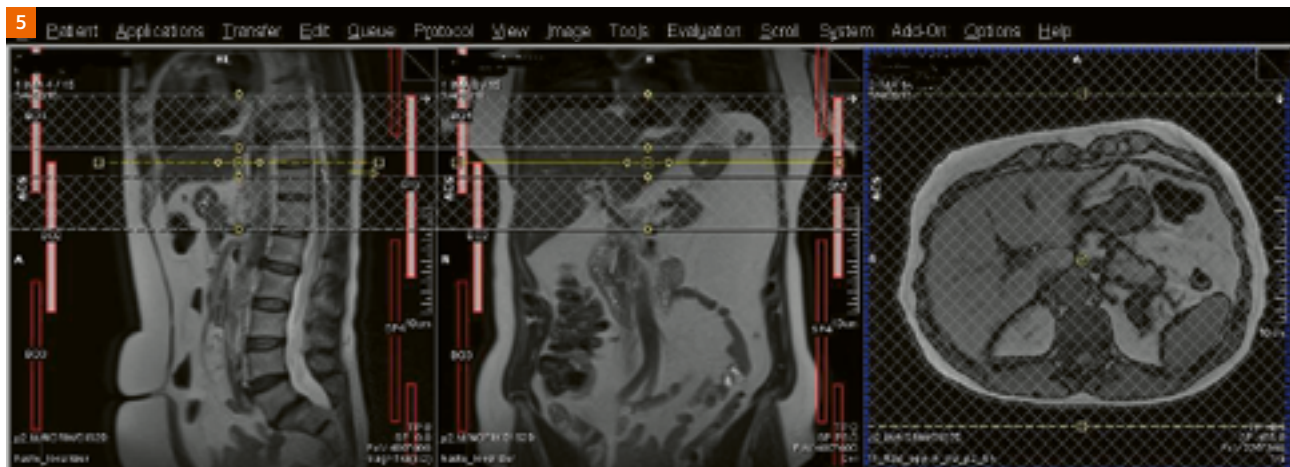
Comparison of methods

A recently published study [11] has compared conventional GRE, RF-GRE, and SE-EPI for MRE. While the study found no equivalent measures of liver stiffness for all techniques, significant differences in terms of failure rates and measureable areas of liver stiffness were found: Both RF-GRE and SE-EPI yielded larger measureable areas than conventional GRE, with RF-GRE having the largest measureable areas. Among patients with iron overload, there was a trend toward a larger measurable area of liver stiffness with SE-EPI. A corresponding example is shown in Figure 2.

Given that liver fibrosis is often spatially heterogeneous, the volume of liver sampled is considered one of the key advantages of MR Elastography compared with liver biopsy and ultrasound elastography. Therefore, RF-GRE appears to be the best choice in patients with normal iron concentrations in the liver, while SE-EPI appears to be superior for patients with iron overload.

Elastography can be performed at the beginning or end of a routine liver examination, this is a site preference.

1. Prior to positioning the patient turn on the Active Driver (Figure 3 – found in the equipment room).
    Note: The Active Driver goes into sleep mode after approximately one hour of inactivity.

2. Position the patient for an abdominal examination. Position the black Velcro Band directly underneath the liver.

3. Place the paddle (Passive Driver) on patient's right upper abdomen so that 1/4 of the paddle is over midline and 1/3 of the paddle is below the bottom of the rib cage (Fig. 4).
    Note: The tubing from the paddle can be placed coming from head or feet depending on scan room configuration.

4. Secure the paddle on the patient using the black Velcro Band. Please ensure that the entire paddle has good contact with the upper abdomen and is flat against the body surface. If the paddle has improper contact or is rocking back and forth try to adjust the position slightly for better contact.
    Note: Please make sure that the black Velcro Band is secured very tight on patient and paddle.

5. Prepare the patient mentally for the examination.
    a. Inform the patient that Elastography is performed at end expiration.
    b. Notify the patient, that she/he will feel pressure coming from the paddle during the examination.

6. Place the Body Array coil on the patient for a liver examination.

7. Register the patient and select the appropriate abdominal imaging protocol.

8. As indicated before, MRE can either be performed at the beginning or in the end of the abdominal examination.
    Note: Please make sure, that the localizer images / images used for planning the MRE exam are acquired in end expiration.

9. Planning of MRE scans: Position the MRE acquisition slice in the mid of the liver as indicated in the images (Fig. 5).

scale indicates shear stiffness values in kPa ranging from 0–8 kPa.

Stiffness Map with 95% confidence mask overlay (hatched areas): With the confidence mask, areas where the calculated relative shear wave stiffness values are unreliable, are hashed out. This allows exclusion of areas of insufficient data quality.

Wave images: Wave images illustrate the propagation of shear waves through tissue with different speed and wave length. Based on this information, the Stiffness Maps are automatically calculated by the software (Fig. 6).

10. Instruct the patient again, that during the exam vibrations will be felt from the paddle.

11. Apply MR Elastography sequence. Perform the breath-holds in the exam at the end expiratory state.

12. Load and review images in Viewing Task Card to assess image quality. The following four series will be displayed (clockwise order):
    Magnitude image: standard MRI image to evaluate general image quality such as breath-hold quality or SNR.
    Stiffness Map / Elastogram: The elastogram is calculated from the shear wave images and represents the relative shear stiffness of tissue. The color

13. Image quality assurance: Check Magnitude images for image quality.
    a. Check if the patient held the breath properly.
    b. Check if the signal quality is sufficient, i.e. signal drops, inhomogeneities.
       • Is the liver very dark?
       • Is there a lot of lung tissue, but not much liver tissue in the FOV?
    Note: If the quality is sub-optimal repeat the acquisition after checking proper slice positioning and reminding the patient to follow the instructions carefully.

14. Depending on the local preferences, repeat the MRE acquisition in different locations of the liver in H-F direction.
    Note: Typically, 3–4 contiguous slices near the center of the liver are used.

15. Image analysis / post-processing: Select the Stiffness 95% Map and draw an ROI inside the grid area, avoiding meshed areas. Ensure that the ROI is drawn in liver tissue only. To draw an ROI select the "Tools" subtask card in the Viewing Task Card. Select the Circle ROI or Freehand ROI tool (Fig. 7).

16. Draw an ROI as described above. The displayed "Mean Value" divided by 100 shows the Relative Shear Stiffness in kPA in the ROI (Fig. 8).

17. Repeat this process for all acquired slices and average the resulting stiffness values.

Image quality troubleshooting tips

Anatomical Masking Failure – occurs when signal levels in the liver are lower than other structures in the slice. Review the GRE Magnitude image.
- Is there tissue that has brighter tissue then the liver (see Figure 9)?
- Does the tissue in the posterior peripheral tissue have brighter signal intensity then the liver does?
- Is the patient's stomach full?
- Tip: Repeat series with Sat band over bright signal (Fig. 9).
- If the entire liver is rejected by the confidence mask, shear waves may be missing in the tissue.
- Is the Active Driver turned off or in sleep mode?
- Did one of the hoses come undone?

References:

1 Perumpail B, Khan MA, Yoo ER, Cholankeril G, Kin D, Ahmed, A. Clinical epidemiology and disease burden of nonalcoholic fatty liver disease. World J Gastroenterol. 2017 Dec 21; 23(47): 8263–8276.

2 Vernon G, Baranova A, Younossi ZM. Systematic review: the epidemiology and natural history of non-alcoholic fatty liver disease and non-alcoholic steatohepatitis in adults. Aliment Pharmacol Ther. 2011;34:274–285.

3 Tang A, Cloutier G, Szeverenyi NM, Sirlin CB. Ultrasound Elastography and MR Elastography for Assessing Liver Fibrosis: Part 1, Principles and Techniques. American journal of roentgenology. 2015;205:22–32.

4 Rizzo L, Calvaruso V, Cacopardo B, et al. Comparison of transient elastography and acoustic radiation force impulse for non-invasive staging of liver fibrosis in patients with chronic hepatitis C. Am J Gastroenterol. 2011;106:2112–2120.

5 Yoon JH, Lee JM, Joo I, et al. Hepatic fibrosis: prospective comparison of MR elastography and US shear-wave elastography for evaluation. Radiology. 2014;273:772–782.

6 Kim YS, Song JS, Kannengiesser S, Seo SY. Comparison of spin-echo echoplanar imaging and gradient recalled echo-based MR elastography at 3 Tesla with and without gadoxetic acid administration. Eur Radiol 2017;27(10):4120-4128.

7 Garteiser P, Sahebjavaher RS, Ter Beek LC, et al. Rapid acquisition of multifrequency, multislice and multidirectional MR elastography data with a fractionally encoded gradient echo sequence. NMR Biomed 2013; 26:1326-1335

8 Mariappan YK, Dzyubak B, Glaser KJ, et al. Application of Modified Spin-Echo-based Sequences for Hepatic MR Elastography: Evaluation, Comparison with the Conventional Gradient-Echo Sequence, and Preliminary Clinical Experience. Radiology 2017; 282:390-398.

9 Chamarthi SK, Raterman B, Mazumder R, Michaels A, Oza VM, Hanje J, Bolster B, Jin N, White RD, Kolipaka A. Rapid acquisition technique for MR elastography of the liver. Magn Reson Imaging. 2014 Jul;32(6):679-83.

10 Rump J, Klatt D, Braun J, Warmuth C, Sack I. Fractional Encoding of Harmonic Motions in MR Elastography. Magnetic Resonance in Medicine 2007(57):388-395.

11 Felker ER, Choi KS, Sung K, Wu HH, Raman SS, Bolster BD Jr, Kannengiesser S, Sorge K, Lu DSK. Liver MR Elastography at 3 T: Agreement Across Pulse Sequences and Effect of Liver R2* on Image Quality. AJR Am J Roentgenol. 2018 Sep;211(3):588-594.
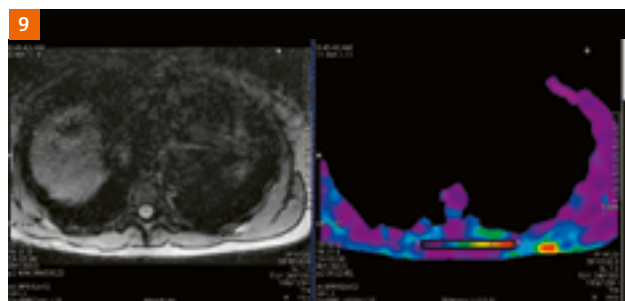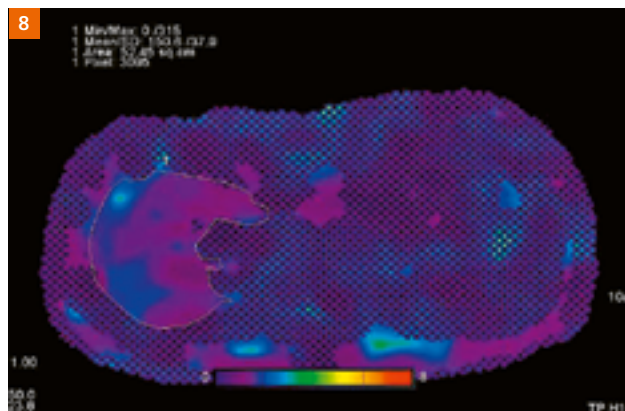
Simultaneous Multi-Slice (SMS) acquisition is a technique that we know from EPI DWI that delivers consistently good results. SMS enables faster scan times and thinner slices, leading to an increase in resolution, better diagnosis, and more productivity at the scanner. The value of SMS is known from extensive experience with the MAGNETOM Aera system. Since SMS TSE (turbo spin echo) is an integral part of MAGNETOM Sola, we were eager to start using SMS in TSE imaging.

Using SMS with a factor 2 on MAGNETOM Sola renders twice the amount of slices in the same time. So, you can either scan faster (halving the number of concatenations in T1 for example), or scan 50% thinner slices, or achieve 200% coverage with the same slice thickness, or combine all of them. Numerous thin slices are especially beneficial in the axial plane; however, where you need many coronal or sagittal slices, SMS is also the best option since it does not consume time or signal.

Using SMS in small joint imaging like wrist, elbow, and ankle, we are able to achieve large coverage with really thin slices. Also it allows us to scan the complete pelvis/both hips with thin slices – as thin as 3 or even 2 mm. This would have required a prohibitive amount of time before SMS TSE. It can also be employed whenever you need the combination of large coverage and thin slices, e.g., to examine the course of a peripheral nerve.

Looking at our initial experiments with SMS TSE, we began by simply ticking the checkbox SMS factor 2 in the acceleration subcard of the resolution card in a coronal T1 TSE sequence and using that SMS factor to bring the number of concatenations from 2 to 1:
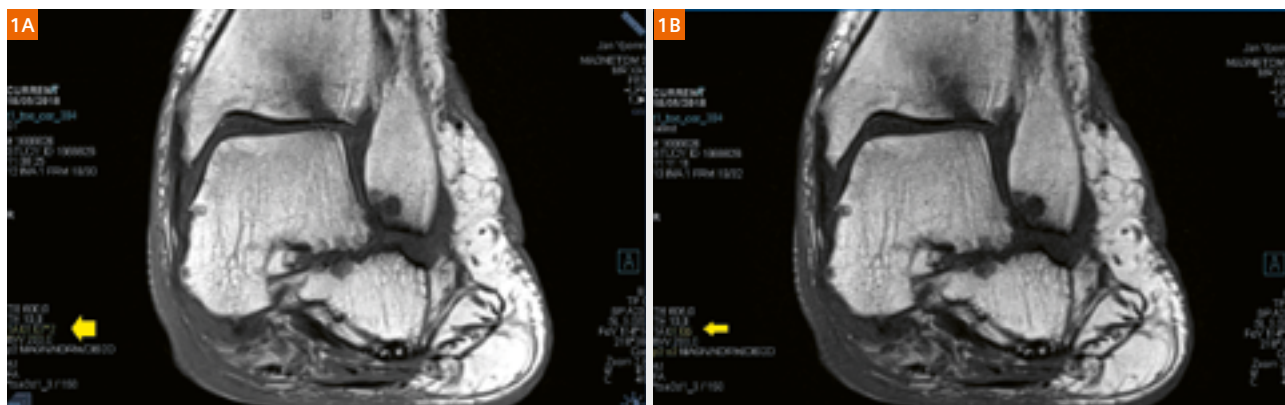
Figure 1:
Corresponding image of the first attempt at SMS: Simply ticking SMS factor 2 halves the number of concatenations from 2 to 1. This effectively halves the acquisition time from 02:14 min to 01:05 min (yellow arrow) without discernable loss in signal or image quality.
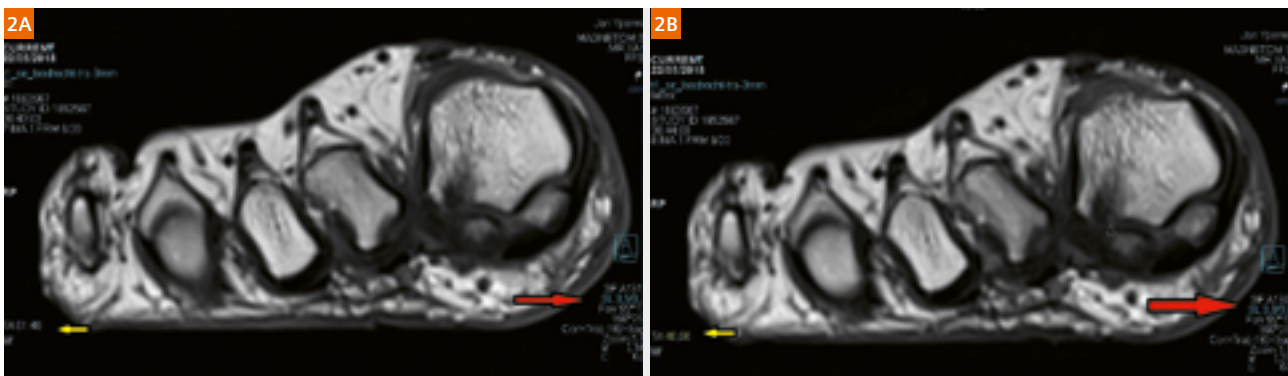
Figure 2:
Another early experiment using SMS to scan with a thinner slice thickness (red arrow). This actually leads to better depiction of osteochondral lesion (top of yellow triangle) and 60% reduction in acquisition time (yellow arrow). **(2A)** 3.5 mm in 100 seconds, **(2B)** 3 mm slice thickness in 40 seconds.

This early experimenting was quite convincing and SMS TSE was subsequently adopted in most of our 2D TSE MSK sequences early on. The only exception was in regions where there is already enough coverage with thin slices, e.g., coronal slices of distal extremities (fingers, toes ...), where only a small number of slices are needed. Our main goal is to scan quickly (SMS halves the number of concatenations in T1; halves the TR in intermediate-weighted sequences) and/or increase resolution by scanning thinner slices where SMS halves the TR. This eliminates the time penalty one normally gets by increasing the number of slices. One can also use SMS to remaster and optimize sequences from scratch to combine thinner slices, more coverage, and a shorter acquisition time. SMS is yet another degree of freedom to further optimize your imaging.

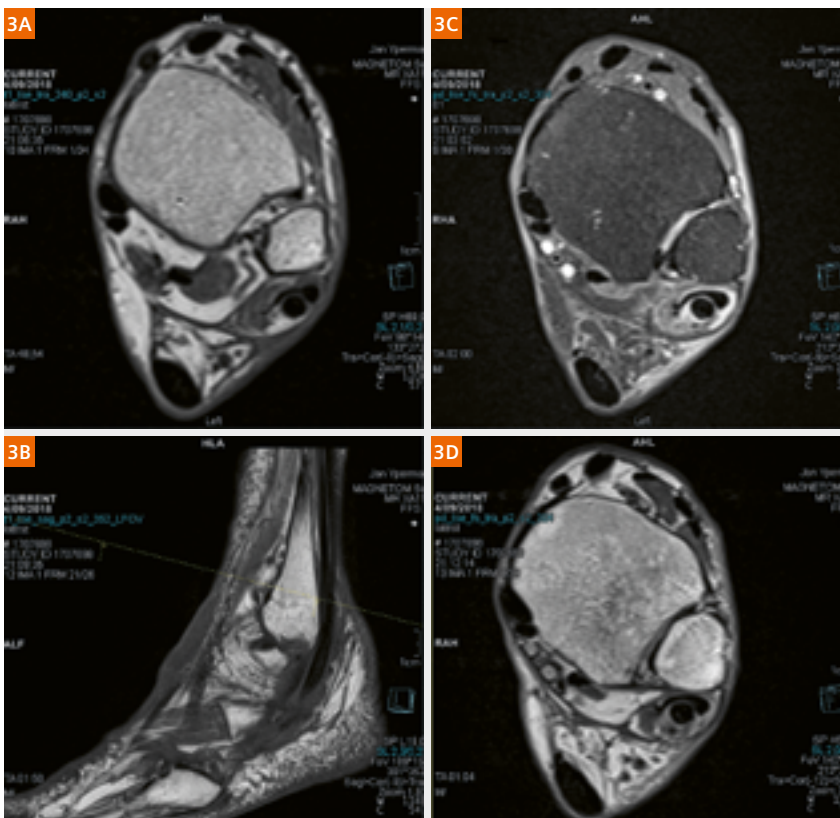Some examples from our clinical routine in the following cases:

Figure 3:
Example of SMS in an ankle exam. Sagittal and axial T1, 2 mm slices **(3A, B)** and axial PD and PD fatsat 2 mm images **(3C, D)** in high resolution and short imaging times nicely demonstrating peroneal tendon rupture.
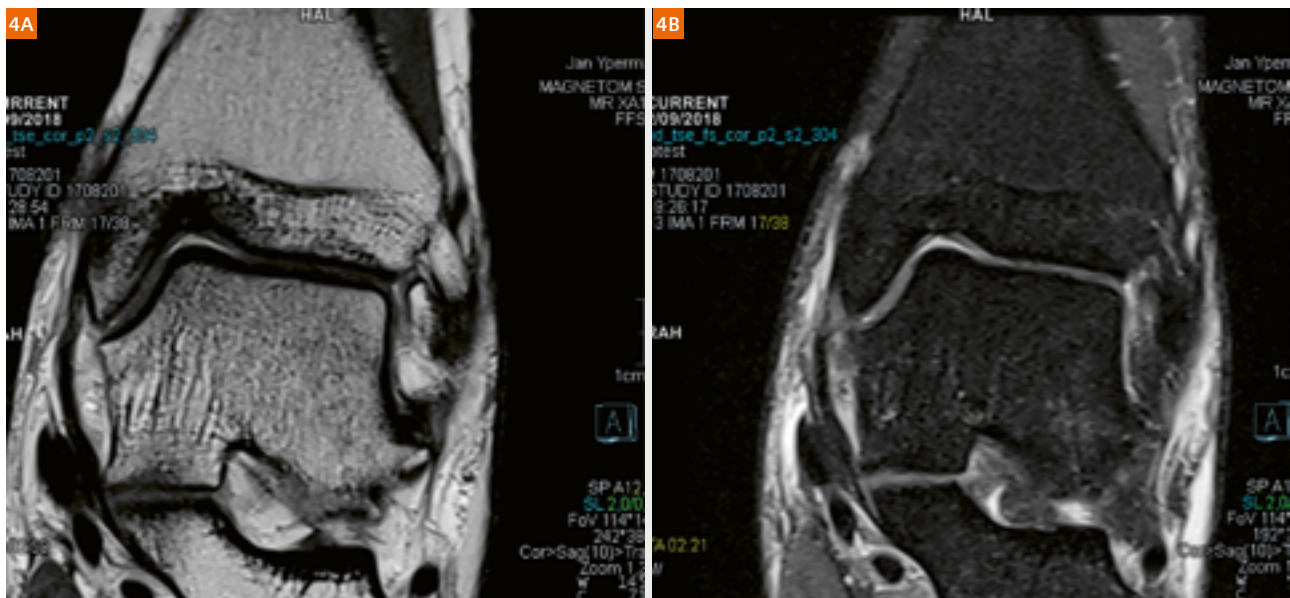
Figure 4:
Coronal PD and PD fatsat 2 mm slice thickness, 0.5 mm in-plane resolution and 38 slices in 2.21 seconds for the PD fatsat.
Great delineation of cartilage in talar dome and distal tibia; at 1.5T.
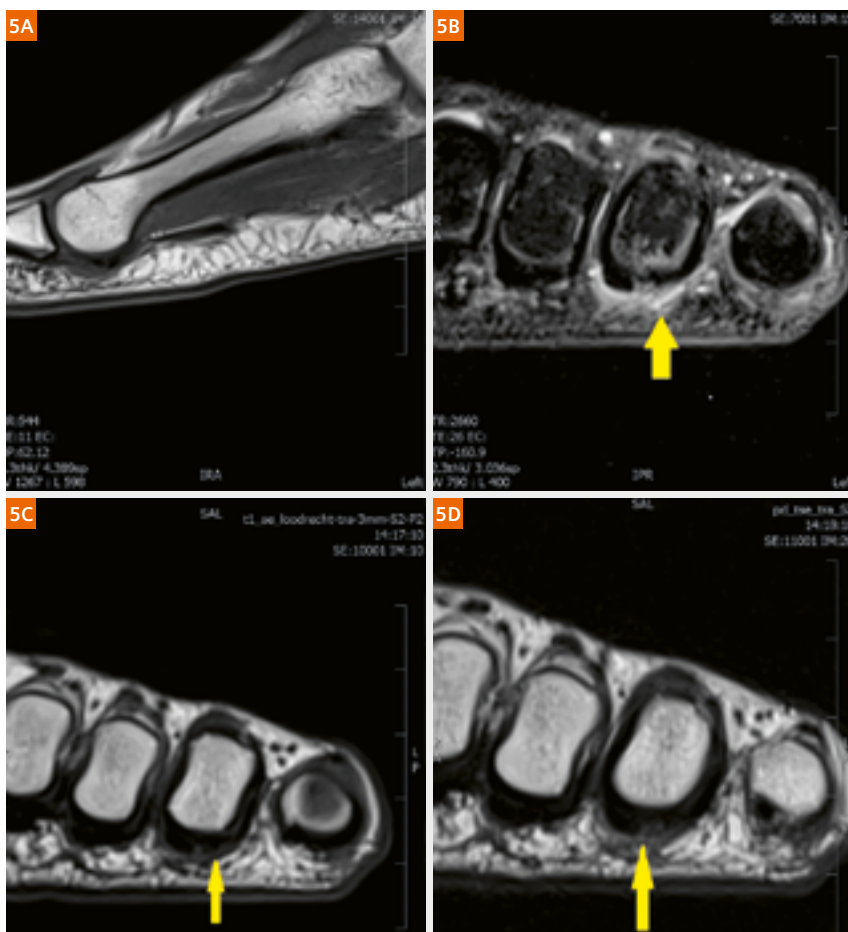

Figure 5:
Plantar plate tear (yellow arrow) easily depicted on thin slice imaging: Fast and with many thin slices is the new adage in foot imaging!

In hip imaging, standard full coverage of both hips and complete pelvis was formerly done with 5 mm slice thickness, since thinner slices would demand more TR and or concatenations, making it impossible to fit this exam into our 20-minute timeslot. Again, SMS imaging is the solution to scan more and thinner slices in the same or shorter acquisition time, leading to standard use of SMS for standard hip/pelvis imaging (Fig. 6).
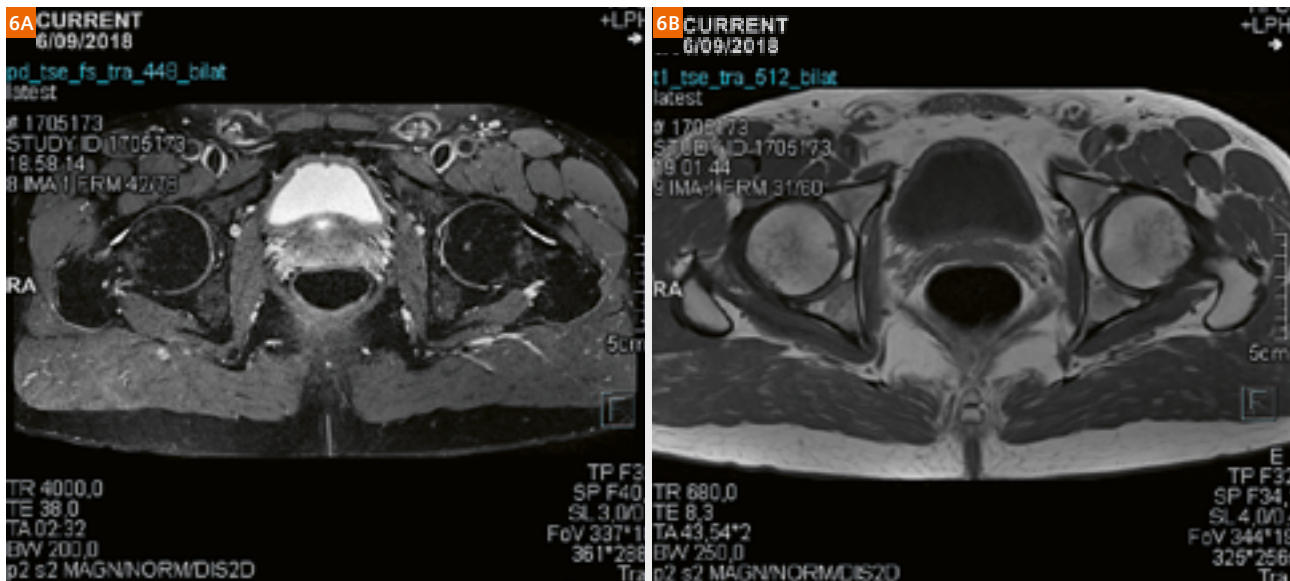
Figure 6:
Standard imaging of both hips: standard SMS PD fatsat 3 mm thick slices covers complete pelvis with 78 slices two and a half minutes and standard SMS T1 4 mm with 60 slices in one and a half minutes.

The combination of large coverage in the z-axis with thin axial slices can be especially challenging, e. g., scrutinizing the course of small peripheral nerves like the gluteal branches of the nervus cutaneus femoralis dorsalis, which is still considered to be a 3T indication. Thin-slice SMS with this convincing image quality in a reasonable time (4 minutes for 90 slices of 2 mm) improves the reputation of your facility by allowing you to say, "Of course we can because Sola is better than the 3T results we have seen in various studies." It takes some nerve, however MAGNETOM Sola and SMS thin slices allow you to perform these scans with confidence.
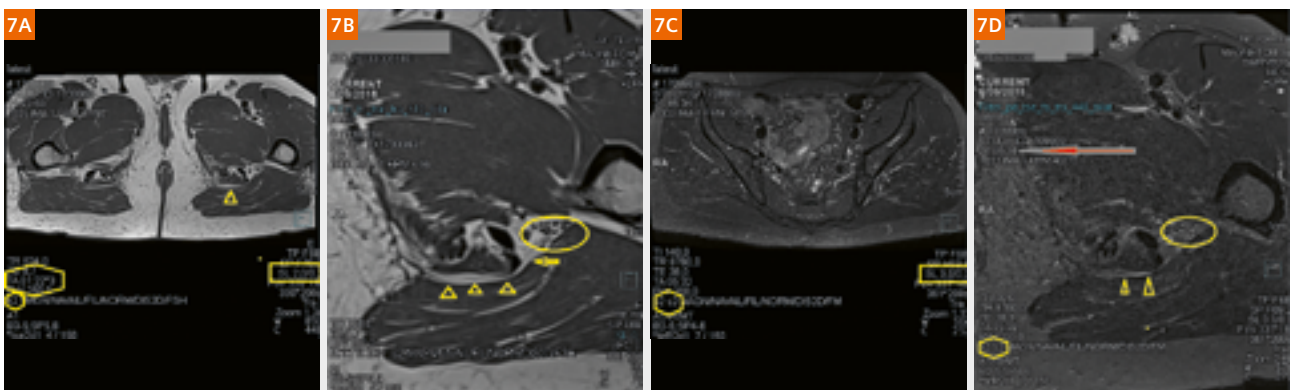
Figure 7:
SMS T1 TSE **(7A, B)**: 2 mm slices, 90 slices in 4 minutes. SMS PD fatsat 3 mm slices thickness **(7C, D)**. The images 7B and 7D are magnified. The yellow arrows point at the upper gluteal branch of the nervus cutaneus femoralis dorsalis dorsal to the semitendinosis, ventral to the gluteus maximus just caudal to tuber ischiadicum. Red arrow points to time in the evening. Sciatic nerve fascicles in yellow circle.

In the wrist, tendons run a long way. A great many thin slices are required to image them properly. SMS handles this task with ease and accuracy, in short acquisition times.
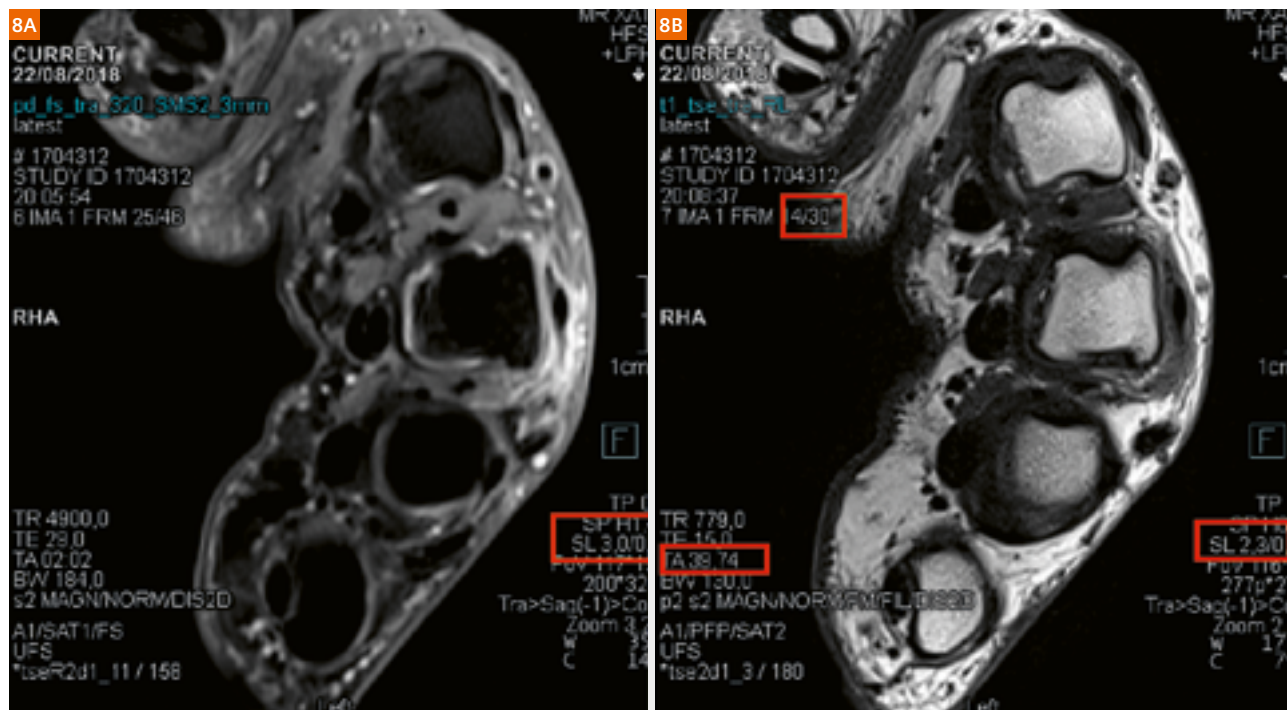
Figure 8:
Axial PD FS 46 slices 3 mm thick in 2 minutes, axial T1 TSE 30 slices 2.3 mm thick in 40 seconds. Ultra Flex Small 18-channel coil, imaged off center. SMS factor 2.
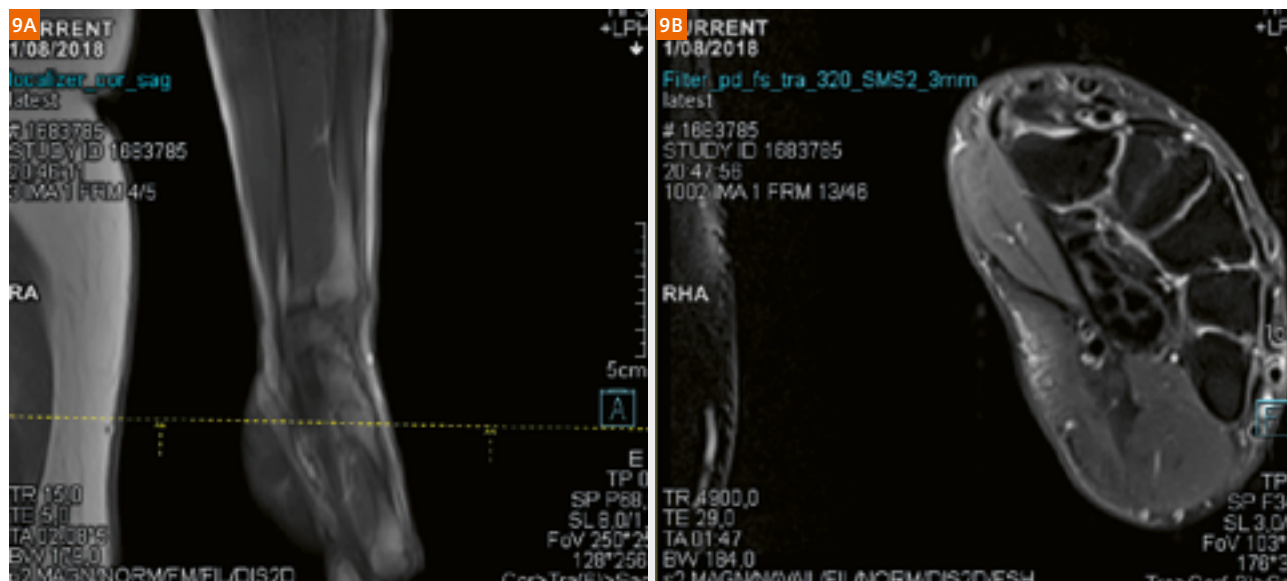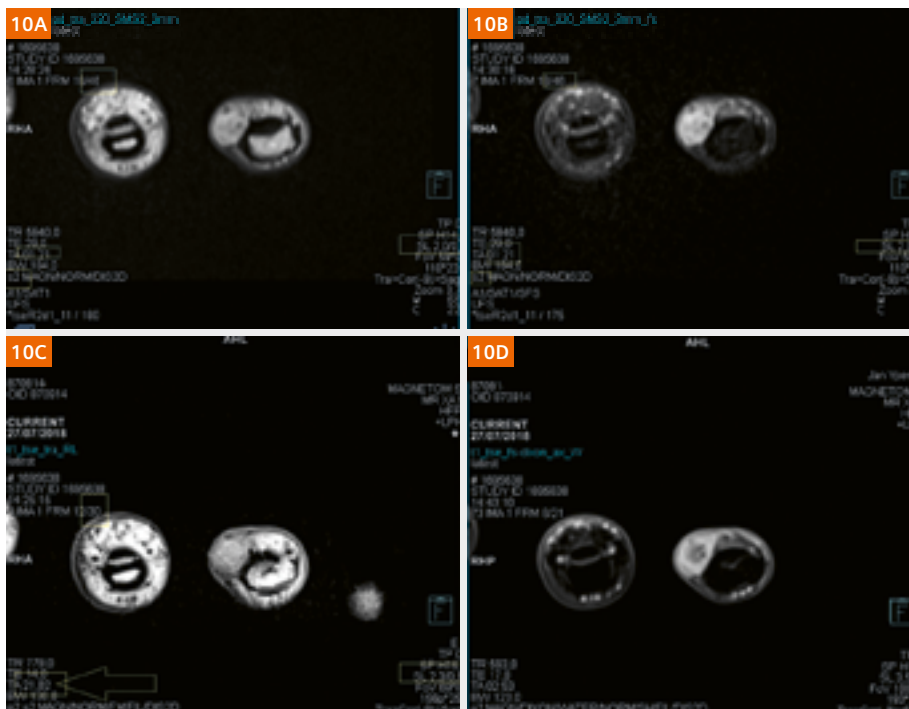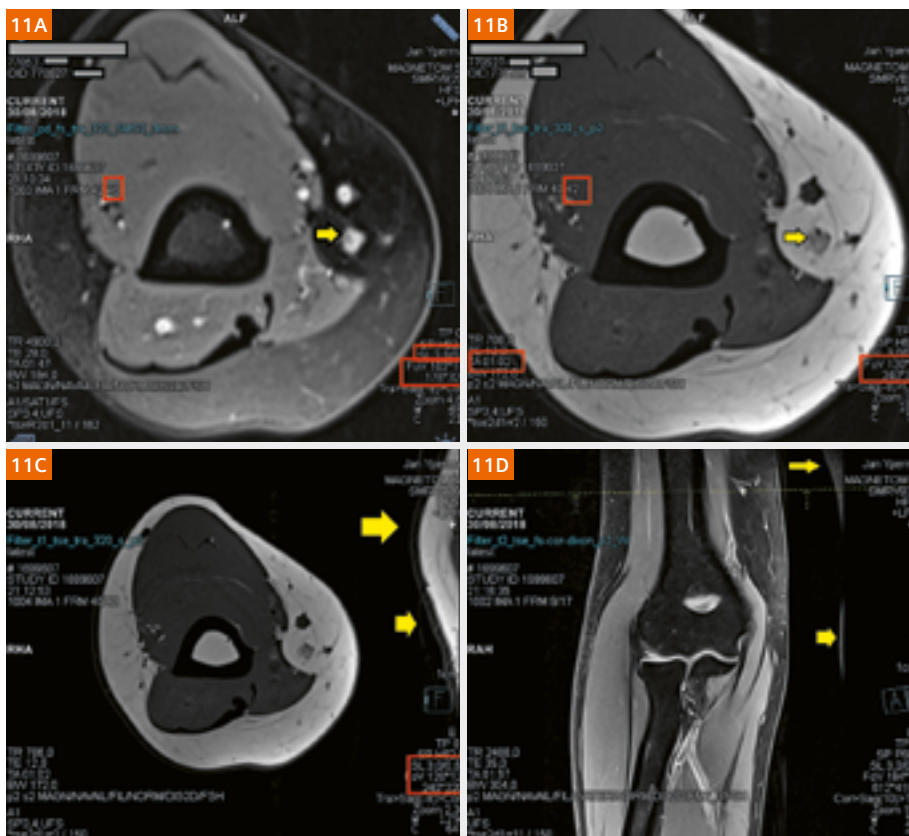
Figure 9:
The days of the superman position are over. Since we have had a MAGNETOM Sola, all wrist exams are done with the wrist comfortably resting next to the body, and the dedicated wrist coil is more often replaced by the comfortable Ultra Flex Small 18-channel coil.

Figure 10:
A 30-year-old female patient presented with bluish discoloration and swelling of the radial side of the ring finger, pain, and acceleration in swelling for several weeks. T1 and Proton Density iso – slightly hyperintense, PD fatstat hyperintense, peripheral fast-enhancing sharply demarcated subcutaneous mass with hypointense spots and hypoenhancing center. SMS makes it possible to have all these high resolution thin slices in an amazingly short acquisition time (notice 22 seconds for 30 slices T1 TSE 2.3 mm see 10C). Surgically confirmed partially thrombosed hemangioma). The T1 after contrast was done using Dixon fatsat since this challenging environment contains more air than tissue. Again, all images are acquired with the Ultra Flex Small coil.

Just as in wrist imaging, elbow imaging is no longer done using the knee coil in superman position, but conveniently off center with the elbow lying comfortably next to the body. Superman no longer holds a position in our department, he just got fired.

Figure 11:
Elbow exam with the arm resting comfortably to the right of the abdomen (right flank indicated by large yellow arrows). SMS imaging T1 and PD fatsat with thin slices 3 mm, high in-plane resolution (0.5 mm) and 42 T1 TSE slices in one minute and two seconds. Notice the high image quality allowing you to zoom in and pick up details like the hilum of a small lymph node (arrows in 11A, B).
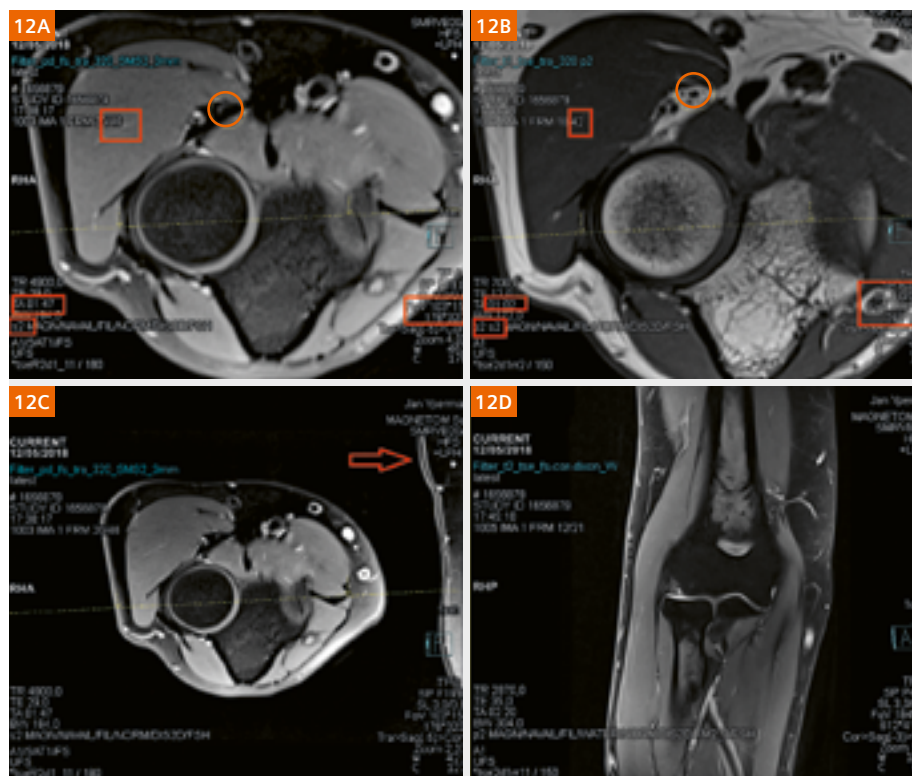
Figure 12:
Our first elbow exam with the Ultra Flex Small coil; off center, arm resting comfortably to the right of the abdomen (right flank indicated by large red arrow). SMS imaging T1 and PD fatsat with thin slices 3 mm, high in-plane resolution (0.5 mm); acquisition of 42! T1 TSE slices in one minute and two seconds. Zoomed images in the upper row show detail such as annular ligament surrounding radial head or, for example, the course of the radial nerve (circle).

GO protocols – consistent results in all joints

The new 18-channel Knee Coil is easy to handle, lightweight, and particularly comfortable for our patients. In the first four months of our experience with 1.5T MAGNETOM Sola to date, we have not yet had a single patient who did not fit in the knee coil. As shown in Figure 13, the patient is laying comfortably with her feet first leaving sufficient room in the knee coil and sufficient room for the other leg.

GOKnee3D, with the appealing concept of high resolution scanning at short examination times using SPACE 3D with CAIPIRINHA-based 4-fold acceleration, was introduced as early as 2017 by Jan Fritz, M.D., of Johns Hopkins University School of Medicine [1]. The GOKnee T2 FS comes out of the 'Siemens sequences box' at 0.8 mm isotropic. We enhanced that resolution to 0.6 isotropic proton density, which still provided us with more than enough signal. The new knee coil has improved patient comfort significantly, allowing patients to lie still. Based on prior experience, meniscal and

cartilage tear detection and characterization are highly facilitated by real 3D high resolution, while bone marrow edema is equally well depicted when compared to standard knee imaging.

Figure 13:
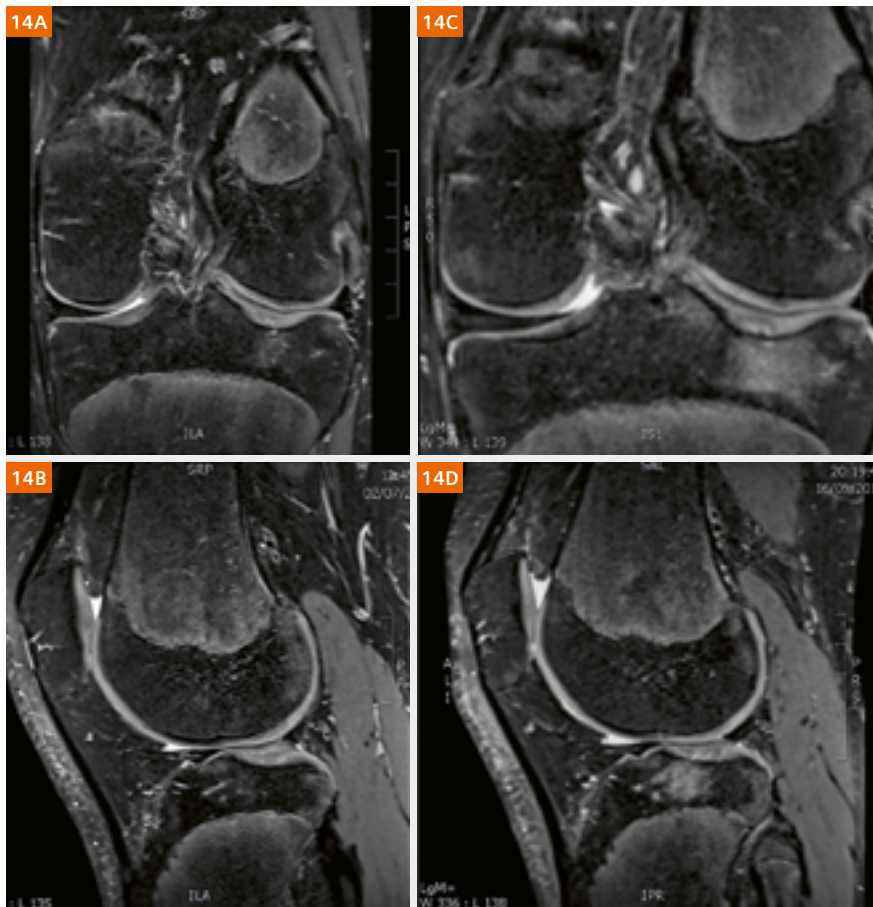Sufficient room in the 18-channel Knee Coil with 1.5T MAGNETOM Sola.

Figure 14:
In May 2016, the GOKnee sequence **(14C, D)** demonstrates subchondral stress fracture and chondral fracture with adjacent bone marrow edema. Marked healing on the follow-up exam in February 2017 **(14A, B)**. Increasing resolution from 0.8 **(14C, D)** to 0.6 isotropic **(14A, B)** sharpens the image a great deal; still there is sufficient signal even at this higher resolution. The acquisition time for this higher resolution of 0.6 isotropic has increased to 6 min. Adding 38 x 3 mm slices, sagittal SMS T1 TSE takes another 40 seconds and an axial GE another 38 seconds, which altogether with the localizer adds up to a table time of less than 10 minutes.

GOKnee3D Protocols
Fast high-res 3D knee exams in 10 min. Download .exar1 files for 1.5 and 3T at
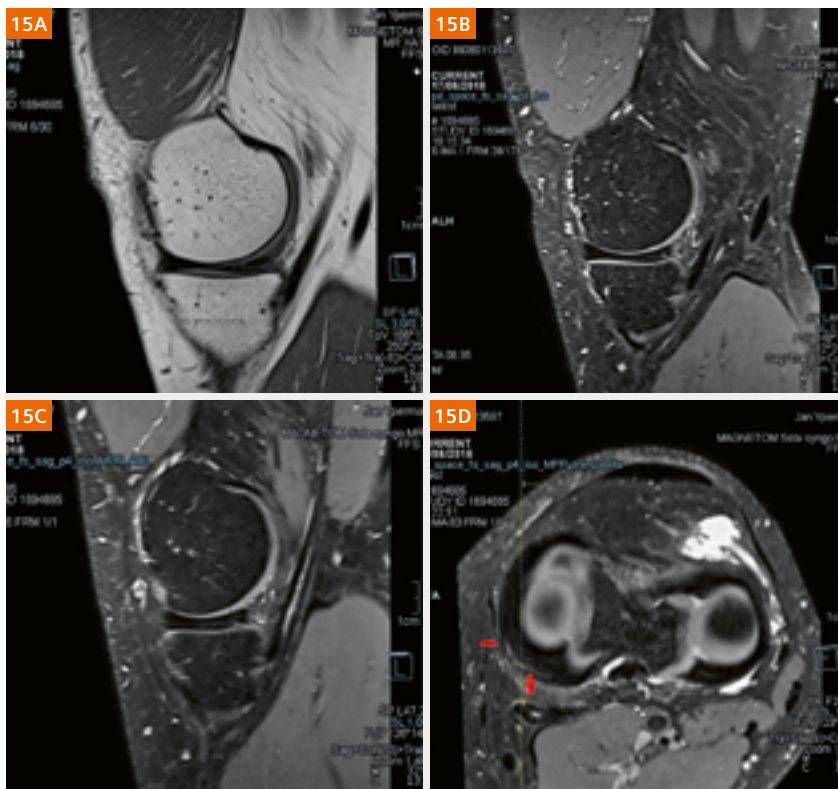
Figure 15:
The axial reconstructions in the meniscal plane **(15D)** make it particularly easy to pick up small tears that were previously unrecognized, as is the case in this peripheral tear in the posterior horn medial meniscus (arrow) with hyperintense signal extending to the cartilage both on the native sagittal slice **(15B)** and 1 mm thick reconstruction **(15C)**. GOKnee3D is excellent at depicting small details.
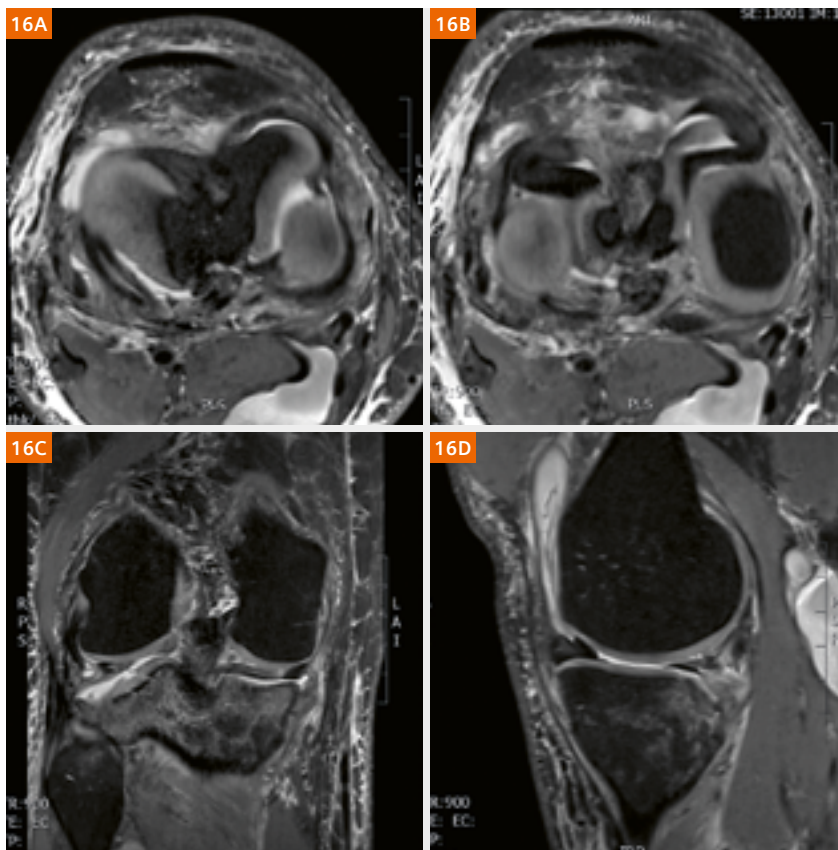
Though not all knee pathology is subtle.

Figure 16:
This patient endured a severe crash during a horse carriage race. GOKnee3D 0.6 isotropic reveals bilateral bucket handle meniscal tears, tibial plateau fracture, and torn cruciate ligaments. This resulted in hemarthrosis, ruptured capsule, and a Baker cyst. Bone marrow edema is easily depicted. Having a comfortable coil and comfortable position even in painful conditions is of real value and key to high image quality.

Seeing these consistent GOKnee3D results on MAGNETOM Sola makes it tempting to expand this concept further to the shoulder, ankle, wrist, hip, and elbow. This is how GOKnee performs on the elbow (same patient as in Figure 12).
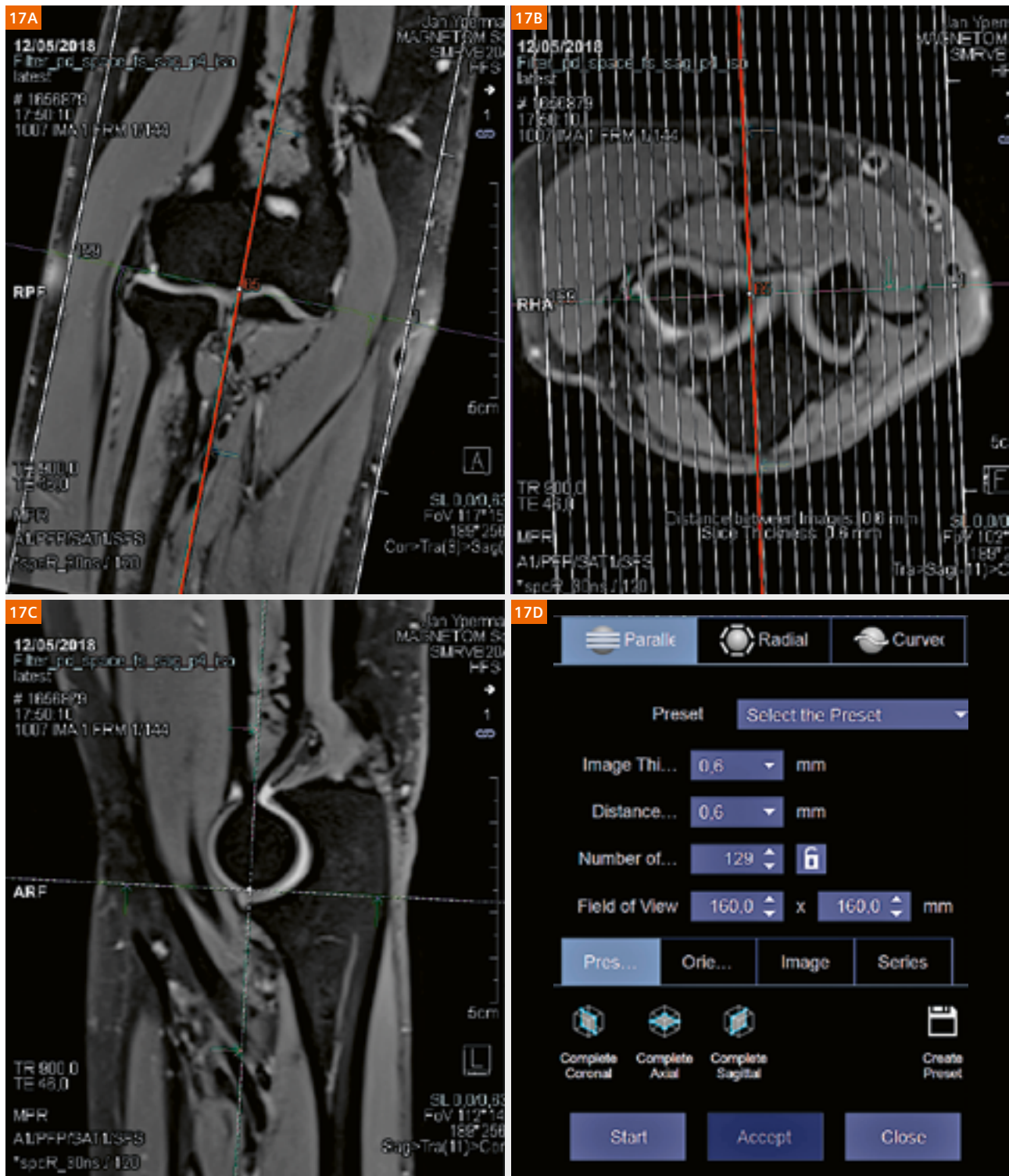

Figure 17:
Screenshot of our very first 'GOElbow'. 0.6 isotropic acquisition enables high resolution reconstructions at will.

Since that first 'GOElbow' (Figures 12 and 17), all of our elbow exams enjoy the high resolution that Space3D_caipi4 technique offers, in addition to the SMS axial acquisitions (except in the presence of metallic hardware[1], that is). Other joints were quick to follow. Here is an example of cartilage lesions in hip imaging using 'GOHip'.
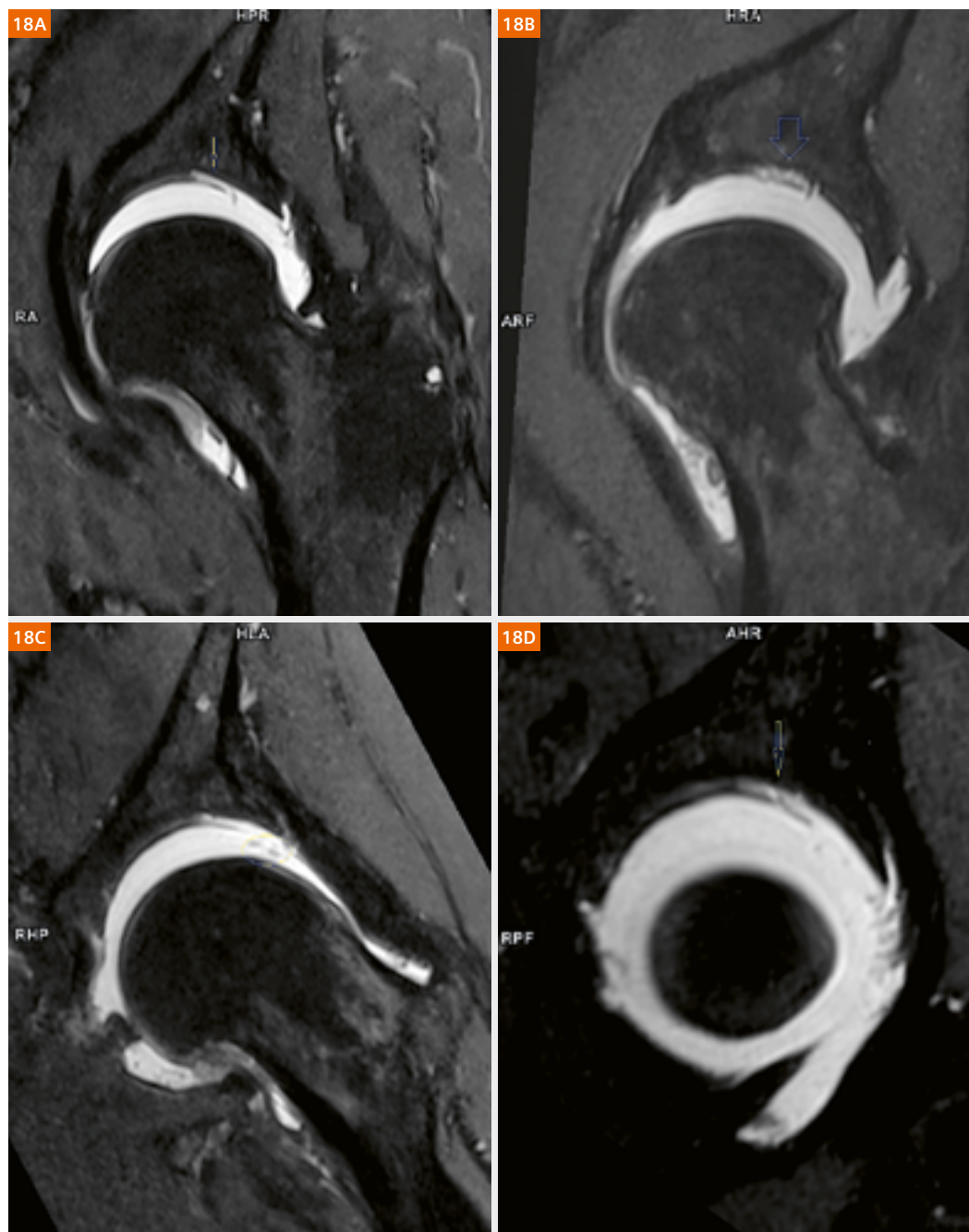

Figure 18: MR arthrogram hip exam (using skin traction), the Space3D_caipi4 sequence further enhanced up to 0.5 isotropic (5 min 41 acquisition time) with native slices **(18A)** and MPR reconstructions depicts cartilage delamination, denudation, and rice bodies in exquisite detail. To be consistent, we call this exam: 'GOHip'.

[1]The MRI restrictions (if any) of the metal implant must be considered prior to patient undergoing MRI exam. MR imaging of patients with metallic implants brings specific risks. However, certain implants are approved by the governing regulatory bodies to be MR conditionally safe. For such implants, the previously mentioned warning may not be applicable. Please contact the implant manufacturer for the specific conditional information. The conditions for MR safety are the responsibility of the implant manufacturer, not of Siemens.
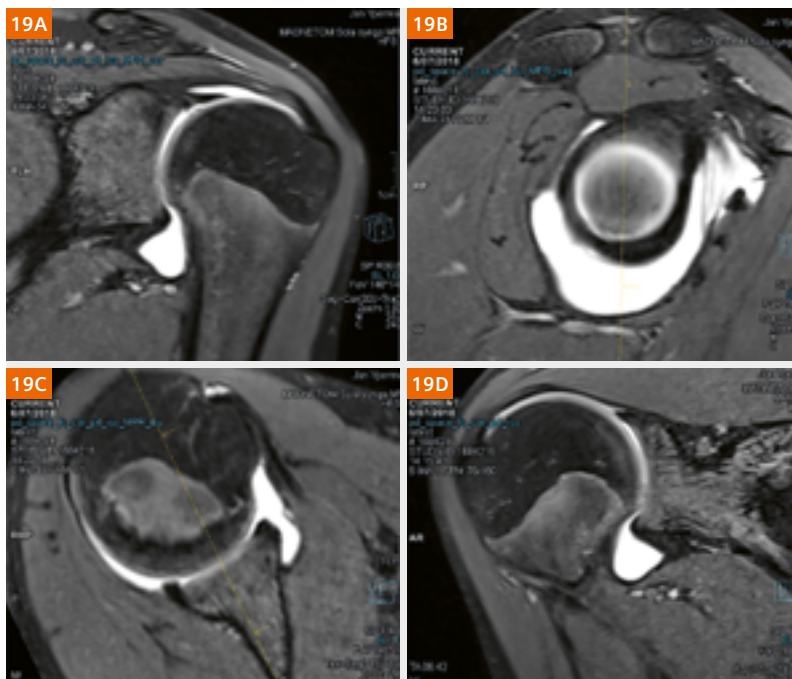
Figure 19:
Normal MR arthrogram using Space3D_caipi4 technique, a.k.a., 'GOShoulder'. Coronal acquisition 0.5 mm isotropic resolution **(19D)** and three orthogonal thin slice MPR reconstructions. Exquisite cartilage delineation is shown.
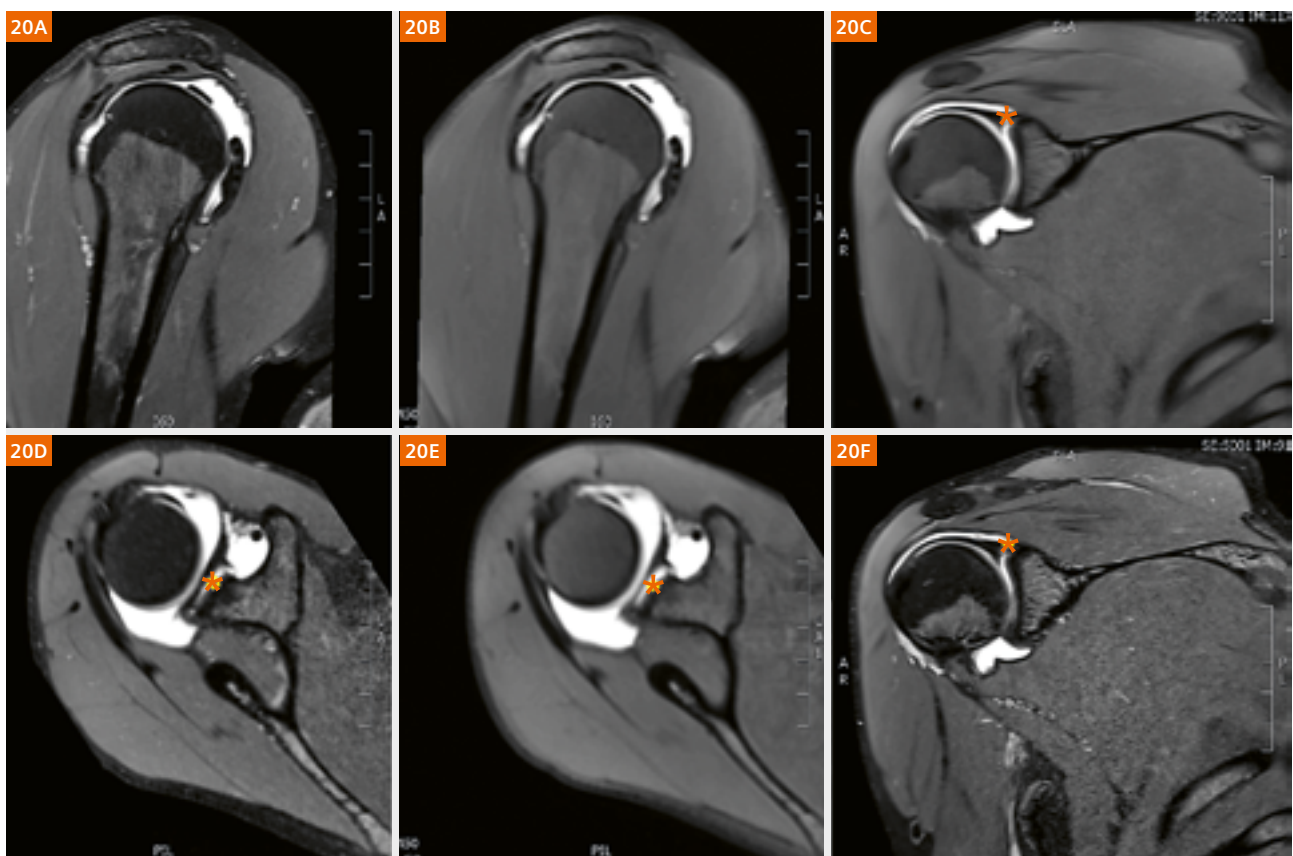
Figure 20:
Changing a few parameters in the Space3D_caipi4 results in a nice T1 CAIPIRINHA 4 SPACE acquisition, ideal for an arthrogram.
This young basketball player had unexplained shoulder pain during and after the game. Slap II lesion (*) easily demonstrated in two 'GOShoulder' acquisitions after arthrogram: T1 fatsat and PD fatsat Space3D_caipi4 each with 0.5 mm isotropic resolution. Coronal acquisition **(20C, F)** with axial **(20A, D)** and sagittal MPR reconstructions **(20A, D** and **20B, E)**.
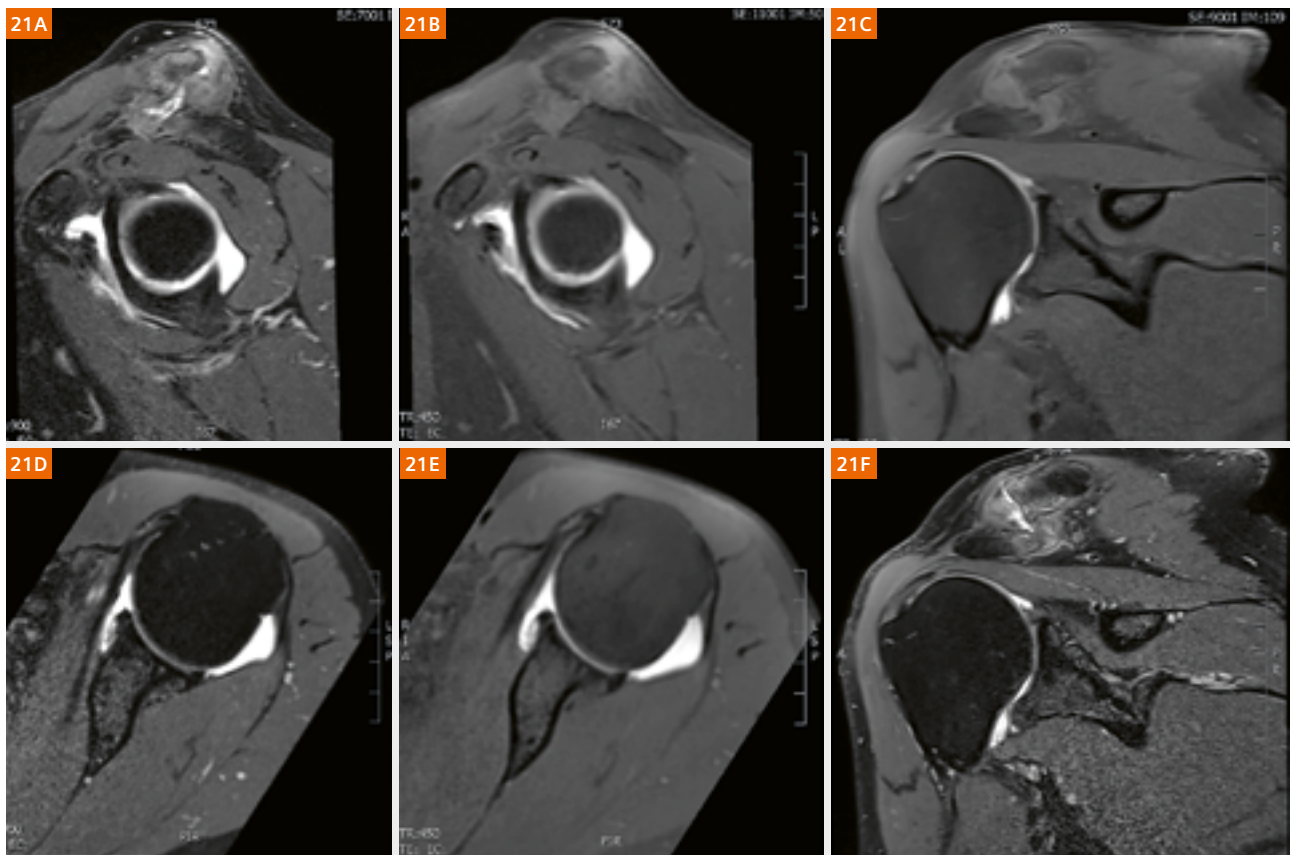
Figure 21:
Luxated AC joint degree III to determine if there was a concomitant labral lesion. Coronal acquisition after arthrogram with axial and sagittal reconstructions performed. The scan was quick, easy, and robust even in this patient in pain.
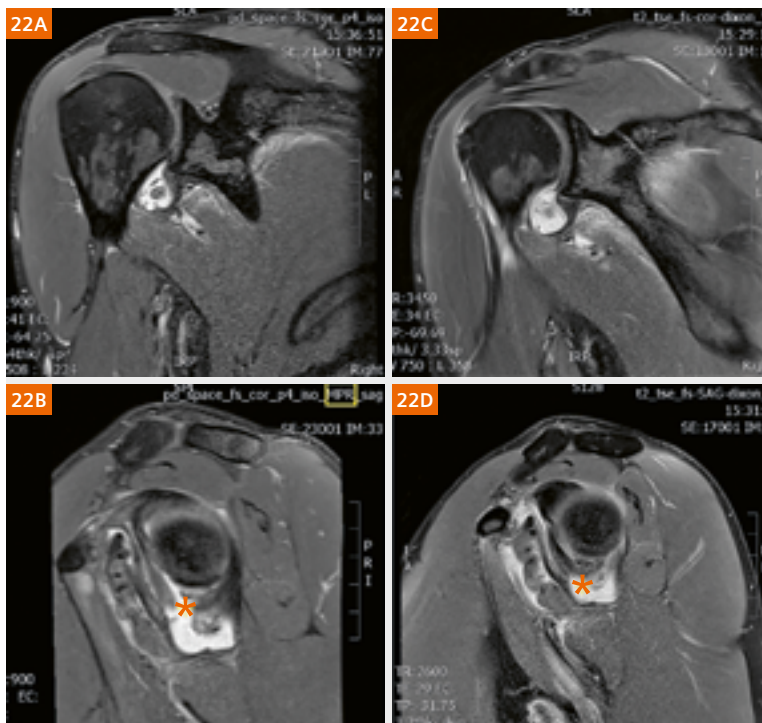
Figure 22:
Patient who fell while cycling and landed on outstretched hand. No arthrogram was performed since the exam was within a week of trauma. 'GOShoulder' PD Space3D_caipi_ fatsat coronal acquisition 0.4 mm isotropic and sagittal 1 mm MPR **(22A, B)** and coronal and sagittal 3 mm Dixon fatsat PD **(22C, D)**.

Thin slices of 'GOShoulder' demonstrate more accurately the bony avulsion (orange star) of the anterior pillar inferior glenohumeral ligament. Even with these thin slices, there is still sufficient signal as compared to the classic 3 mm slices.

In conclusion, for larger joints GO is go-ing well with the "GO" meaning go-od. Things are going similarly well for smaller joints such as the ankle and wrist.

Figure 23: A basketball player presented with an ankle sprain. 3D isotropic imaging 0.5 mm. Overview in 3D left screenshot **(23A–D)**. Right Screenshot **(23E–H)** shows axial MPR reconstruction **(23G)** together with 2D ax SMS PD FS **(23E)** and ax SMS PD 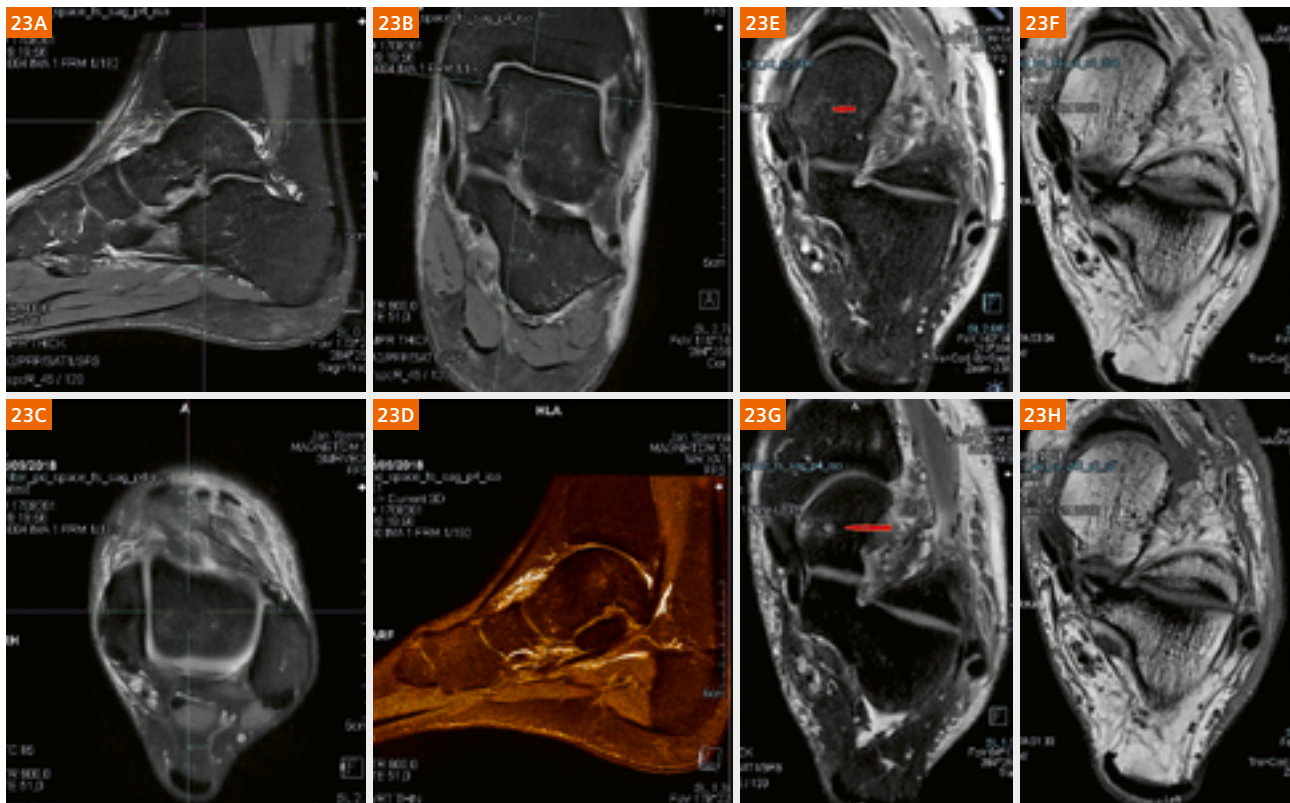**(23F)** and SMS T1 TSE **(23H)**. MPR axial reconstruction 'GOAnkle' demonstrates bone edema (red arrow) actually even better than the 2D intermediate weighted FS. 'GOAnkle'!
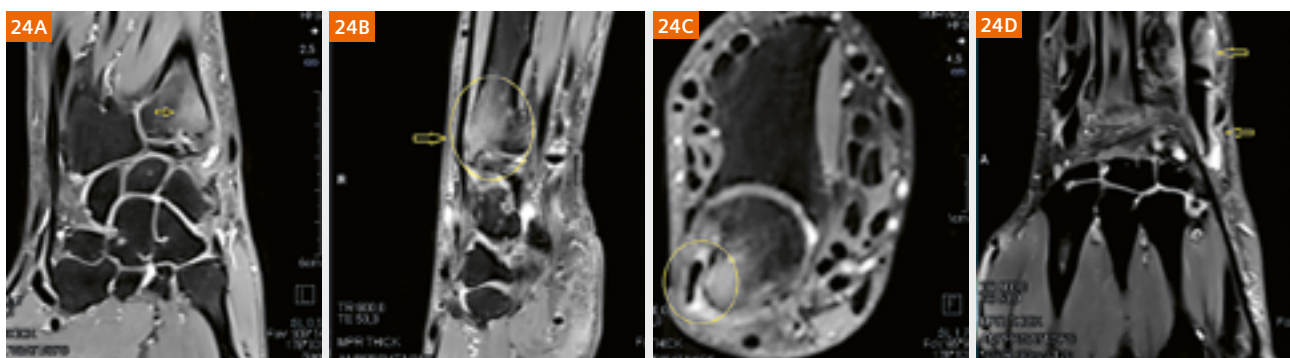
Figure 24: 'GOWrist' with 0.5 mm 3D isotropic acquisition (5 minutes acquisition time) and MPR reconstructions in 3 directions with bone edema (yellow circle and arrow, 24A and B) distal ulna and styloid process and friction tenosynovitis (yellow circle and arrow, 24C and D) extensor carpi ulnaris tendon. Scan provides exquisite detail in sagittal and coronal planes with this 0.5 isotropic resolution. Even the axial MPR is diagnostic.

In conclusion: MAGNETOM Sola, SMS TSE, and 3D SPACE CAIPIRINHA 4 make a formidable team. The MAGNETOM Sola platform does indeed play an important role in the background with stable homogeneity of the magnetic field, stable RF pulses, and abundant gradient power to run rather than walk through *k*-space and, finally, high density coils to start with. Indeed, the success of 'GO-PickYourJoint' as well as the success of SMS TSE is highly dependent on the signal we get from the 18-channel Knee Coil, UltraFlex Small and Large, and even Body 30.

Figure 25: When comparing the axial MPR reconstruction 2 mm thickness and 0.5 inplane resolution, to the high resolution PD and T1 images, there is a clear difference in the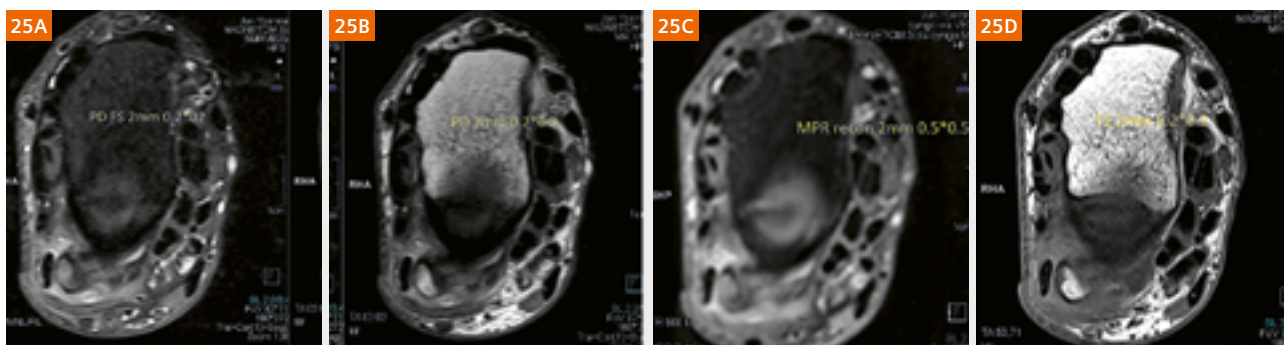 inplane resolution, still the tenosynovitis and the bone edema are easy to interpret but thin slice high resolution axial images using SMS is clearly the winner here. Check acquisition time T1 **(25D)**: 54 seconds for 30 slices 2 mm "thick" 0.2 inplane resolution.

To prove the force of MAGNETOM Sola you need only take a look at the hips. The first hip exams caught my eye immediately. The signal is there in the cartilage.
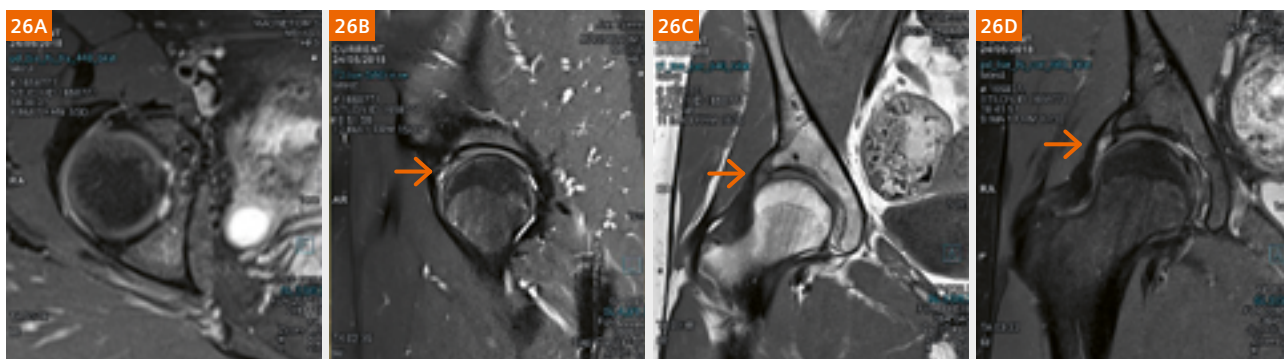
Figure 26: Right side hip pain in a 28-year-old female patient. Axial and coronal intermediate-weighted fatsat 3 mm slices, coronal T1 3 mm slices and 4 mm sagittal SPAIR fatsat revealing labral tear and cyst. The signal in the cartilage looks like what one might expect from a 3T system. Remember, these images are zoomed in and still this detail is present due to the 640 matrix, FOV 309 x 389.
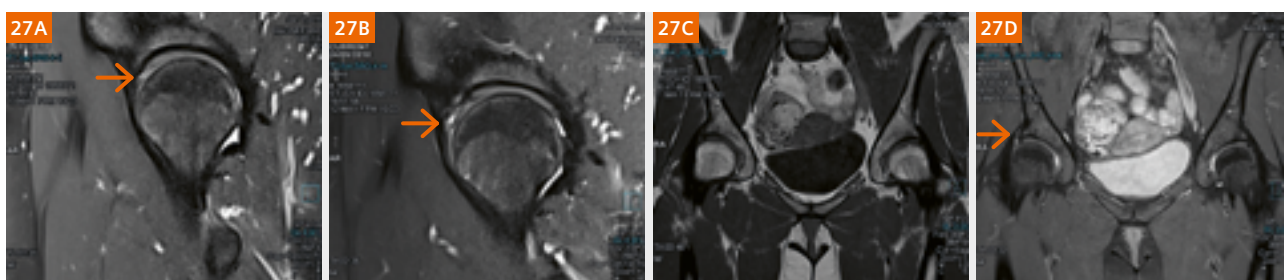
Figure 27: Same patient as in Figure 26. Coronal intermediate-weighted fatsat and T1 TSE 3 mm slices and 4 mm sagittal SPAIR fatsat revealing labral tear and cyst on right side and cartilage tears left side.

Reference

1 Kalia V, Fritz B, Johnson R, Gilson WD, Raithel E, Fritz J. CAIPIRINHA accelerated SPACE enables 10-min isotropic 3D TSE MRI of the ankle for optimized visualization of curved and oblique ligaments and tendons. Eur Radiol. 2017 Sep;27(9):3652-3661.

MR Imaging of Joint Replacements

Reto Sutter, M.D.[1]; Mathias Nittka, Ph.D.[2]

[1] Balgrist University Hospital, University of Zurich, Zurich, Switzerland
[2] Siemens Healthineers, Erlangen, Germany

Introduction

The last 10 years have seen large technological advances in MR imaging of metal implants[1], and these are coming at the right time, as the number of patients with joint replacements has increased substantially over the last decade. Patients often arrive in the imaging suite with metal implants that can produce distortion artifacts that are detrimental to image quality. Thankfully, these image distortions can be reduced or even eliminated with the use of new MR imaging techniques.

In general, MR imaging relies on a highly constant magnetic field inside the bore. Even slight perturbations, such as those occurring at interfaces between human tissue and surrounding air may cause significant artifacts. The physical property behind this effect is called 'magnetic susceptibility' and unfortunately, the magnetic susceptibility of metal is much higher than that of tissue. Resulting distortions of the magnetic field can reach out far beyond the metal surface and affect the diagnostic quality of the surrounding anatomical structures.

This does not mean, however, that a patient with a metal implant cannot be helped diagnostically with MRI; it means that we must dig deeper into the MR toolkit to produce the best possible diagnostic MRI (Fig. 1).

Determining the type of artifact

The course of action is, in part, dictated by the type and extent of artifact. In some cases, the signal piles up to produce a very bright signal on the MR image. In other instances, signal is lost and only a large, dark area can be seen. There is also signal displacement, where a voxel is shifted from one place to a different location. The signal may be shifted within the imaged slice along the frequency encoding direction (but not along the phase encoding direction!), the so called in-plane distortion. It may be also dislocated with respect to the selected slice position, i.e. the displayed signal originates from a different spatial position than the expected image plane, what is called through-plane distortion [2]. Commonly applied spectral fat suppression techniques are also extremely susceptible to resonance frequency variations. Combating the issues created by insufficient fat suppression is critical to the diagnostic process.

[1] The MRI restrictions (if any) of the metal implant must be considered prior to patient undergoing MRI exam. MR imaging of patients with metallic implants brings specific risks. However, certain implants are approved by the governing regulatory bodies to be MR conditionally safe. For such implants, the previously mentioned warning may not be applicable. Please contact the implant manufacturer for the specific conditional information. The conditions for MR safety are the responsibility of the implant manufacturer, not of Siemens.

Drill fragment
(Stainless steel)

Total knee arthroplasty
(Titanium)

Metal artifacts may extend far beyond the actual metal object

Massive metal implant imaged with a STIR SEMAC sequence

Figure 1: How do metal artifacts arise?
The degree of artifact around the implant[1] is not only induced by its size, but also by the metal composition. **(1A, C)** Objects made of stainless steel, even when very small in size, induce a substantially augmented local magnetic field. Therefore, a conventional coronal STIR sequence without metal artifact optimization exhibits extensive artifacts induced by a broken off drill fragment (arrow) in a patient with anterior cruciate ligament (ACL) reconstruction. **(1B, D)** Titanium implants in general induce less distortions, however, in particular large structures require dedicated metal artifact reduction techniques to enable a diagnostic image quality.
Image reproduced with permission from [1], © Georg Thieme Verlag KG.

Reducing metal artifacts

A simple, yet effective technique to reduce metal artifacts is to increase the bandwidth of the sequence. The bandwidth describes a property of the imaging sequence, linking the applied magnetic field gradients to the frequency spectrum required for encoding the image. In short, a high bandwidth applied to both signal excitation and signal reception turns the sequence less sensitive to distortions of the static magnetic field. A recent study from Johns Hopkins Hospital [3] analyzing the effect of increased receiver bandwidth on imaging of ankle arthroplasty confirmed that this renders substantially improved images (Fig. 2). High bandwidth does come with some disadvantages: An increased readout bandwidth decreases the signal to noise ratio (SNR). Furthermore, the specific absorption rate (SAR) is higher when using a high excitation bandwidth. As a consequence, high bandwidth protocols tend to exhibit longer scan times. To a certain degree, this may be compensated by longer echo train length when applying turbo spin echo sequences. However, it should be noted that long echo trains may cause an additional degradation of image quality around implants [3]. Other basic steps to improve MRI diagnostic quality are to:

1. Use thin sections, a small voxel size, and small field of view (FOV);
2. Perform the exam at a field strength of 1.5T rather than 3T, as the severity of the artifacts is in most cases directly proportional to the field strength;
3. Use turbo spin echo sequences rather than gradient or 3D sequences; and,
4. Set the frequency encoding gradient parallel to the long axis of the prosthesis/implant.

These and other techniques are an integral part of *syngo* WARP, providing a comprehensive set of sequence optimizations for metal implant imaging.

The problem with fat saturation

Fat saturated sequences are some of the most important sequences in any musculoskeletal MR imaging protocol, with the ability to visualize e.g. the anatomical distribution of fluid collections, bone marrow edema, and soft tissue edema. However, the presence of large or multiple metal artifacts often impedes fat saturation techniques and may result in a non-diagnostic image. Standard spectral fat saturation is based on different resonance frequencies of water and fat; when metal is present, the fat peak shifts to a different frequency and keeps the RF pulse from suppressing the signal from fat tissue. However, there is a technique that allows us to tackle this issue: short-tau inversion recovery (STIR).

Capitalizing on the different relaxation times of water and fat, first a 180-degree pulse inverts the longitudinal magnetization. Fat has a much shorter T1 relaxation time than water, so when during signal relaxation the fat is at a magnetization of zero, the excitation pulse only affects the water molecules and not the fat molecules, and this technique results in a more stable fat saturation in the presence of metal. Even better results are achieved by combining STIR with high bandwidth, but this still would not be sufficient for clinical use [4].

The *syngo* WARP STIR sequence employs a dedicated bandwidth matching for each RF pulse within the sequence, which is critical for robust STIR contrast around metal implants while still covering a large anatomical field of view (Fig. 3). Further improvements can be achieved by adding the View-Angle Tilting technique (VAT), another feature of the *syngo* WARP toolkit. VAT applies an additional compensation gradient which effectively cancels the in-plane displacement (Fig. 4). This technique allows to visualize periprosthetic tissues with only little residual artifacts, and with reasonable acquisition times.

80 Hz/Pixel

390 Hz/Pixel

Figure 2: Increasing the receiver bandwidth
A simple but very effective step for reducing metal artifacts is increasing the receiver bandwidth, as shown in a 76-year-old patient with total hip arthroplasty. **(2A)** Coronal T2-weighted turbo-spin echo sequence with a standard receiver bandwidth of 80 Hz/Pixel shows large artifacts around the acetabular component. **(2B)** When the same sequence is repeated with an increased receiver bandwidth of 390 Hz/Pixel the artifacts around the acetabular component are substantially smaller.

Dealing with severe metal artifacts

For some implants it may be not sufficient to apply sequences with high bandwidth as described above. Typically structures composed of stainless steel or hardened surfaces frequently containing CoCr alloys are very difficult to handle.

In these cases an excessive distortion of the slice profile is the dominating factor, requiring a more powerful tool, which is able to correct for signal dislocated in through-plane direction.

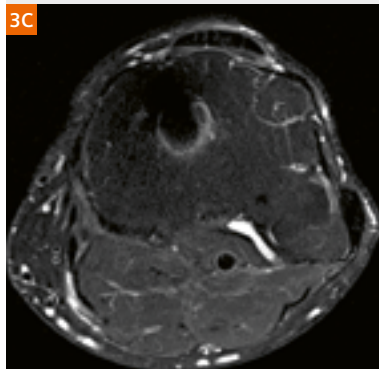A break-through in this field was achieved with the invention of the SEMAC (slice encoding for metal artifact correction) method [5] that has meanwhile been applied successfully in clinical imaging for several years [2]. The SEMAC technique employs the through-plane distortion correction to significantly reduce what can be called the "Potato Chip Effect". When you visualize the warped artifacts that occur because of through-plane distortion, the imaged plane looks like a potato chip, with distortions affecting several adjacent image planes. Image reconstruction using SEMAC substantially mitigates these distortions, allowing the radiologist to appreciate areas of osteolysis and other conditions that are obscured when imaging is performed without through-plane distortion correction (Fig. 5).

Spectral fat saturation

STIR WARP

Figure 3: Two types of fat saturation
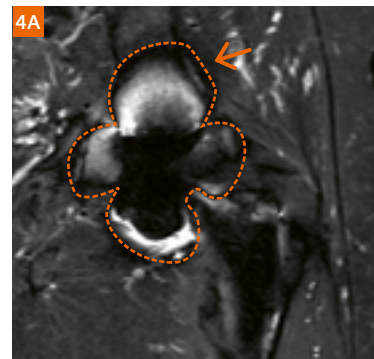Anterior cruciate ligament (ACL) reconstruction in a 69-year-old patient. **(3A)** Radiograph of the left knee showing large Ligamys screw in the tibial head. **(3B)** Axial intermediate-weighted turbo-spin echo sequence with spectral fat saturation and increased bandwidth shows complete fail of the spectral fat saturation at the level of the tibial head. **(3C)** Axial STIR WARP sequence with optimized inversion pulse shows stable and homogeneous fat saturation of the whole image.
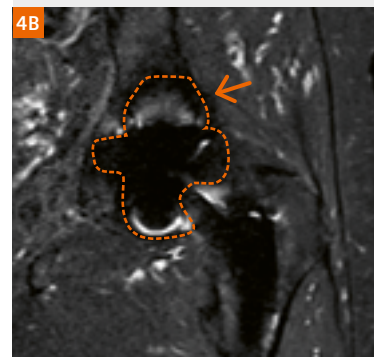
Standard STIR hiBW

STIR WARP

STIR WARP + VAT

Figure 4: STIR WARP and View-angle Tilting (VAT)
Different methods for metal artifact reduction in a 66-year-old patient with total hip arthroplasty (THA). **(4A)** The standard coronal STIR sequence with increased receiver bandwidth (hiBW) often allows for a basic diagnostic image quality, but suffers from many areals with failed fat saturation (arrow). **(4B)** STIR WARP with an optimized inversion pulse is much more stable for reduction of metal artifacts, with a smaller area of insufficient fat saturation. **(4C)** An additional compensation gradient shifts the view-angle during the readout, and this view-angle displacement cancels the in-plane displacement, resulting in an even better reduction of metal artifacts.

SEMAC depends on numerous slice encoding steps to gain the most benefit, requiring considerable additional scan time and thus poses some challenges, both to the time scheduling of a busy practice and also with respect to patient comfort.

In recent years a new technique emerged, known as Compressed Sensing (CS). It has opened new perspectives to accelerate the MR acquisition process in various fields and can now also be applied to SEMAC (Figs. 10, 11). The CS-SEMAC[2] technique is facilitated by the inherent sparsity of the acquired SEMAC data, since the actual distortions make up for just a small fraction of the acquired signal. Compressed Sensing SEMAC applies 8-fold undersampling of k-space in combination with an iterative reconstruction algorithm. As a result, images with very comparable diagnostic quality can be created from e.g. a six minute CS-SEMAC scan that would otherwise take approximately twelve minutes even with parallel imaging acceleration.

The number of recommended slice encoding steps for CS-SEMAC according to a recent study was 19 for STIR and T1-weighted images, and 11 slice encoding steps for T2-weighted images [6]. A study on knee implants by Fritz et al. [7] found that CS-SEMAC allows the acquisition of accelerated MR imaging with acquisition times of less than 5 minutes.

[2]The product is still under development and not commercially available yet. It is not for sale in the US. Its future availability cannot be ensured.

The plan in action

A sample protocol for hip prosthesis
At Balgrist University Hospital a protocol with a mix of techniques is in use for scanning hip implants: The first two sequences cover the whole prosthesis. A coronal STIR CS-SEMAC sequence gives the best visibility of the bone-metal-interface with an acquisition time of approximately six minutes. Additionally, a transverse STIR WARP sequence is acquired, allowing the coverage of a large field of view in less than 4 minutes. The second part of the protocol is focused on the joint and the periarticular muscles with turbo-spin echo sequences that feature a high receiver bandwidth, allowing to visualize soft tissue pathology with sequences that only require acquisition times of 2–3 minutes.

What is the clinical impact?
In patients with residual pain after total arthroplasty, soft-tissue related complications are the most common problem, followed by aseptic loosening and infection. Soft-tissue related complications include e.g., damaged or detached external rotator tendons and scarred abductor tendons with associated muscle atrophy and fatty muscle degeneration (Fig. 6).

One place where MRI can be of significant help is in differentiating between osteolysis and diffuse osteopenia next to the implant: While in conventional radiographs and computed tomography (CT) this can be difficult or even impossible, MR imaging allows the accurate differentiation between these two entities (Fig. 7). In patients with suspected infection the extent of the infected areas can be determined using STIR WARP or CS-SEMAC (Fig. 8). Naturally, aspiration is still required to determine the pathogen. Other complications can also be visualized such as the hypointense masses seen in metal-on-metal hip implants called pseudotumors (Fig. 9).

Figure 5: Unicompartmental knee arthroplasty
This 58-year-old male with unicompartmental knee arthroplasty underwent MRI to evaluate those parts of the knee joint that were not replaced.

(5A) Radiograph of the left knee shows prosthesis components in the medial compartment. **(5B)** In the standard coronal STIR sequence optimized with high receiver bandwidth (hiBW) both the collateral ligament and the intercondylar notch are obscured (arrows). **(5C)** STIR SEMAC (slice encoding for metal artifact correction) and its reduction of through-plane metal artifacts improves the visualization of the collateral ligament and the intercondylar notch.
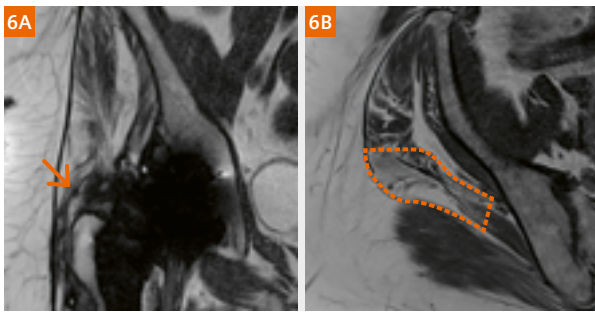
STIR hiBW   STIR SEMAC
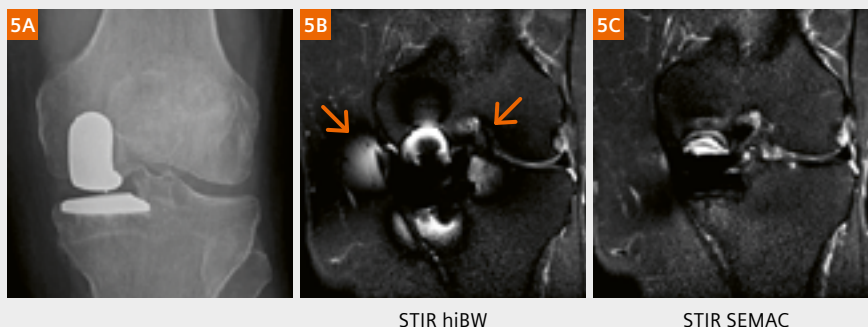
Figure 6: Abductor insufficiency
61-year-old female patient with pain and unsteady gait after total hip arthroplasty (THA), and positive Trendelenburg sign at clinical examination. **(6A, B)** At MR imaging improved with high receiver bandwidth a rupture of the gluteus medius tendon (arrow) and fatty degeneration of the respective part of the gluteus medius muscle (outlined areas) are depicted on a coronal T2-weighted and axial T1-weighted sequence.
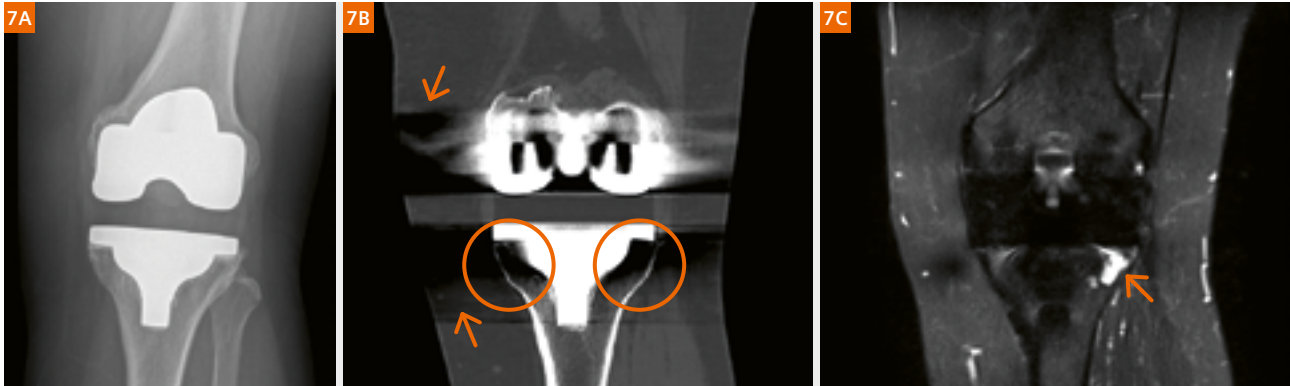
Figure 7: Osteolysis vs. Osteopenia
Painful total knee arthroplasty (TKA) in a 57-year-old female patient. **(7A)** Radiograph of the left knee is unremarkable. **(7B)** At computed tomography (CT) suspected areas of osteolysis are visible next to the tibial component (circles), however this region is partially masked by beam hardening artifacts (arrows). **(7C)** At MR imaging an osteolysis (arrow) is detected on a coronal STIR SEMAC sequence only on one side of the tibial component, but not on the other side.
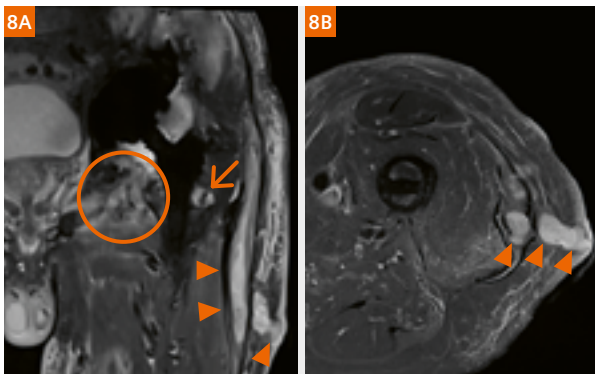
Figure 8: Infection
70-year-old patient with infected total hip arthroplasty.
(8A) Coronal CS-SEMAC STIR sequence shows extensive soft tissue edema adjacent to the left hip joint, e.g. in the adductor region (circle), periprosthetic osteolysis (arrow) and soft tissue abscesses (arrowheads) with a cutaneous fistula. **(8B)** Soft tissue abscesses (arrowheads) and cutaneous fistula depicted on axial STIR WARP image at the level of the femoral shaft.
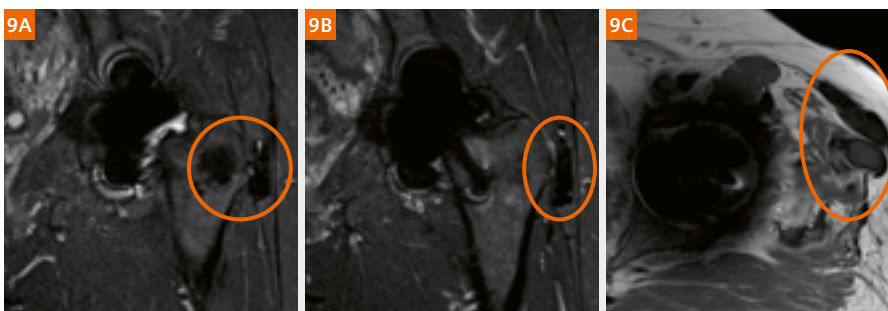
Figure 9: Metal-on-metal hip
42-year-old female patient with pseu-dotumors after short-stem metal-on-metal prosthesis. **(9A, B)** Coronal STIR SEMAC sequence shows intraosse-ous hypointense mass (circle) that is connected to a paratrochanteric soft tissue mass (circle) with similar morphology. **(9C)** The pseudotumors show finger-like extensions (circles) into the soft tissues that are visible on the axial T1-weighted turbo-spin echo sequence with high receiver bandwidth.

SEMAC

CS-SEMAC

Figure 10: Compressed sensing SEMAC of total knee arthroplasty
Patella baja (low lying patella) due to arthrofibrosis in a 61-year-old patient with total knee arthroplasty (TKA). **(10A)** Sagittal intermediate-weighted image of the left knee with SEMAC [11 slice encoding steps, acquisition time 4:50 min] shows low lying patella (line and arrow) due to arthrofibrosis (asterisk), but residual through-plane artifacts at the level of the joint and the tip of the tibial peg (cir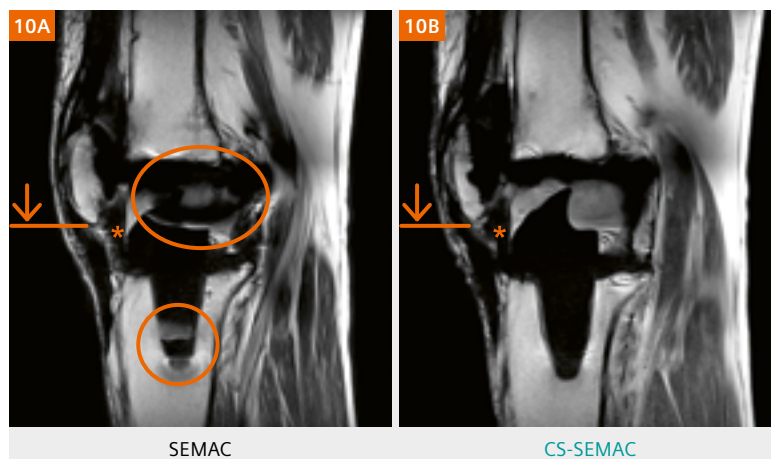cles). **(10B)** Sagittal intermediate-weighted compressed sensing (CS) SEMAC image [15 slice encoding steps, acquisition time 4:22 min] is free of through plane artifacts and even faster than the standard SEMAC sequence.
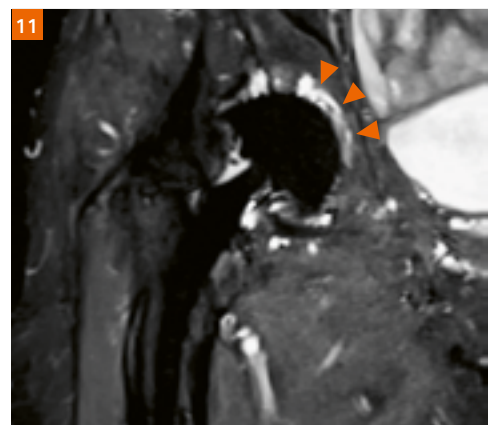

Figure 11: Compressed sensing SEMAC of total hip arthroplasty
Periprosthetic osteolysis (arrowheads) in a 66-year-old patient with painful total hip arthroplasty of the right hip. The compressed sensing (CS) SEMAC STIR sequence was acquired with 19 slice encoding steps, allowing for complete removal of through-plane artifacts and stable fat saturation with an acquisition time of 6:19 min.

Conclusion

Imaging joint replacements can be successfully done in clinical MRI if distortion from metal artifacts are reduced. In our experience, the quality of the MR images can be significantly improved using the following steps:

1. Increase the receiver bandwidth of the sequences. This simple and effective technique delivers improved diagnostic quality right away.
2. Use STIR instead of spectral fat saturation to gain a good overview of the pathology.
3. Acquire and utilize the advanced techniques such as *syngo* WARP and CS-SEMAC.

These reliable techniques will render a much clearer and, therefore, much more diagnostically powerful MR image. Not only does this make the MR suite a more valuable resource for the diagnosing physicians, but it also gives the patients the chance of better outcomes.

References

1 Sutter R, Dietrich T. Reduction of metal artefacts in musculoskeletal imaging. Radiologie up2date 2016; 16(02): 127-144.
2 Sutter R, Ulbrich EJ, Jellus V, Nittka M, Pfirrmann CW. Reduction of metal artifacts in patients with total hip arthroplasty with slice-encoding metal artifact correction and view-angle tilting MR imaging. Radiology. 2012;265(1):204-14.
3 Kumar NM, de Cesar Netto C, Schon LC, Fritz J. Metal Artifact Reduction Magnetic Resonance Imaging Around Arthroplasty Implants: The Negative Effect of Long Echo Trains on the Implant-Related Artifact. Invest Radiol. 2017;52(5):310-316.
4 Ulbrich EJ, Sutter R, Aguiar RF, Nittka M, Pfirrmann CW. STIR sequence with increased receiver bandwidth of the inversion pulse for reduction of metallic artifacts. AJR Am J Roentgenol. 2012;199(6):W735-42.
5 Lu W, Pauly KB, Gold GE, Pauly JM, Hargreaves BA. SEMAC: Slice Encoding for Metal Artifact Correction in MRI. Magn Reson Med. 2009;62(1):66-76.
6 Jungmann PM, Bensler S, Zingg P, Fritz B, Pfirrmann CW, Sutter R. Improved Visualization of Juxtaprosthetic Tissue Using Metal Artifact Reduction Magnetic Resonance Imaging: Experimental and Clinical Optimization of Compressed Sensing SEMAC. Invest Radiol 2018; epub before print. http://doi.org/10.1097/RLI.0000000000000504
7 Fritz J, Ahlawat S, Demehri S, Thawait GK, Raithel E, Gilson WD, Nittka M. Compressed Sensing SEMAC: 8-fold Accelerated High Resolution Metal Artifact Reduction MRI of Cobalt-Chromium Knee Arthroplasty Implants. Invest Radiol. 2016;51(10):666-76.

Further reading

Jungmann PM, Agten CA, Pfirrmann CW, Sutter R. Advances in MRI Around Metal. JMRI.2017;46(4):972-991.

Michel Paret[1]; Pr FG Barral[2]; Christophe Barles[3]; Sylvain Doussin, Ph.D.[4]

[1] GIE IRMAS, Saint-Priest-en-Jarez, France
[2] Department of Neuroradiology, University Hospital Saint-Etienne, France
[3] Siemens Healthineers, Aix-en-Prevence, France
[4] Siemens Healthineers, Erlangen, Germany

Introduction

"MRI is, or is becoming, the medical imaging modality of choice in more and more diverse applications ..." [1].

Magnetic resonance imaging can be described as the success story of medical imaging mainly due to two characteristics: its harmlessness and its ability to manipulate contrast. However, the acquisition technique, which is relatively slow, can be considered a limiting factor, inducing patient discomfort and patient motion. Furthermore, data acquired is mainly 2D.

Acquisition time acceleration has become a major target in these last few years, on the one hand to reduce examination time and, on the other hand, to make MRI accessible to patients suffering from pain and/or non-cooperative patients.
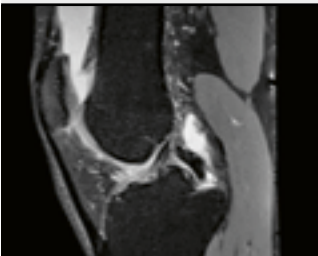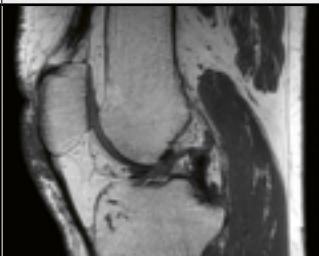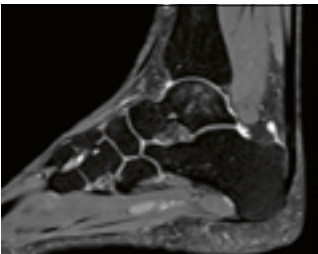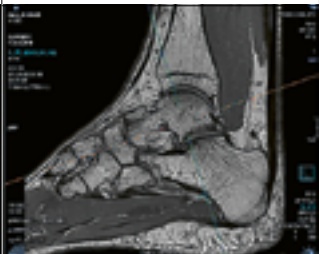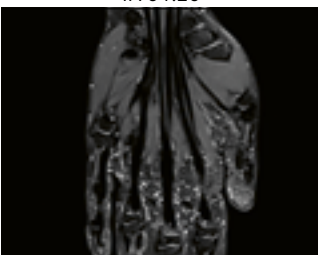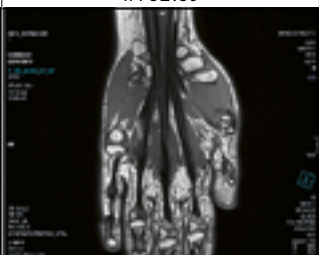
SPACE var T2 with fatsat	SPACE var T1	CAIPIRINHA	Slice thickness (mm)	Voxel size R (mm)	Total TA min:sec Without adjustment
TA 04:46	TA 01:50	p4: 2 x 2	0.6	0.5 x 0.5 x 0.6	06:36
TA 04:20	TA 02:09	p4: 2 x 2	0.6	0.5 x 0.5 x 0.6	06:39
TA 03:27	TA 01:49	p4: 2 x 2	0.5	0.5 x 0.5 x 0.6	05:16

Table 1: It is now possible to perform a 3D MSK examination in less than 10 minutes including patient setup (in and out). SPACE with variable (var) flip angle mode for T1 and T2.

Several questions, however, remain:
- How can speed and diagnostic potential be combined? (The GOBrain protocol is the perfect answer to this question [2–4]).
- Is speed related to 2D acquisition? (Jan Fritz et al. propose GOKnee3D for efficient 3D imaging of the knee joint [5]).

GOKnee3D is the explosive combination, mixing SPACE acquisition technique (Sampling Perfection with Application optimized Contrasts using different flip angle Evolution) and the parallel imaging technique CAIPIRINHA (Controlled Aliasing in Parallel Imaging Results in Higher Acceleration) [6, 7]. This protocol gives to radiologists the possibility to explore the knee joint in 3D without acquisition time constraints.

If this combination 3D and parallel imaging technique answers radiologists' expectations for the knee joint, it is justified to consider it for other body regions. We focused on the CAIPIRINHA-SPACE evaluation for various body parts.

Method

Patients were examined with 1.5T MRI MAGNETOM Aera and 3T MAGNETOM Prisma. In our first step, we used the GOKnee3D for other body parts and compared it with conventional 2D acquisitions as regards sensitivity and specificity for the targeted pathologies. We were immediately faced with the tough reality of MRI: tissue characteristics, coils (different g-factors), and protocol parameters (fatsat type, contrast type for SPACE: various proton density or T2 values) are different for each body region and it is necessary to revisit the CAIPIRINHA-SPACE parameters to adapt to the anatomical region of interest. Detection of bone edema was a typical example.

To avoid testing the infinite possible combinations, we decided to use a SPACE with various T2 contrast parameters and add, when needed, other protocol parameters (fatsat mode, shim, etc.). This philosophy made it possible to combine our needs in terms of sensibility/specificity and an acceleration factor of 4 (2 x 2 using CAIPIRINHA).

The main optimization strategy was focused on time reduction in 3D acquisition to enable its use in clinical routine without compromise on diagnostic potential.

The second step was to compare conventional SPACE to the new CAIPIRINHA SPACE technique. Main body parts were studied on a 1.5T MRI system. Only the brain could also be studied on 3T, because our 3T system configuration does not include MSK coils. We use this 3T system exclusively for neurology.
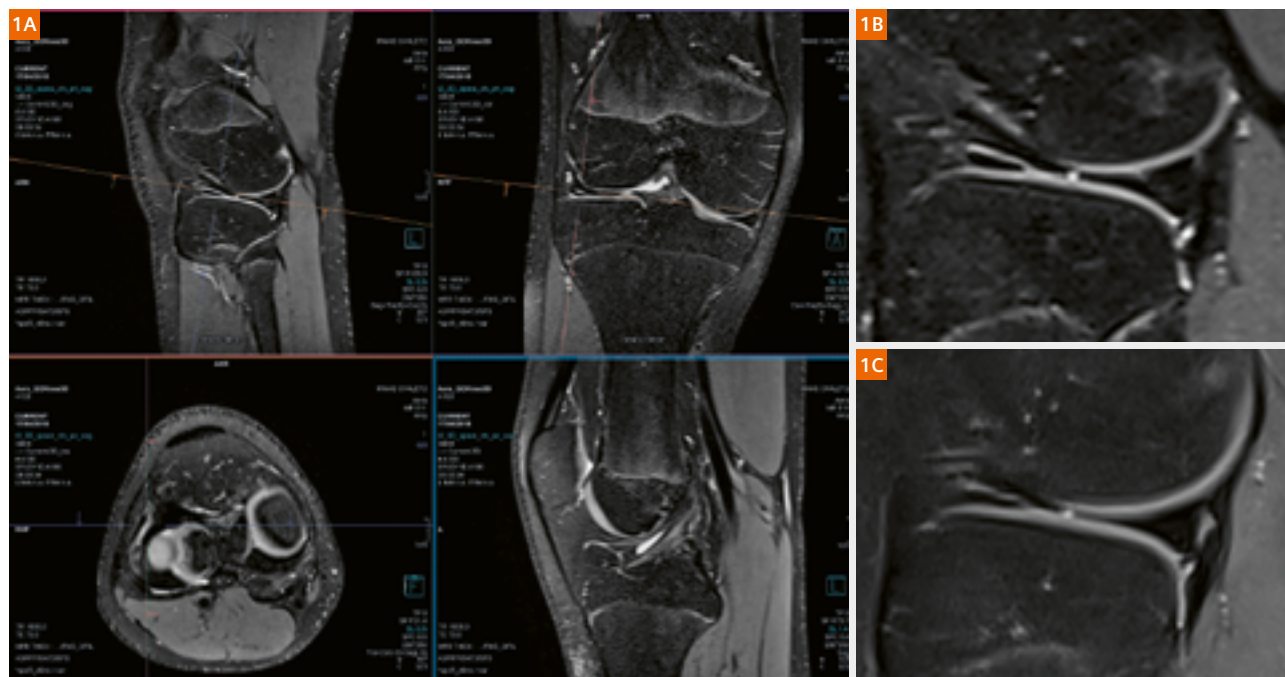
Figure 1:
MPR reconstruction of 3D SPACE T2 fatsat **(1A)**. Sagittal plane **(1B)** shows meniscus tear better than 2D **(1C)**.

Optimizing MR acquisition and reducing scan times

MSK

Acquisition time reduction is significant. It is now possible to perform a 3D MSK examination in less than 10 minutes including patient setup (in and out) (Table 1). Two fast protocols, 3D T2 fatsat, and T1 are acquired. From a radiologist's perspective, it is no longer necessary to multiply acquisition planes and contrasts; it also avoids a situation in which you have to skip one plane or one contrast.

The multiplanar reconstruction (MPR) potential enables the radiologist to adapt to different patients and pathologies, in a similar approach to MSK in ultrasound (Fig. 1). Complex joint imaging, for example of the ankle or elbow, is facilitated (Figs. 2, 3).

Neurology

CAIPIRINHA SPACE really demonstrated its full potential in this application. It represents, for us, a solution to a major diagnostic challenge. It made it possible to examine in 3D, with a similar examination time compared to the time needed with our two protocols: brain and spine

Figure 2:
3D T2 fatsat and T1 in the ankle. These two acquisitions, with MPR reconstructions of 0.6 mm nicely visualize the Achilles tendon and the bone reactions close to calcaneal insertion.

Figure 3:
3D T2 fatsat of the elbow. Acquired using the 15-channel knee coil. We have used the knee protocol without modification of acquisition parameters. Here the test was focused on the coil.

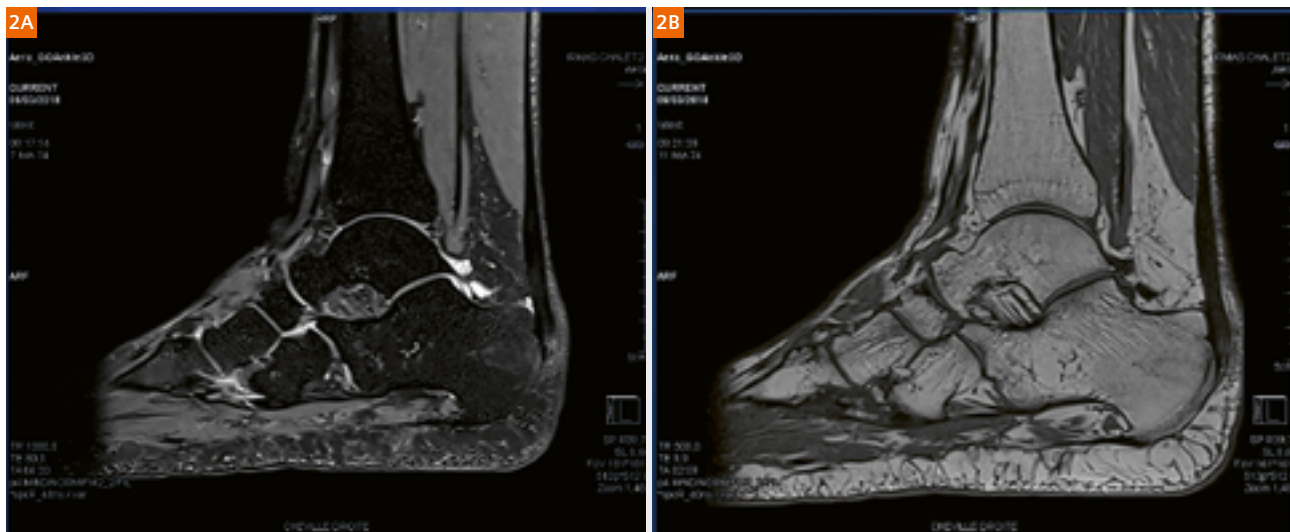(Table 2, Fig. 4). 3D imaging for difficult patients becomes possible in MRI and is compatible with examination time constraints. It is the case for non-cooperative patients (e.g., pain symptoms, dementia) or unstable patients (requiring medical assistance: e.g. pediatric anesthesia ...) (Fig. 5).

The AutoAlign localizers started this philosophy of initiating an examination with a 3D protocol. Today, CAIPIRINHA SPACE enables 3D to do more than automating protocols by really imaging the brain. 2D protocols would be used in addition to bring ultra-high resolution and specific contrasts for specific pathologies.
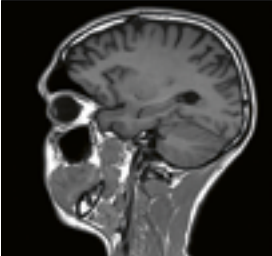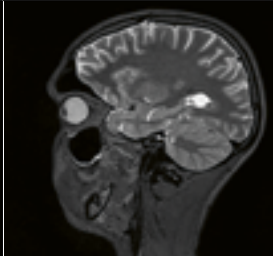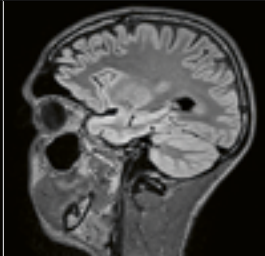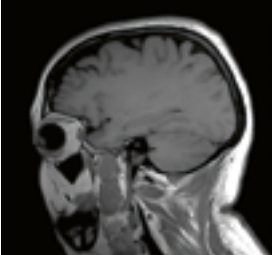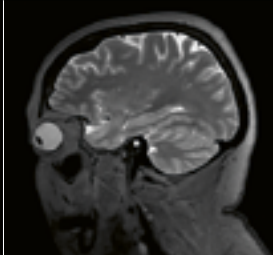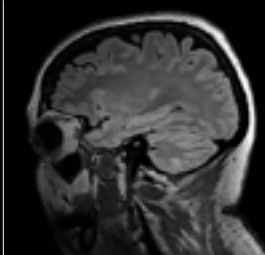
SPACE var T1	SPACE var T2	SPACE FLAIR	Slice thickness (mm)	Voxel size R (mm)	Total TA min:sec Without adjustment
MAGNETOM Aera 1.5T					
TA 02:39	TA 02:50	TA 02:27	1	0.5 x 0.5 x 1	07:56
MAGNETOM Prisma 3T			CAIPIRINHA p4: 2 x 2		
TA 02:43	TA 02:02	TA 02:35	0.9	0.5 x 0.5 x 0.9	07:20

Table 2: CAIPIRINHA SPACE really demonstrated its full potential in brain imaging. SPACE with variable (var) flip angle mode for T1 and T2.

T1 TSE 2D
TA 01:35

T2 SPACE
CAIPIRINHA 4
TA 03:29

T2 SPACE
CAIPIRINHA 6
TA 03:00
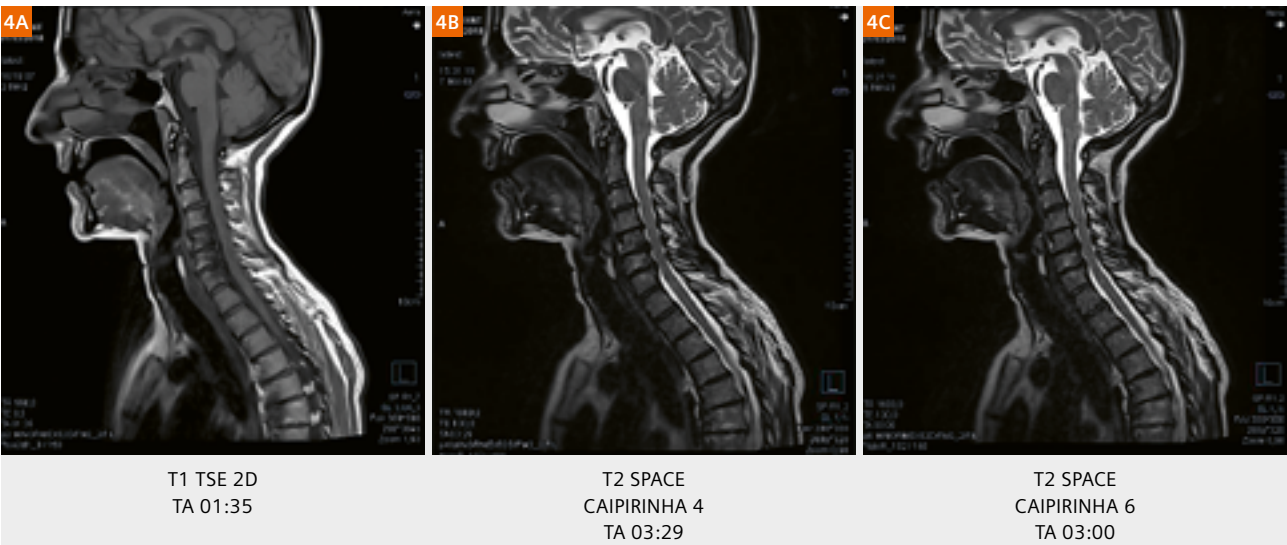
Figure 4:
Time necessary for c-spine exploration in T1 TSE 2D 3 mm and T2 3D 1 mm can be less than 5 minutes. The Head/Neck 20-channel coil used here enables the use of CAIPIRINHA factor 6 (3 x 2) without reconstruction artifacts.
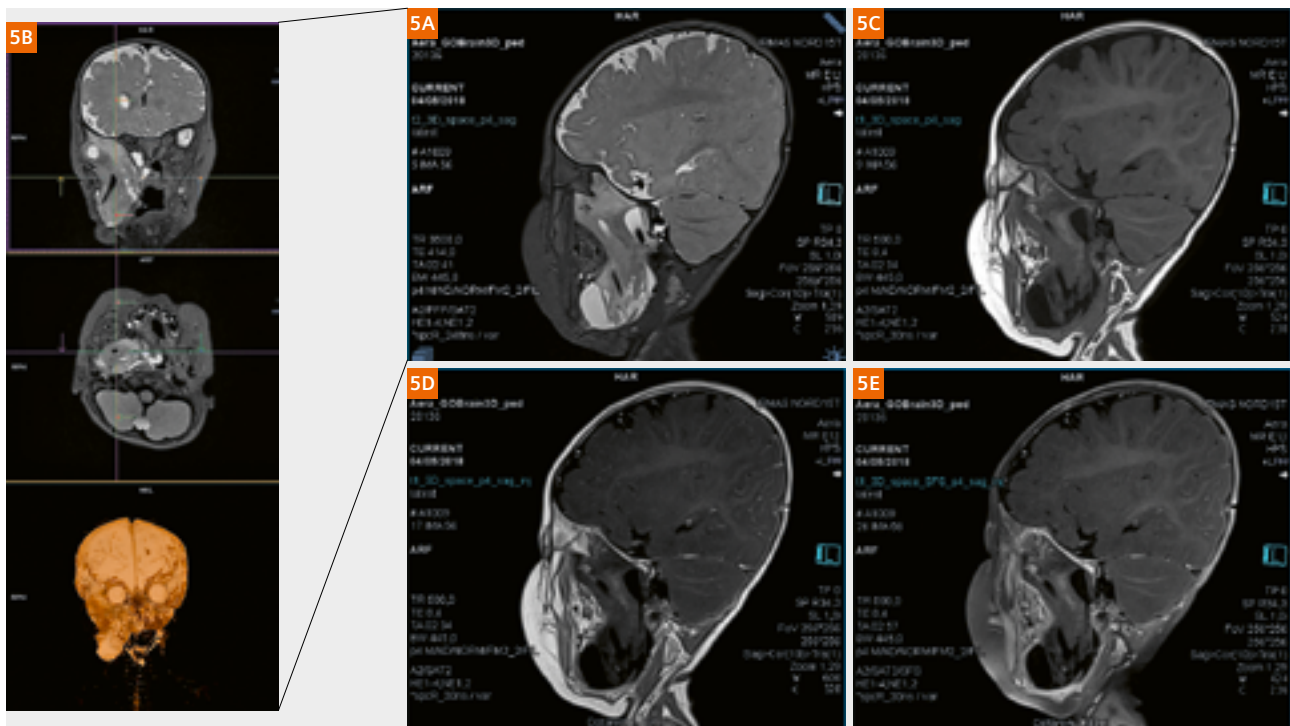
Figure 5:
Examination of a 10-months-old child[1] under general anesthesia, in the context of ENT pathology follow-up. Target was to provide to radiologist all necessary information to evaluate patient response to therapy, in a very short acquisition time. In 10 minutes it was possible to run four 3D protocols with different contrasts (T2, T1, T1 with contrast enhancement, T1 fatsat with contrast enhancement), with MPR reconstructions (all consistent as done by the system through MPR Planning Dot AddIn). Anesthesia has been shorter, with easier recovery. A win/win examination for both patient and radiologist!

[1] *Siemens Healthineers disclaimer does not represent the opinion of the author. MR scanning has not been established as safe for imaging fetuses and infants less than two years of age. The responsible physician must evaluate the benefits of the MR examination compared to those of other imaging procedures.*

With the spine version of CAIPIRINHA SPACE, one usual argument of 3D spine imaging detractors disappears. Acquisition time and MPR reconstruction quality make it possible to outperform 2D protocols (Table 2).

Our institution owns eight MR scanners (including five MAGNETOM Aera 1.5T). As a result, homogeneity within our fleet is a major issue. The more MRIs you have, the harder it is to reach this target. Using our MRIs in a coordinated way as well as being faster and more efficient in the optimization process of CAIPIRINHA-SPACE for multiple body parts made it possible to examine more patients. To improve reactivity and for better ease-of-use, this process was achieved with the help of teamplay

Protocols for real-time distribution (Fig. 6). The distribution of the different versions, the exchange between different systems via the web platform of teamplay, in real time, realized a true gain in efficiency. The MR protocol hub option also gives access to the protocol/ study files (.exar) published on MAGNETOM World at **www.siemens.com/magnetom-world** > Clinical Corner > Protocols.

Conclusion and outlook

CAIPIRINHA SPACE represents more than an acquisition technique; it really is a new acquisition philosophy where 3D finally takes the place it deserves in our imaging specialty. No body region is excluded (Fig. 7). CAIPIRINHA SPACE is currently accessible on all *syngo* MR E11C AP04 platforms, without an additional software license.
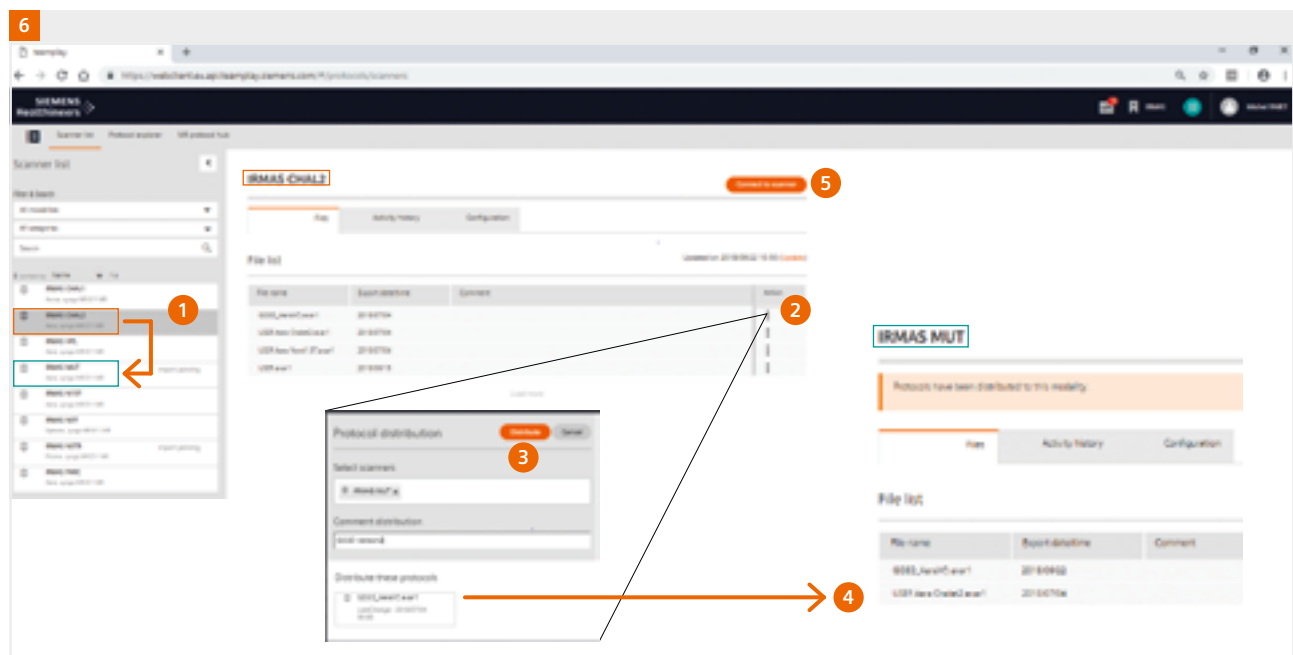
Figure 6:
CAIPIRINHA SPACE protocol distribution (protocol name GO3D), using .exar file format, from one system to another. First the GO3D protocol is exported from the source system to be accessible in the teamplay Protocols interface. Protocol distribution is done from the teamplay interface, by first selecting the source system protocol, and then the destination system. Once distributed, the .exar file GO3D is accessible on the selected system. Two solutions are possible for the .exar file importation in the client user: either let the remote site import it through shared folder, or initiate a remote control session from the source system.
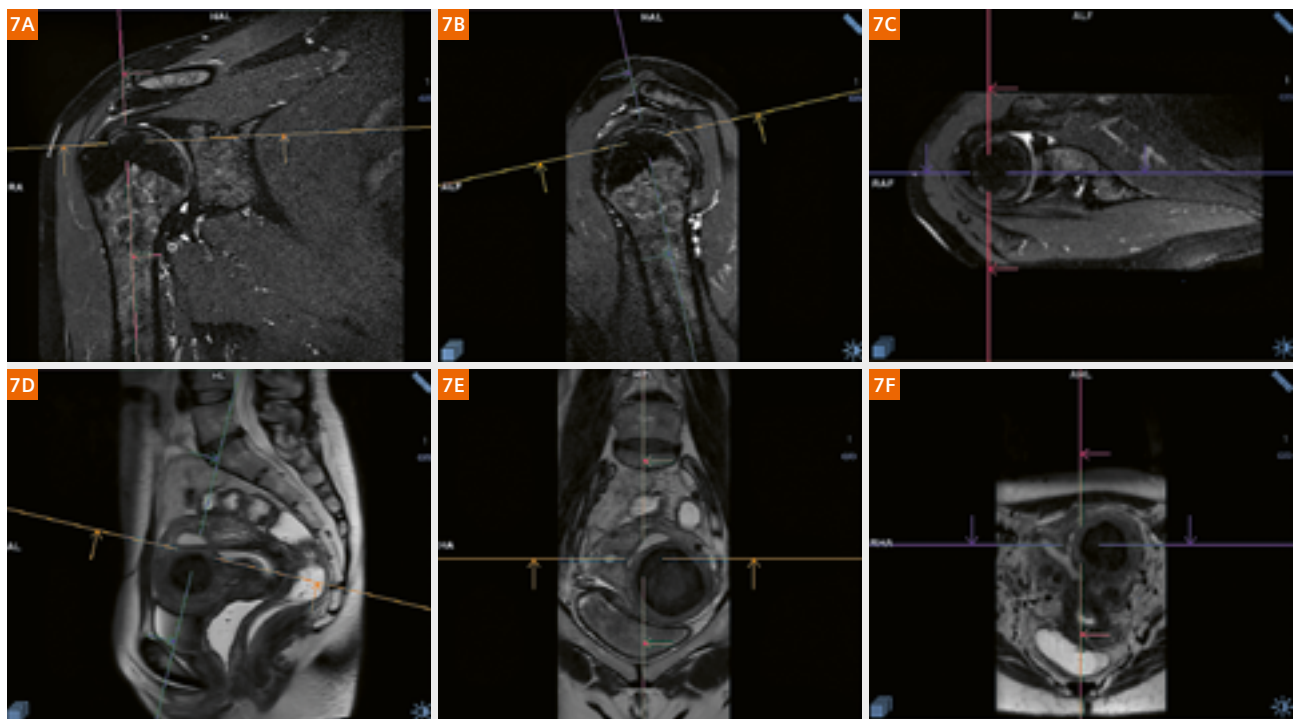
Figure 7:
The CAIPIRINHA SPACE technique is robust enough to be used on more complex organs, sensitive to motion like shoulder **(7A–C)** or pelvis **(7D–F)**.

Acknowledgements

References

1 Meder J, Pruvo J (2011). Magnetic resonance imaging: round-up of current applications and outlook. Controle ASN (Paris), (192), 40-42.
2 Miller E, Smith B. Pediatric GOBrain-5-Minute Protocol MR Imaging at 3 Tesla. MAGNETOM Flash (68)2/2017, 14-18.
3 Prakkamakul S, et al. Ultrafast Brain MRI: Clinical Deployment and Comparison to Conventional Brain MRI at 3T. J Neuroimaging, 2016(5):503-10.
4 Fagundes J, Longo M, Huang S, Rosen B, Witzel T, Heberlein K, Gonzalez R, Schaefer P, Rapalino O. Diagnostic Performance of a 10-Minute Gadolinium-Enhanced Brain MRI Protocol Compared with the Standard Clinical Protocol for Detection of Intracranial Enhancing Lesions, American Journal of Neuroradiology, 38, 9, 1689.
5 Fritz J, et al. Three-dimensional CAIPIRINHA SPACE TSE for 5-minute high-resolution MRI of the knee. Invest Radiol 2016; 51: 609-617.
6 Mugler III J, Optimized Three-Dimensional Fast-Spin-Echo MRI. Journal of MRI 39:745–767 (2014).
7 Breuer F, et al. Controlled aliasing in volumetric parallel imaging (2D CAIPIRINHA). MagnReson Med 2006 55(3),549-556.

Clinical Utility of Amide Proton Transfer Imaging in Patients with Brain Tumors

Linda Knutsson, Ph.D.; Pia Sundgren, M.D., Ph.D.

Lund University, Lund, Sweden

Introduction

Amide Proton Transfer-weighted (APTw) MRI is an emerging technique that does not require using gadolinium contrast. It is a promising tool for tumor grade characterization [1, 2] and for separating tumor recurrence and treatment related changes [3–5]. The concept is based on that exchangeable protons will amplify the MR imaging signal using a method called chemical exchange saturation transfer (CEST) [6]. In APTw imaging it is the amide protons of mobile proteins and peptides in the tissue that are saturated using a selective radio frequency (RF) pulse at 3.5 ppm from the water resonance. This amide proton saturation is then transferred to water protons through physical exchange and by repeating this process one can detect the MR signal of these low concentration proteins and peptides with sensitivity enhancements of a factor of about fifty or more. This allows imaging of the signal from millimolar concentration of the exchangeable amide protons with the molar sensitivity of water protons.

Case 1: Pseudo progression of a high-grade glioma
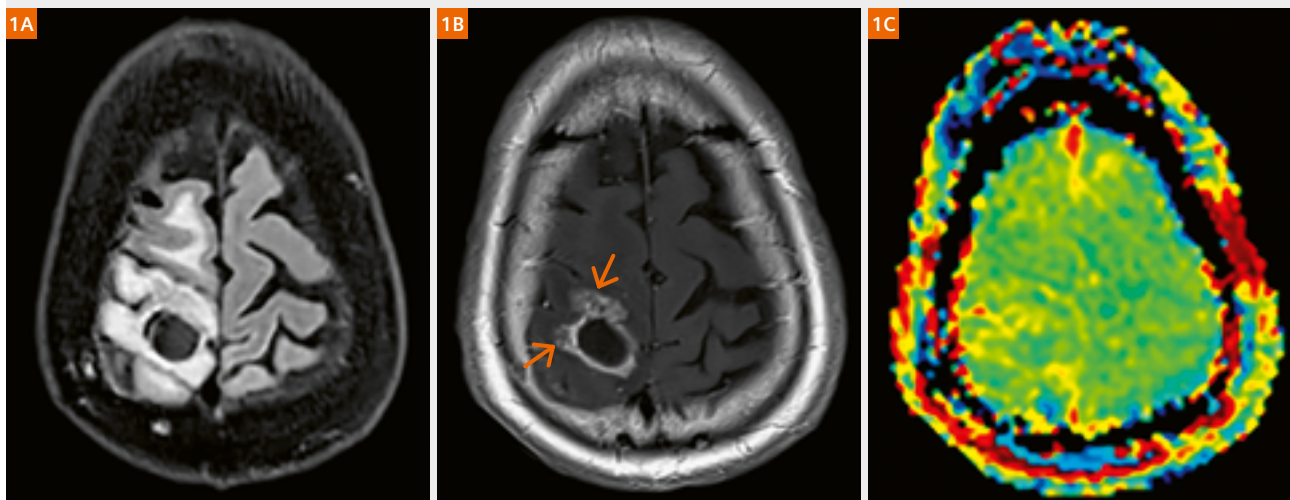
Case 1 shows post-resection MR imaging in a patient with a high-grade glioma. **(1A)** FLAIR images show heterogeneous signal changes surrounding the resection area. **(1B)** Post-Gd, T1-weighted images demonstrate ring enhancement and focal areas (arrows) of scattered enhancement indicating tumor progression. **(1C)** In contrast to FLAIR and post-GD T1-weighted imaging, APT images demonstrate no measurable tumor. The assumption of pseudo progression in FLAIR and T1-weighted imaging was confirmed on follow-up MR examinations.

A tumor has other protein characteristics than normal tissue, leading to a difference in the number of amide protons between these tissues [1]. While other signal contributions are mixed in, leading to the term APT-weighted (APTw) MRI, the contrast at 3.5 ppm is due, in main part, to the mobile proteins and peptides. Previous studies have shown that APTw MRI can separate tumor from edema [1, 7] and correctly detect non-enhancing high grade tumors as malignant and enhancing low-grade tumors as nonmalignant [2]. In addition, the technique has shown the ability to separate tumor recurrence from treatment related changes [4, 5].

Patient cases

We present our first experience with the CEST[1] WIP on a 3T scanner (MAGNETOM Prisma, Siemens Healthcare, Erlangen, Germany). APTw images were generated based on 3D GRE (22 slices, 2 x 2 x 4 mm^3) acquisition of a water saturation spectrum (Z-spectrum, 21 offset points

---

[1] WIP, the product is currently under development and is not for sale in the US and in other countries. Its future availability cannot be ensured.

from -610 to 610 Hz, B1 = 2 µT, tsat = 600 ms, 5 HS pulses, 60 ms spacing, TA 6:50 min), followed by B_0 correction and processing optimized for APT-weighted contrast at 3.5 ppm, providing the typical green brain background and tumor signal highlighted by hyperintensity (yellow or red). Note that blood vessels have a high protein content and may also show up red. In addition, field inhomogeneity may cause enhancement at the brain edges. Figure 1 shows a post-treatment glioma case where APTw MRI could distinguish treatment necrosis from recurrent tumor; In Figure 2, APTw hyperintensity confirmed a high grade glioma, and in Figure 3, APTw MRI identified a recurrent tumor for a case where Gd-enhancement was unclear.

Conclusion

Our early results confirm the promise of APTw MRI for assessing tumor grade and distinguishing recurrent tumor from treatment necrosis. In the future, it might offer a potential surrogate for contrast-enhanced scanning in patients undergoing follow-up scans and may help to better classify the aggressiveness and infiltrative growth of tumors.

Case 2: Classification of a high-grade glioma
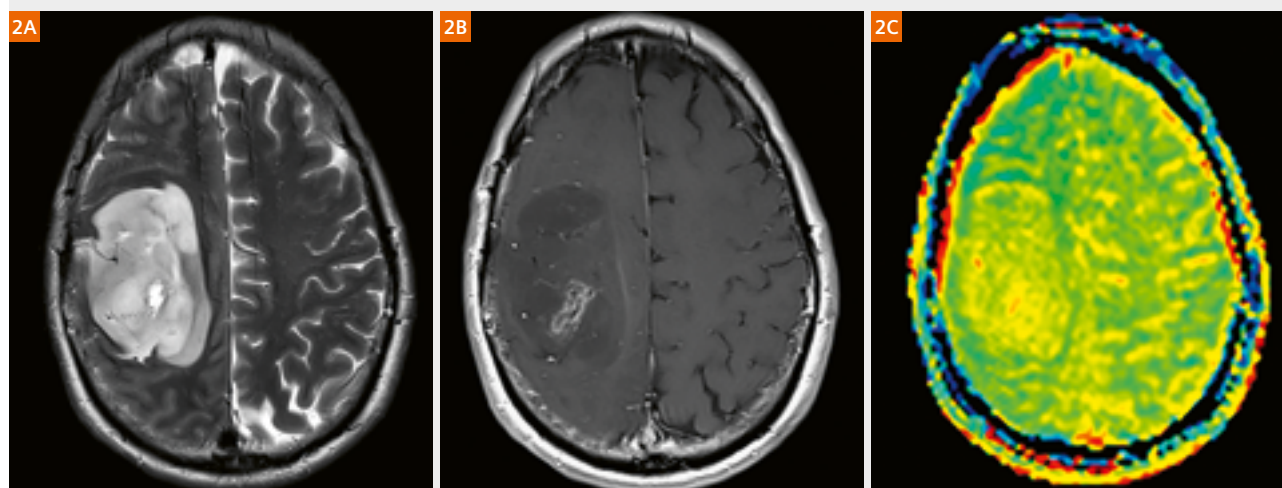
The patient presents with a heterogeneous, well-circumscribed lesion in the right frontoparietal region as seen on **(2A)** T2-weighted and **(2B)** T1-weighted images after GD administration. Although it is a large tumor, the mass effect is moderate. There is only a small, central region of patchy contrast uptake in the tumor, indicating high-grade cancer cells. **(2C)** APT images show a well-circumscribed lesion with moderately increased APT signal and a small central region of higher metabolic activity corresponding to the location of pronounced contrast uptake in T1-weighted images. There is a second area of high activity in the tumor that is not visible in T1-weighted images.

Histopathology after surgery confirmed a high-grade glioma with an isocitrate dehydrogenase (IDH) mutation. Location and appearance, that is a unilateral pattern of growth, sharp tumor margins, and moderate contrast enhancement on MRI, correlate well with the findings of a recent study [8] on the most common locations and prognosis of IDH-mutated gliomas. The results of that study suggest that the prolonged survival of patients with IDH-mutated gliomas is primarily due to a less aggressive biological behavior according to tumor site and MRI features. APT images in the case presented here appear to confirm these findings.

Case 3: Monitoring of a high-grade glioma under treatment presenting progression
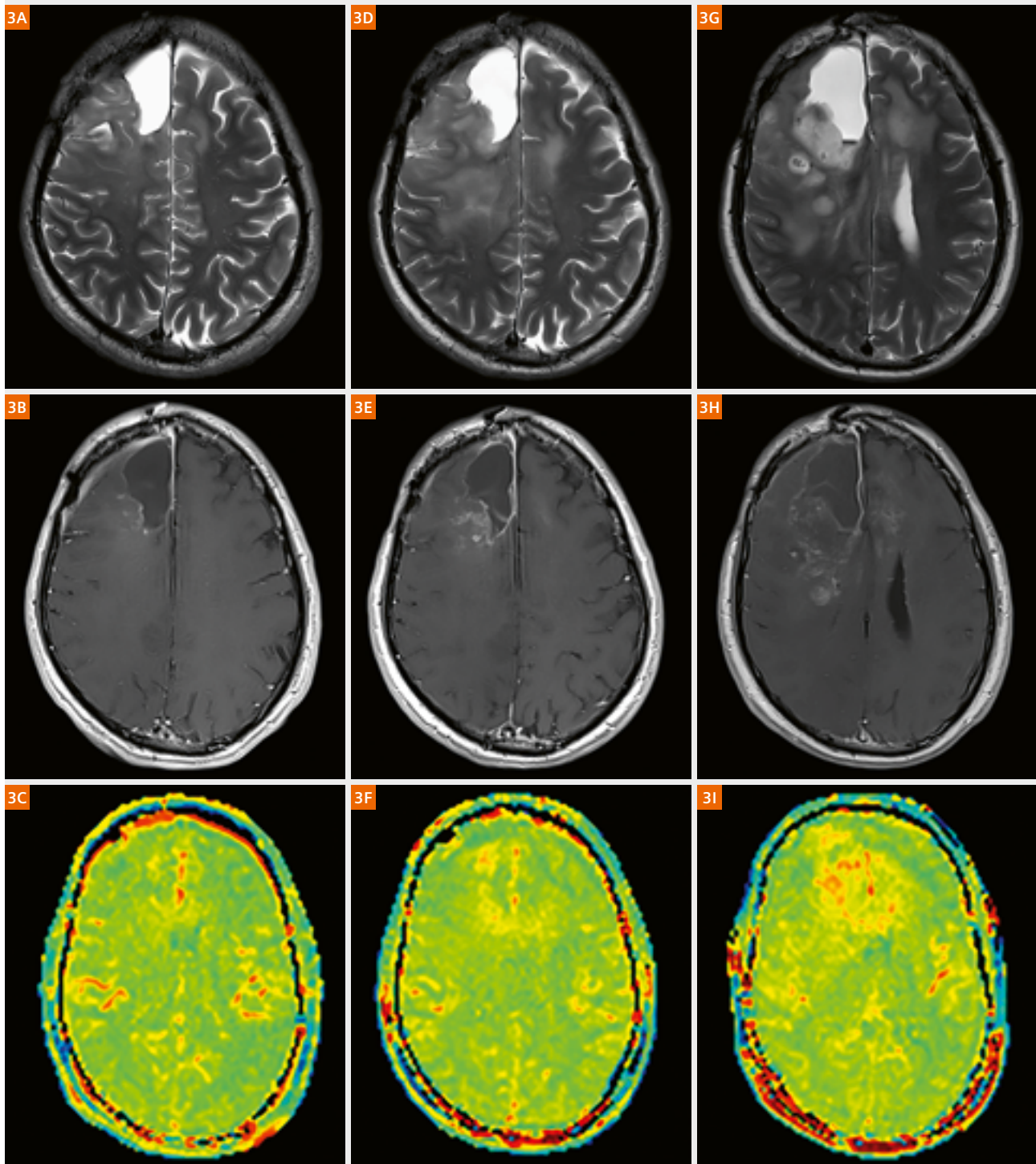
This case illustrates true progression of a high-grade glioma located in the right frontal lobe. **(3A)** Post-surgical edema in T2-weighted images and small, focally enhancing areas in the close vicinity of the resection area in post-GD T1-weighted images **(3B)** are visible. **(3C)** Corresponding APT images show a markedly increased signal in the same region also indicating a further infiltration than visible on T1-weighted images. Follow-up exams after 3 **(3D–F)** and 6 months **(3G–I)** show fast infiltrating tumor growth with diffuse scattered contrast enhancement and progression into the left hemisphere. **(3I)** APTw MRI also shows some hyperintensity in the lateral sulci due to the presence of blood vessels.

References

1   Zhou J, Lal B, Wilson DA, Laterra J, van Zijl PC. Amide proton transfer (APT) contrast for imaging of brain tumours. Magn Reson Med. 2003; 50(6): 1120-6.

2   Zhou J, Zhu H, Lim M, Blair L, Quinones-Hinojosa A, Messina SA, Eberhart CG, Pomper MG, Laterra J, Barker PB, van Zijl PC, Blakeley JO. Three-dimensional amide proton transfer MR imaging of gliomas: Initial experience and comparison with gadolinium enhancement. J Magn Reson Imaging. 2013; 38(5): 1119-28.

3   Zhou J, Tryggestad E, Wen Z, Lal B, Zhou T, Grossman R, Wang S, Yan K, Fu DX, Ford E, Tyler B, Blakeley J, Laterra J, van Zijl PC. Differentiation between glioma and radiation necrosis using molecular magnetic resonance imaging of endogenous proteins and peptides. Nat Med. 2011; 17(1): 130-4.

4   Ma B, Blakeley JO, Hong X, Zhang H, Jiang S, Blair L, Zhang Y, Heo HY, Zhang M, van Zijl PC, Zhou J. Applying amide proton transfer-weighted MRI to distinguish pseudoprogression from true progression in malignant gliomas. J Magn Reson Imaging. 2016; 44(2): 456-62.

5   Park JE, Kim HS, Park KJ, Kim SJ, Kim JH, Smith SA. Pre- and Posttreatment Glioma: Comparison of Amide Proton Transfer Imaging with MR Spectroscopy for Biomarkers of Tumour Proliferation. Radiology. 2016; 278(2): 514-23.

6   van Zijl PC, Yadav NN. Chemical exchange saturation transfer (CEST): what is in a name and what isn't? Magn Reson Med. 2011; 65(4): 927-48.

7   Jones CK, Huang A, Xu J, Edden RA, Schär M, Hua J, Oskolkov N, Zacà D, Zhou J, McMahon MT, Pillai JJ, van Zijl PC. Nuclear Overhauser enhancement (NOE) imaging in the human brain at 7T. Neuroimage 2013; 77: 114-24.

8   Qi S, Yu L, Li H, Ou Y, Qiu X, Ding X, Han H, Zhang X. Isocitrate dehydrogenase mutation is associated with tumor location and magnetic resonance imaging characteristics in astrocytic neoplasms. Oncology Letters 2014;7:1895-1902.
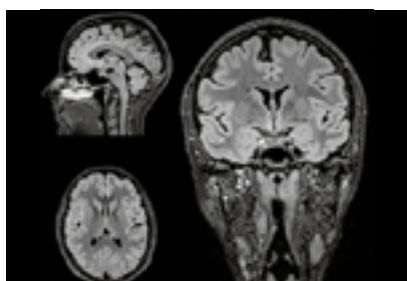
Neuro Imaging
3D CAIPIRINHA SPACE
1 x 1 x 1 mm resolution
TA 2:40 min
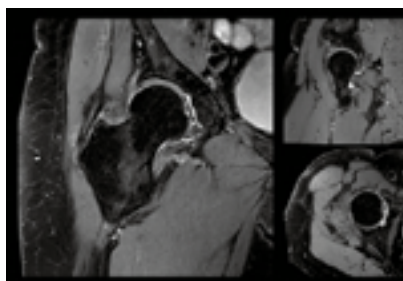
MSK Imaging
PD fatsat 3D CAIPIRINHA SPACE
TA 4:14 min
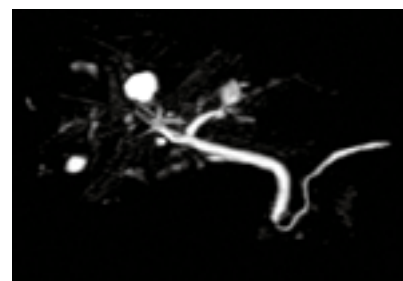
Abdominal Imaging
3D CAIPIRINHA SPACE MRPC
TA 21 seconds

Introduction

Arterial spin labeling (ASL) is an MR perfusion technique which uses magnetically labeled arterial blood as tracer for measuring local tissue perfusion [1–4]. Quantitative brain imaging – i.e., absolute measurements of regional cerebral blood flow (CBF) – is achievable with simple, conventional kinetic modeling of labeled blood [5]. The greatest benefit of ASL is that it is completely noninvasive, with no need for radioactive tracers as in other modalities or exogeneous contrast agents. However, despite numerous research efforts since the initial reports on continuous ASL (CASL) were published in 1992 [6, 7], it is only quite recently that ASL has been adequately applied in clinical settings. The primary problem was that ASL images had an intrinsically low signal-to-noise ratio due to the rapid T1 decay of labeled blood. This situation changed radically in the 2010s, with the introduction of pseudo-continuous ASL (PCASL) [8, 9] combined with rapid 3D readout sequences on commercially available MR scanners. These technical innovations greatly improve the image quality, and therefore encourage routine clinical use of ASL. Increased use of ASL imaging is evidenced by the recent rapid rise in the number of research publications on the topic (Fig. 1). To address the diversity of ASL methodologies and implementations, various research communities,

the Perfusion Study Group of the International Society for Magnetic Resonance in Medicine (ISMRM), and the European consortium ASL in Dementia (AID) held workshops in 2012 to formulate a consensus statement on current recommendations for ASL imaging. This was then published as a consensus paper, or white paper, in 2015 [2]. The statement strongly recommends PCASL acquisition combined with a segmented 3D readout sequence and a background suppression (BS) technique. The recommended ASL implementations are currently available as a prototype[1] on Siemens Healthineers MR scanners.

Quantitative imaging for cerebral circulation plays a critical role in the understanding of brain pathophysiology and in making decisions about treatment courses for patients with cerebrovascular steno-occlusive disease [10–12]. Imaging modalities used in modern clinical practice – i.e., molecular imaging methods including positron emission tomography (PET) and single photon emission tomography, and bolus-tracking techniques with computed tomography or MR imaging – have various advantages and disadvantages [13]. Although ASL is entirely noninvasive and has the potential to replace the other methods, its technical limitations and pitfalls are not yet fully understood. In addition, the clinical

---

[1] WIP, the product is currently under development and is not for sale in the US and in other countries. Its future availability cannot be ensured.

Figure 1:
Number of ASL publications per year (based on PubMed search results).
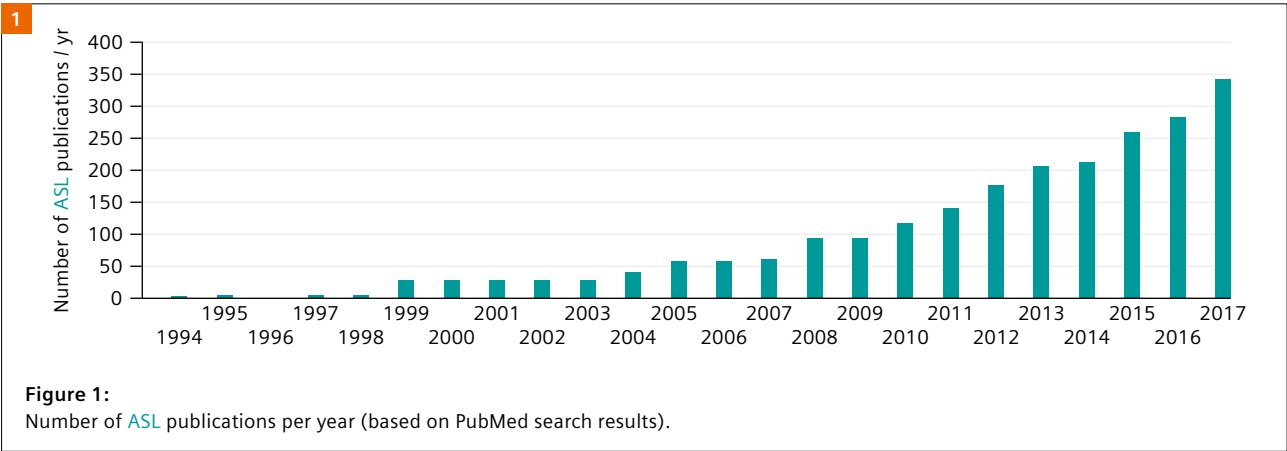
value of ASL imaging has yet to be widely accepted. Under these circumstances, we believe that a comparative study with the other imaging modalities will be of great value for gaining a deeper understanding of ASL. Among the imaging modalities, PET with ^{15}O-labeled compounds (^{15}O PET) is regarded as the gold standard for assessing cerebral circulation and oxygen metabolism [12, 14]. It can quantitatively measure CBF, cerebral blood volume (CBV), oxygen extraction fraction (OEF), and cerebral metabolic rate of oxygen (CMRO$_2$) in a single examination session and thereby enable a comprehensive assessment of the patient's cerebral perfusion status. In this report, we use direct comparisons with [15]O PET in patients with cerebrovascular steno-occlusive disease to present the clinical benefits and some key pitfalls of brain ASL imaging.

Arterial spin labeling methods

Two types of labeling have been used in ASL imaging: CASL and pulsed ASL (PASL) [15]. With the Siemens prototype package[1], both of these techniques – i.e., PCASL and FAIR Q2TIPS – are available combined with a segmented 3D GRASE readout and BS module [16, 17]. Bolus duration (TI$_1$) and inversion time (TI) are major sequence parameters. In PCASL, TI$_1$ and the difference between TI and TI$_1$ are usually referred to as, respectively, labeling duration (LD) and post-labeling delay (PLD) (Fig. 2).

Pseudo-continuous Arterial Spin Labeling (PCASL)
CBF maps for PCASL with single PLD are calculated with the standard equation

$$f = \frac{\lambda \Delta M R_{1a}}{2\alpha M_0 (\exp(-wR_{1a}) - \exp(-(\tau+w)R_{1a}))}$$

where f is regional CBF in mL/100g/min, λ is blood/tissue water partition coefficient (0.9 mL/g), α is inversion efficiency (85% for PCASL), M_0 and ΔM are respectively fully relaxed image intensity and signal difference (control/label), τ is LD (or TI$_1$), w is PLD (or TI–TI$_1$), and R_{1a} is longitudinal relaxation rate of blood (0.606 s-1 at 3T).

Pulsed Arterial Spin Labeling (PASL)
In PASL, multiple inversion time (multi-TI) acquisition is available. CBF and arterial transit time (ATT) maps are calculated by analyzing the time series of ASL images using a simple kinetic model [5]. ATT can be a useful measure for evaluating hemodynamic ischemia, as we will show below.

Figure 2:
Timing diagram for PCASL.
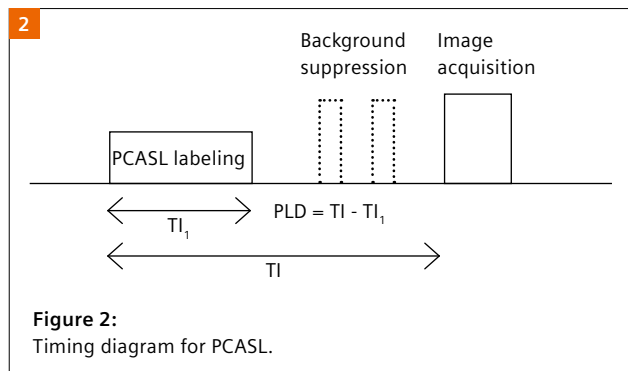
Scanner	MAGNETOM Verio	
ASL module	PCASL	PASL
LD (PCASL) / TI$_1$ (PASL)	1800 ms	700 ms
PLD (PCASL) / TI (PASL)	2000 ms	470–3770 ms (16 time-points)
Readout module	3D GRASE	
TR / TE	4600 / 18 ms	4600 / 21.8 ms
Number of repetitions	6	1
GRAPPA acceleration factor	2	
EPI factor	21	31
Turbo factor	12	
Field-of-view	256 x 256 x 144 mm	
Voxel size	4.0 x 4.0 x 6.0 mm³	
Acquisition time	4 min 6 sec	5 min 11 sec

Table 1: Imaging parameters.

Our imaging protocol includes two sequential ASL acquisitions [18]: A single-PLD PCASL with a high number of averages for sufficiently high-quality CBF maps, and a multi-TI PASL for obtaining ATT maps. The 3T scanner, a MAGNETOM Verio with a 32-channel head coil, used the imaging parameters presented in Table 1, at the recommended setting [2].

Case reports: Comparisons with [15]O PET

In our institute, patients with occlusion or severe stenosis of major cerebral arteries – the internal carotid artery (ICA) and the middle cerebral artery (MCA) – are routinely examined by [15]O PET, mainly to assess indications for revascularization surgery. We present five representative cases that highlight the utility and pitfalls of clinical ASL imaging.

Case 1: Chronic infarction due to occlusion of the right MCA

PCASL images show a marked hypoperfused lesion in the right parietal lobe. Corresponding T2-weighted images show a marked hyperintense lesion in the ischemic core. CBF and $CMRO_2$ (both measured by

^{15}O PET) are severely reduced in the right parietal lobe. The lesion with markedly decreased signal in the PCASL images is almost identical to the perfusion defect in the PET CBF and $CMRO_2$ maps.

| PCASL | PET | PET | T2w |
| CBF | CBF | $CMRO_2$ | |
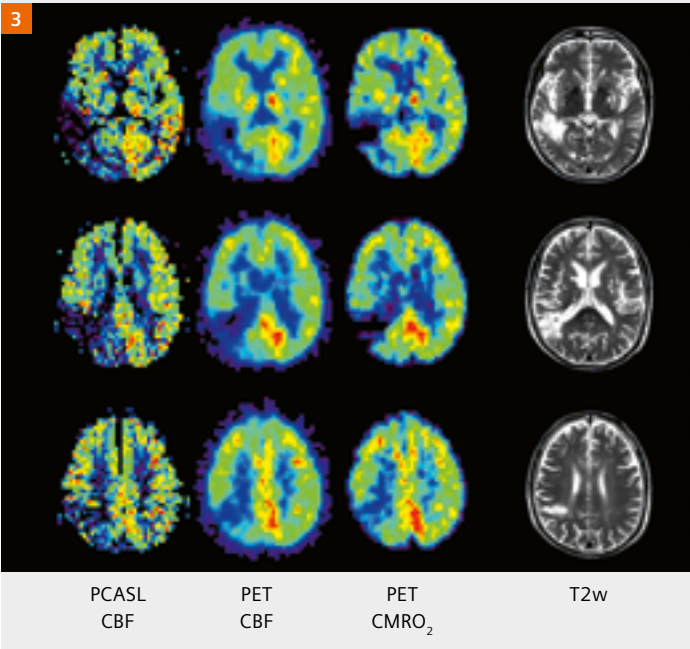
Figure 3:
A patient with right MCA occlusion;
left to right: PCASL CBF, PET CBF, PET $CMRO_2$,
T2-weighted images.

Case 2: Severe stenosis of the right ICA

PCASL images show hypoperfusion in the right cerebral hemisphere. Subtle but definitely increased vascular signal is visible in the hypoperfused lesion. ATT is slightly prolonged in the right cerebral hemisphere. MRA shows severe stenosis of the terminal segment of the right ICA (arrow). PET CBV is increased

in the right cerebral hemisphere. CBF is reduced more than $CMRO_2$, and OEF is mildly increased. These ^{15}O PET findings indicate misery perfusion. PCASL imaging can clearly visualize a hypoperfused lesion with vascular signal in cases with severe stenosis of a major artery.

| PCASL | PASL | PET | PET | PET | PET |
| CBF | ATT | CBF | CBV | OEF | $CMRO_2$ |

Figure 4:
A patient with right ICA stenosis;
left to right: PCASL CBF, PASL ATT, PET CBF, PET CBV, PET OEF, PET $CMRO_2$, MRA.

Case 3: Moyamoya disease

PCASL imaging shows relative hypoperfusion with small foci of high signal in the right cerebral hemisphere. ATT is relatively prolonged in the right cerebral hemisphere. MRA shows multiple large-vessel occlusions in both anterior and posterior circulation with abnormally prominent collateral formation. Cortical branches of the right MCA are poorly visualized on MRA images, indicating hypoperfusion in the right MCA territory. The collateral pathway via leptomeningeal anastomosis is thought to be poorly developed because distal branches of the bilateral posterior cerebral arteries (PCAs) are insufficiently visualized with MRA. ^{15}O PET images show higher CBV and OEF, and lower CBF in the right cerebral hemisphere. Increased OEF with minimally decreased $CMRO_2$ may lead to a diagnosis of misery perfusion. Arterial transit artifact (ATA) in PCASL images, which is characterized by increased high vascular signal, occurs with misery perfusion because decreased perfusion pressure results in labeled blood stagnating in the vasculature before it enters tissue capillaries [18–20], which is consistent with prolonged ATT.

PCASL
CBF   PASL
ATT   PET
CBF   PET
CBV   PET
OEF   PET
$CMRO_2$
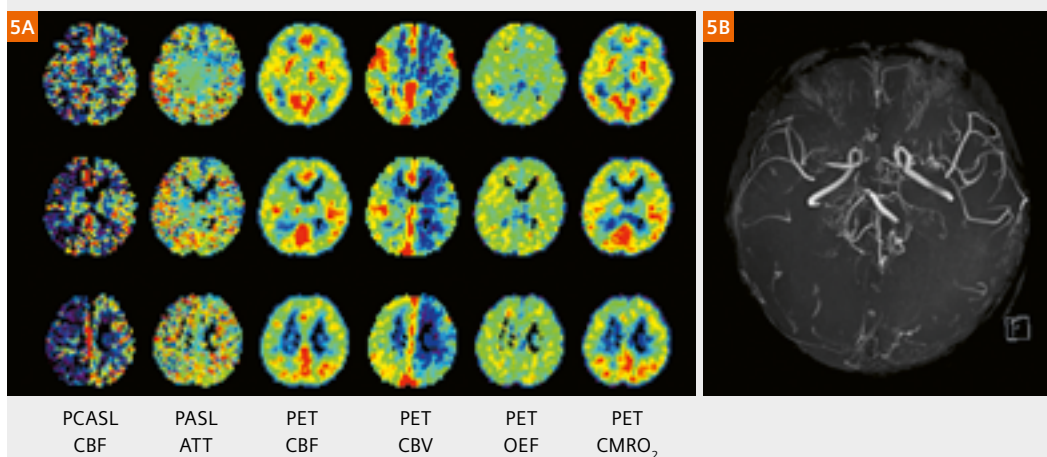
Figure 5:
A patient with moyamoya disease; left to right: PCASL CBF, PASL ATT, PET CBF, PET CBV, PET OEF, PET $CMRO_2$, MRA.

Case 4: Occlusion of the right ICA

PCASL images show increased signal mimicking hyperperfusion in the right cerebral hemisphere. ATT is markedly prolonged in the right cerebral hemisphere. Areas with delayed ATT correspond to high signal foci with PCASL. MRA shows occlusion of the right ICA with prominent PCA reflecting good collateral circulation through leptomeningeal anastomosis. ^{15}O PET images show higher CBV and OEF, and lower CBF with a minimal decrease in $CMRO_2$ in the right cerebral hemisphere, suggesting misery perfusion in the right cerebral hemisphere. ATA frequently appears in focal misery perfusion on PCASL images. Increased signal due to ATA should not be misdiagnosed as hyperperfusion.

PCASL
CBF   PASL
ATT   PET
CBF   PET
CBV   PET
OEF   PET
$CMRO_2$

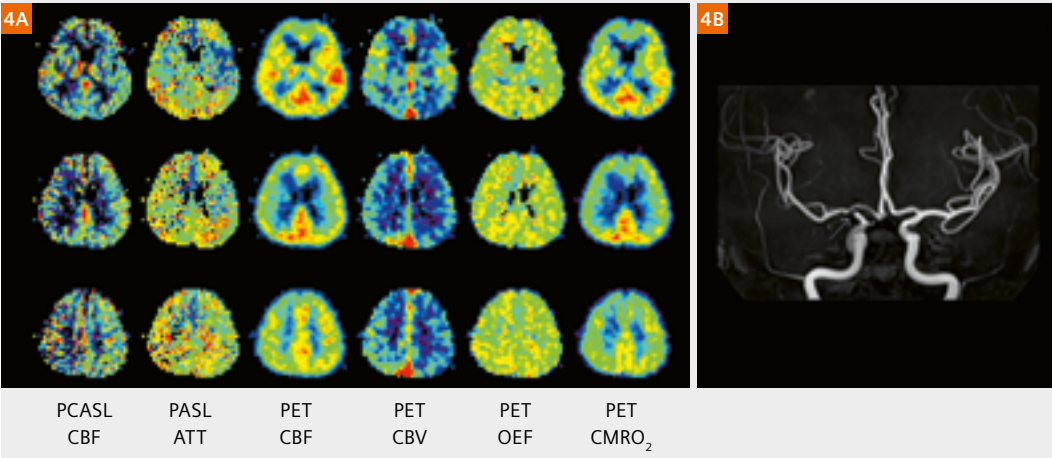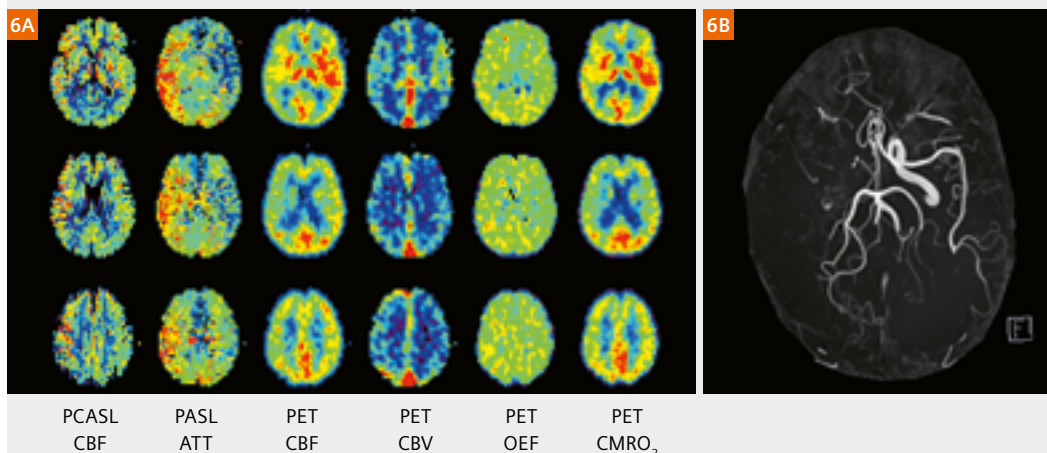**Figure 6:**
A patient with right ICA occlusion; left to right: PCASL CBF, PASL ATT, PET CBF, PET CBV, PET OEF, PET $CMRO_2$, MRA.

Case 5: Right ICA aplasia

MRA shows filling of the right distal ICA via the right posterior communicating artery with non-visualization of the right proximal ICA. PCASL imaging shows relatively decreased signal in the right cerebral hemisphere. ATT is not prolonged in the right cerebral hemisphere. CBF measured with ^{15}O PET is normal.

In PCASL imaging, blood-flow-velocity-dependent and/or vessel-geometry-related variations in labelling efficiency are possible sources of error [21]; labeling efficiency in the vertebral artery might be different from that in the carotid artery, and this difference might produce left-right asymmetric PCASL images.

PCASL CBF   PASL ATT   PET CBF
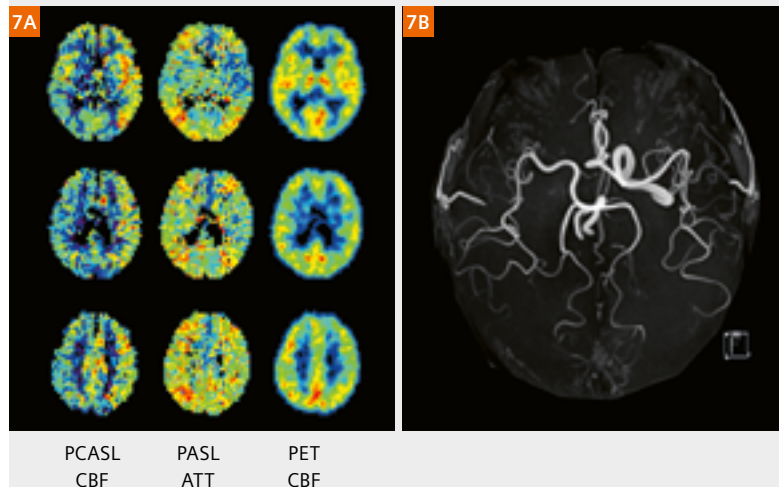
Figure 7:
A patient with right ICA aplasia;
left to right: PCASL CBF, PASL ATT, PET CBF, MRA.

Summary

ASL, a completely non-invasive perfusion imaging technique, has now become a clinical tool for evaluating cerebral ischemia. In this report, we presented our clinical experiences of 3D ASL imaging in patients with cerebrovascular steno-occlusive disease, and emphasized comparisons with the gold standard ^{15}O PET. We can summarize the clinical utility and some pitfalls of current ASL imaging in the evaluation of hypoperfusion state accompanied by severe stenosis or occlusion of a major artery:

1. ASL imaging can clearly visualize lesions of territorial or superficial divisional MCA infarction as areas with severe hypoperfusion and significantly reduced CBF.
In a patient with severe stenosis or occlusion of major arteries, delays to the regional arrival time of labeled bloods occur frequently in hypoperfused areas. This is clearly visualized as prolonged ATT with multiple inversion time ASL acquisition. Delayed arrival results in bright vascular signals in CBF maps with single-PLD PCASL acquisition. This ATA sign should not be misdiagnosed as hyperperfusion.

2. In PCASL imaging, variations in labeling efficiency between feeding vessels are a possible source of error, but they are rarely detected without additional clinical and other imaging information. The variations in labeling efficiency may cause an asymmetrical PCASL CBF map in a case of unilateral ICA aplasia or occlusion.
When unexpected, uninterpretable CBF maps occur, the above methodological errors (i.e., ATA and labeling efficiency variations) should be considered. MRA findings can provide important information about the pathway of the labeled bloods and thereby help us to better interpret ASL images.

Acknowledgements

References

1 Detre JA et al. Applications of arterial spin labeled MRI in the brain. J Magn Reson Imaging. 2012 May;35(5):1026-37.
2 Alsop DC et al. Recommended implementation of arterial spin-labeled perfusion MRI for clinical applications: A consensus of the ISMRM perfusion study group and the European consortium for ASL in dementia. Magn Reson Med. 2015 Jan;73(1):102-16.
3 Grade M et al. A neuroradiologist's guide to arterial spin labeling MRI in clinical practice. Neuroradiology. 2015 Dec;57(12):1181-202.
4 Haller S et al. Arterial Spin Labeling Perfusion of the Brain: Emerging Clinical Applications. Radiology. 2016 Nov;281(2):337-356.
5 Buxton RB et al. A general kinetic model for quantitative perfusion imaging with arterial spin labeling. Magn Reson Med. 1998 Sep;40(3):383-96.
6 Detre JA et al. Perfusion imaging. Magn Reson Med. 1992 Jan;23(1):37-45.
7 Williams DS et al. Magnetic resonance imaging of perfusion using spin inversion of arterial water. Proc Natl Acad Sci U S A. 1992 Jan;89(1):212-6.
8 Wu WC et al. A theoretical and experimental investigation of the tagging efficiency of pseudocontinuous arterial spin labeling. Magn Reson Med. 2007 Nov;58(5):1020-7.
9 Dai W et al. Continuous flow-driven inversion for arterial spin labeling using pulsed radio frequency and gradient fields. Magn Reson Med. 2008 Dec;60(6):1488-97.
10 Powers WJ, Grubb RL Jr, Raichle ME. Physiological responses to focal cerebral ischemia in humans. Ann Neurol. 1984 Nov;16(5):546-52.
11 Gibbs JM et al. Evaluation of cerebral perfusion reserve in patients with carotid-artery occlusion. Lancet. 1984 Feb;1(8372):310-4.
12 Okazawa H, Kudo T. Clinical impact of hemodynamic parameter measurement for cerebrovascular disease using positron emission tomography and (15)O-labeled tracers. Ann Nucl Med. 2009 May;23(3):217-27.
13 Wintermark M et al. Comparative overview of brain perfusion imaging techniques. Stroke. 2005 Sep;36(9):e83-99.
14 Ito H, Kanno I, Fukuda H. Human cerebral circulation: positron emission tomography studies. Ann Nucl Med. 2005 Apr;19(2):65-74.
15 Detre JA. Arterial Spin Labeled Perfusion MRI. MAGNETOM Flash. 2008;1:6-9.
16 Günther M, Oshio K, Feinberg DA. Single-shot 3D imaging techniques improve arterial spin labeling perfusion measurements. Magn Reson Med. 2005 Aug;54(2):491-8.
17 Feinberg D, Ramanna S, Günther M. Evaluation of new ASL 3D GRASE sequences using parallel imaging, segmented and interleaved k-space at 3T with 12- and 32-channel coils. In: Proc Int Soc Magn Reson Med. 2009 17;623.

18 Ibaraki M et al. Spatial coefficient of variation in pseudo-continuous arterial spin labeling cerebral blood flow images as a hemodynamic measure for cerebrovascular steno-occlusive disease: A comparative (15)O positron emission tomography study. J Cereb Blood Flow Metab. 2018 Jan;1:271678X18781667.
19 Amukotuwa SA, Yu C, Zaharchuk G. 3D Pseudocontinuous arterial spin labeling in routine clinical practice: A review of clinically significant artifacts. J Magn Reson Imaging. 2016 Jan;43(1):11-27.
20 Zaharchuk G et al. Arterial spin-label imaging in patients with normal bolus perfusion-weighted MR imaging findings: pilot identification of the borderzone sign. Radiology. 2009 Sep;252(3):797-807.
21 Barkeij Wolf JJ et al. Unilateral fetal-type circle of Willis anatomy causes right-left asymmetry in cerebral blood flow with pseudo-continuous arterial spin labeling: A limitation of arterial spin labeling-based cerebral blood flow measurements? J Cereb Blood Flow Metab. 2016 Sep;36(9):1570-8.

Introduction

The world's population aged 60 years or over is predicted to grow by 56% from 901 million to 1.4 billion by the year 2030 [1]. It is well known that aging is associated with impaired cognitive performance and an increased risk for developing dementia. As a result, the social

challenges and the burden for healthcare systems and on society directly related to increases in the aging population will become enormous. A healthy lifestyle – consisting of a healthy diet combined with increased physical activity levels – protects against cognitive impairment [2]. Underlying mechanisms still remain unclear, but it has been considered that improving brain

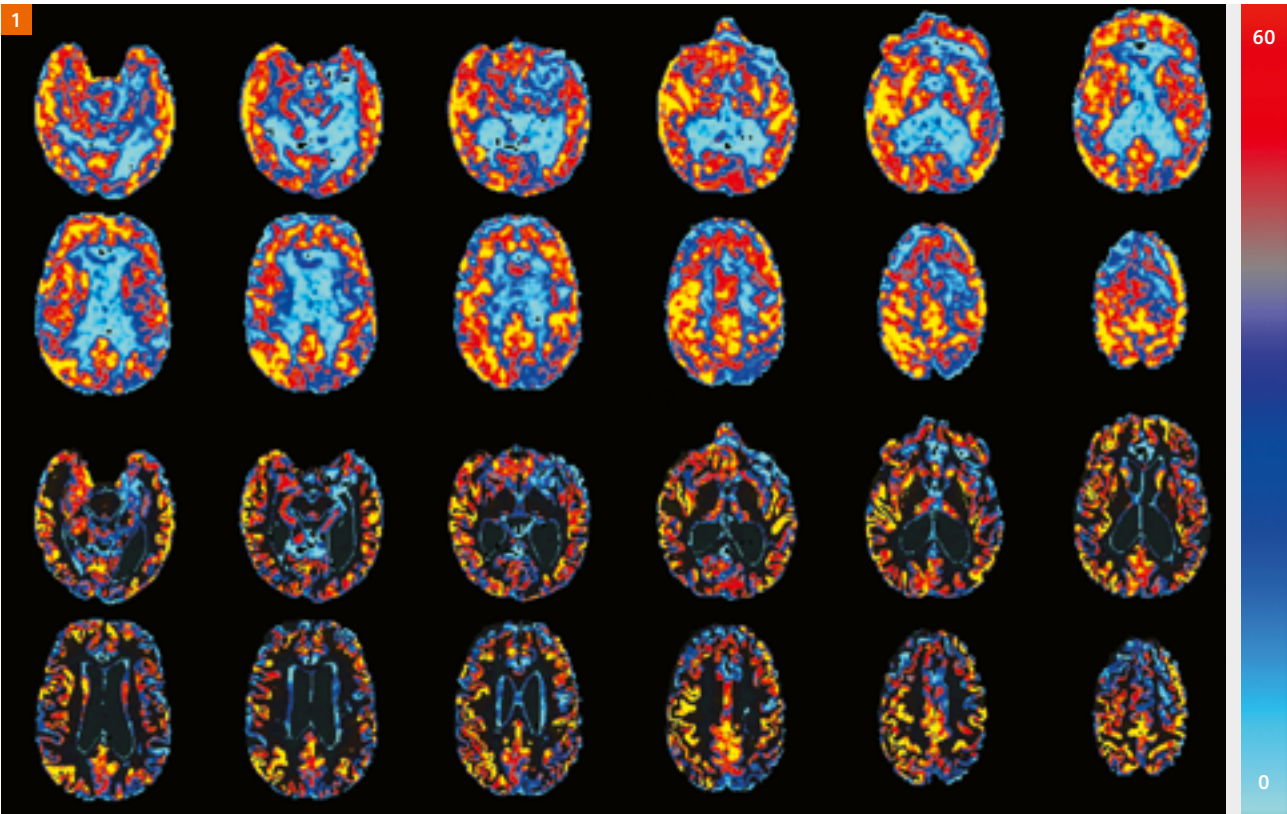

Figure 1:
Cerebral blood flow (CBF) maps showing the amount of blood flow in a particular region of the brain in mL/100 g tissue/min (scale shown by color bar). The lower two rows depict gray matter CBF, while other brain tissues are masked.

vascular health may be a key aspect [2–5]. In this respect, effects on cerebral blood flow (CBF), which is defined as a sensitive physiological marker of brain vascular health [6, 7], are of major interest because compromised vascular health in the human brain most likely precedes the development of an impaired cognitive performance [8–10]. Normal aging is associated with a progressive decline in global CBF by approximately 0.45% to 0.50% per year in middle-aged and elderly adults [3, 11, 12], and these perfusion changes are strongly associated with changes in cognitive performance and the risk to develop dementia [3, 10, 13]. Therefore, many trials have focused on middle-aged and elderly adults who are also at increased vascular risk, allowing for improvement through lifestyle-based intervention strategies. Furthermore, age-related changes in cognitive performance are mainly attributed to a decrease in gray matter CBF, which results in an suboptimal removal of metabolic waste products, and supply of oxygen and nutrients to the cerebral cortex [14]. In fact, the mean gray matter CBF was 15% lower in late middle-aged subjects suffering from metabolic syndrome compared to age-matched healthy controls, and was also associated with lower cognitive performance [15]. In addition, CBF in specific cognitive control brain regions, such as the fusiform gyrus (attention), hippocampus (memory) and prefrontal cortex (executive function), are also of major interest [16]. Furthermore, hypoperfusion in the posterior cingulate cortex and precuneus (combines attention with information from memory and perception), which are part of the default mode network that is also associated with cognitive control, has been consistently observed in subjects with decreased cognitive performance [17].

Methods for measuring CBF in humans include Positron Emission Tomography (PET) and MRI techniques, such as Dynamic Susceptibility Contrast (DSC), Dynamic Contrast Enhanced (DCE) and Arterial Spin Labeling (ASL) [3]. PET measures the amount of ^{15}O-labeled water radiotracer delivered to the brain tissue by blood flow and is considered the current gold standard approach to quantify CBF [18, 19]. However, the invasive nature, the requirement of an onsite cyclotron and large partial volume effects, which are caused by low spatial resolution, reduce the usefulness of this technique [19]. Also, DSC and DCE are invasive as they employ injections of gadolinium-based contrast agents. As a promising alternative approach, ASL enables the non-invasive assessment of CBF using magnetically-labeled water molecules in arterial blood as an endogenous tracer. The signal difference between label and control images (with and without prior labeling of the arterial blood water) can be scaled to yield highly repeatable quantitative measures of CBF [6]. In a recent systematic review, PET was compared with ASL to measure CBF. The work concluded that ASL is an appropriate alternative method for accurate and reproducible quantification of gray matter CBF [19].

In our recent review, we summarized the impact of specific dietary determinants and physical exercise on CBF, and examined the relation between these effects and potential changes in cognitive performance [3]. We concluded that these lifestyle factors may increase CBF, thereby improving cognitive performance. However, well-designed intervention studies investigating the potential of diet and exercise on CBF are still warranted. Especially, longitudinal studies involving middle-aged and elderly adults at increased vascular risk, who are also known to be at increased risk of cognitive impairment and dementia, would be of major interest [3]. Therefore, our current research at the Department of Nutrition and Movement Sciences at Maastricht University is focused on the long-term impact of specific dietary components and physical exercise on both CBF and cognitive performance. We primarily target overweight and slightly obese elderly while using ASL to quantify changes in (regional) CBF. For example, in one of our ongoing projects, we are conducting a tightly-controlled, progressive, intervention study investigating the specific effects of aerobic-based exercise training – three times a week at 70% maximal power for a total duration of eight weeks – on brain vascular health. Besides potential beneficial effects on CBF, a healthy lifestyle may also
 • preserve the structural integrity of white matter,
 • protect from iron accumulation and
 • attenuate brain athrophy [20–23].

Therefore, fluid-attenuated inversion recovery (T2-FLAIR), R2* maps calculated from T2*-weighted gradient-echo (GRE), and T1-weighted magnetization-prepared rapid gradient-echo (MPRAGE) images are also obtained to assess structural status of the brain. These MRI-scans are used to visualize, for example, white matter signal abnormalities (T2-FLAIR), iron accumulation (R2*) and brain volume (MPRAGE). In fact, these brain changes are age-dependent, and are also associated with cognitive performance and the risk of developing dementia [24–29]. A detailed description of this trial has been provided on ClinicalTrials.gov (NCT03272061).

The purpose of this article is to demonstrate the utility of ASL for the non-invasive (region-specific) quantification of CBF in elderly, and to discuss the potential link between CBF and structural brain status (e.g. presence of white matter signal abnormalities, iron accumulation and brain athrophy).

Material and methods

Participant

During this ongoing study, multiple study participants will be scanned. Below, we present example data from one of them. The participant was a 67-year-old male with a body mass index (BMI) of 28.9 kg/m^2 without known medical complaints. He did not use medication prior to and during the study and was sedentary as assessed by the international physical activity questionnaire (IPAQ).

Data acquisition and sequence

Measurements were performed on a 3T MAGNETOM Prisma[fit] MRI-system (Siemens Healthcare, Erlangen, Germany) using a 64-channel head-neck coil (Siemens Healthcare, Erlangen, Germany) at the Scannexus research facilities in Maastricht. The participant was placed head-first-supine in the scanner. The eye centers were taken as a reference for the magnet isocenter position, which was at the level of the pons to minimize B_0 offsets in the labeling region. Furthermore, the labeling plane was positioned perpendicular to the carotid and vertebral arteries.

Perfusion-weighted images were acquired using pseudo-continuous arterial spin labeling (PCASL)[1] with a background-suppressed 3D GRASE readout (TR 4000 ms, TE 13.6 ms, GRAPPA 2, labeling duration 1750 ms, post-labeling delay (PLD) 2000 ms and ten label-control repetitions, duration: 9 min). Nineteen slices with a voxel resolution of 3.0 mm isotropic were acquired. PCASL was used because it has a higher temporal signal-to-noise ratio (tSNR) as compared to pulsed ASL (PASL) and continuous ASL (CASL) [30]. In order to allow CBF quantification, an M_0 image without magnetization preparation and with a TR of 20 s was also acquired [31].

A prototype PCASL sequence1 from Siemens Health-care was used which includes an optimized background suppression containing four inversion pulses, which results in a tissue signal suppression > 99% [32, 33]. This strong background suppression guarantees both a reduced influence of physiological noise and an increased CBF tSNR without compromising temporal resolution or efficiency. The latter is especially useful in frail elderly populations, who are prone to head motion.

One high-resolution anatomical MPRAGE scan was also performed (TR 2400 ms, TE 2.18 ms, TI 1040 ms, 1.0 mm isotropic resolution, 8° flip angle and 160 sagittal slices, duration 6 min). In addition, a T2-FLAIR image was acquired (TR 9000 ms, TE 89 ms, TI 2500 ms, voxel size 1.0 x 1.0 x 3.0 mm, 150° flip angle and 50 axial slices, duration 3 min). Furthermore, a GRE

sequence with four echo times was obtained (TR 31 ms, TE1 2.73 ms, TE2 7.65 ms, TE3 13.61 ms, TE4 21.86 ms, voxel size 0.9 x 0.9 x 1.0 mm, 12° flip angle and 144 axial slices, duration 5 min). The field-of-view across the various sequences was kept constant for accurate registration and anatomical localization.

Processing

A quantitative CBF map was estimated from the ASL-data using FSL software (http://fsl.fmrib.ox.ac.uk/fsl)[2]. Brain extraction, along with tissue segmentation was performed for the MPRAGE image using Volbrain [34]. First, all ASL images and the corresponding M_0 image were realigned separately employing rigid-body co-registration to the middle ASL run using the FLIRT routine to correct for motion. Next, the mean difference between label and control images was calculated. Analysis was performed following the recommendations of the ASL White Paper and using the Bayesian kinetic inference method [31, 35, 36], the BASIL tool was used and voxel-wise calibration was performed with the M_0 image. Each of the four background suppression pulse has an efficiency of 0.93, which results in a cumulative labeling efficiency of 0.64. Blood hemoglobin concentrations (ctHb) were also determined as the kinetic model inversion depends on the T1 of blood. The T1 of blood can be estimated based on the ctHb using the following equation: 1000/T1a (ms) = 0.016 x ctHb (g/dL) + 0.317 [37]. The used T1 of gray matter was 1330 ms, while for bolus arrival time 1300 ms was assumed. Spatially regularized partial volume correction was performed according to the paper of Zhao et al. [38]. As an alternative method, the CBF in each voxel could also be calculated for PCASL using the formula as proposed by Alsop et al. [31]:

$$CBF = \frac{6000 * \lambda * (SI_{control} - SI_{label}) * e^{\frac{PLD}{T1_{blood}}}}{2 * \alpha * T1_{blood} * SI_{PD} * (1 - e^{-\frac{\tau}{T1_{blood}}})} \quad (mL/100\ g\ tissue/min)$$

Where λ is the brain/blood partition coefficient in mL/g, $SI_{control}$ and SI_{label} are the time-averaged signal intensities in the control and label images respectively, $T1_{blood}$ is the longitudinal relaxation time of blood in seconds, α is the labeling efficiency, SI_{PD} is the signal intensity of a proton density weighted image, and τ is the label duration [31].

---

[1]WIP, the product is currently under development and is not for sale in the US and in other countries. Its future availability cannot be ensured.

[2]The information shown herein refers to products of 3rd party manufacturers and thus are in their regulatory responsibility. Please contact the 3rd pary manufacturer for further information.

The final ASL image containing CBF values in mL/100 g tissue/min was co-registered using affine transformation to the brain extracted MPRAGE image using the FLIRT routine. The mean gray matter CBF was calculated by taking the mean CBF over the gray matter mask (with a threshold of 0.6). The regional gray matter CBF was calculated using the Oxford-Harvard atlas, which was co-registered using the affine transformation matrix from the Montreal Neurological Institute (MNI) to MPRAGE image. T2* maps were obtained from the multi-echo GRE data using a mono-exponential fit ($f(TE) = S_0 e^{-TE/T2*}$). In a subsequent step, all T2* values above 500 ms were set to 0 and the R2* map (= 1/T2*) was obtained. T2-FLAIR and R2* images were also co-registered to the MPRAGE image using Rigid Body Transformations (FLIRT routine).

Results and discussion

Figure 1 shows CBF maps representing the local brain perfusion, which has been quantified for each voxel in mL/100 g tissue/min. Since our main outcome is gray matter CBF, we masked the remaining brain tissues as illustrated in the lower two rows. Mean gray matter CBF has been reported to be significantly lower in apparently healthy elderly as compared to younger subjects ($n = 37$, mean age: 72.1 ± 8.7 years; 42.7 ± 8.8 mL/100 g/min vs. $n = 11$, mean age: 29.3 ± 5.3 years; 52.6 ± 9.3 mL/100 g/min) [39]. The case presented in this article had a mean gray matter CBF of 28.7 mL/100 g/min (see Figure 1), which may partly be explained by his high BMI (28.9 kg/m^2) that falls in the overweight range and by his sedentary behavior. Also,

regional CBF in, for example, the precuneus that is strongly dependent on age [40] was found to be significantly lower in the elderly compared to the young population (43.3 ± 11.5 mL/100 g/min vs. 51.4 ± 8.7 mL/100 g/min) [39]. The presented case showed a CBF in the precuneus region of 24.4 mL/100 g/min. Interestingly, the T2-FLAIR showed the presence of white matter signal abnormalities (Fig. 2A) that can be classified as periventricular and deep white matter hyperintensities [41]. In addition, the high R2* showed iron accumulation in deep gray matter regions (Fig. 2B), while the MPRAGE image demonstrated ventricular enlargement and brain athrophy (Fig. 2C).

White matter signal abnormalities and iron accumulation in deep gray matter areas have been associated with aging, cognitive performance and dementia [26, 27]. Age-related patterns of brain atrophy have also been linked to cognitive performance and the risk of dementia [28]. Furthermore, ventricular enlargement has been suggested to be an age-dependent risk marker for cognitive decline [42]. A potential relationship between CBF and structural brain status has been suggested. Reduced gray matter CBF may be associated with subcortical brain athrophy in the presence of white matter signal abnormalities [43], and may also relate to iron accumulation [27]. In fact, gray matter CBF was associated with white matter signal abnormalities independent of age. However, the decline of CBF with advancing age may also possibly exacerbate deterioration of white matter integrity [44–46]. Additionally, iron accumulation may plausibly reflect reduced CBF [47], due to a reduced delivery of iron binding complexes to

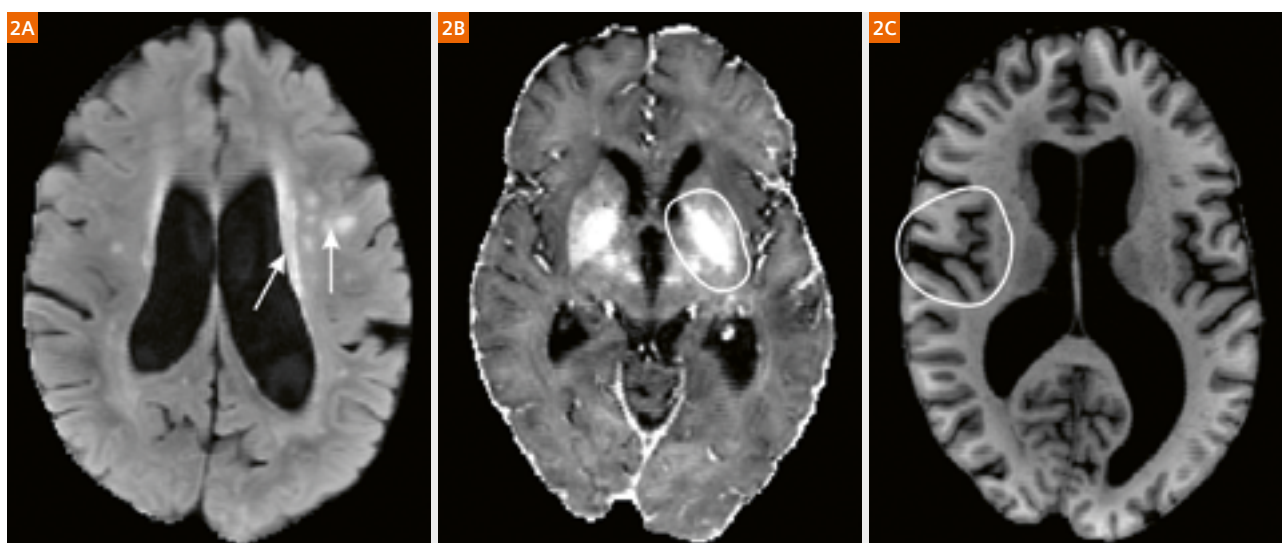**Figure 2:**
(2A) T2-FLAIR, **(2B)** R2* maps calculated from T2*-weighted gradient-echo (GRE) and **(2C)** MPRAGE images showing structural brain status. White matter signal abnormalities and iron accumulation appear bright (i.e. hyperintense) on the T2-FLAIR image and the R2*-weighted gradient-echo image, respectively. The MPRAGE shows a decrease in brain volume and ventricular enlargement.

the brain [48]. In contrast, others have reported that age-associated reductions in regional CBF may be independent of concurrent age-dependent brain athrophy.

Therefore, CBF can remain unaltered in regions of brain atrophy [39]. These studies demonstrate a potential dissociation between brain atrophy and hypoperfusion specific to normal aging.

The development of the aforementioned structural brain changes is relatively slow and mostly without noticeable onset of symptoms linked to dementia. In fact, decreases in cognitive performance may be determined by the severity of these structural brain changes. Cognitive impairment may remain asymptomatic until structural brain changes have affected a significant proportion of the brain [29]. However, the causal relationship between CBF and structural brain changes still remains unclear. Therefore, innovative research investigating a potential causal relationship between lifestyle-induced structural brain changes and changes in CBF – using different MRI modalities – is urgently needed.

In conclusion, a healthy lifestyle may attenuate the age-related cognitive decline by improving CBF, which serves as a sensitive physiological marker of brain vascular health, maintaining sufficient CBF throughout the brain. Additionally, CBF can be quantified using ASL – an accurate and reproducible non-invasive MRI method – and may be associated with structural brain status assessed by T2-FLAIR, R2* maps and MPRAGE images.

Acknowledgements

References

1　United Nations Department of Economic Social Affairs Population Division. World population prospects: the 2015 revision. Available from: https://esa.un.org/unpd/wpp/Publications/Files/WPP2015_DataBooklet.pdf

2　Gorelick PB, Scuteri A, Black SE, Decarli C, Greenberg SM, Iadecola C, et al. Vascular contributions to cognitive impairment and dementia: a statement for healthcare professionals from the american heart association/american stroke association. Stroke. 2011;42(9):2672-713.

3　Joris PJ, Mensink RP, Adam TC, Liu TT. Cerebral Blood Flow Measurements in Adults: A Review on the Effects of Dietary Factors and Exercise. Nutrients. 2018;10(5).

4　Schmidt W, Endres M, Dimeo F, Jungehulsing GJ. Train the vessel, gain the brain: physical activity and vessel function and the impact on stroke prevention and outcome in cerebrovascular disease. Cerebrovascular diseases (Basel, Switzerland). 2013;35(4):303-12.

5　Brown BM, Peiffer JJ, Martins RN. Multiple effects of physical activity on molecular and cognitive signs of brain aging: can exercise slow neurodegeneration and delay Alzheimer's disease? Molecular psychiatry. 2013;18(8):864-74.

6　Liu TT, Brown GG. Measurement of cerebral perfusion with arterial spin labeling: Part 1. Methods. J Int Neuropsychol Soc. 2007;13(3):517-25.

7　Brown GG, Clark C, Liu TT. Measurement of cerebral perfusion with arterial spin labeling: Part 2. Applications. J Int Neuropsychol Soc. 2007;13(3):526-38.

8　Kelleher RJ, Soiza RL. Evidence of endothelial dysfunction in the development of Alzheimer's disease: Is Alzheimer's a vascular disorder? American journal of cardiovascular disease. 2013;3(4):197-226.

9　Grove T, Taylor S, Dalack G, Ellingrod V. Endothelial function, folate pharmacogenomics, and neurocognition in psychotic disorders. Schizophrenia research. 2015;164(1-3):115-21.

10　Wolters FJ, Zonneveld HI, Hofman A, van der Lugt A, Koudstaal PJ, Vernooij MW, et al. Cerebral Perfusion and the Risk of Dementia: A Population-Based Study. Circulation. 2017;136(8):719-728.

11　Zhang N, Gordon ML, Goldberg TE. Cerebral blood flow measured by arterial spin labeling MRI at resting state in normal aging and Alzheimer's disease. Neuroscience and biobehavioral reviews. 2017;72:168-175.

12　Parkes LM, Rashid W, Chard DT, Tofts PS. Normal cerebral perfusion measurements using arterial spin labeling: reproducibility, stability, and age and gender effects. Magnetic resonance in medicine. 2004;51(4):736-43.

13　Hshieh TT, Dai W, Cavallari M, Guttmann CR, Meier DS, Schmitt EM, et al. Cerebral blood flow MRI in the nondemented elderly is not predictive of post-operative delirium but is correlated with cognitive performance. Journal of cerebral blood flow and metabolism: official journal of the International Society of Cerebral Blood Flow and Metabolism. 2017;37(4):1386-1397.

14　De Vis JB, Hendrikse J, Bhogal A, Adams A, Kappelle LJ, Petersen ET. Age-related changes in brain hemodynamics; A calibrated MRI study. Human brain mapping. 2015;36(10):3973-87.

15　Birdsill AC, Carlsson CM, Willette AA, Okonkwo OC, Johnson SC, Xu G, et al. Low cerebral blood flow is associated with lower memory function in metabolic syndrome. Obesity (Silver Spring). 2013;21(7):1313-20.

16　Kullmann S, Heni M, Hallschmid M, Fritsche A, Preissl H, Häring H-U. Brain Insulin Resistance at the Crossroads of Metabolic and Cognitive Disorders in Humans. Physiological reviews. 2016;96(4):1169-1209.

17　Sierra-Marcos A. Regional Cerebral Blood Flow in Mild Cognitive Impairment and Alzheimer's Disease Measured with Arterial Spin Labeling Magnetic Resonance Imaging. International journal of Alzheimer's disease. 2017;2017:5479597.

18　Raichle ME, Martin WR, Herscovitch P, Mintun MA, Markham J. Brain blood flow measured with intravenous H2(15)O. II. Implementation and validation. Journal of nuclear medicine: official publication, Society of Nuclear Medicine. 1983;24(9):790-8.

19　Fan AP, Jahanian H, Holdsworth SJ, Zaharchuk G. Comparison of cerebral blood flow measurement with [15O]-water positron emission tomography and arterial spin labeling magnetic resonance imaging: A systematic review. Journal of cerebral blood flow and metabolism: official journal of the International Society of Cerebral Blood Flow and Metabolism. 2016;36(5):842-61.

20　Tseng BY, Gundapuneedi T, Khan MA, Diaz-Arrastia R, Levine BD, Lu H, et al. White matter integrity in physically fit older adults. NeuroImage. 2013;82:510-6.

21　Gons RA, Tuladhar AM, de Laat KF, van Norden AG, van Dijk EJ, Norris DG, et al. Physical activity is related to the structural integrity of cerebral white matter. Neurology. 2013;81(11):971-6.

22　Tarumi T, Zhang R. Cerebral blood flow in normal aging adults: cardiovascular determinants, clinical implications, and aerobic

fitness. Journal of neurochemistry. 2017;144(5):595-608.

23 Pirpamer L, Hofer E, Gesierich B, De Guio F, Freudenberger P, Seiler S, et al. Determinants of iron accumulation in the normal aging brain. Neurobiology of aging. 2016;43:149-55.

24 Riphagen JM, Gronenschild EHBM, Salat DH, Freeze WM, Ivanov D, Clerx L, et al. Shades of white: diffusion properties of T1- and FLAIR-defined white matter signal abnormalities differ in stages from cognitively normal to dementia. Neurobiology of aging. 2018;68:48-58.

25 Prins ND, Scheltens P. White matter hyperintensities, cognitive impairment and dementia: an update. Nature reviews Neurology. 2015;11(3):157-65.

26 Hagemeier J, Geurts JJG, Zivadinov R. Brain iron accumulation in aging and neurodegenerative disorders. Expert review of neuro-therapeutics. 2012;12(12):1467-1480.

27 Daugherty AM, Raz N. Appraising the Role of Iron in Brain Aging and Cognition: Promises and Limitations of MRI Methods. Neuro-psychology review. 2015;25(3):272-287.

28 Pini L, Pievani M, Bocchetta M, Altomare D, Bosco P, Cavedo E, et al. Brain atrophy in Alzheimer's Disease and aging. Ageing Research Reviews. 2016;30:25-48.

29 Brickman AM, Siedlecki KL, Muraskin J, Manly JJ, Luchsinger JA, Yeung LK, et al. White matter hyperintensities and cogni-tion: testing the reserve hypothesis. Neurobiology of aging. 2011;32(9):1588-98.

30 Dolui S, Vidorreta M, Wang Z, Nasrallah IM, Alavi A, Wolk DA, et al. Comparison of PASL, PCASL, and background-suppressed 3D PCASL in mild cognitive impairment. Human brain mapping. 2017;38(10):5260-5273.

31 Alsop DC, Detre JA, Golay X, Gunther M, Hendrikse J, Hernandez-Garcia L, et al. Recommended implementation of arterial spin-labeled perfusion MRI for clinical applications: A consensus of the ISMRM perfusion study group and the European consortium for ASL in dementia. Magnetic resonance in medicine. 2015;73(1):spcone.

32 Dai W, Garcia D, de Bazelaire C, Alsop DC. Continuous flow-driven inversion for arterial spin labeling using pulsed radio frequency and gradient fields. Magnetic resonance in medicine. 2008;60(6):1488-97.

33 Dai W, Robson PM, Shankaranarayanan A, Alsop DC. Reduced resolution transit delay prescan for quantitative continuous arterial spin labeling perfusion imaging. Magnetic resonance in medicine. 2012;67(5):1252-65.

34 Manjón JV, Coupé P. volBrain: An Online MRI Brain Volumetry System [10.3389/fninf.2016.00030]. Frontiers in Neuro-informatics. 2016;10:30.

35 Chappell MA, Groves AR, Whitcher B, Woolrich MW. Variational Bayesian Inference for a Nonlinear Forward Model. IEEE Transactions on Signal Processing. 2009;57(1):223-236.

36 Woolrich MW, Jbabdi S, Patenaude B, Chappell M, Makni S, Behrens T, et al. Bayesian analysis of neuroimaging data in FSL. NeuroImage. 2009;45(1 Suppl):S173-86.

37 Li W, Liu P, Lu H, Strouse JJ, van Zijl PCM, Qin Q. Fast measure-ment of blood T1 in the human carotid artery at 3T: Accuracy, precision, and reproducibility. Magnetic resonance in medicine. 2017;77(6):2296-2302.

38 Zhao MY, Mezue M, Segerdahl AR, Okell TW, Tracey I, Xiao Y, et al. A systematic study of the sensitivity of partial volume correction methods for the quantification of perfusion from pseudo-continuous arterial spin labeling MRI. NeuroImage. 2017;162:384-397.

39 Chen JJ, Rosas HD, Salat DH. Age-associated reductions in cerebral blood flow are independent from regional atrophy. NeuroImage. 2011;55(2):468-78.

40 Beason-Held LL, Kraut MA, Resnick SM. Stability Of Default-Mode Network Activity In The Aging Brain. Brain imaging and behavior. 2009;3(2):123-131.

41 Griffanti L, Jenkinson M, Suri S, Zsoldos E, Mahmood A, Filippini N, et al. Classification and characterization of periventricular and deep white matter hyperintensities on MRI: A study in older adults. NeuroImage. 2018;170:174-181.

42 Apostolova LG, Green AE, Babakchanian S, Hwang KS, Chou Y-Y, Toga AW, et al. Hippocampal atrophy and ventricular enlargement in normal aging, mild cognitive impairment and Alzheimer's disease. Alzheimer disease and associated disorders. 2012;26(1):17-27.

43 Appelman APA, van der Graaf Y, Vincken KL, Tiehuis AM, Witkamp TD, Mali WPTM, et al. Total Cerebral Blood Flow, White Matter Lesions and Brain Atrophy: The SMART-MR Study. Journal of Cerebral Blood Flow & Metabolism. 2007;28(3):633-639.

44 Chen JJ, Rosas HD, Salat DH. The relationship between cortical blood flow and sub-cortical white-matter health across the adult age span. PloS one. 2013;8(2):e56733.

45 Brickman AM, Zahra A, Muraskin J, Steffener J, Holland CM, Habeck C, et al. Reduction in cerebral blood flow in areas ap-pearing as white matter hyperintensities on magnetic resonance imaging. Psychiatry research. 2009;172(2):117-120.

46 Promjunyakul N, Lahna D, Kaye JA, Dodge HH, Erten-Lyons D, Rooney WD, et al. Characterizing the white matter hyperintensity penumbra with cerebral blood flow measures. NeuroImage: Clinical. 2015;8:224-229.

47 Grundy SM, Cleeman JI, Daniels SR, Donato KA, Eckel RH, Franklin BA, et al. Diagnosis and management of the meta-bolic syndrome: an American Heart Association/National Heart, Lung, and Blood Institute Scientific Statement. Circulation. 2005;112(17):2735-52.

48 Hare D, Ayton S, Bush A, Lei P. A delicate balance: Iron metabolism and diseases of the brain. Frontiers in aging neuroscience. 2013;5:34.

Abstract

Brain perfusion MRI can help us better understand and monitor the metabolic and functional correlates of a stroke lesion, both in the acute and chronic phase and beyond the local tissue damage. Arterial spin labeling (ASL) allows repeated perfusion measurements and quantifications of cerebral blood flow (CBF) over the whole brain without the need for exogenous contrast. When it comes to monitoring stroke patients, ASL can therefore provide useful information about the short-term (dynamic) or long-term (e.g., chronic vs. acute)

effects of pharmacological treatments or surgical interventions with respect to stroke onset.

Here we report a case of thalamic stroke where the relationship between the whole-brain CBF pattern and the tissue outcome is illustrated in the subacute and chronic phases, before and after five months of pharmacological treatment, by co-registering CBF maps from 3D pseudo-continuous ASL (3D PCASL)[1] images and T2-weighted fluid-attenuated inversion recovery

---

[1]WIP, the product is currently under development and is not for sale in the US and in other countries. Its future availability cannot be ensured.
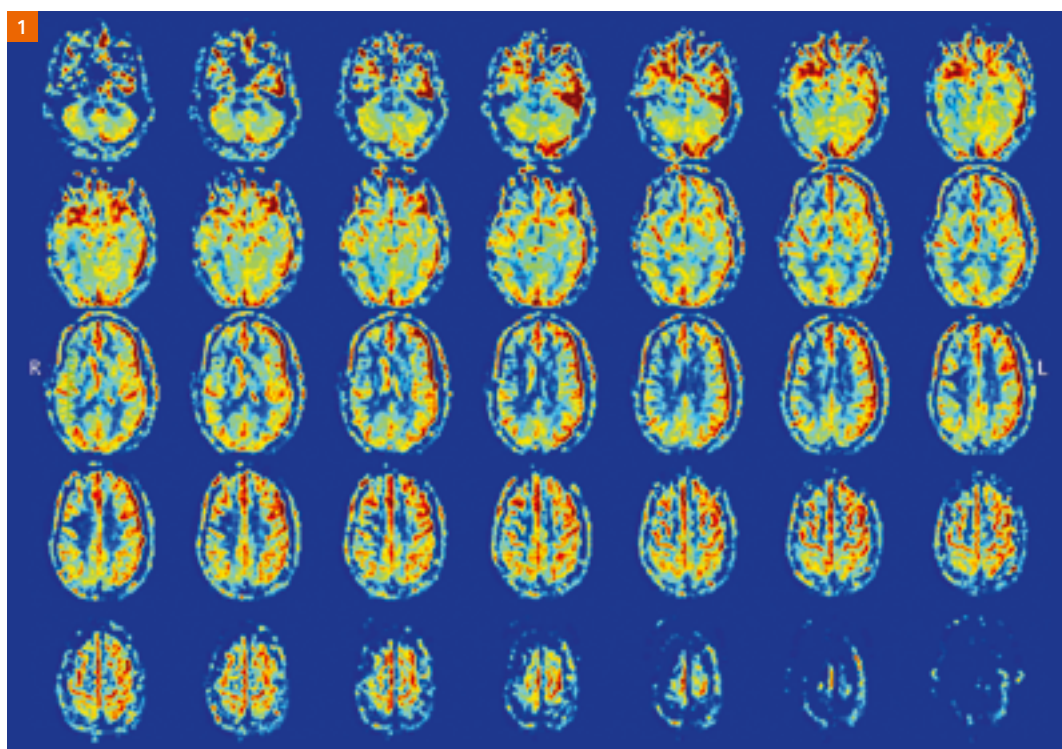

Figure 1:
rCBF map (mL / 100 g / min) of a 31-year-old woman with a stenosis of the distal basilar artery, acquired in the subacute phase using 3D PCASL. The color map "jet" (blue/green: low perfusion, yellow/red: high perfusion) was used to map the image values.

(3D FLAIR) images. We compare these to conventional magnetic resonance angiography (MRA) images.

Visualizing changes in perfusion patterns provided significant information that could not be easily produced with conventional non-invasive MRI techniques, and might therefore provide new insight into the functional, vascular, and neuronal changes that follow an ischemic brain injury. If introduced to a routine clinical setting, 3D PCASL could certainly allow the non-invasive and rapid collation of quantitative parameters that might be useful predictors of outcome. It could also provide a deeper understanding of metabolic and vascular phenomena caused by cerebro-afferent vessel occlusion, and therefore help improve tailored approaches to ischemic stroke.

Introduction

Monitoring brain perfusion helps us to understand the metabolic and functional correlates of both acute and chronic cerebrovascular lesions in a way that goes beyond the local tissue damage associated with the structural lesion. Compared to dynamic susceptibility contrast (DSC), arterial spin labeling (ASL) allows repeat perfusion measurements within a few hours and over weeks or months. It also provides absolute quantifica-

tions of cerebral blood flow (CBF) across the entire brain without the need for exogenous contrast [1]. When it comes to managing patients with acute stroke, ASL can therefore provide useful information about the short-term (dynamic) or long-term (e.g., chronic vs acute) effects of pharmaco-logical treatments or surgical interventions [2]. Among the different ASL implementations on clinical MRI scanners, pseudo-continuous 3D ASL[1] is recommended by the ISMRM Perfusion Study Group as the method of choice for clinical imaging [3].

Here we report on a patient with vertebrobasilar stroke caused by spontaneous basilar artery vasospasm. We illustrate the relationship between the whole-brain CBF pattern and the narrowing of the intracranial artery in the subacute phase, and show the tissue outcome and the consequences of ischemia in strategic brain regions (hippocampus and thalamus) after five months of pharmacological treatment. In particular, we postprocessed ASL images obtained with a prototype version of the 3D pseudo-continuous ASL (3D PCASL) sequence. CBF maps from 3D PCASL images were coregistered between two MRI studies and with T2-weighted fluid-attenuated inversion recovery (3D FLAIR) images. Conventional magnetic resonance angiography (MRA) was performed with 3D time-of-flight (3D TOF), and maximum intensity projection (MIP) views were obtained.
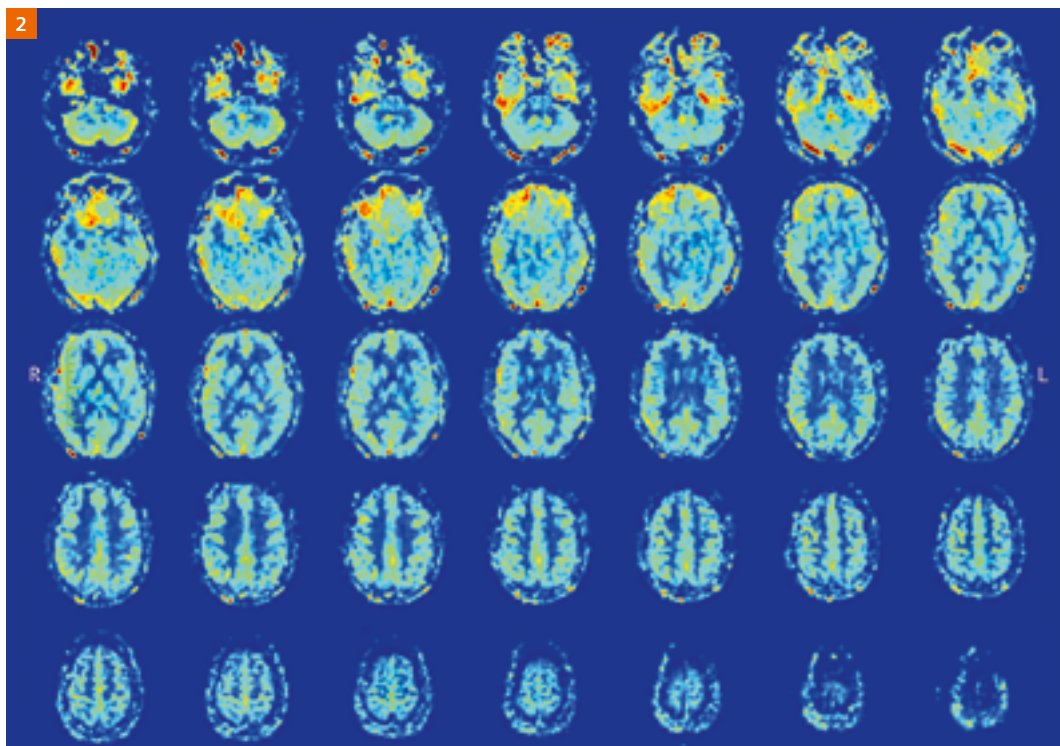

Figure 2:
rCBF map (mL / 100 g / min) of a 31-year-old woman, acquired in the chronic phase using 3D PCASL five months from stroke onset when the basilar artery appeared normalized. The color map "jet" (blue/green: low perfusion, yellow/red: high perfusion) was used to map the image values.

Case report

In September 2017, a 31-year-old woman presented with a sudden severe headache, confusion, and amnesia that had developed after physical exertion. Conventional MRA showed an acute posterior circulation stroke involving the hippocampal formation and the anterior thalamus on the right side in particular. It also showed a stenosis of the distal basilar artery consistent with vasospasm. The patient was treated with nimodipine, which stopped the headache and rapidly improved her cognitive performance. Basilar artery lumen slowly normalized in the subsequent month.

Both during the subacute phase and five months later, besides MRA, we also assessed tissue lesions and brain perfusion with, respectively, 3D FLAIR and 3D PCASL sequences on a 3T MR scanner (MAGNETOM Skyra, Siemens Healthcare, Erlangen, Germany) equipped with a 20-channel head-neck coil. MRA images were obtained from 3D time-of-flight (3D TOF) images using the maximum intensity projection (MIP) in the Siemens Healthcare *syngo* software. The 3D FLAIR sequence was set up with the following parameters: Repetition/echo time (TR/TE): 5000/387 ms; inversion time (TI): 1800; slice thickness: 1 mm; matrix: 384 x 384; field of view (FOV): 229 x 229 mm2. The 3D PCASL sequence employs the 3D GRASE readout module and uses a pseudo-continuous labeling scheme with optional background suppression as described in [4–6]. It was set up with the following parameters: TR/TE: 4600/15.6 ms; FOV: 192 x 192 mm^2; slice thickness: 3 mm; labeling duration: 1500 ms; post-labeling delay: 1500 ms; M0 prescan. Total scan time including M0 was 5:27 min:sec (1 M0 image, 6 control/label image pairs). A rCBF map was also calculated from the prescan M0 and the label-control series using the formula in [3] and provided by the inline scanner software. 3D T1-weighted MPRAGE images were acquired as anatomical references to improve coregistration between series and exams (time points). The 3D T1 MPRAGE sequence used the following parameters: TR/TE: 5000/387 ms; TI: 1800; slice thickness: 1 mm; matrix: 256 x 256; FOV: 256 x 256 mm^2.

To facilitate a visual comparison of the results across the two time points, FLAIR and PCASL images were first registered to their corresponding MPRAGE images (acquired at the same time point) and then jointly registered to the common anterior-posterior commissure (ACPC) plane, as determined on the MPRAGE images, using affine transformations. Thereby, the FLAIR images and CBF maps from the two time points could be displayed using exactly the same transversal slice, which was selected on the FLAIR images to bisect a bilateral thalamic lesion that appeared as two hyperintense spots. The rCBF maps were obtained from perfusion-weighted maps using the M0 prescan and parameters in [7]. In addition, for display purposes, the same maps were also normalized to the maximum rCBF value (map peak).

Figures 1 and 2 show the rCBF maps provided from the inline scanner software from the 3D PCASL series acquired respectively in the subacute phase and after five months. The color maps were identically scaled using the same window.

Figure 3 shows the MRA and the 3D FLAIR/PCASL results after postprocessing (coregistration to the common ACPC plane, calculation of the rCBF values, and normalization to the maximum). For the MRA study, the coronal MIP views from the 3D TOF data show the stenosis of the distal basilar artery in the subacute phase (3A) and its normali-zation after five months (3E). The 3D FLAIR images and CBF maps are also shown in the subacute phase (3B, C) and after five months (3F, G). The FLAIR images show a bilateral thalamic lesion as two symmetrical hyperintense spots, which remained sub-stantially unchanged between the subacute (3B) and chronic (3F) phases. The rCBF map in the subacute phase (3C) shows a serpiginous, high absolute CBF surrounding the lesion in the right thalamus, but not in the left. The CBF map normalized to the maximum rCBF value (3D) emphasizes this effect and further highlights inhomogeneous perfusion throughout the gray matter, with relatively low perfusion in the posterior circulation territories and in the right hemisphere. After five months, the rCBF map (3G) shows globally reduced levels of perfusion. However, the normalized CBF map (3H) in particular shows a more homogeneous perfusion pattern throughout the gray matter.

This case illustrates how 3D PCASL CBF measurements can potentially add value beyond the conventional MRA findings. In fact, although MRA allows (in this case) to locate the stenosis, the CBF map provides a richer pattern of the stroke effects, even beyond the territory supplied by the narrowed artery. Specifically, the CBF map in the subacute phase seems to indicate the possible presence (and the distant metabolic consequences) of collateral circulation induced by the hemodynamic adaptation to the stroke event. In fact, when the arterial arrival time exceeds the post-labeling delay (the time required for spins to travel from the labeling plane to the imaged slice), labeled spins become visible as bright intra-arterial high signals. This effect is known as "arterial transit artefact" (ATA) [8] to emphasize that the signal
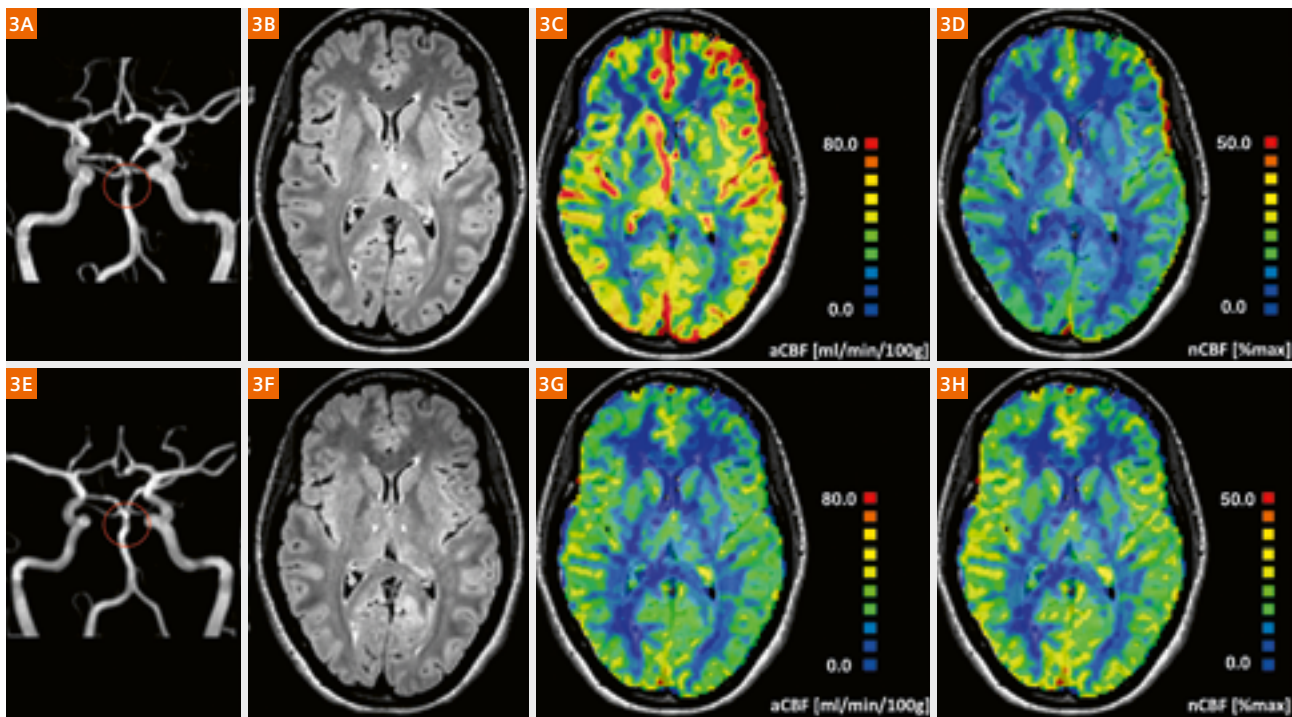
Figure 3:
MRA-FLAIR-ASL study re-elaboration (coregistration to common ACPC plane, CBF normalization): **(3A)** A 31-year-old woman with a stenosis of the distal basilar artery on MRA (coronal MIP from 3D TOF images); **(3B)** the FLAIR image in the subacute phase shows bilateral thalamic lesions; **(3C)** 3D PCASL shows a serpiginous, high absolute CBF close to the lesion in the right thalamus, but not in the left; **(3D)** normalized CBF shows inhomogeneous perfusion throughout the gray matter, and relatively low perfusion in the posterior circulation territories and the right hemisphere; **(3E)** after five months, the basilar artery has normalized on MRA (coronal MIP from 3D TOF images); **(3F)** the thalamic lesions did not change substantially on the FLAIR image; **(3G)** absolute CBF from 3D PCASL images shows globally reduced perfusion; **(3H)** normalized CBF shows more homogeneous perfusion throughout the gray matter.

comes not from the parenchyma but from the vessel (an unwanted effect under physiological conditions). Such intravascular signals can be attributed to the slow-flowing (stagnant) blood upstream of the occlusion site, and it has repeatedly been shown [9] that detecting stagnant flow using a PCASL sequence can fruitfully complement MRA in localizing occlusions in acute stroke. This notion was substantially supported by our case, where the ATA disappeared during the chronic phase once the artery lumen was normalized. In previous studies, the presence of ATA has also been correlated with an improved outcome (lack of progression to infarct and better clinical outcome) after acute stroke [10]. It could, therefore, indicate the presence of compensating collat-eral flow, which would be a useful prognostic marker. Alternatively, regional increases in CBF values might indicate a "luxury perfusion", which is a maximal arteriolar vasodilation caused by loss of autoregulatory mechanisms in the tissue damaged by recent ischemia [11]. Luxury perfusion is also associated with an improved outcome for the ischemic penumbra.

Of particular interest is the detection of CBF changes in regions far beyond the territory supplied by the affected artery. In this case, CBF probably indicates functional phenomena due to the involvement of strategic brain regions (such as the thalami and the hippocampal formations) that might result in cerebral diaschisis with metabolic suppression far away from the ischemic territory.

Overall, 3D PCASL can provide significant information that cannot be easily produced with other noninvasive techniques, and might provide new insight into the functional, vascular, and neuronal changes that often coexist with an ischemic brain accident.

These techniques, when used in a routine clinical setting, will make it possible to noninvasively and rapidly collate quantitative parameters that could be useful predictors of outcome and provide a more in-depth understanding of metabolic and vascular phenomena caused by a cerebro-afferent vessel occlusion. Ultimately, this could improve tailored approaches to treating ischemic stroke.

References

1 Haller S, Zaharchuk G, Thomas DL, Lovblad K-O, Barkhof F, Golay X. Arterial Spin Labeling Perfusion of the Brain: Emerging Clinical Applications. Radiology. 2016;281(2):337–56.
2 Harston GWJ, Okell TW, Sheerin F, Schulz U, Mathieson P, Reckless I, et al. Quantification of serial cerebral blood flow in acute stroke using arterial spin labeling. Stroke. 2017;48(1):123–30.
3 Alsop DC, Detre JA, Golay X, Günther M, Hendrikse J, Hernandez-Garcia L, et al. Recommended implementation of arterial spin-labeled Perfusion mri for clinical applications: A consensus of the ISMRM Perfusion Study group and the European consortium for ASL in dementia. Magn Reson Med. 2015;73(1):102–16.
4 Dai W, Garcia D, De Bazelaire C, Alsop DC. Continuous flow-driven inversion for arterial spin labeling using pulsed radio frequency and gradient fields. Magn Reson Med. 2008;60(6):1488–97.
5 Dai W, Robson PM, Shankaranarayanan A, Alsop DC. Reduced resolution transit delay prescan for quantitative continuous arterial spin labeling perfusion imaging. Magn Reson Med. 2012;67(5):1252–65.
6 Wu W-C, Fernández-Seara M, Detre JA, Wehrli FW, Wang J. A theoretical and experimental investigation of the tagging efficiency of pseudocontinuous arterial spin labeling. Magn Reson Med. 2007 Nov;58(5):1020–7.
7 Wang J, Zhang Y, Wolf RL, Roc AC, Alsop DC, Detre JA. Amplitude-modulated Continuous Arterial Spin-labeling 3.0-T Perfusion MR Imaging with a Single Coil: Feasibility Study. Radiology. 2005 Apr;235(1):218–28.
8 Detre JA, Samuels OB, Alsop DC, Gonzalez-At JB, Kasner SE, Raps EC. Noninvasive magnetic resonance imaging evaluation of cerebral blood flow with acetazolamide challenge in patients with cerebrovascular stenosis. J Magn Reson Imaging. 1999 Nov;10(5):870–5.
9 Sogabe S, Satomi J, Tada Y, Kanematsu Y, Kuwayama K, Yagi K, et al. Intra-arterial high signals on arterial spin labeling perfusion images predict the occluded internal carotid artery segment. Neuroradiology. 2017 Jun 10;59(6):587–95.
10 Chng SM, Petersen ET, Zimine I, Sitoh Y-Y, Lim CCT, Golay X. Territorial Arterial Spin Labeling in the Assessment of Collateral Circulation: Comparison With Digital Subtraction Angiography. Stroke. 2008;39(12):3248–54.
11 Viallon M, Altrichter S, Pereira VM, Nguyen D, Sekoranja L, Federspiel A, et al. Combined Use of Pulsed Arterial Spin-Labeling and Susceptibility-Weighted Imaging in Stroke at 3T. Eur Neurol. 2010;64(5):286–96.
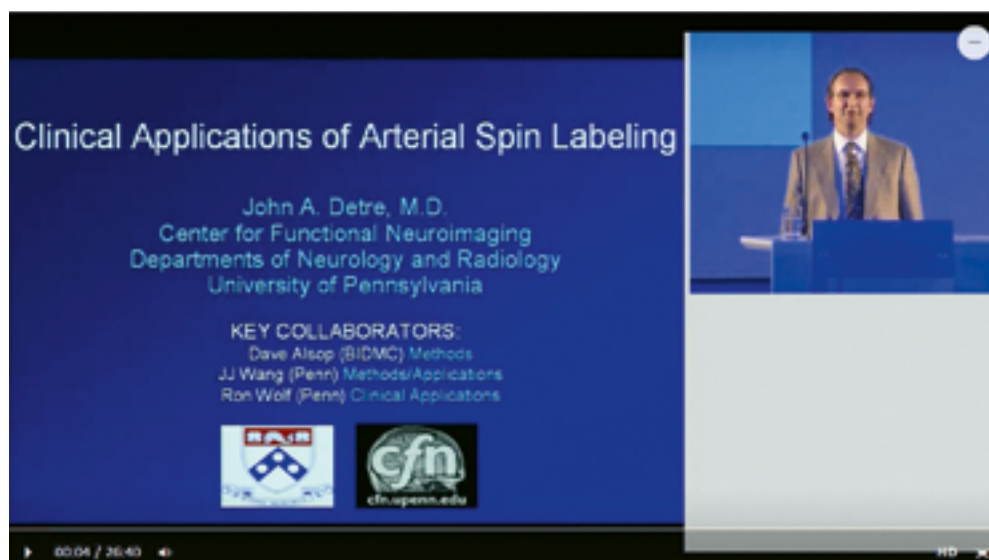
MR Spectroscopy in Neuroimaging – A Practical Guide to Integrate a Complex Technology into a Clinical Workflow

Marco Essig, M.D., Ph.D., FRCPC[1]; Craig Snell[1]; Lawrence Ryner, Ph.D.[1,2]

[1]Department of Radiology, Health Sciences Center Winnipeg, Canada
[2]Department of Physics and Astronomy, University of Manitoba, Winnipeg, Canada

Introduction

After the introduction of NMR spectroscopy in chemistry laboratories in the 1950s, it took decades for MR spectroscopy to eventually be used in a clinical neuroimaging environment. Even as late as 1996, Mauricio Castillo noted that magnetic resonance spectroscopy (MRS) had received little attention from the clinical radiology community. Indeed, most MR spectroscopic studies were initially performed by a small and dedicated group of individuals, mostly basic scientists, partly because MR spectroscopy did not produce "pictures" but resulted in "graphs" called "spectra", and also because of long acquisition times. Much has been done over the years to make the acquisition and processing of spectroscopy data easy, faster, and user friendly, but, still, the full integration of MR spectroscopy seems a challenge for many clinical Radiology departments.

In this article, we describe how MR spectroscopy and MR spectroscopic imaging can be integrated into the clinical workflow of a busy, high-volume MRI department using the example of brain tumor imaging.

MRS for brain tumor imaging
The goals and requirements for brain tumor imaging are making a diagnosis and/or a differential diagnosis, while accurately grading and delineating lesions for tumor description and risk assessment. Imaging is also involved in the decision-making process for treatment such as precise planning of surgical or radiotherapeutic interventions both of which require an optimal lesion detection and delineation. Following therapy, neuroimaging techniques have been shown to be very important for monitoring of disease and to identify and monitor possible therapy related side effects.

In recent years, functional neuroimaging techniques were implemented to optimize tumor characterization, with an emphasis on improved specificity to separate benign from malignant features. Specific characterization facilitates planning of the most appropriate treatment. Furthermore, functional neuroimaging of central nervous system (CNS) neoplasms can be expanded to the monitoring of ongoing therapy and for early detection of therapeutic side effects. The predictive assessment of therapy response and the monitoring of ongoing therapy to guide therapeutic intervention are major challenges in the current treatment of CNS neoplasms.

Proton magnetic resonance spectroscopy is one of the most important functional imaging techniques and provides detailed tumor information beyond the morphologic characteristics observed in standard images. Single Voxel Spectroscopy (SVS) is used to assess a single voxel covering the brain lesion or for larger lesions just a selection of the lesion. Chemical Shift Imaging (CSI), also known as MR spectroscopic imaging (MRSI), is used to assess multiple voxels within and surrounding the tumor. Both methods have become valuable clinical tools, especially in the diagnostic work-up of tumors and the differentiation of normal from pathological conditions.

^{1}H protons are used most commonly in clinical practice because of the abundance of ^{1}H protons in body tissue and the consequently high signal-to-noise ratio, although it is possible to acquire signal from phosphorous-31, carbon-13 and other nuclei. The spectroscopic characterization of brain abnormalities relies mostly on the calculations of ratios between the major proton metabolites including N-acetylaspartate (NAA – a neuronal marker), choline-containing compounds (Cho – a marker of membrane turnover), and creatine-phosphocreatine (Cr – important in the tissue cell energy cycle), and on the presence of lactate (Lac – a marker of anaerobic glycolysis), and lipids [1-6]. Brain tumors typically have a loss of NAA and an increase of the Cho content (Fig. 1).
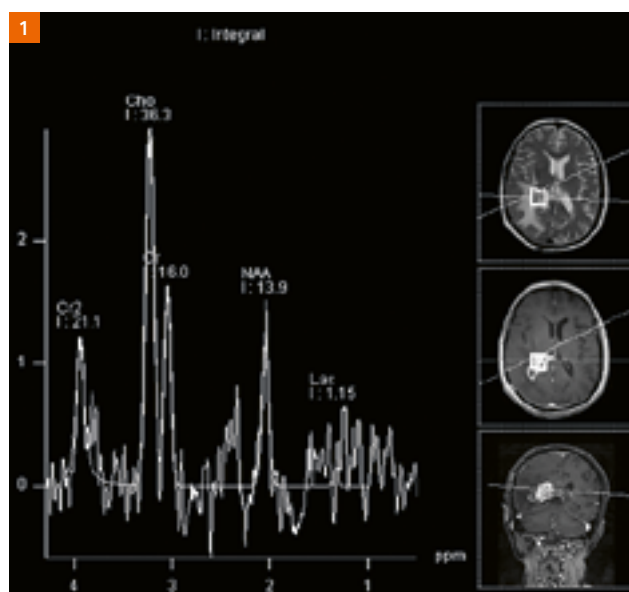
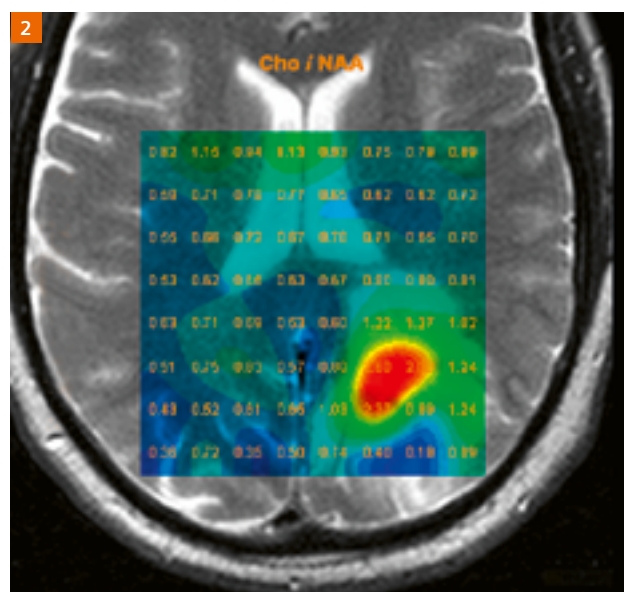Figure 1: Brain tumor spectrum showing increased Cho and reduced NAA.

Figure 2: CSI example showing the spatial distribution of the Cho/NAA ratio.

MR spectroscopy has been used to differentiate non-tumor lesions, like harmatomas from gliomas [7-8]. In several studies, it has been reported that harmatomas did not differ significantly from the normal brain or physiological changes, while gliomas had lower NAA/Cr, Cr/Cho, and NAA/Cho ratios. In patients with seizures it is important to identify tumor changes from scar as this has a major impact on the further management of patients. In a study by Vuori et al. [6], patients experiencing seizures who also had a cortical brain lesion on MR images were studied with proton MR spectroscopy. A metabolite ratio analysis was performed, and the metabolite signals in the lesion core were compared with those in the contralateral centrum semiovale and in the corresponding brain sites of control subjects to separately obtain the changes in NAA, Cho, and Cr. In their study, ten patients had a low-grade glioma (three, oligodendrogliomas; three, oligoastrocytomas; three, astrocytomas; and one, pilocytic astrocytoma), and eight had FCDM (five, focal cortical dysplasias and three, dysembryoplastic neuroepithelial tumors). They found that loss of NAA and increase of Cho were more pronounced in low-grade gliomas than in subjects with cortical developmental malformations. MR spectroscopy was also able to differentiate between subtypes of gliomas.

In a study by Law et al. [9], MR spectroscopy and MR perfusion enabled identification at a high sensitivity and a high positive predictive value for tumor grading when compared with conventional contrast enhanced MR imaging. It is well known that there are a certain percentage of high-grade tumors that do not present with a blood-brain-barrier disruption or vice versa. For the

planning of biopsy and for the treatment decision and management, it is essential to identify the highest tumor grade in those often very morphologically homogeneous appearing tumors. The authors were also able to provide thresholds for the metabolite ratios for the diagnosis of a high-grade tumor. A review of the literature, taking into account differences in MR spectroscopic technique such as the choice of echo time (TE) and method for determination of metabolite ratios, demonstrated that the mean maximal values obtained for Cho/Cr and Cho/NAA and mean minimum values for NAA/Cr ratios in their study (1,7) were comparable to previously published data in differentiating between low- and high-grade gliomas.

As in many functional techniques, one of the challenges is the use of standardized data acquisition and post-processing techniques. For data acquisition, the same echo time (TE) should be used, and data from the contralateral unaffected brain tissue should be acquired. Studies comparing long and short TE acquisition found that a short TE provided a slightly better tumor classification [10-11]. In a study by Majos et al., long TE acquisitions were only beneficial in studies of meningiomas [12].

The development in modern scanner technology further allows for the simultaneous measurement of spectroscopic data from more than just a single voxel. This technique is called chemical shift imaging (CSI) or magnetic resonance spectroscopic imaging (MRSI) and enables the acquisition of multiple small voxels in two or even three dimensions, providing better information about the spatial heterogeneity of a lesion (Fig. 2). The voxel information can be used to calculate metabolite

ratios, which can then be color-coded and superimposed on the anatomic images to better visualize hot spots within a tumor.

Follow-up assessment of cerebral tumors is a promising field for MR spectroscopy. Increases in size and contrast enhancement are typical findings in tumor progression but also reflect therapeutic-induced changes and/or postoperative changes. The ratio of choline to normal creatine level is usually significantly elevated in those areas consistent with tumor compared to those containing predominantly treatment effect. In fact, treatment effect is generally indicated by a marked depression of all the intracellular metabolite peaks from choline, creatine, and N-acetyl compounds.

MR spectroscopy alone may not be helpful in instances where patients have mixed histologic findings comprised of necrosis and tumor. Because of this heterogeneity and as a result of low spatial resolution, MRS findings of choline and NAA resonances below the normal range may indicate variable histologic findings ranging from radiation necrosis, gliosis, and macrophage infiltration to mixed tissues that contain some regions of tumor. The careful choice of voxel placement and interpretation of results in concordance with other imaging and clinical findings are critical in distinguishing between tumor and treatment-related changes. Furthermore, validation studies using image-guided tissue biopsy need to be performed to correlate imaging with histologic findings.

How to – MR Spectroscopy

Getting started

Before discussing the details of processing MR spectroscopy data using *syngo*.via, it is important to ensure that the acquisition of the spectroscopy data is optimized. This section provides some tips to assist in acquiring the single voxel and chemical shift imaging data.

As mentioned in the previous section, when setting up the CSI sequence selecting a lower TE (i.e., 30 ms) will yield better spectral quality in terms of tumor classification. Typically, the CSI sequence should be placed after the initial imaging sequences. This allows for the acquisition of imaging data in each plane so that the spectroscopy excitation voxel can be accurately placed on the contrast-enhancing or most suspicious tumor components. There are several important scanning parameters to keep in mind (Fig. 3):

1. Table position, found in the menu under System/ Miscellaneous/Position Mode, should be "REF mode". If ISO or FIXED mode is used, the isocenter will move and *syngo*.via will not be able to triangulate where the voxel was placed on the images with different ISO centers.
2. When the voxel is placed, click on the scroll header and select nearest, confirm placement on all three planes, and confirm that the voxel is not encroaching on any extraneous tissues.

Figure 3: Setting up the CSI acquisition.

3. 2D Distortion Correction must be turned off when acquiring an imaging localizer for spectroscopy. If this is left on, the voxel location may be affected by the amount of distortion correction applied to the images. Note that distortion correction can be retroactively reversed so that images can still be used for voxel positioning.

Placing a voxel, whether for single voxel or CSI, will follow similar principles: Avoid including any lipid signal within the excitation voxel as this will cause a large lipid peak to dominate the spectrum; stay away from the skull as the bone marrow will also result in an overwhelming lipid peak; and try to stay from the sinuses where it might be difficult to optimize the magnetic field homogeneity, i.e., the shim. The voxel in Single Voxel Spectroscopy (SVS) is usually small enough (20 x 20 x 20 mm³) that it can be accurately placed to avoid such extraneous tissues. Take care that the SVS voxel size is not set too small as this will result in very noisy spectra. CSI will require placement of several saturation bands to prevent contamination from tissues outside of the volume-of-interest (VOI). Saturation bands in all three planes are extremely helpful in eliminating these signals. Take care that the CSI voxel size does not get too small, as this will result in noisy metabolite images.

MR spectroscopy is extremely sensitive to **any** metal that might cause magnetic field inhomogeneities. Items such as metal dentures, belt buckles, shoes, metal clothing snaps, removable body piercings, etc., should be removed from the patient prior to the scan (standard MRI practice). In addition, the closer the voxel is to isocenter, the better the shim will be, as measured with the Full Width Half Maximum (FWHM). The FWHM indicates how broad or narrow the peaks in the spectrum will be. Typically for SVS the FWHM should be under 12 Hz and for 2D multi-voxel under 15 Hz, although these values are for 1.5T and can vary significantly depending on VOI location and size.

Locating data on *syngo*.via
Once logged into *syngo*.via, the data should be located. There are two ways to do this; send the dataset directly from the modality to the *syngo*.via server or query/retrieve the data from PACS on *syngo*.via. Configuration of a PACS node by the local service engineer will be required when sending from the modality (AE title, IP address, and port number will need to be provided).

Query/Retrieve PACS
Searching for cases on PACS is done in the DICOM retrieve header in the bottom third of the home screen. Identify the Source selection which is the local PACS server the data is stored on. The search filters header is where the patient demographics will be put in. Click the search button and observe all cases on PACS meeting the search criteria. Find the desired patient exam and select the retrieve icon (Fig. 4).

Browser search
Now that the data has been downloaded on to the server, search for it in the patient browser. In the top half of the patient browser, type the name in and search for the data (Fig. 5). Search the database manually if the search function is not working.

Now that the dataset has been located, open it with the MR Spectro Analysis program by right-clicking on the patient in the browser, select OPEN WITH, and scroll down to find "MR SPECTRO". Selecting the star icon beside "MR Spectro" will identify this workflow as a favorite and make it easily accessible for subsequent analyses.

Selecting the protocol
After selecting the MR Spectro workflow, wait for the data to load, process, and display on the screen. This might take ten seconds or so. When MR SPECTRO opens,
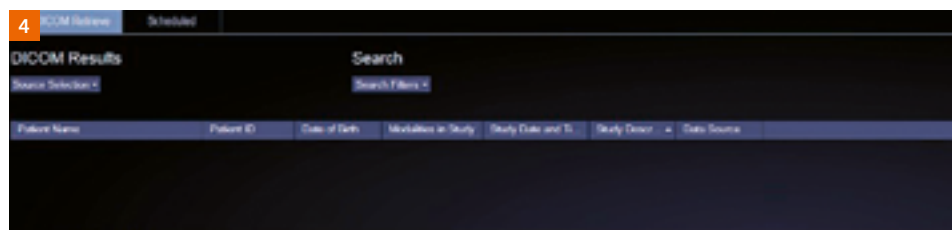

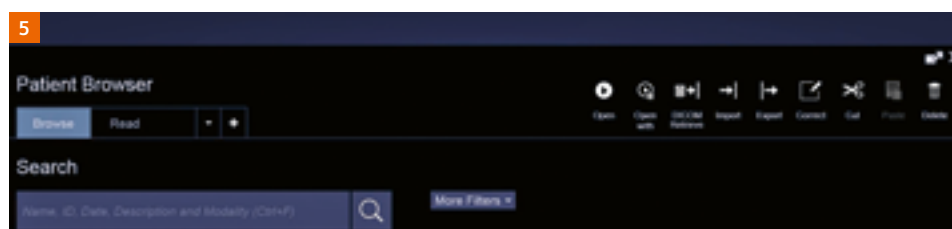**Figure 4:** Query/Retrieve window

Figure 5: Browser search

multiple windows appear showing the spectral grid overlay on the anatomical image, the spectrum for the selected voxel, the orthogonal image planes with the spectral grid overlay, and the color metabolite map. The complete list of data series can be viewed by clicking the small arrow located to the side. The series that are highlighted in blue in the Data Groups window are the ones that have been automatically selected by the program (Fig. 6). Different series can be dragged and dropped into any window as long as the requirements mentioned in "Getting started" were followed. Every window will have tools in each corner to alter that specific window if needed. Note that the default screen window configuration will be different depending on the monitor resolution and size.

Figure 6: Data Groups

Furthermore, there are many different configurations that can be used for viewing. Simply click the "4 windows" icon located just to the right of MR Spectro Analysis label (Fig. 7) and select the desired template.

The next step is only required if you wish to add metabolites to the analysis. You should only have to do this once – *syngo*.via will remember the workflow protocol. To select the metabolites that are to be analyzed, click the Spectro browser icon (Fig. 8) found at the bottom of the MR Spectro Analysis window.

The following example shows how to add the lactate metabolite to the analysis. Highlight csi_se_30 (Fig. 9) and select edit. A new window will appear. Select "Prior Knowledge" and click the + icon (Fig. 10). Another window will appear – this is where all the metabolites are listed. Scroll down, highlight lac_se_30, and click the select icon (Fig. 11). This loads the lactate metabolite acquired with a spin echo sequence at an echo time of 30 ms into the analysis. Save the protocol with a new name. Select "Save as" and save the new protocol as "csi_se_30_lac".

The last step is to select the new protocol. Right click on the series in the MR Spectro window and click on "Select Protocol". Choose the new protocol that was just created (Fig. 12). The program will automatically reprocess the data and queue it at the bottom of the Spectro workflow.

Defining the result table
The next step is to modify the Result Table to select the desired metabolites and metabolite. Select myo-inositol (mIns), NAA, Cho, Cr1, Cr2, and Lac. Creatine is often used as a baseline in spectral analysis since its concentration stays fairly constant. The choline to NAA ratio (Cho/NAA) is another common ratio used in assessing brain tumor spectra, since the choline peak is often elevated and the NAA peak is often reduced. In the spectrum window, click on the ruler in the top right corner. This will be where the result table is defined (see Fig. 13). In the pop-up window, there are useful examples of how to enter the desired equations. Using creatine as the base, defined values will display when adding the Integrals.
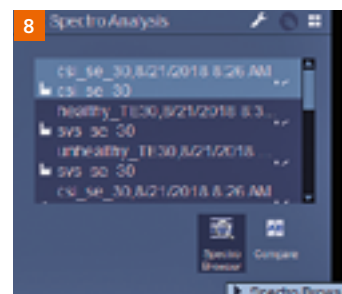

Figure 7: Configuration icon

Figure 8: Spectro browser icon

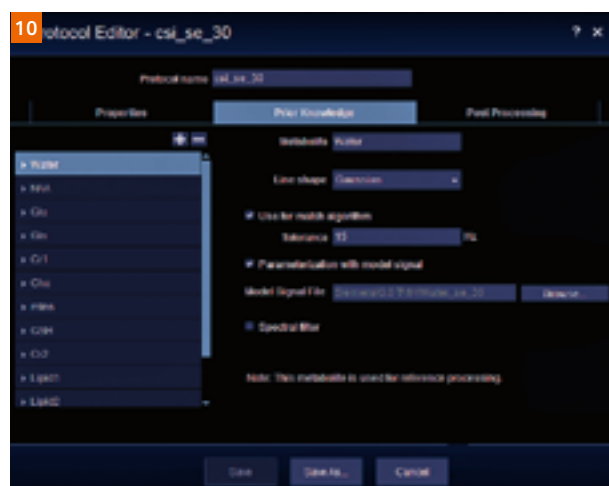**Figure 9:** Editing the csi_se_30 protocol

Figure 10: Entering prior knowledge

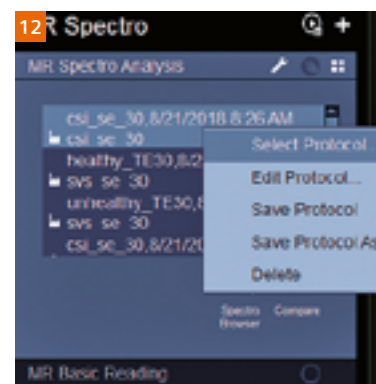**Figure 11:** Selecting the lac_se_30 protocol

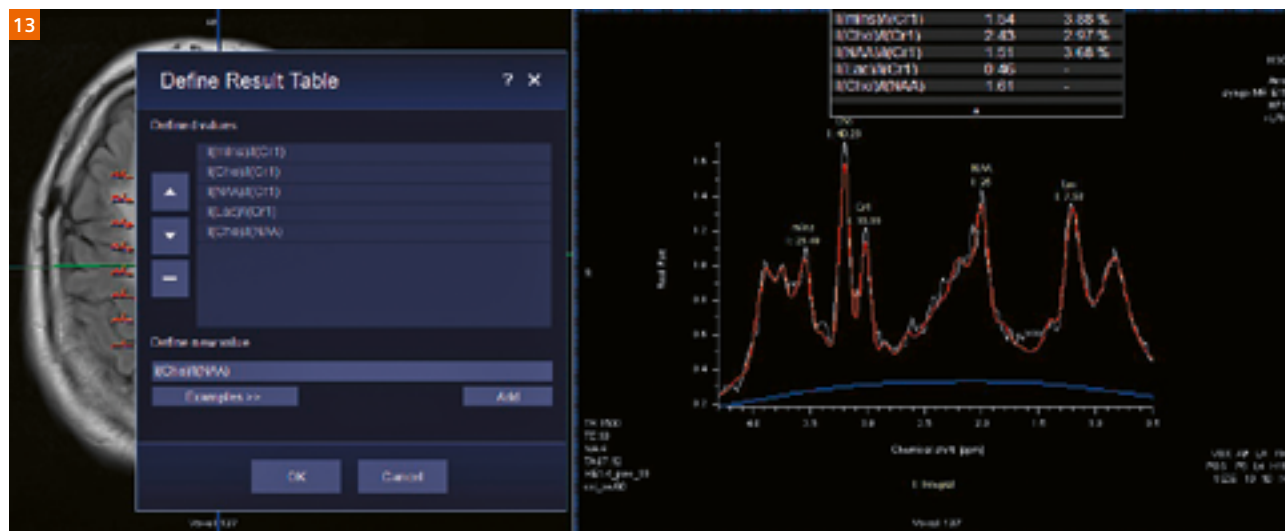**Figure 12:** Selecting the analysis protocol

Figure 13: Defining the result table

The first column in the table is the label of the metabolite ratio. The second column is the actual value of that ratio. The third column is the percent variation which is a measure of how good the spectral fit was. A rule-of-thumb is that metabolite ratios with percent variations greater than 20% should not be considered accurate. The lower this number is, the better the fit.

The result table can be manipulated in many ways; adding and subtracting different combinations of ratios will yield results tailored to specific differential diagnoses. After the result table is properly defined, click "OK" and *syngo*.via will remember these values for all subsequent analyses when the protocol is saved.

Defining metabolite maps

Metabolite images or maps are another way of visualizing the spatial variation of metabolites across the brain, and for seeing "hot spots" for certain metabolites and ratios. The "Define Metabolite Image" window (Fig. 14) is used to define which maps to display, using equations similar to the way the result table was defined. Metabolite map windows are typically on the right-hand side of the monitor. First, drag and drop the image-underlay series into the window from the Data Groups (Fig. 6). Note that the available series are displayed as "Data groups" by default, but can be viewed as "Thumbnails", or "Study/Series" by selecting the dropdown. Any image series can be chosen (usually axial T1 post gad) as long as the series was scanned under the specifications mentioned in getting started, i.e., same isocenter, no 2D distortion correction, etc. Once the series is loaded in the window, select the ruler (define metabolite image) in the upper right-hand corner and define any type of color map that is required (Fig. 15) Whether they are single metabolite maps, or ratios, use the same method as was used for defining the result table.

If gaps are seen in the metabolite image, it might be because a spectrum has been automatically identified as a "Low quality voxel". This means that the spectral fitting was unreliable in this voxel and it shouldn't be used in the diagnosis. It is also possible to manually identify voxels as "Low quality", should this be necessary. For example, if the metabolite map for lactate shows a very bright spot, click on that voxel and examine the spectrum. If a very high lipid signal is observed, then mark that voxel as "Low quality" so that it doesn't mislead the radiologist.

Exporting results to PACS

Now that the Result Table has been generated and the metabolite images have been defined, the results can be sent to PACS for reporting and archiving purposes. Under Tools (bottom third of screen), click the arrow below the "layout snapshot" icon. There are three options. Snapshot
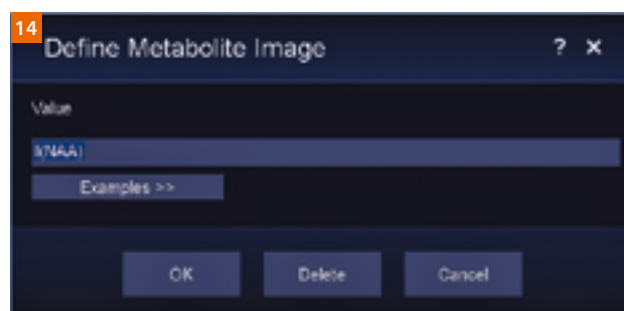

Figure 14: Defining the metabolite image

will take a screen shot of every window that is highlighted blue. Layout Snapshot will take a screen shot of all 4, or 6 windows, depending on the window configuration. "Snapshot to finding" will add the selected windows into the chosen findings folder that is identified by a checkmark. A new findings folder is created for each new snapshot; therefore once the initial snapshot is done, use the "Snapshot to finding" icon. These preceding snapshots to findings will be archived into the findings folder that were selected. Each findings folder should be exported to PACS in a different series. Review all snapshots made in the findings navigator by double clicking on the small picture icon. When all the snapshots are done, right click on the findings and select export to PACS (Fig. 16). For CSI, ensure that the full voxel position is included in the snapshot, as in Fig. 17 and 18.

Healthy vs. unhealthy analysis

It can be useful to select two spectra from the full CSI dataset, one corresponding to the spectrum with the most abnormal spectral ratios (labeled "Unhealthy") and another from contralateral normal appearing brain tissue (labeled "Healthy"). Once the *syngo*.via spectroscopy analysis is configured with all the tables and all the maps defined, select the two representative "Healthy" and "Unhealthy" voxels (Figs. 17, 18) and collect a snapshot of each for export to PACS for interpretation by the radiologist.

Strengths/limitations

Overall, the *syngo*.via MR spectroscopy analysis software is extremely user-friendly and easy for technologists, radiologists, and other clinical staff to use.
- The modern graphic user interface makes full use of multiple windows, context-sensitive mouse-clicks, and a well thought out workflow.
- A key benefit is that the software package is ready-to-use, right from the start, and does not require the acquisition of any additional scans on various spectroscopy phantoms.
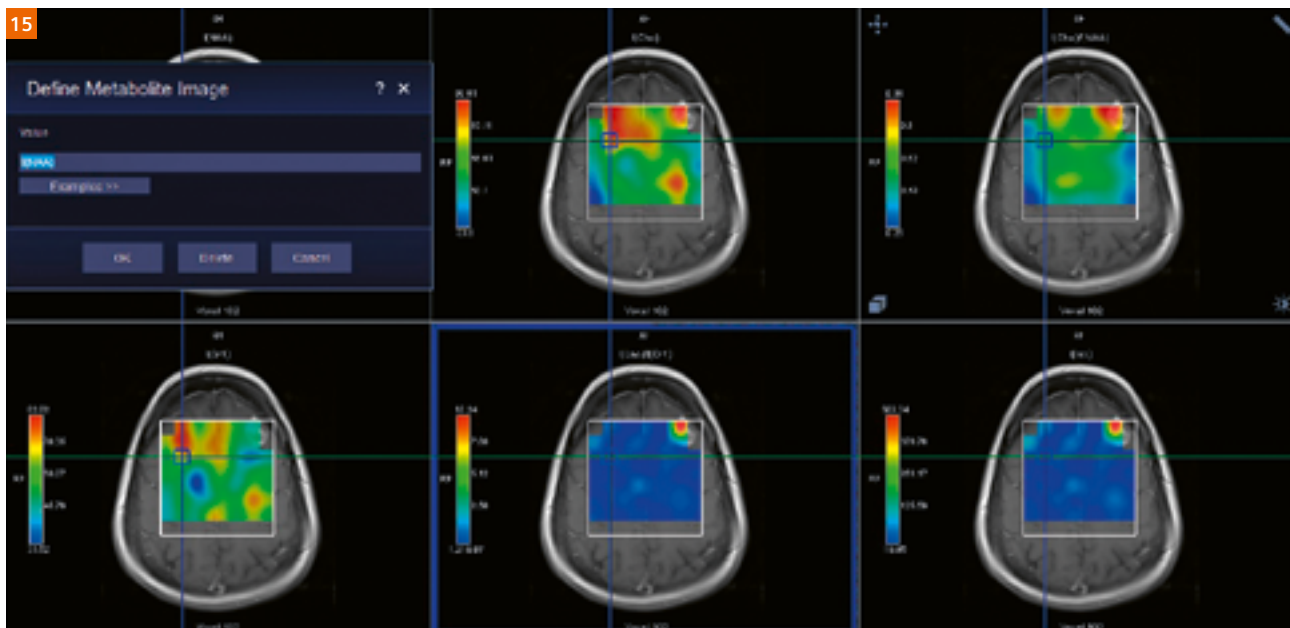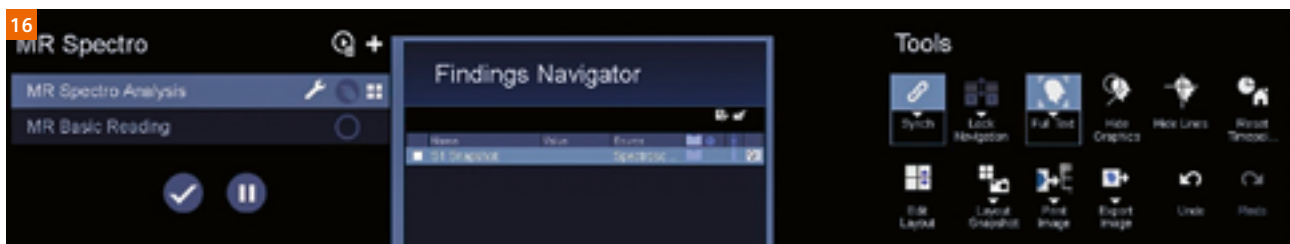
Figure 15: Examples of metabolite maps

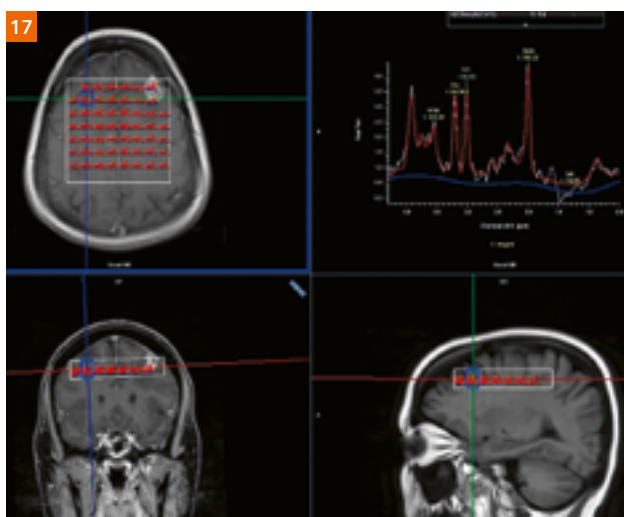**Figure 16:** Exporting to PACS

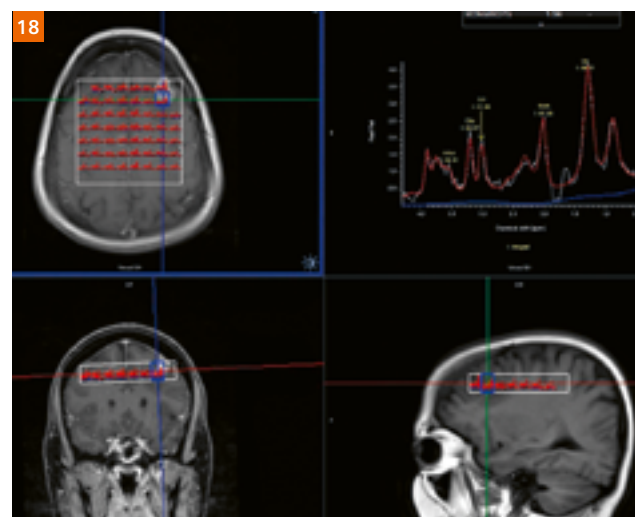**Figure 17:** Selecting the voxel for the "Healthy spectrum"

Figure 18: Selecting the voxel for the "Unhealthy spectrum" corresponding to the brain tumor spectrum with the "worst" spectral ratios
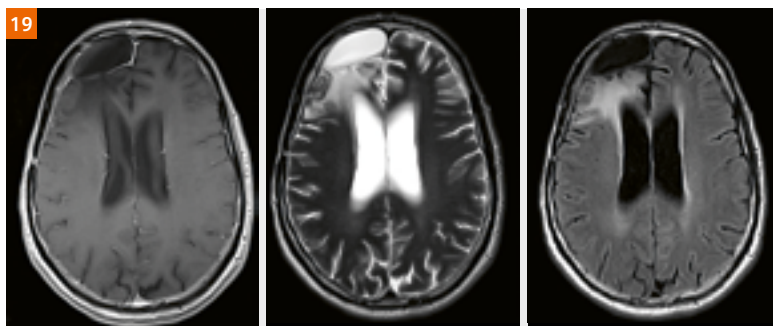
Figure 19:
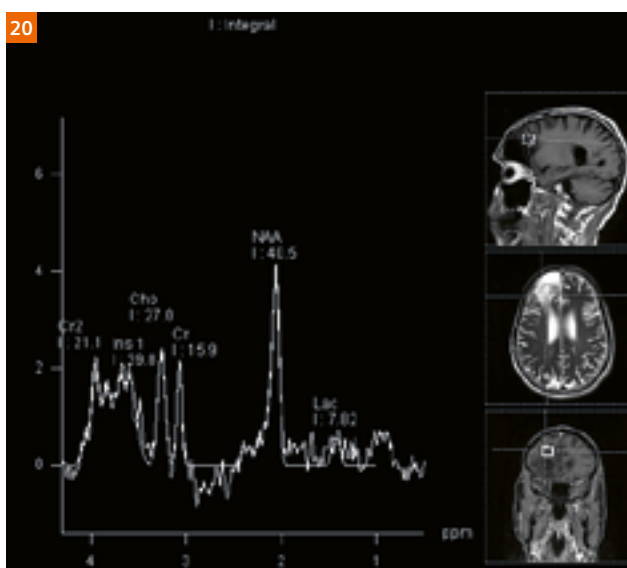T1, T2, and FLAIR images of a patient following radiation therapy of a high-grade oligodendroglioma

Figure 20: Single voxel spectrum from the suspicious area showing relatively normal Cho to NAA ratio
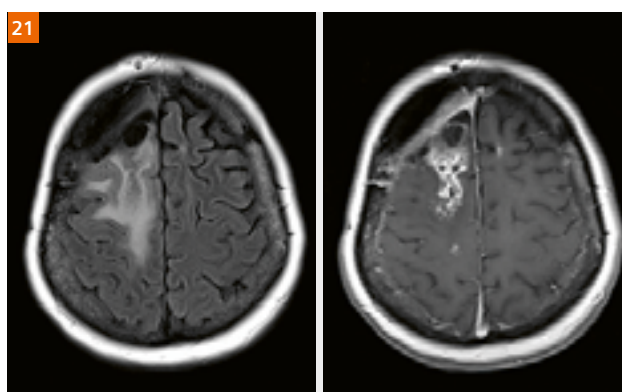

Figure 21: Second patient with a glioblastoma multiforme showing FLAIR and T1-weighted image

- The spectral fitting routine has been fully updated from previous versions and now utilizes robust time-domain fitting which is less dependent on perfect phasing as is required for spectral domain fits.
- Inclusion of a goodness of fit measure in the Results Table helps in determining which spectral fits are reliable (e.g., rule of thumb is a variation of less than 20%).
- Automatic marking of spectra with low quality fits helps the user determine which fits are reliable and which aren't.

Any software package comes with limitations that are often fixed in subsequent releases, based on customer feedback.

- The lack of an ability to sum multiple spectra from a user-selected region of interest in the CSI grid makes it hard to fully assess larger tumors extending over multiple voxels.
- Other advanced CSI software packages come with the ability to shift the CSI grid in order to position voxels more precisely over suspicious regions in the image; this ability is lacking in this software package.

It should also be noted that there is an Advanced Mode that can be configured in the Workflow Step Configuration which provides some additional functionality to the software. Users wishing to have this enabled should consult Siemens service.
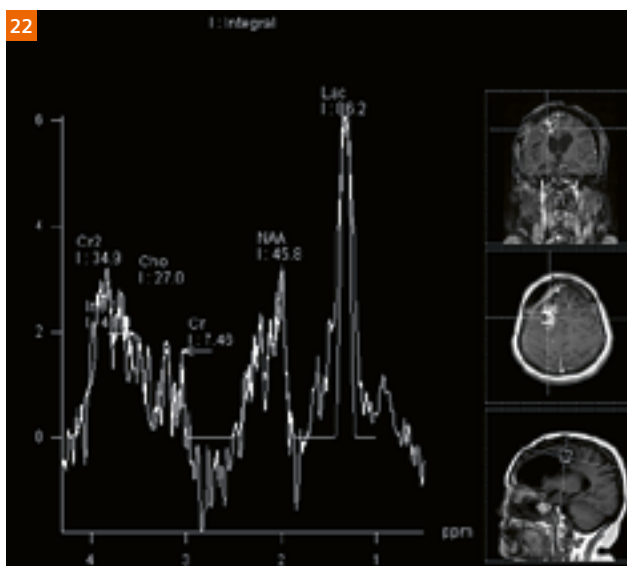

Figure 22: Single voxel spectrum from the suspicious area showing relatively normal Cho to NAA ratio, with some changes in the lactate/lipid region

Patient cases

Two patient cases are presented to demonstrate the utility of MR spectroscopy in helping to differentiate treatment-related changes from progressing tumor as observed in standard MR imaging.

In this first patient case, the standard T1- and T2-weighted imaging (Fig. 19) appeared to demonstrate an increase in tumor size after radiation therapy of the high-grade oligodendroglioma.

Single voxel spectroscopy from the suspicious region indicated (Fig. 20) showed a relatively normal ratio of Cho to NAA signal without the signature elevation of the Cho to NAA ratio found in brain tumor tissue, thus indicating that the changes are not likely related to tumor progression but rather related to treatment effects..

A second patient case with glioblastoma multiforme shows a suspicious area posterior to the resected region following chemotherapy and radiation therapy (Fig. 21).

Single voxel spectroscopy from a voxel located in the middle of the suspicious region is shown in Figure 22. With no increase in the Cho to NAA ratio and some changes in the lactate/lipid region at 1.3 ppm, these changes in the MR imaging are most likely treatment-related changes and not a progressing tumor.

Conclusion

The *syngo*.via MR spectroscopy analysis software is a powerful, easy-to-use tool that streamlines and simplifies the use of MRS and MRSI as a routine functional imaging method in a high-volume MRI department. Using a standardized acquisition and analysis workflow, as outlined in this article, enables the use of this complex technology in a quick, easy-to-implement process on a day-to-day routine basis that provides key information to the radiologist. This functional information can be used for better workup and differential diagnosis of brain tumors, for treatment planning, and for differentiation between tumor progression and pseudo effects following treatment.

Acknowledgements

References

1   Alger JR, Frank JA, Bizzi A, et al. Metabolism of human gliomas: assessment with H-1 MR spectroscopy and F-18 fluorodeoxyglucose PET. Radiology 1990; 177:633-641.
2   Negendank WG, Sauter R, Brown TR, et al. Proton magnetic resonance spectroscopy in patients with glial tumors: a multicenter study. J Neurosurg 1996; 84:449-458.
3   Meyerand ME, Pipes JM, Mamourian A, Tosteson TD, Dunn JF. Classification of biopsy-confirmed brain tumors using single-voxel MR spectroscopy. AJNR Am J Neuroradiol 1999; 20:117-123.
4   Dowling C, Bollen AW, Noworolski SM, et al. Preoperative proton MR spectroscopic imaging of brain tumors: correlation with histopathologic analysis of resection specimens. AJNR Am J Neuroradiol 2001; 22:604-612.
5   Demaerel P, Johannik K, van Hecke P, et al. Localized 1H NMR spectroscopy in fifty cases of newly diagnosed intracranial tumors. J Comput Assist Tomogr 1991; 15:67-76.
6   Vuori K, Kankaanranta L, Hakkinen AM et al. Low-grade gliomas and focal cortical developmental malformations: differentiation with proton MR spectroscopy. Radiology 2004 Mar; 230(3):703-8.
7   Wilson M, Cummins CL, Macpherson L, et al. Magnetic resonance spectroscopy metabolite profiles predict survival in paediatric brain tumours. Eur J Cancer 2013; 13:457-464
8   Norfray JF, Darling C, Byrd S, et al. Short TE proton MRS and neurofibromatosis type 1 intracranial lesions. J Comput Assist Tomogr 1999; 23:994-1003
9   Law M. MR spectroscopy of brain tumors. Top Magn Reson Imaging 2004 Oct; 15(5):291-313.
10 Delorme S, Weber MA. Applications of MRS in the evaluation of focal malignant brain lesions. Cancer Imaging 2006 Jun 22; 6:95-9.
11 Galanaud D, Nicoli F, Chinot O, Confort-Gouny S, Figarella-Branger D, Roche P, Fuentes S, Le Fur Y, Ranjeva JP, Cozzone PJ. Noninvasive diagnostic assessment of brain tumors using combined in vivo MR imaging and spectroscopy. Magn Reson Med 2006 Jun; 55(6):1236-45.
12 Majos C, Julia-Sape M, Alonso J, Serrallonga M, Aguilera C, Acebes JJ, Arus C, Gili J. Brain tumor classification by proton MR spectroscopy: comparison of diagnostic accuracy at short and long TE. AJNR Am J Neuroradiol 2004 Nov-Dec; 25(10):1696-704.

Contact

Lawrence Ryner   Marco Essig   Craig Snell

Since I work in an ultra-high-field (UHF) MRI[1] facility, I often give tours. Obviously, a common question is, "What are the advantages of higher magnet fields?" It is easy to answer this by rattling off the usual reasons: Higher signal-to-noise ratio (SNR), which can be used for higher image resolution, faster scan times, etc., as well as better spectral separation for Magnetic Resonance Spectroscopy (MRS). You can then talk about quantitative susceptibility mapping (QSM) and the anisotropic susceptibility of white matter, which even goes as far as being dependent on the orientation of the subject's head to the field [1]. This was an unexpected contrast at 7T, which proves that you shouldn't rely entirely on expectations when attempting new experiments. After all, it wasn't so long ago that people thought higher field MRI would be absolutely impossible due to RF penetration effects.

However, I would like to describe a different journey – one in which an artifact becomes anatomical history.

When setting up prototype equipment, you end up spending a lot of time at the console, often repeating the same types of scans over and over, looking to improve performance, reduce artifacts, and so on. Since T2*-weighted imaging is particularly interesting at 7T, I have seen many, many examples of these scans. Soon after starting to work at Neurospin (Saclay, France), certain things began to catch my eye – in particular, a pattern of parallel lines that often appeared on sagittal views of the corpus callosum (CC).

Initially, I dismissed this as an artifact. UHF is very attractive in many ways, but the higher SNR can also show up artifacts. In this case, I presumed that eye movement during the scanning was causing ripples in the phase encode (PE) direction, particularly as the PE direction was generally set to anterior-posterior (AP) in order to allow a head-feet (HF) read direction, which in turn avoided fold-in from the neck or shoulders.

Somehow, though, this explanation did not satisfy me. I started looking more closely, and had the impression that the parallel lines, which appeared somewhat radial in direction on a sagittal image, were reproduced in neighboring slices. When I studied this more closely, I found that, with the protocol I was using, I could best see the stripes on slices that were slightly off the midline by one to two centimeters. Even then, the stripes could be elusive. One experiment I tried involved two parallel slices with two repetitions. The results showed these fine lines in both slices on the first repetition, but on the second repetition they only appeared on one (Fig. 1).
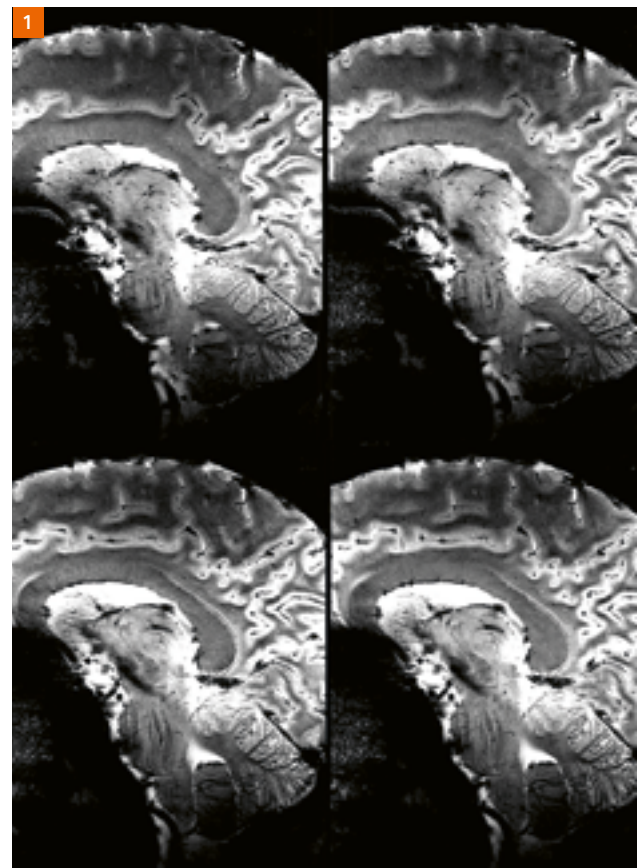

Figure 1:
Two 2D slices imaged with two repetitions as a single GRE scan. On the upper row are the two slices, with the repetitions below. The stripes can be seen in both slices in the first repetition, but only in one (bottom left) in the second.

[1]MAGNETOM 7T is for research only. All data shown are acquired using a non-commercial system under institutional review board permission.

However, this was still enough to convince me that there was really something in the data – but what was it we were seeing?

As I discussed this with colleagues, some more information and examples came forth. I remember a colleague presenting me with a 7T advertising, where these lines were clearly visible. Another colleague simply went to his office and picked up an anatomical atlas and – *voila*! – the CC was drawn with a similar set of radial lines. Indeed, a simple web search will bring up the Wikipedia page for the CC, which shows the *Gray's Anatomy* [2] drawing with exactly the pattern I was seeing.

Now I had to work out whether this was really the same thing. The devil's advocate in the discussion – Denis Le Bihan – argued that relying on these old atlases was putting me on shaky ground. The drawings could show the anatomist's or artist's preconceived ideas of how these structures *should* look, or they could even be inherited from earlier atlases. So the comparison

was intriguing, but not definitive. We also looked at the spherical decomposition of DTI data, but saw nothing that supported any structure beyond the main L-R fiber direction.

The next step was to bring in an expert. We consulted a local neuroanatomy professor, but the answer was that there was no known structure in the CC. In other words, we were seeing an artifact.

Shortly afterwards I was invited to give a talk at the Max Planck Institute for Human Cognitive and Brain Sciences (CBS, Leipzig, Germany). I included my slide with the two-slice, two-repetition experiment to see if anyone had any insights beyond the artifact hypothesis. As I recall, Professor Robert Turner saw this and said to himself, "*Pah*! It's just an artifact." and returned to his office. There, though, he picked up Cho's 7T atlas [3], which shows MRI images with corresponding cadaver slices. The stripes were visible on Cho's images, and Bob became a believer. I had gained my first CC-stripes disciple!
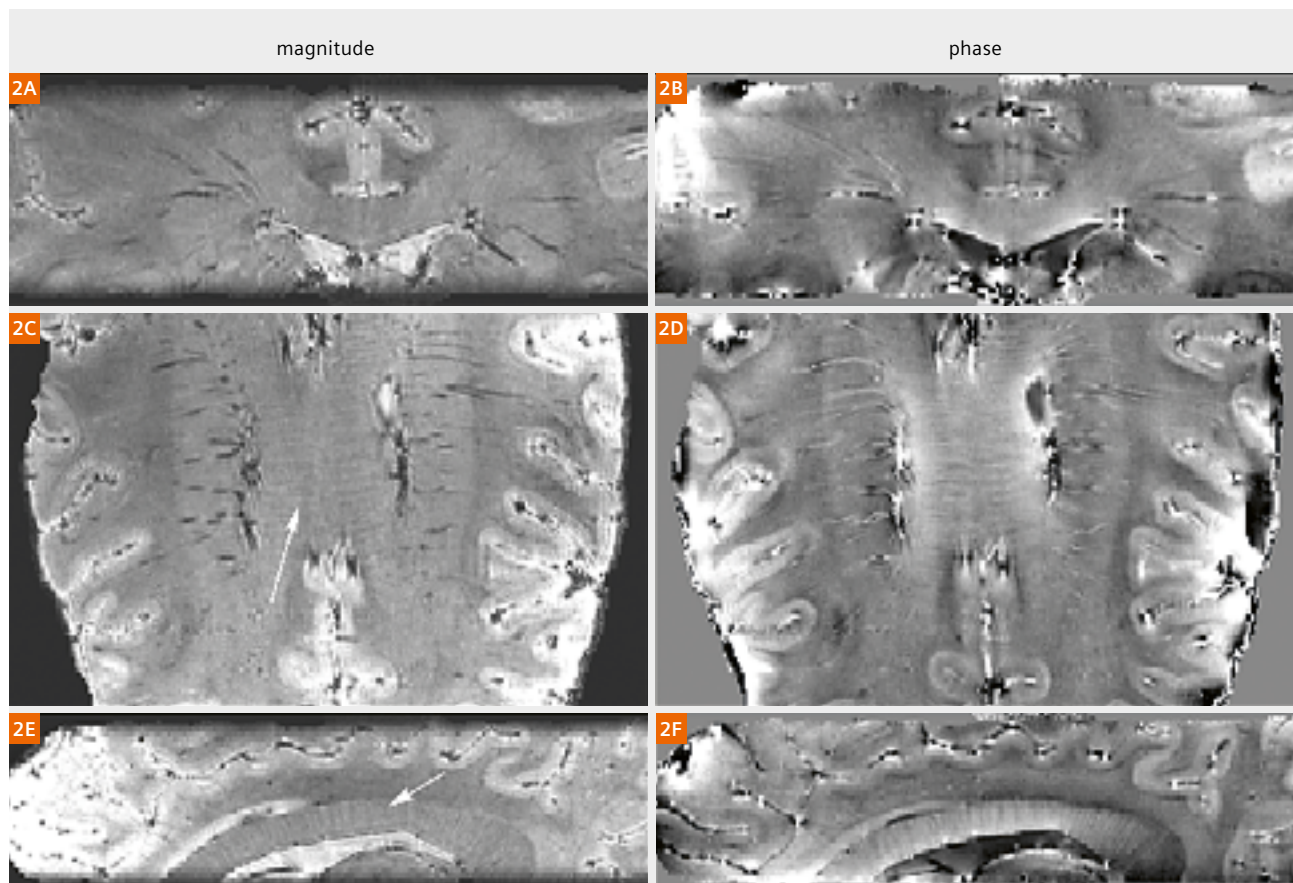

Figure 2:
3D GRE shows the stripes in the corpus callosum in both magnitude and phase images.
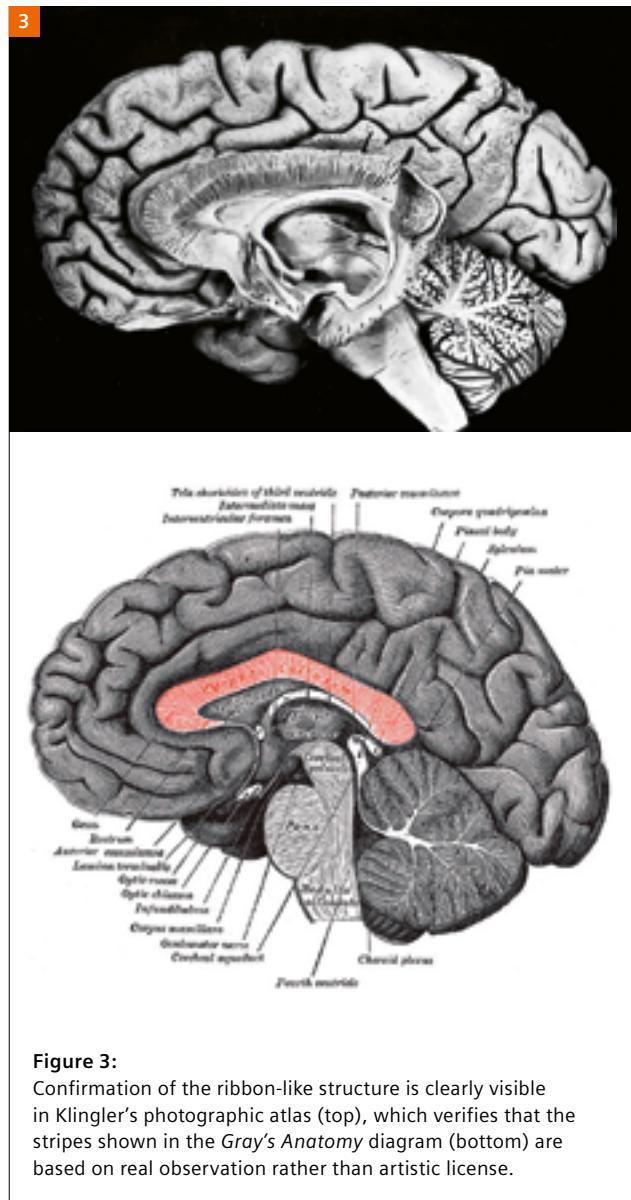
Like any true disciple, Bob began spreading the word. He started a collaboration and asked the members of his team to look into these stripes. Soon we had better images, with 3D GRE images with 0.5 mm isotropic resolution showing the stripes in orthogonal planes (Fig. 2). Such a pattern can only be explained by a 2D plane, rather than a linear structure, so that eliminated the suggestion that the stripes were purely vasculature. Additionally, an examination of the *second* eigenvector of DTI datasets showed a very similar radial pattern. Bob found literature from prenatal brains [4, 5] showing that septa exist in early brain development in just the sort of pattern we were seeing, but then seem to vanish around the time of birth. Another CBS researcher pointed us to Klingler's photographic atlas [6]. Klingler's preparation of brain samples involved fixation, freezing, and thawing, and then exposing the fiber bundles by gently removing tissue. The CC in the atlas clearly has a ribbon-like or foliate appearance. Since this is a *photographic* atlas, we could now counter the argument that the drawn atlases were not a true representation of anatomy (Fig. 3).

However, judging from the Editors remarks to our first submission, much more evidence was required. I began trying to find out how often this structure appeared in published anatomical atlases. Searching for this was fairly easy – there are many digitalized anatomical atlases available online, and one can spend many happy hours perusing them. The pictures are often very beautiful in their own right. I set myself a target of finding the oldest representation of the stripes, and ended up with a selection that included Gray [2], Dejerine [7], Bell [8], and Vicq d'Azyr [9].

This allowed me to show that the CC has been represented with these radial stripes for over 200 years (Fig. 4). I could therefore say that UHF MRI can now show *in vivo* something that for two centuries had only been available from *ex vivo* preparations – and indeed largely forgotten about.

Armed with numerous representations and a more complete analysis of the data, our paper entitled "After over 200 years, 7T magnetic resonance imaging reveals the foliate structure of the human corpus callosum *in vivo*" was accepted by the *British Journal of Radiology* in March 2017 [10].

So why use UHF MRI? Well, my experience shows that it allows you to see things that you really cannot see otherwise – not with lower field MRI, not with CT, not with PET, and perhaps most importantly, not without cutting the subject open!

Figure 3:
Confirmation of the ribbon-like structure is clearly visible in Klingler's photographic atlas (top), which verifies that the stripes shown in the *Gray's Anatomy* diagram (bottom) are based on real observation rather than artistic license.
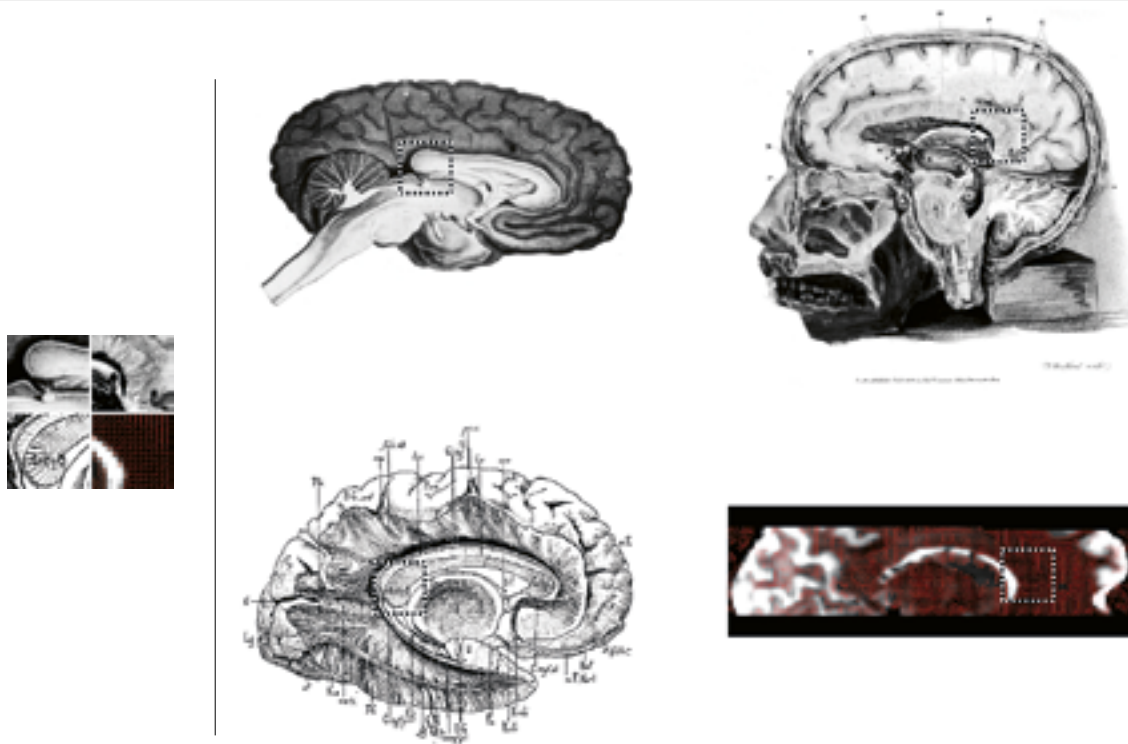
Acknowledgements

Figure 4:
Further confirmation can be seen in the atlases by Vicq d'Azyr (1786, top left),
Bell (1802, top right), and Dejerine (1895, bottom left), as well as from the
second eigenvector of DTI data (bottom right).

References

1. Wiggins CJ, Gudmundsdottir V, Le Bihan D, et al.
Orientation dependence of white matter T2* contrast at 7 T:
a direct demonstration. Proceedings of the 16th Annual Meeting
of ISMRM; Toronto, Canada. 2008. p. 237.
2. Gray H. Anatomy of the human body.
Philadelphia, USA: Lea & Febiger; 1918.
3. Zang-Hee Cho. 7.0 Tesla MRI Brain Atlas: In Vivo Atlas with
Cryomacrotome Correlation. New York, USA: Springer Science +
Business Media LLC; 2010.
4. Jovanov-Milosević N, Benjak V, Kostović I. Transient cellular
structures in developing corpus callosum of the human brain.
Coll Antropol. 2006; 30(2):375–81.
5. Jovanov-Milosević N, Culjat M, Kostović I. Growth of the human
corpus callosum: modular and laminar morphogenetic zones.
Front Neuroanat. 2009; 3:6.
6. Ludwig E, Klingler J. Atlas cerebri humani.
Basel, Switzerland: S. Karger; 1956.
7. Dejerine J, Dejerine-Klumpke A. Anatomie des centres nerveux.
Paris, France: Rueff; 1895. Available from: the Medical Heritage
Library (http://www.archive.org/details/anatomiedescentr01dj)
8. Bell C. The anatomy of the brain, explained in a series
of engravings. London, UK: T.N. Longman and O. Rees, 1802.
9. Vicq d'Azyr F. Traité d'anatomie et de physiologie.
Paris, France: Didot; 1786. Available from:
(text) http://www.biusante.parisdescartes.fr/histmed/medica/
cote?00519x01;
(plates) http://www.biusante.parisdescartes.fr/histmed/medica/
cote?00519x02
10. Wiggins CJ, Schäfer A, Dhital B, et al. After over 200 years,
7 T magnetic resonance imaging reveals the foliate structure
of the human corpus callosum in vivo.
Br J Radiol. 2017; 90(1073):20160906.

Fetal MR Imaging: An Overview

Xianyun Cai[1]; Xin Chen[1]; Cong Sun[1]; Tuantuan Wang[1]; Hong Tang[1]; Jinxia Zhu[2]; Guangbin Wang[1]

[1]Department of MR, Shandong Medical Imaging Research Institute, Shandong University, China
[2]Siemens Healthineers, MR Collaboration, Beijing, China

The primary objective of prenatal diagnosis is to obtain genetic, anatomical, biochemical, and physiological information about the fetus that will allow the detection of any abnormalities that may have implications for the fetal and postnatal periods. This will make it possible to offer the family information, genetic counseling, and therapeutic alternatives. The main imaging method used for routine fetal examinations is ultrasonography (US). It is noninvasive, inexpensive, widely available, and can provide real-time studies without ionizing radiation. However, in cases of advanced gestational age, patient obesity, oligohydramnios, improper fetal position, and interposition of intestinal gas or pelvic acoustic shadows, US might have technical limitations and be unable to confirm findings. In our department, we consider using MRI when the US findings are equivocal or when the US images are difficult to interpret due to factors such as late pregnancy or an inaccessible fetal position. Fetal MR imaging[1] is regarded as a valuable adjuvant imaging tool for dedicated cases at field strengths of 3T or less. In general, with appropriate sequence adaptations, examinations of the fetus at 3T are comparable with images obtained at 1.5T. Also, because of the higher image resolution and signal-to-noise ratio (SNR), finer structures and lesions can be delineated at 3T. However, a major drawback is that examinations at 3T are more prone to artifacts, which complicates imaging the fetus for traditional referrals (maternal obesity, polyhydramnios). It is therefore important to decide which system might be better suited to address certain indications [1]. Investigation of normal organ development with fetal MRI has been described by Prayer et al. [2]. Maturational processes in utero are characterized by changes in the shape, size, and content/composition of organs, and by their relationship to each other.

In our institution, all the MRI examinations were performed on a 1.5T MAGNETOM Amira (Siemens Shenzhen Magnetic Resonance, Shenzhen, China) with spine and body array coils positioned over the lower pelvic area. Since our department introduced fetal MRI in June 2006, a total of 15,000 pregnant women with various anomalies (screened by ultrasonography) have been referred for fetal MRI examinations at our institution. The cases include brain, spine, chest, and abdominal anomalies. A placental MRI scan was performed for the first time in 2009, and 1,102 such scans have been performed to date. A total of 235 fetal spine scans have been performed since 2015, when susceptibility-weighted imaging (SWI) – a technique developed by Siemens [3], which conventionally uses the BOLD mechanism to generate venograms of the brain and to quantify venous oxygenation levels [4] – was first modified for fetal spine imaging with fast data acquisition by Robinson et al. [5]. In recent years, the development of MR sequences has led to major changes in fetal MRI imaging in our unit.
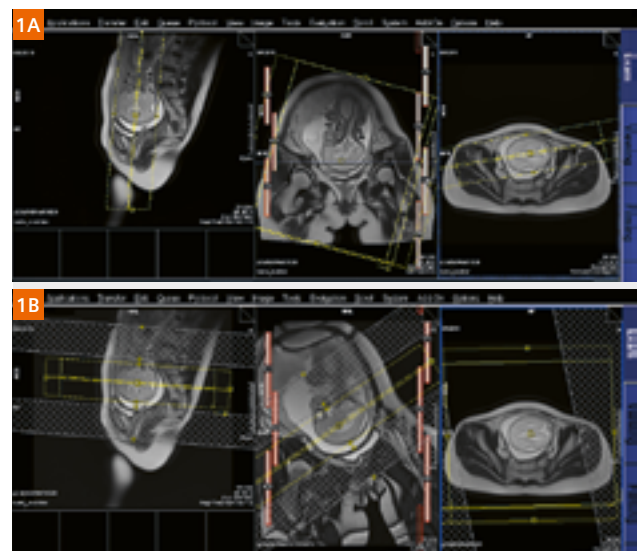
Figure 1:
Sagittal and coronal localizer images of the fetal brain.

---

[1]*Siemens Healthineers disclaimer does not represent the opinion of the authors: MR scanning has not been established as safe for imaging fetuses and infants less than two years of age. The responsible physician must evaluate the benefits of the MR examination compared to those of other imaging procedures.*

The rise and development of fetal magnetic resonance imaging

Origins

Since fetal MR imaging was first used in 1983 [6], no consistent or convincing evidence has emerged to suggest that briefly exposing a fetus to the changing electromagnetic fields of MR imaging has any harmful effects. In the early days, however, the acquisition time was too long and the motion artifacts were severe, which resulted in poor image quality and hindered the development of fetal MRI. With the development of ultrafast sequences in the 1990s, such as single-shot steady-state free precession (SSFP), half-fourier acquisition single-shot turbo spin echo (HASTE), fast T1-weighted gradient echo, and echo planar imaging, MR imaging became a noninvasive modality that could complement US in detecting fetal abnormalities, establishing prognoses, and assisting in perinatal management.

Safety

With fetal MRI, safety considerations such as exposure times, gradient field switching, noise, and radiofrequency power deposition should be kept in mind while following established guidelines [5–9]. No documented indications exist for using contrast agents in fetal MR imaging. Generally speaking, fetal MR imaging should be avoided in the first trimester, since the fetal cells are rapidly dividing and differentiating, and the influence of MRI on organogenesis is still unclear. Also, it is difficult to obtain good-quality images in very young fetuses.

Another important issue to consider in fetal MRI concerns gadolinium-based intravenous contrast media. These agents have been shown to cross the placenta and may appear in the fetal bladder, which means they are reabsorbed from the amniotic fluid by swallowing. The use of gadolinium-based contrast agents for MR imaging in pregnant women remains controversial. Recently, an animal experiment was conducted to determine whether gadolinium remains in juvenile nonhuman primate tissue after maternal exposure to intravenous gadoteridol during pregnancy. The study concluded that gadoteridol could cross the placenta. Given the similarities between human and nonhuman primate placental physiology, the study suggests there could be relatively little deposition in human fetal tissues after maternal gadoteridol injection. However, the long-term risk of such low levels of gadolinium deposition is still unknown. At our institution, no intravenous injection (of gadolinium agents or sedation agents) was used for any of the examinations, and specific absorption rate limits were in keeping with departmental protocols.

Moreover, maternal indications for prenatal MRI also need to be taken into account.

Fetal MR imaging

All the patients were imaged in supine or left-lateral position, depending on what was most comfortable. Fetal images are obtained in three orthogonal planes in the mother to plan the sagittal, coronal, and axial views of the fetus. The last sequence is used as a reference for planning the next sequence to compensate for fetal movement. All sequences are performed in all three planes through the fetus. Additional imaging planes, such as oblique sagittal or coronal positions, were obtained as needed. An axial T2-weighted sequence may be performed through the fetal brain for purposes of gestational dating. In recent years, ultrafast MR imaging sequences have provided short image acquisition times and usually prevent fetal motion from degrading image quality.

Figure 2: Corpus callosum agenesis
Sagittal HASTE **(2C)** shows complete absence of the corpus callosum. Axial TrueFISP **(2A)** shows parallel orientation of lateral ventricles. Coronal TrueFISP **(2B)** shows steer-horn-shaped frontal horns (arrows) resulting from the impression of Probst bundles.

1. **T2-weighted sequences**

   T2-weighted imaging (T2WI) includes single-shot, and half-Fourier single shot turbo spin echo (SSTSE, HASTE) T2-weighted sequences, and balanced sequences such as true fast imaging with steady-state precession (TrueFISP), which produces high tissue contrast and highlights the hyperintense amniotic fluid. At our institution, T2 HASTE and T2 TrueFISP were the most frequently used sequences for evaluating fetal anatomy. The TrueFISP sequence also allows vascular studies that require no intravenous contrast agent and can reveal hyperintense fetal vessels (vessels appear hypointense on SSTSE T1-weighted and T2-weighted images).

2. **T1-weighted sequences**

   T1-weighted imaging (T1WI), including 3D dual gradient echo (GRE), 2D fast spoiled GRE (FISP), and 3D liver acquisition and volume acquisition (3D VIBE), show less tissue contrast than T2WI sequences. T1WI sequences are primarily used to identify subacute bleeding, calcification, and lipoma, which appear as hyperintense loop structures in studies of congenital diaphragmatic hernia (CDH). T1WI sequences are also used to assess the presence and distribution of meconium, which enables accurate diagnosis of gastrointestinal abnormalities, reveals the size and location of the fetal liver, and can identify fetal, placental, or maternal hemorrhage.

3. **Susceptibility-weighted imaging**

   Susceptibility-weighted imaging (SWI) uses the intrinsic nature of local magnetic fields to enhance image contrast and thereby improve the visibility of various susceptibility sources and facilitate diagnostic interpretation [7]. It is worth mentioning that calcification is strongly diamagnetic and therefore decreases the magnetization in bone compared to the applied magnetic field. The technique results in a high contrast between bone and soft tissue, but a low contrast between different types of soft tissue. The low-signal bone is therefore easily distinguishable from the surrounding soft tissue.

4. **Diffusion-weighted imaging**

   As well as being used to diagnose cerebral infarction, diffusion-weighted imaging (DWI) sequences are currently being developed for fetal applications. The technique is already being used to study the maturity of lung parenchyma.

Fluid-sensitive short T1 inversion recovery (STIR), intravoxel incoherent motion imaging (IVIM), MR hydrography, and other sequences are not part of the routine fetal protocol but may be performed in specific cases where necessary.
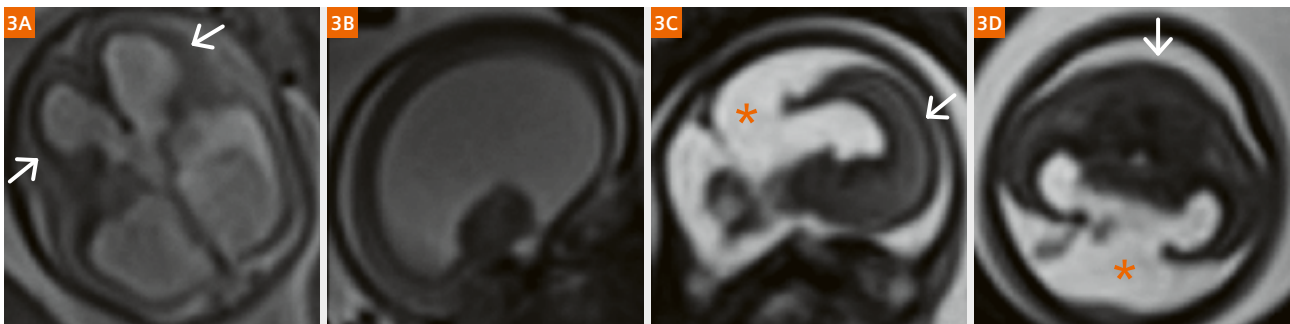

Figure 3: Severe hydrocephalus (3A, B) and alobar holoprosencephaly (3C, D)
Axial and coronal **(3A)** T2 HASTE imaging shows the marked dilation of the cerebral bilateral ventricle stenosis with only a thin mantle of overlying cerebral cortex (arrows). Sagittal **(3C)** and coronal **(3D)** T2 TrueFISP imaging shows only minimal frontal cerebral mantle (white arrows in 3A and B) and replacement of the majority of the brain with CSF (star). Coronal **(3C)** and axial **(3D)** T2 TrueFISP show a complete absence of falx, an interhemispheric fissure, and corpus callosum. Also visible is a horseshoe-shaped monoventricle communicating with a dorsal cyst (star).
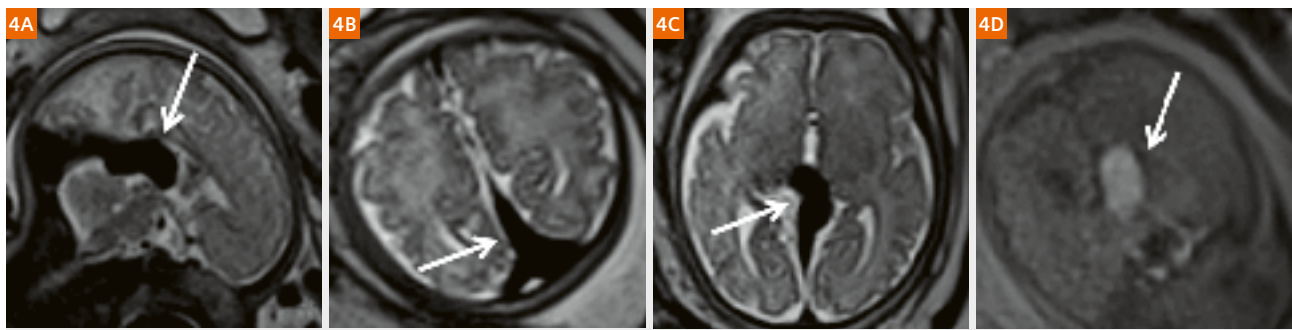
Figure 4: Galen vein malformation
Sagittal **(4A)** and coronal and axial **(4B)** T2 HASTE show a large varix (arrow) replacing the Galen vein, which exhibits hyperintensity on T1WI (**4D**, arrow).

The anatomy and anomalies in fetal MRI

Brain and spine

Imaging the central nervous system (CNS) anatomy and relevant pathology is clinically important for the early identification of cranial and spinal malformations and anomalous development. Fetal MRI has been shown to have higher contrast resolution and SNR than ultrasonography when it comes to illustrating the morphological changes in cranial and spinal brain abnormalities [8]. Most of the literature describing the results of MRI in large series of fetuses with CNS abnormalities deals with cerebral pathology. Spinal anomalies are usually described using examinations of smaller groups of patients or in case reports.

MR images of the developing fetal brain reflect changes in histogenesis and myelination. Subsequent changes are seen in the brain volume, surface configuration (sulcation), and internal configuration. Detailed information provided by MRI is necessary to evaluate the differentiation of white and gray matter, migration and myelination disorders, brain morphology and pathologies, and cranial posterior fossa and midline structures. Here, localizer brain scans (Fig. 1) provide the basis for images demonstrating different developmental deformities (Figs. 2–4).

The spinal canal and cord anomalies are among the CNS abnormalities which occur as a result of disruptions in formation and maturation. During the first three to five weeks of gestation (neurulation period), the neural tube, notochord, spine, and cranium develop. Disorders that occur at this stage of gestation (i.e., most spinal canal defects) are called "dorsal induction abnormalities". The dysraphic spinal canal and spinal cord disorders are divided into three groups: open dysraphic abnormalities, occult dysraphic abnormalities, and latent dysraphic

abnormalities (e.g., diastematomyelia, hydromyelia, syringomyelia, dorsal dermoid sinus, teratoma, hamartoma, lipoma, dermoid/epidermoid cyst, and caudal regression syndrome).

Congenital anomalies of the spine occur at four to six weeks of gestation due to abnormal vertebral development that causes asymmetric growth of the spine. Anomalies in the ossification center of the fetal vertebral body result in bony defects such as hemivertebrae, butterfly vertebrae, and block vertebrae, which cause congenital scoliosis. MRI of fetuses diagnosed with osseous anomalies of the spine remains largely unexplored. Recently, we adapted and improved a clinically available SWI sequence for fetal spine imaging to evaluate vertebral malformations and anomalous vertebral development (in bony structures). We also typically used T2 TrueFISP and HASTE sequences to evaluate the recognition of the fetal spinal canal and spinal cord pathologies, as described in previous studies [9].

For MR imaging of the fetal spine, the protocol first involved a scout imaging sequence to gather information about the orientation of the fetus. Subsequent routine clinical sequences included T1WI, DWI, HASTE, T2-weighted TrueFISP, and SWI sequences. The HASTE, TrueFISP, and SWI sequences were obtained in the axial, coronal, and sagittal planes. The axial plane is best for assessing the neural arches, the coronal plane allows an additional assessment of the ribs and of pedicular widening in cases of spina bifida, and the sagittal plane is best for assessing the whole spine lengthways. The SWI sequence is best run immediately after routine HASTE or TrueFISP sequences, depicting the required anatomy by simply copying the slice parameters and thereby minimizing the time between sequences and reducing the chance of fetal motion. Here, localizer spine scans (Fig. 5) provide the basis for demonstrating various developmental deformities as follows (Figs. 5–9).
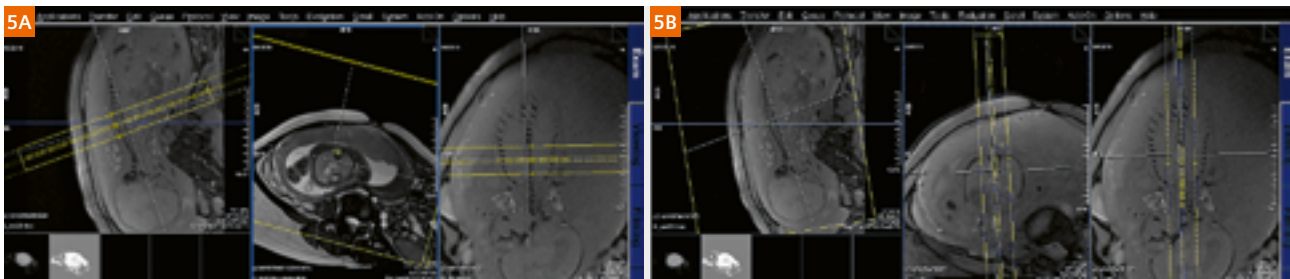
Figure 5:
Axial, sagittal, and coronal localizer images of the fetal spine.
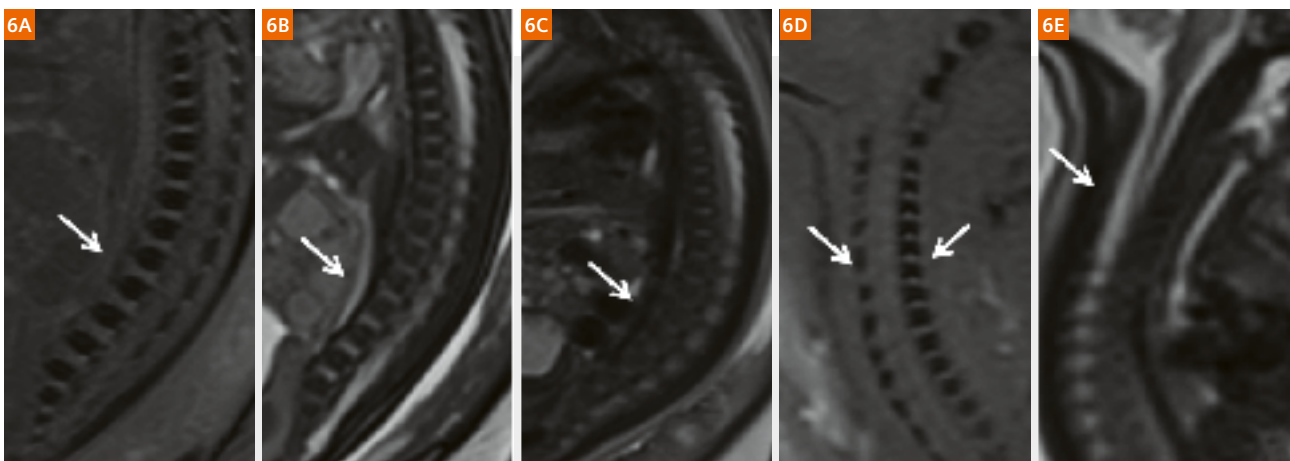

Figure 6:
Images at 32 weeks' gestation (6A–C) and 26 weeks' gestation (6D–E) with normal fetal spine structures. Sagittal view of the thoraco-lumbar spine, MR images including SWI (6A), TrueFISP (6B), and HASTE (6C). The SWI **(6A, D)** clearly shows the vertebral bodies and the posterior elements (arrows). On a similar plane in the same position using TrueFISP **(6B, E)** and HASTE **(6C)**, the vertebral column (arrows) is shown poorly but could reveal the structures of the intraspinal canal.
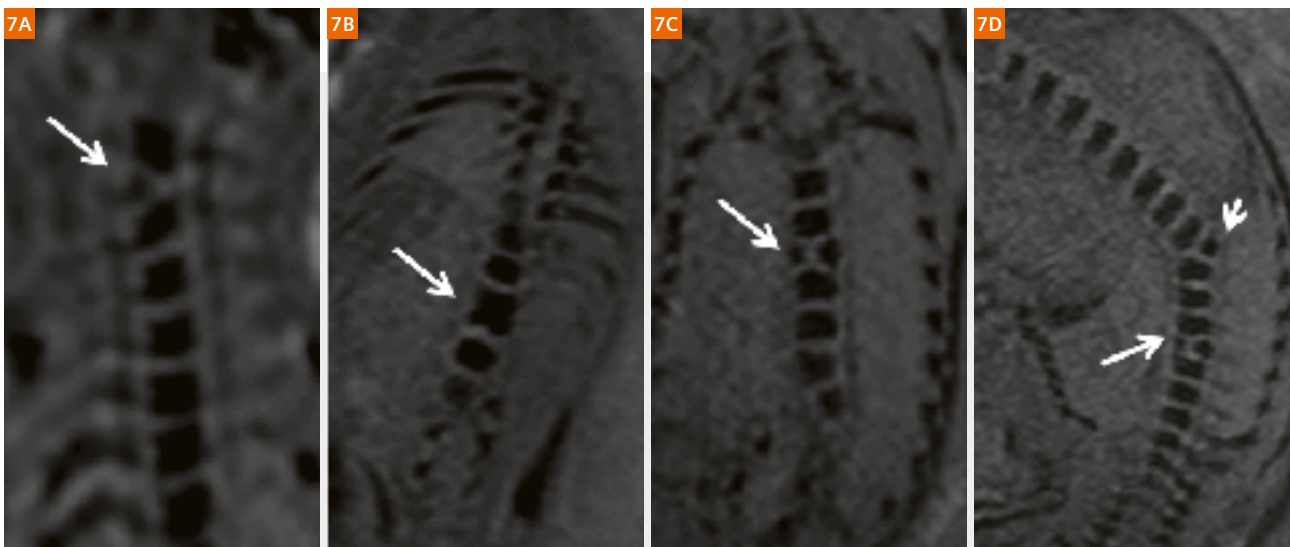

Figure 7:
SWI images at 26 weeks' gestation (7A), 25 weeks (7B), 33 weeks (7C), and 34 weeks with fetal vertebral anomalies. Coronal views of the cervical **(7A)**, lumbar **(7B)**, and thoracic **(7C)** spine show hemivertebrae, block vertebrae, and butterfly vertebrae. Multiple vertebral anomalies with hemivertebrae (short arrows) and butterfly vertebrae (long arrows) are clearly visible in coronal 2D SWI **(7D)**.
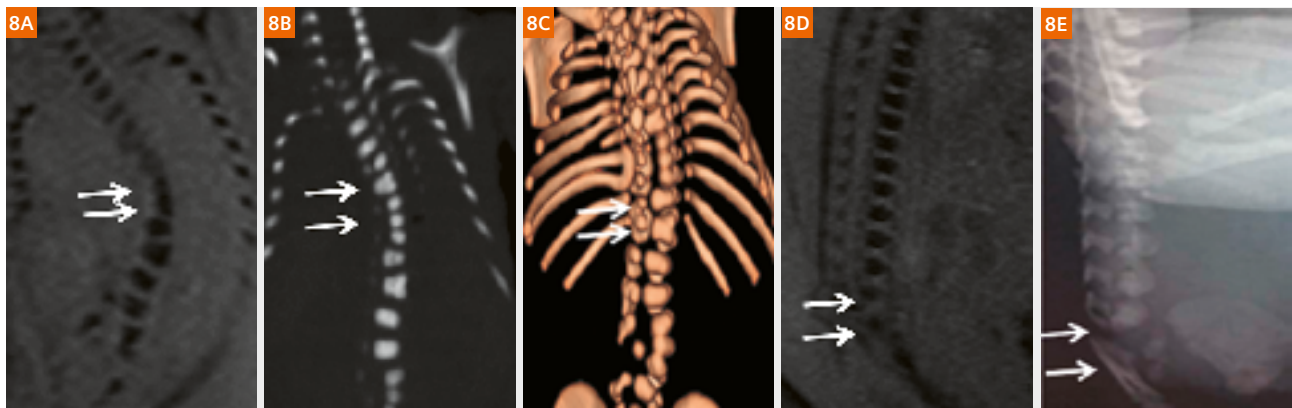
Figure 8:
Images at 24 weeks' gestation (8A–E) with multiple vertebral anomalies (8A–C) and at 32 weeks' gestation (8D–E) with caudal regression syndrome. SWI **(8A)** shows multiple vertebral anomalies (arrows) that were consistent with the postmortem CT (**8B, C**, arrows). SWI shows dysplasia of the sacrococcygeal vertebrae (arrows) that was consistent with the postmortem X-ray (**8E**, arrows).
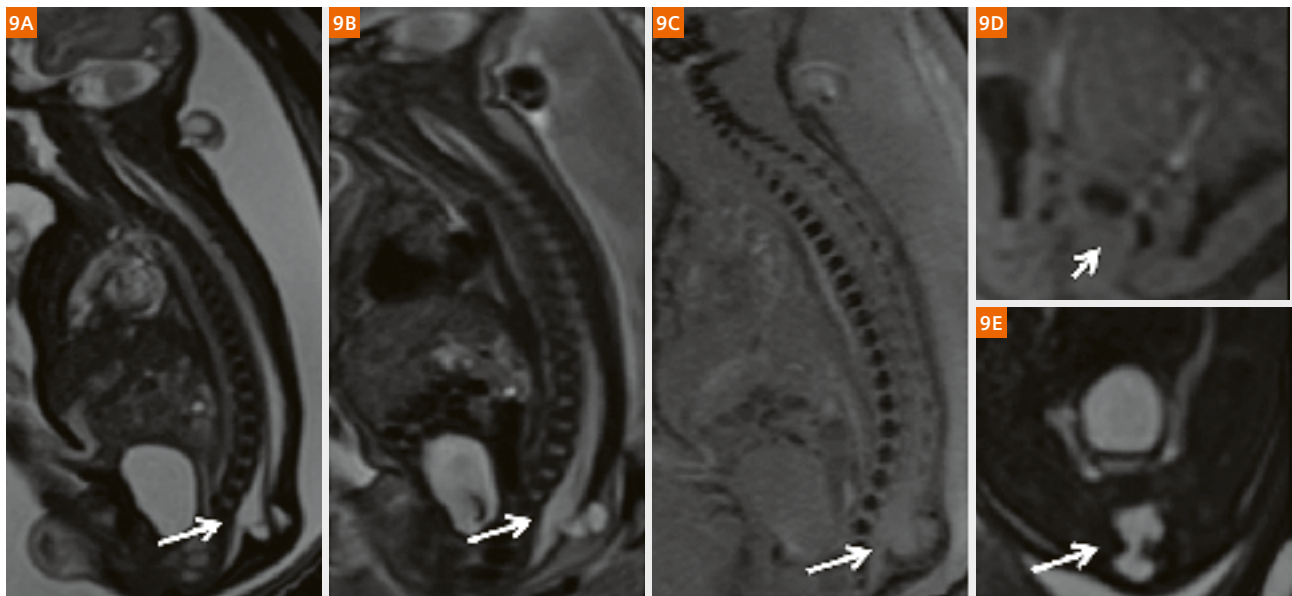

Figure 9:
Images at 32 weeks' gestation with spinal dysraphism (9A–E). Sagittal view of the MR images include HASTE **(9A)**, TrueFISP **(9B, E)**, and SWI **(9C, D)**. The pocket-like processes protruding from the sacrococcygeal spinal canal were all visible, and the spinal cord was found to extend from the spinal canal to the dilated dural capsule (9A, B, E, long arrow), which could not be seen with SWI (9C, D). However, SWI showed excellent osseous spinal structures and demonstrates the pedicular widening (9C, long arrow; 9D, short arrow).

Chest

At present, ultrasound and MRI are the only diagnostic tools that can examine fetal lungs noninvasively. MRI provides additional biochemical and functional information that cannot be obtained by ultrasound as well as detailed structural information. This therefore makes it a valuable diagnostic adjunct for assessing fetal lung development [10]. Congenital chest malformations can range from small and asymptomatic entities to large, space-occupying masses that require immediate surgical treatment. An understanding of fetal chest masses is essential for appropriate monitoring during pregnancy, and for treatment recommendations and delivery management. The most common congenital chest anomalies include congenital cystic adenomatoid malformation (CCAM), congenital diaphragmatic hernia (CDH), bronchopulmonary sequestration (BPS), congenital hydrothorax, and congenital lobar emphysema. Less common entities include congenital high airway obstruction syndrome (CHAOS), congenital bronchogenic cyst, bronchial atresia, pulmonary arteriovenous malformation (PAVM), congenital pulmonary lymphangiectasia, pulmonary hypoplasia-aplasia, mediastinal teratoma, and mediastinal lymphangioma. These pulmonary abnormalities are not mutually exclusive; they frequently occur together as hybrid conditions.

The MRI sequences used to evaluate the fetal chest include HASTE, fast single-shot echo, and TrueFISP. In our unit, HASTE and TrueFISP images are the most useful for evaluating the lung anatomy. The lungs typically contain a significant amount of alveolar fluid, which is homogeneously hyperintense relative to the chest wall muscle on T2-weighted images.

Congenital diaphragmatic hernia and extralobar pulmonary sequestration were demonstrated as follows (Figs. 10, 11).
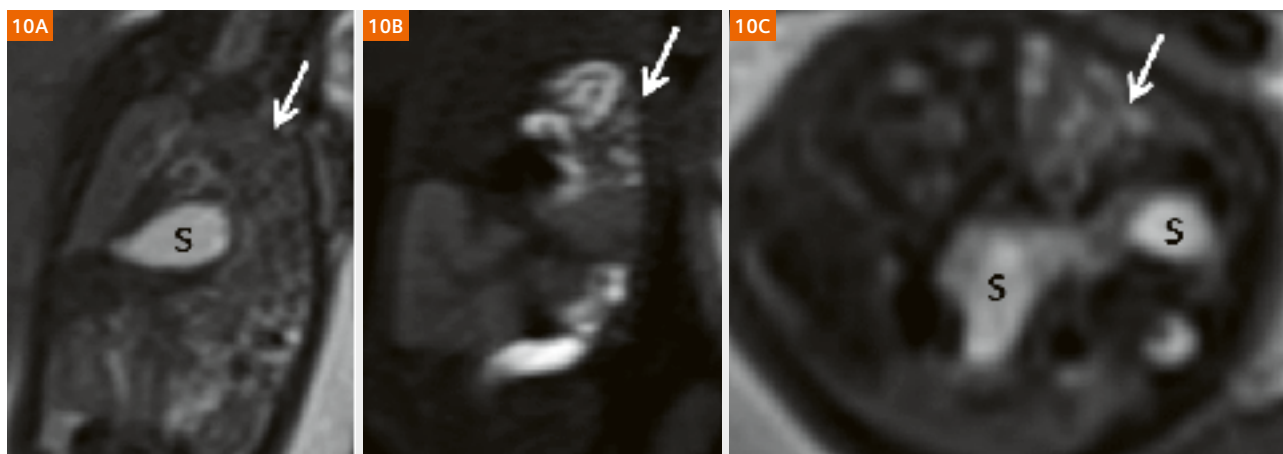
Figure 10: Congenital diaphragmatic hernia at 28 weeks' gestation
Coronal **(10A)** and axial **(10C)** T2 HASTE, and T1w imaging **(10B)** show herniated content (arrow) displacing the heart and compressing the unilateral lung and portions of the bowel (10B, arrow) and stomach (S) occupying the unilateral hemithorax.
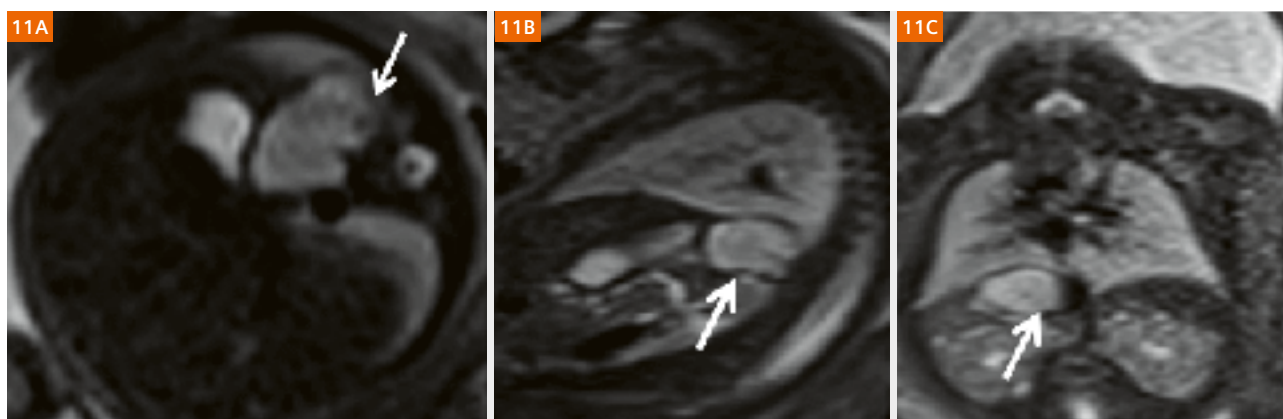
Figure 11: Extralobar pulmonary sequestration at 32 weeks' gestation
Axial **(11A)**, sagittal **(11B)**, and coronal **(11C)** T2 HASTE show a homogeneous, high T2WI signal between the left subphrenic space and left kidney with a clear boundary (arrow). Postnatal CT (not shown) enhancement shows a vascular shadow connected to the aorta.

Abdominal abnormalities and tumors

Fetal abdominal deformities and tumors vary in their location, and can be derived from the gastrointestinal tract, liver, kidney, and retroperitoneum. Congenital tumors are defined as those that are present during the fetal stage or at birth. In some cases, MRI can provide important information and even add important findings to prenatal US for perinatal management by visualizing fetal tumors with common tumor-related complications and other exceptional congenital abnormalities [11]. Common indications for fetal gastrointestinal (GI) MRI include suspected esophageal, small bowel, and large bowel obstruction, bowel malrotation, and bowel perforation resulting in meconium peritonitis or meconium pseudocyst. MRI is also particularly useful

for evaluating rare GI abnormalities, such as megacystis microcolon intestinal hypoperistalsis syndrome (MMIHS), cloacal exstrophy, and cloacal malformation. Although US remains the modality of choice for investigating fetal anomalies, the findings are often nonspecific and may relate to transient normal variants [12]. In addition, urine and fluid in the colon beyond 24 weeks may have a similar sonolucent appearance on US and opposite appearances on MR images, allowing better identification and discrimination. In our department, a T1-weighted breath-hold sequence is completed in the coronal plane and, if necessary, in the sagittal and axial planes.

Different developmental deformities in the abdomen were demonstrated as follows (Figs. 12–16).

Figure 12: Localized intestinal dilatation at 30+4 weeks' gestation, and imperforate anus at 28 weeks' gestation
Coronal T2 HASTE **(12A)** and T1w **(12B)** images show the dilated loops of one part of the gastrointestinal tract. It is markedly hyperintense on T1WI (arrow) and hypointense on T2WI (arrow). Coronal T1WI **(12C, D)** and T2 TrueFISP **(12E)** images show a prominent rectum (arrowhead) with high T1 signal intensity and low T2 signal intensity. The abnormality of the large bowel was identified and diagnosed as rectal atresia during a postnatal physical examination. B = urinary bladder, S = stomach
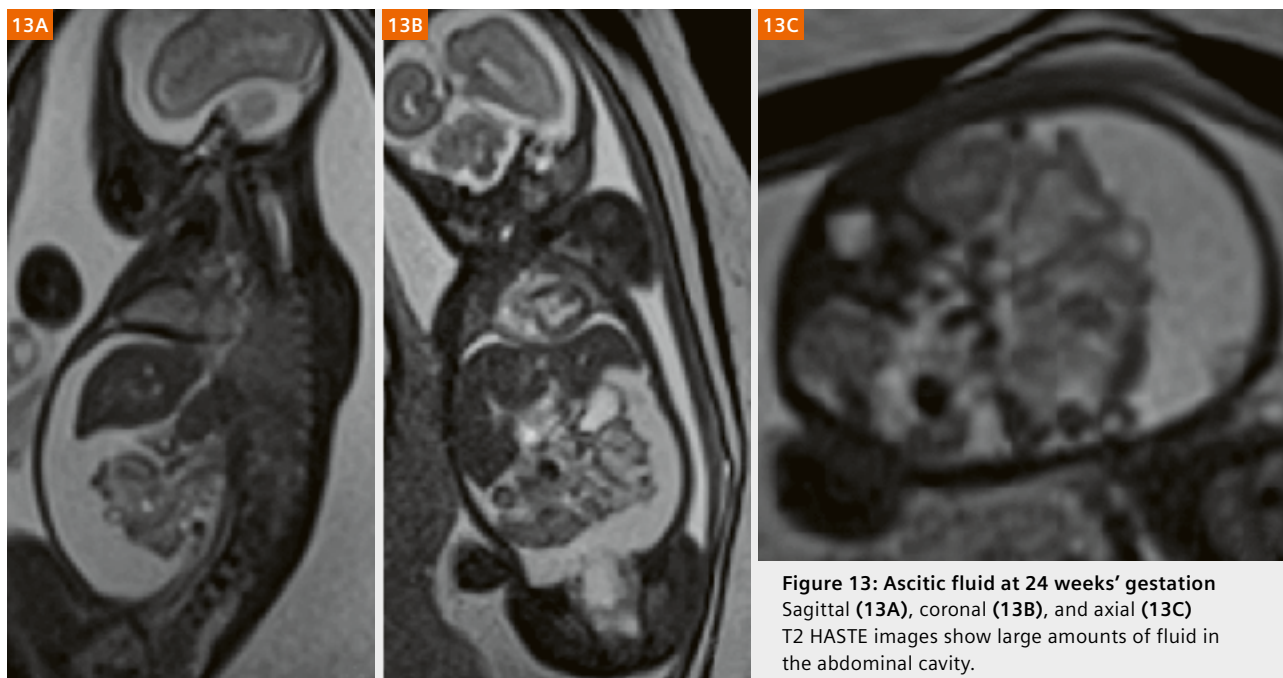

Figure 13: Ascitic fluid at 24 weeks' gestation
Sagittal **(13A)**, coronal **(13B)**, and axial **(13C)** T2 HASTE images show large amounts of fluid in the abdominal cavity.

Figure 14: Neuroblastoma at 28 weeks' gestation
Axial **(14A)**, sagittal **(14B)**, and coronal **(14C)** T2 HASTE images show a solid mass with a clear boundary above a lateral kidney that is hyperintense on a T2-weighted sequence (arrow) and was found to be neuroblastoma after birth.
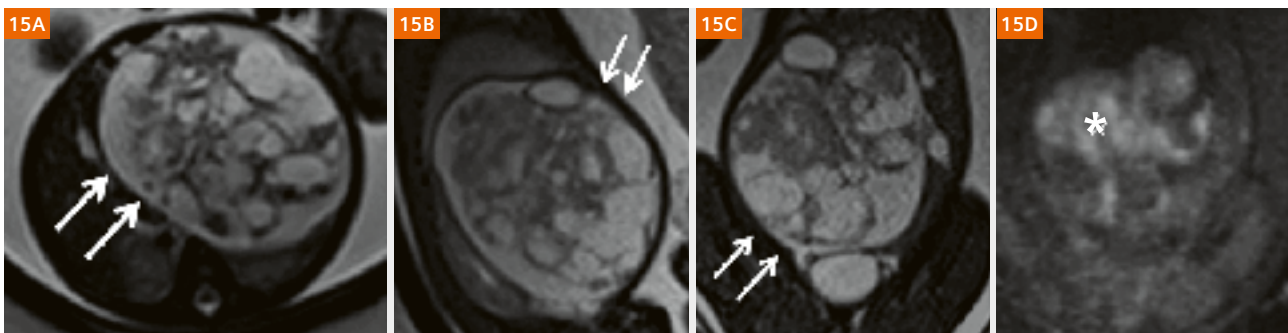

Figure 15: Teratoid tumors at 30 weeks' gestation
Axial T2 HASTE **(15A)**, sagittal **(15B)**, and coronal **(15C)** T2 TrueFISP images show a heterogeneous solid cystic mass with a high-intensity heterogeneous signal (arrows), and surrounding tissue that was markedly squeezed. The giant lesions showed restricted diffusion with DWI **(15D**, star). A histopathological diagnosis of teratoid tumors was made after birth.
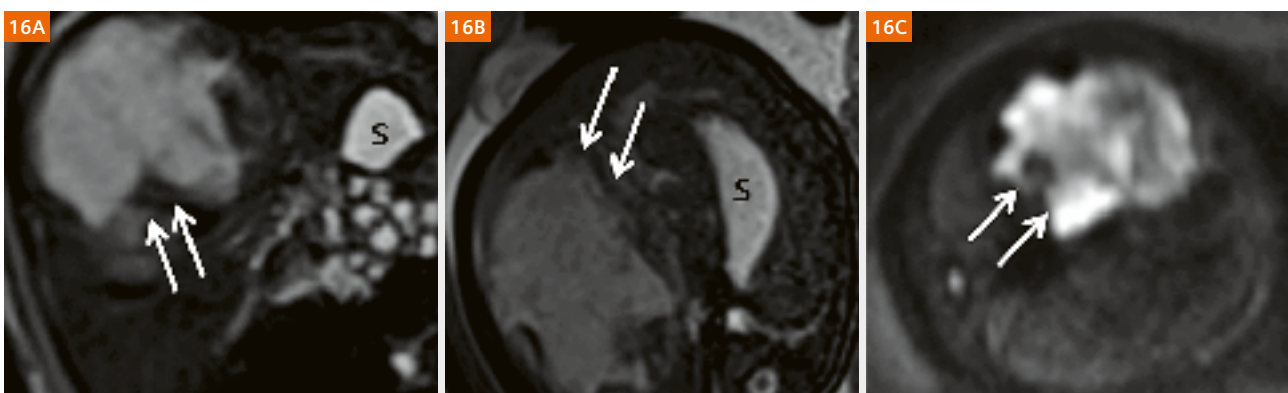

Figure 16: Hepatic hemangioendothelioma at 32 weeks' gestation
Coronal T2 HASTE **(16A)** and axial T2 TrueFISP **(16B)** images show a large heterogeneous and high-signal mass in the liver parenchyma, and highly restricted diffusion with DWI **(16C)**. A histopathological diagnosis of hepatic hemangioendothelioma was made after birth.

Maternal indications for prenatal MRI

In addition to fetal indications, there are several maternal indications for prenatal MR imaging. They include the possibility of uterine rupture, the need to differentiate between placenta accreta and percreta, a large myoma interfering with the pregnancy, and MR pelvimetric measurements. In our unit, the technique of placental MRI and the diagnostic level are increasingly convincing and compelling.

Abnormal invasive placenta (AIP) is a disease with a spectrum of severity characterized by abnormal, firmly adherent placental implantation into the uterus at varying depths. It is typically referred to as placenta accreta, increta, and percreta [13]. When AIP occurs, the placenta may not be completely separated from the uterus at the time of delivery, resulting in potentially life-threatening intrapartum or postpartum massive hemorrhage and associated morbidity such as multisystem organ failure, disseminated intravascular coagulation, and even death. Placenta percreta (PP) is the most dangerous type of AIP. It is characterized by trophoblasts fully penetrating the myometrium and in some cases extending to or breaching the serosa and even invading surrounding structures [14]. An accurate prenatal diagnosis of PP is therefore imperative.

In 2017, our team published an article on placenta accreta [15] that aimed to identify specific MRI features for differentiating PP from placenta accreta (PA), and to characterize the features of invasive placenta previa. Our studies showed a series of MRI features, including myometrial thinning, interrupted myometrium, loss of the placental-myometrial interface, marked placental heterogeneity, dark intraplacental bands, abnormal intraplacental vascularity, abnormal uterine bulge, placental bulge (type I and type II, Fig. 2), uterine serosal hypervascularity, bladder wall nodularity, and extrauterine placental extension. Our results suggest that type II placental bulge and uterine serosal hypervascularity are useful MRI features for differentiating PP from PA. Profoundly abnormal vessels are associated with greater blood loss during caesarean section. Our results could contribute to accurate prenatal diagnosis of PP and help minimize the risk of massive hemorrhage [15].

In our center, all the patients with suspected invasive placenta previa (IPP) were imaged in the supine or left-lateral position with bladders moderately full. T2-weighted HASTE and T2-weighted TrueFISP images were obtained without breath-hold in the axial, coronal, sagittal, and oblique sagittal planes. Additional imaging planes perpendicular to the placenta-uterus interface or uterus-bladder interface were obtained in the region of the suspected AIP.

Several placenta increta and placenta percreta were demonstrated as follows (Figs. 17–20).

Figure 17: Placenta increta (PI) in a 40-year-old woman at 35 weeks' gestation
A sagittal T2 HASTE MR image **(17A)** demonstrates type I placental bulge (white arrows) with an intact uterine outline. A photograph **(17B)** of gross specimens after hysterectomy shows that the placenta has invaded the myometrium (white arrows) with intact uterine serosa, consistent with PI. A photomicrograph **(17C**, magnification x 400, hematoxylin and eosin stain) shows chorionic villi (black arrowheads) implanted in the myometrium (white arrowhead), consistent with PI.
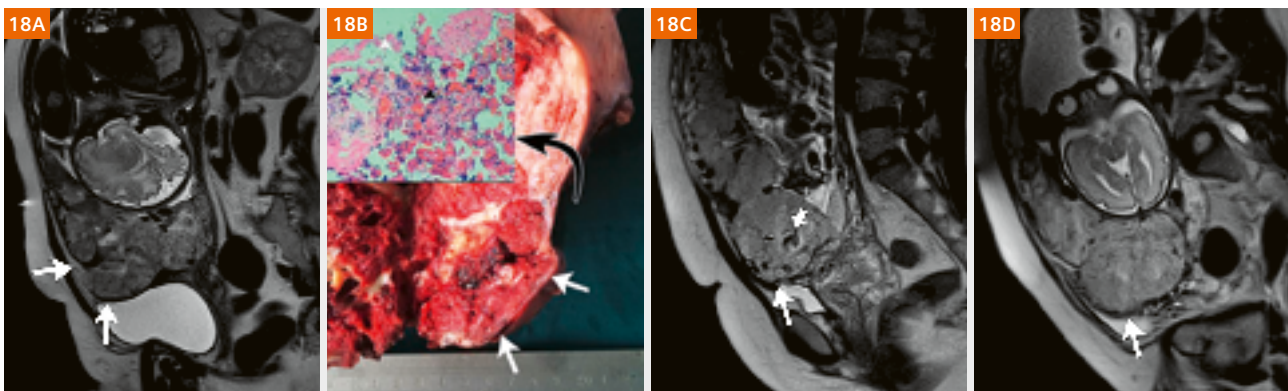
Figure 18: Placenta percreta (PP, 18A, B) in a 39-year-old woman at 30 weeks' gestation
A sagittal T2 HASTE MR image **(18A)** shows type II placental bulge (white arrows) protruding from the uterine outline. A photograph **(18B)** of gross specimens after hysterectomy shows placental invasion (white arrows) through the uterine wall, consistent with PP. A photomicrograph (magnification: x 400, hematoxylin and eosin stain) shows chorionic villi (black arrowhead) penetrating the myometrium (white arrowhead), consistent with PP. Sagittal T2 HASTE MR images show a type IIa placental bulge (long arrow, a focal outward bulge protruding from the uterine outline) with bridging vessels (short arrow) in a 31-year-old woman at 35 weeks' gestation with PP **(18C)** and type IIb placental bulge (long arrow) without bridging vessels in a 29-year-old woman at 32 weeks' gestation with PP **(18D)**.
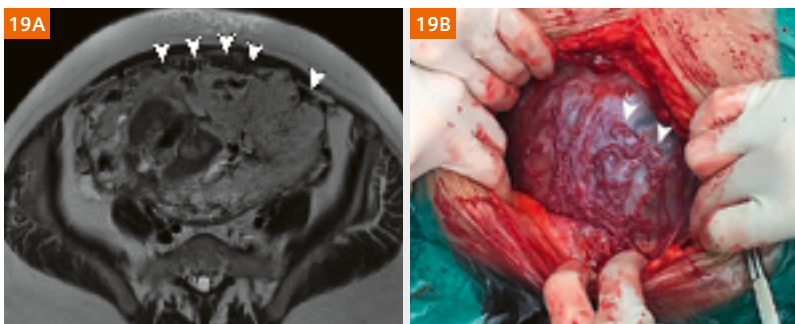

Figure 19: Placenta percreta (PP) in a 35-year-old woman at 29 weeks' gestation
An axial T2 HASTE image **(19A)** shows uterine serosal hypervascularity (arrowheads, tortuous and closely packed vessels along the uterine serosa) in the lower uterine segment.
A photograph **(19B)** taken during cesarean delivery shows the tortuous abnormal vessels in the uterine serosa (arrowheads), consistent with their appearance on MR images.
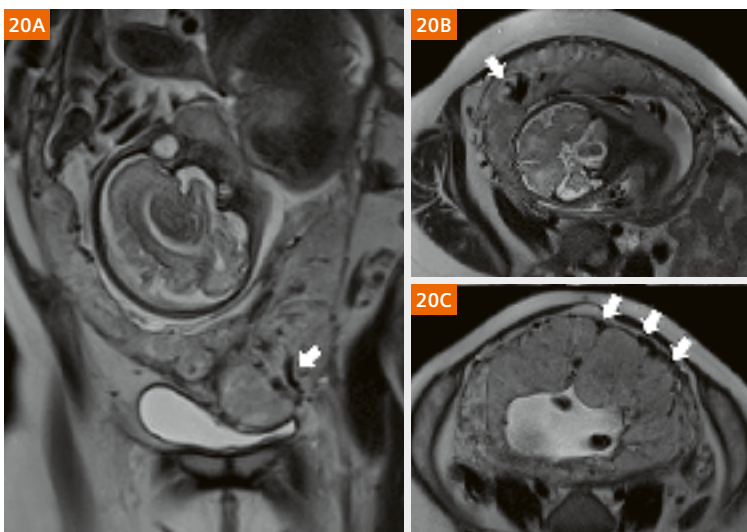

Figure 20:
A coronal T2 HASTE MR image **(20A)** shows bridging vessels (arrow) through the bulging placenta in a 25-year-old woman at 32 weeks' gestation with placenta percreta (PP). An axial T2 HASTE MR image **(20B)** shows abnormal intraplacental vascularity (arrow) in a 28-year-old woman at 30 weeks' gestation with placenta increta (PI). An axial T2 HASTE MR image **(20C)** demonstrates uterine serosal hypervascularity (arrows) in a 34-year-old woman at 35 weeks' gestation with PP.

As outlined in this article, fetal MR imaging is playing an increasingly important role in prenatal diagnostics. Nevertheless, US will and should remain the first choice for prenatal screening due to its low cost, ease of availability, and superb safety profile. Advances in fetal MRI have given clinicians powerful tools to identify fetal pathologies. These can range from small and symptomatic abnormalities to large, space-occupying masses that require immediate surgical treatment. The information obtained with fetal MR imaging can be helpful and allow early planning of prenatal management.

References

1   Weisstanner C, Gruber GM, Brugger PC, et al. Fetal MRI at 3T – ready for routine use? Br J Radiol. 2017; 90(1069):20160362.
2   Prayer D, Brugger PC. Investigation of normal organ development with fetal MRI. Eur Radiol. 2007; 17(10):2458-2471.
3   Haacke EM, Xu Y, Cheng YC, et al. Susceptibility weighted imaging (SWI). Magn Reson Med. 2004; 52(3):612-618.
4   Reichenbach JR, Jonetz-Mentzel L, Fitzek C, et al. High-resolution blood oxygen-level dependent MR venography (HRBV): a new technique. Neuroradiology 2001; 43(5):364-369.
5   Robinson AJ, Blaser S, Vladimirov A, et al. Foetal "black bone" MRI: utility in assessment of the foetal spine. Br J Radiol. 2015; 88(1046):20140496.
6   Smith FW, Adam AH, Phillips WD. NMR imaging in pregnancy. Lancet. 1983; 1(8314-5):61-62.
7   Reichenbach JR, Venkatesan R, Schillinger DJ, et al. Small vessels in the human brain: MR venography with deoxyhemoglobin as an intrinsic contrast agent. Radiology. 1997; 204(1):272-277.
8   Coakley FV, Glenn OA, Qayyum A, et al. Fetal MRI: a developing technique for the developing patient. AJR Am J Roentgenol. 2004; 182(1):243-252.
9   Duczkowska A, Bekiesinska-Figatowska M, Herman-Sucharska I, et al. Magnetic resonance imaging in the evaluation of the fetal spinal canal contents. Brain Dev. 2011; 33(1):10-20.
10 Kasprian G, Balassy C, Brugger PC, et al. MRI of normal and pathological fetal lung development. Eur J Radiol. 2006; 57(2):261-270.
11 Nemec SF, Horcher E, Kasprian G, et al. Tumor disease and associated congenital abnormalities on prenatal MRI. Eur J Radiol. 2012; 81(2):e115-e122.
12 Veyrac C, Couture A, Saguintaah M, et al. MRI of fetal GI tract abnormalities. Abdom Imaging. 2004; 29(4):411-420.
13 Belfort MA. Placenta accreta. Am J Obstet Gynecol. 2010; 203(5):430-439.
14 Silver RM, Barbour KD. Placenta accreta spectrum: accreta, increta, and percreta. Obstet Gynecol Clin North Am. 2015; 42(2):381-402.
15 Chen X, Shan R, Zhao L, et al. Invasive placenta previa: Placental bulge with distorted uterine outline and uterine serosal hypervascularity at 1.5T MRI – useful features for differentiating placenta percreta from placenta accreta. Eur Radiol. 2018; 28(2):708-717.
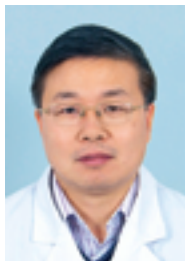
Guangbin Wang   Xianyun Cai

Small Structures Big Challenges: Fetal Cardiac Magnetic Resonance Imaging

Veronica Bianchi[1]; Jérôme Yerly[1,2]; Jerome Chaptinel[1]; Yvan Mivelaz[3]; Milan Prsa[3]; Leonor Alamo[1]; Chantal Rohner[1]; Jean-Baptiste Ledoux[1,2]; Davide Piccini[1,5]; Chris Roy[1]; Matthias Stuber[1,2]

[1] Department of Radiology, University Hospital (CHUV) and University of Lausanne (UNIL), Lausanne, Switzerland
[2] Center for Biomedical Imaging (CIBM), Lausanne, Switzerland
[3] Department of Pediatrics, University Hospital (CHUV) and University of Lausanne (UNIL), Lausanne, Switzerland
[4] Department of Gynecology-Obstetrics, University Hospital (CHUV) and University of Lausanne (UNIL), Lausanne, Switzerland
[5] Advanced Clinical Imaging Technology, Siemens Healthineers, Lausanne, Switzerland

Introduction

Congenital heart disease (CHD) is the most common birth defect affecting nearly 1% of pregnancies in Europe [1, 2]. Gestational screening has greatly improved antenatal diagnosis of heart malformations and several prenatal interventions now exist to treat CHD in utero, or soon after birth. The timing and type of treatment relies heavily on the ability to accurately visualize a given cardiac malformation. Echocardiography is the gold standard for fetal cardiac imaging [3]. This imaging technique is safe and non-invasive but, despite the progress made in the field of fetal ultrasonography, its quality varies in the presence of maternal obesity, oligohydramnios, multiple gestations, or imaging during late gestation, among other conditions [4]. Since its early applications [5], cardiac magnetic resonance imaging (MRI) has been increasingly investigated for fetal[1] heart imaging in the last decade and has now become an active area of research. A growing number of studies are exploring its applicability in the evaluation of cardiac morphology and function for both normal and abnormal hearts [6–13]. Despite encouraging advances, there remain significant challenges for fetal cardiac MRI, including the small size and the high rate of the fetal heart, the absence of a conventional fetal cardiac gating signal, and the numerous sources of motion artifacts, such as gross fetal movement, and maternal respiration [4]. However, if these challenges can be addressed, it has been shown that MRI has the potential to provide complementary information to echocardiography, improve our ability to monitor CHD diagnosed *in* utero, and better help guide treatments and decision making.

The aim of this project was to develop an MR image acquisition and reconstruction framework that can overcome the aforementioned challenges and visualize the fetal heart with high spatial and temporal resolution [8]. In this article, we describe such an approach, which combines maternal breath-hold, compressed sensing, and self-gating to produce high quality CINE images of the fetal heart. In addition, here we show preliminary results using our reconstruction framework to produce high quality CINE images of the fetal heart. For comparison, we include ultrasound images in the same orientation of those acquired with MR.

Image reconstruction framework

Our reconstruction framework for golden angle radial acquisitions is composed of three main steps. First, intermediate low-resolution images are reconstructed using compressed sensing. Second, an ECG-like self-gating signal is extracted from the intermediate images. Third, the acquired data are reordered into the identified cardiac phases (Fig. 1) [8].

Initially, low spatial and temporal resolution images are reconstructed with a sliding window approach using 15 radial readouts per window and 70% view-sharing, leading to a temporal resolution of 18.5 ms (Fig. 1B). Subsequently, the obtained images are analyzed off-line with a custom-built semi-automatic tool in MATLAB[2] (MathWorks, Natick, MA, USA). The gating signal that reproduces the contraction cycles of the fetal heart is computed by cross-correlating each intermediate frame to a diastolic and a systolic reference image, focusing on a region of interest circumscribed around the fetal heart (Fig. 1C). Finally, and owing to the characteristics that the golden angle acquisition scheme is providing us with,

---

[1] *Siemens Healthineers disclaimer does not represent the opinion of the authors: MR scanning has not been established as safe for imaging fetuses and infants less than two years of age. The responsible physician must evaluate the benefits of the MR examination compared to those of other imaging procedures.*

[2] *The information shown herein refers to products of 3rd party manufacturers and thus are in their regulatory responsibility. Please contact the 3rd party manufacturer for further information.*

the radial readouts are retrospectively binned into different cardiac phases (Fig. 1D) with a bin width of 25 ms and a view-sharing equal to 50%, improving the temporal resolution to 12.5 ms. Both intermediate and retro-gated images are reconstructed using an in-house script implementing a *k-t* sparse SENSE algorithm model [14].

Image acquisition and analysis

To validate the proposed framework, six pregnant patients (gestational age 29.7 ± 2.1 weeks at the time of the MRI exam) with a suspicion of fetal non-cardiac pathology were recruited to undergo both MRI and fetal echocardiography. Written informed consent, according

to the recommendations of the local ethics committee, was obtained from all subjects prior to examination.

MR acquisition was performed on a 1.5T clinical MR scanner (MAGNETOM Aera, Siemens Healthcare, Erlangen, Germany) with a 32-channel spine coil and an 18-channel body array coil for signal measurement. Data were collected under maternal breath-hold with a prototype radial golden angle bSSFP sequence (Fig. 1A) and acquisition parameters are summarized in Table 1 [8]. For each patient, three standard views (four-chamber, three-vessel and short-axis view), that are routinely targeted in the clinical fetal echocardiographic examination, were acquired (Fig. 2) in 20.1 s each. Echocardiographic images were acquired on a Voluson E8 Expert or Voluson E10 (GE Healthcare, Waukesha, WI, USA)
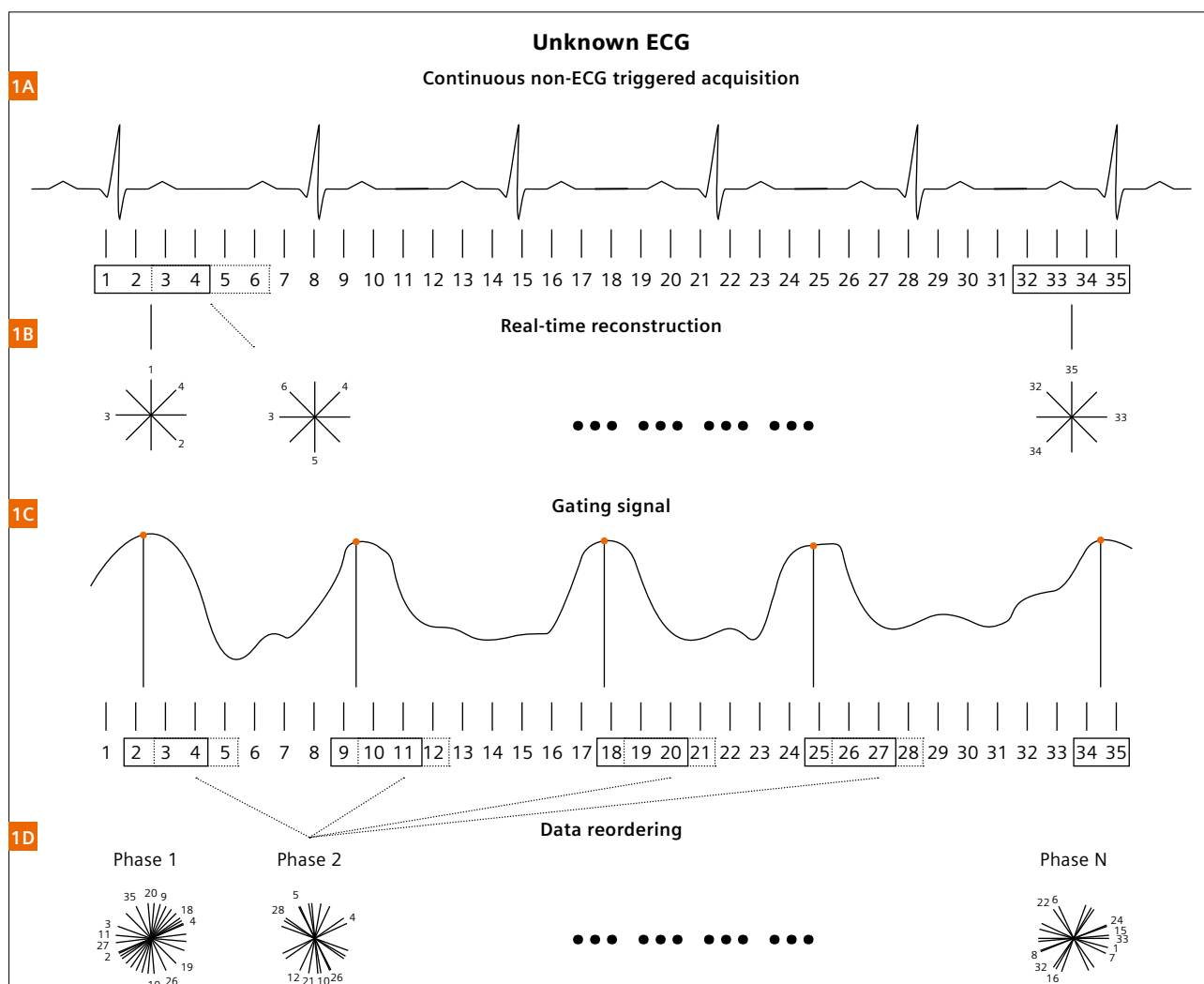

Figure 1:
Schematic overview of the MRI acquisition and reconstruction framework. The data, acquired with a golden angle continuous acquisition technique **(1A)**, were reconstructed applying a sliding window binning **(1B)** and intermediate images were obtained. The low-resolution images were subsequently analyzed to extract an ECG-like gating signal that represents the contraction cycles of the fetal heart **(1C)**. The self-gating signal was then used to retrospectively bin the radial data in different cardiac phases during which they were acquired **(1D)**. *(Figure adapted from Chaptinel et al. [8], with permission according to https://creativecommons.org/licenses/by/4.0/).*

Parameter	Value
Field-of-view	260 x 260 mm^2
Base resolution	256 x 256 pixels
Pixel size	1.0 x 1.0 mm^2
Slice thickness	4.0 mm
TE/TR	1.99/4.1 ms
RF excitation angle	70°
Slices	3
Shot per slice	1
Radial readouts per slice	1600
Acquisition time per slice	6.7 s
Bandwidth	1028 Hz/pixel
Reconstructed temporal resolution	12.5 ms (shared phases)

Table 1: Values of the MR acquisition parameters.

with the RM6C 3D/4D curved array transducer with a frequency comprised in the range 1.0–7.0 MHz. Finally, MR and echocardiographic images were qualitatively and quantitatively compared to demonstrate the capability of both imaging techniques to visualize and measure heart structures. Two experienced pediatric cardiologists visually evaluated the quality of the images obtained with both modalities. Subsequently, they measured the diameter of aorta, main pulmonary artery, mitral valve annulus and tricuspid valve annulus using ClearCanvas (Synaptive Medical, Toronto, Canada) on both MR and echocardiographic images for each patient.

Results and discussion

MR images were successfully acquired on all patients. Figure 3 shows an example of fetal heart images in a 4-chamber (Fig. 3A), a short-axis (Fig. 3B) and a three vessel view (Fig. 3C) acquired in a 31-week-old fetus. MR images (columns on the left) are visually compared to the images obtained with the gold standard, echocar-
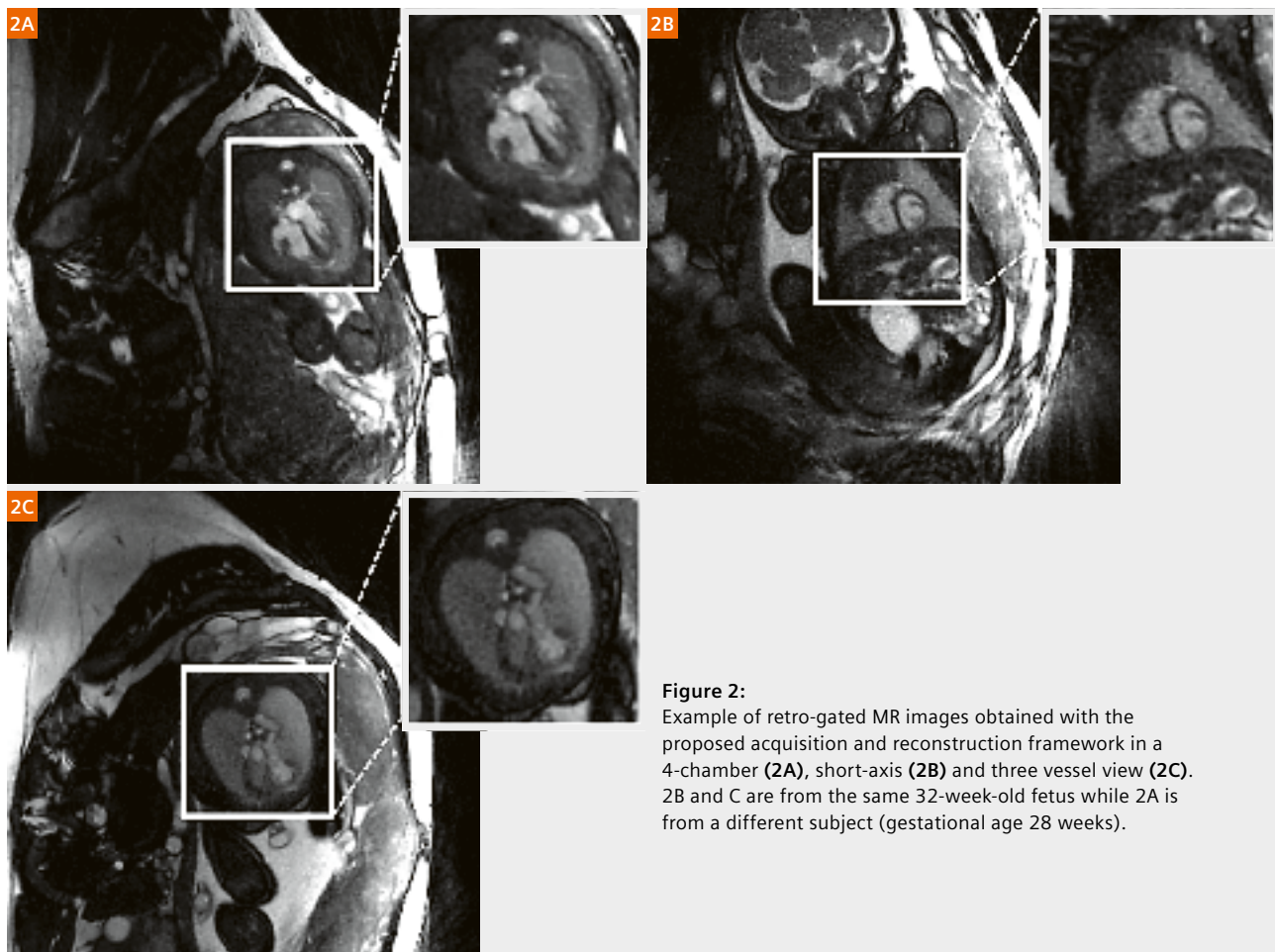
Figure 2:
Example of retro-gated MR images obtained with the proposed acquisition and reconstruction framework in a 4-chamber **(2A)**, short-axis **(2B)** and three vessel view **(2C)**. 2B and C are from the same 32-week-old fetus while 2A is from a different subject (gestational age 28 weeks).

diography (column on the right). The two imaging techniques proved to be comparable in terms of qualitative visualization of cardiac structures. The overall MR image quality was considered satisfying to perform quantitative measurements for all patients except for one in which the mitral valve and the tricuspid valve were not clearly recognizable. Moreover, one patient was excluded from the quantitative comparison because the echocardiographic images were not compatible with the software used for the analysis. Therefore, the diameter of aorta and main pulmonary artery were measured in five patients, while instead mitral valve annulus and tricuspid valve annulus were measured on the images of four patients. As shown in Figure 4, the quantitative measurements performed on the MR images are in good agreement with the measurements by
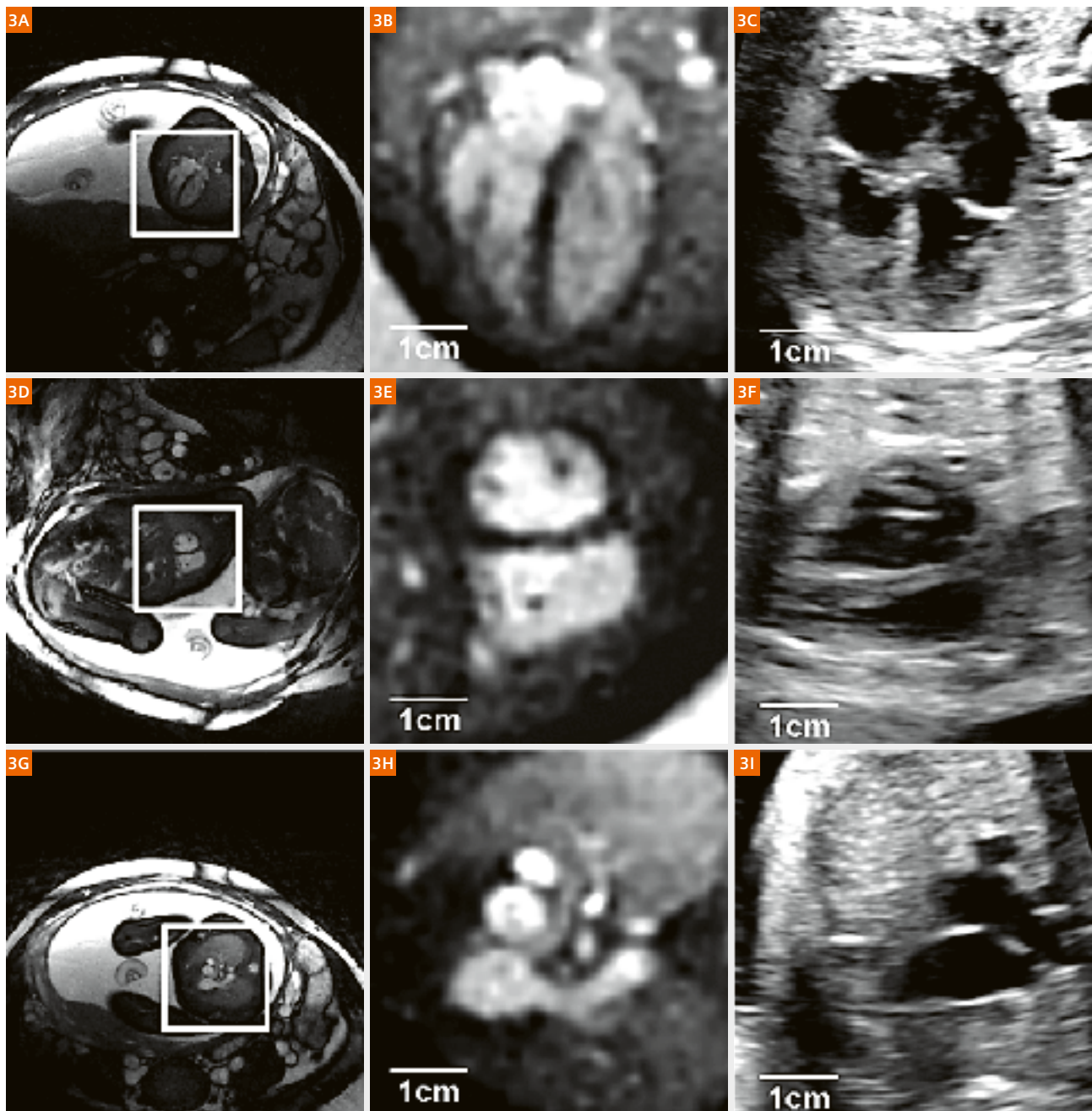

Figure 3:
Comparison between MR and echo images in 4-chamber **(3A–C)**, short-axis **(3D–F)** and three vessel view **(3G–I)** from one of the patient.
(Figure adapted from Chaptinel et al. [8] with permission according to https://creativecommons.org/licenses/by/4.0/).

echocardiography. This study demonstrated that MRI is a promising technique for acquiring high spatial and high temporal resolution images of the fetal heart, and that it is critically enabled by advanced acquisition and reconstruction schemes that have recently been developed. These include golden angle acquisition, self-gating that obviates the need for an ECG, and compressed sensing reconstruction. Preliminary results show the potential of our acquisition and reconstruction framework for the

visualization and measurement of normal fetal cardiac structures. MRI could offer a reliable easily repeatable and safe complementary imaging modality for patients in whom echocardiography is inconclusive. Further study is now required to assess the diagnostic capability of fetal cardiac MRI in the presence of cardiac abnormalities.

Figure 4:
Comparison between quantitative measurements performed on MR and echocardiographic images of normal fetal hearts. The graph shows the average values of the measurements performed by two pediatric cardiologists on the best-quality image for each methodology. The diameter of aorta and main pulmonary artery were measured on five fetal patients, while the mitral valve annulus and the tricuspid valve annulus were quantified for four fetal patients.

References:

1 Dolk H, Loane M, Garne E, for the European Surveillance of Congenital Anomalies (EUROCAT) Working Group. Congenital heart defects in Europe: prevalence and perinatal mortality, 2000 to 2005. Circulation 2011; 123:841–9.

2 EUROCAT Access Prevalence Tables. Available at: http://www.eurocatnetwork.eu/ACCESSPREVALENCEDATA/PrevalenceTables. Accessed September 11, 2018.

3 Donofrio MT, Moon-Grady AJ, Hornberger LK, et al. Diagnosis and treatment of fetal cardiac disease: A scientific statement from the american heart association. Circulation 2014; 129:2183–2242. doi: 10.1161/01.cir.0000437597.44550.5d.

4 Wielandner A, Mlczoch E, Prayer D, Berger-Kulemann V. Potential of magnetic resonance for imaging the fetal heart. Seminars in fetal & neonatal medicine 2013; 18(5):286-297.

5 Meyer-Wittkopf M, Cook A, McLennan A, Summers P, Sharland GK, Maxwell DJ. Evaluation of three-dimensional ultrasonography and magnetic resonance imaging in assessment of congenital heart anomalies in fetal cardiac specimens. Ultrasound Obstet Gynecol 1996; 8(5):303–8. doi: 10.1046/j.1469-0705.1996.08050303.x.

6 Votino C, Jani J, Damry N, Dessy H, Kang X, Cos T, Divano L, Foulon W, De Mey J, Cannie M. Magnetic resonance imaging in the normal fetal heart and in congenital heart disease. Ultrasound Obstet Gynecol 2012; 39(3):322-329. doi: 10.1002/uog.10061.

7 Manganaro L, Savelli S, Di Maurizio M, et al. Assessment of congenital heart disease (CHD): Is there a role for fetal magnetic resonance imaging (MRI)? Eur J Radiol 2009; 72:172-180. doi: 10.1016/j.ejrad.2008.06.016.

8 Chaptinel J, Yerly J, Mivelaz Y, Prsa M, Alamo L, Vial Y, Berchier G, Rohner C, Gudinchet F Stuber M. Fetal cardiac cine magnetic resonance imaging in utero. Sci Rep 2017; 7(1):15540. doi: 10.1038/s41598-017-15701-1.

9 Gorincour G, Bourliere-Najean B, Bonello B, Fraisse A, Philip N, Potier A, Kreitmann B, Petit P. Feasibility of fetal cardiac magnetic resonance imaging: preliminary experience. Ultrasound Obstet Gynecol 2007; 29:105-108. doi: 10.1002/uog.3924.

10 Tsuritani M, Morita Y, Miyoshi T, Kurosaki K, Yoshimatsu J. Fetal Cardiac Functional Assessment by Fetal Heart Magnetic Resonance Imaging. J Comput Assist Tomogr 2018; 00:00–00. doi: 10.1097/RCT.0000000000000781.

11 Roy CW, Seed M, Kingdom JC, Macgowan CK. Motion compensated cine CMR of the fetal heart using radial undersampling and compressed sensing. J Cardiovasc Magn Reson 2017;19:1–14. doi: 10.1186/s12968-017-0346-6.

12 Amerom JFP, Lloyd DFA, Murgasova K, et al. King's Research Portal Fetal Cardiac Cine Imaging Using Highly Accelerated Dynamic MRI with Retrospective Motion Correction and Outlier Rejection. doi: 10.1002/mrm.26686.

13 Haris K, Hedström E, Bidhult S, et al. Self-gated fetal cardiac MRI with tiny golden angle iGRASP: A feasibility study. J Magn Reson Imaging 2017 doi: 10.1002/jmri.25599.

14 Yerly J, Ginami G, Nordio G, Coristine AJ, Coppo S, Monney P, Stuber M. Coronary endothelial function assessment using self-gated cardiac cine MRI and k-t sparse SENSE. Magn Reson Med 2016; 76:1443–1454. doi: 10.1002/mrm.26050.
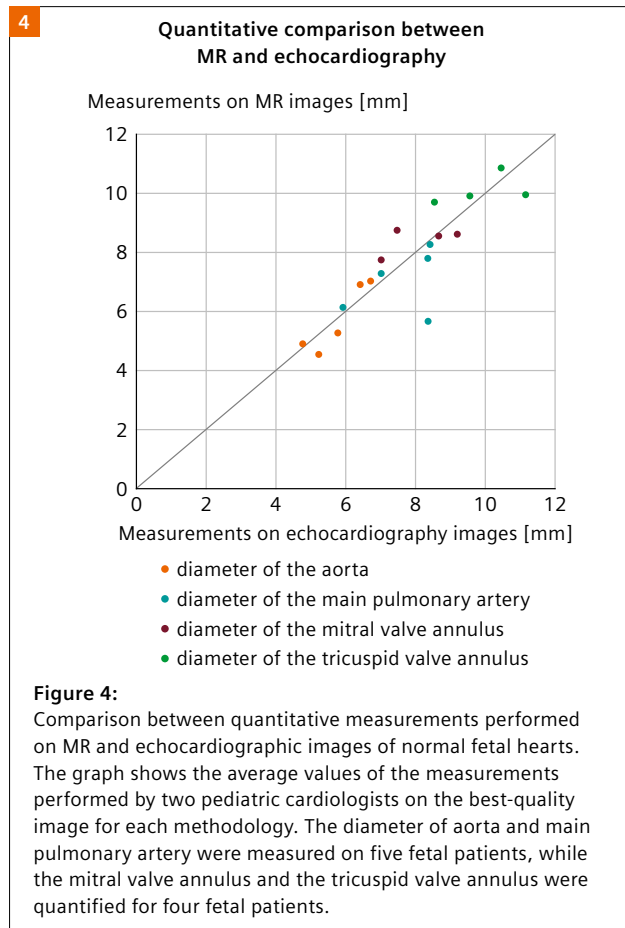
Three Years of PI-RADS v2: Achievements, Open Questions and Future Perspectives

Bernd Hamm, M.D.

Department of Radiology, Charité University Hospital, Humboldt-Universität zu Berlin and
Freie Universität Berlin, Germany

The Prostate Imaging-Reporting and Data System version 2 (PI-RADS v2) was designed to set requirements for multiparametric MR (mpMRI) imaging of the prostate, to optimize image quality and standardize prostate MRI reporting and to reduce variability in image interpretation by proposing assessment categories for detection or exclusion of clinically significant cancer of the prostate. Three years after the introduction of PI-RADS v2, Anwar Padhani and other members of the PI-RADS committee summarize the current state of research and clinical experience with PI-RADS v2, name the strengths and weaknesses and propose directions for future research and improvements of the standard to contribute to value-based health care [1].

Summary

The range of genomic diversity and prognosis of prostate cancer (PCa), the variable prevalence in different populations as well as known limitations of established diagnostic tools, e.g., non-cancer-specific reasons for increased prostate-specific antigen (PSA) levels, and the semi-randomness of transrectal ultrasound (TRUS) biopsies lead to major challenges in the diagnostic management of these patients:

1. Men without clinically significant prostate cancer but elevated PSA levels undergo unnecessary biopsies with attendant morbidity [2].
2. Men with indolent (non-significant) cancers are diagnosed with the disease and undergo therapies which are not positively affecting their overall survival but instead may have severe side effects that significantly impact their quality of life [3].
3. Men having clinically significant cancer are underdiagnosed or the disease may even remain undiagnosed, resulting in suboptimal treatment decisions due to poor tissue sampling.

While there are several diagnostic options besides imaging, including molecular diagnostics, that allow more accurate PCa diagnosis, prostate mpMRI plays an increasingly important role in ruling out or detecting clinically significant cancer in men with elevated PSA levels.

The promotion of PI-RADS v2 as a global standard reduces variation in the acquisition, interpretation and reporting of prostate mpMRI exams and has thus made an important contribution to overcoming the limitations associated with highly variable imaging protocols (and quality of studies), high intra-reader variability and in particular the difficulties in communicating findings to referring urologists. Today, PI-RADS v2 has developed into the universal standard for prostate mpMRI interpretation and reporting, significantly improving communication among radiologists and urologists.

Multiple patient- and lesion-level analyses have shown that PI-RADS v2 assessment categories are effective and improve sensitivity for detection of clinically significant prostate cancer compared to PI-RADS v1. On the lesion level, however, studies indicate that non-index lesions tend to be overlooked (e.g., low-grade and very small prostate cancers). Furthermore, there

is a large body of evidence that both PI-RADS v2 and non-PI-RADS standardized scoring systems (Likert) have a very high "rule out" performance for clinically significant PCa. This has important implications for men with negative MRI findings and may help to significantly reduce the number of patients undergoing random biopsy of the prostate. Two recent prospective studies with excellent study designs – the PROMIS (2017, published in Lancet) and the PRECISION study (2018, published in NEJM) – have shown that mpMRI detects more significant prostate cancers and fewer non-significant cancers compared with random TRUS biopsy [4, 5]. These results will lead to the wider use of mpMRI prior to the first transrectal prostate biopsy in the mid-term.

Beyond summarizing recent studies and developments, the authors also point out limitations of PI-RADS v2, such as the still high intra-reader variability, vaguely defined assessment categories for the transition zone, and the unclear role of dynamic contrast-enhanced (DCE) MRI. While the authors announce some improvements in this regard with the pending update of PI-RADS (version 2.1), general questions and challenges remain and require further investigation.

Accordingly, there is a call to action to address the lack of quantitative metrics in the assessment of diffusion-weighted imaging (DWI) and DCE MRI, to improve the performance of MRI in the transition zone and to work on an expansion of PI-RADS, i.e., for Active Surveillance and recurrent cancer.

Conclusion

PI-RADS v2 was designed to assist in the selection of patients who should undergo prostate biopsy and to establish standards for imaging. It has been shown that the test performance of PI-RADS v2 in research and clinical practice is improved, retaining higher accuracy over systematic TRUS biopsies for PCa diagnosis. Another advantage of PI-RADS is that it markedly improves communication and understanding among radiologists and urologists. Diagnostic strategies that include imaging detect more clinically significant prostate cancers and less low-risk disease. PI-RADS has facilitated the standardization of mpMRI acquisition, interpretation and reporting but open questions and tasks remain.
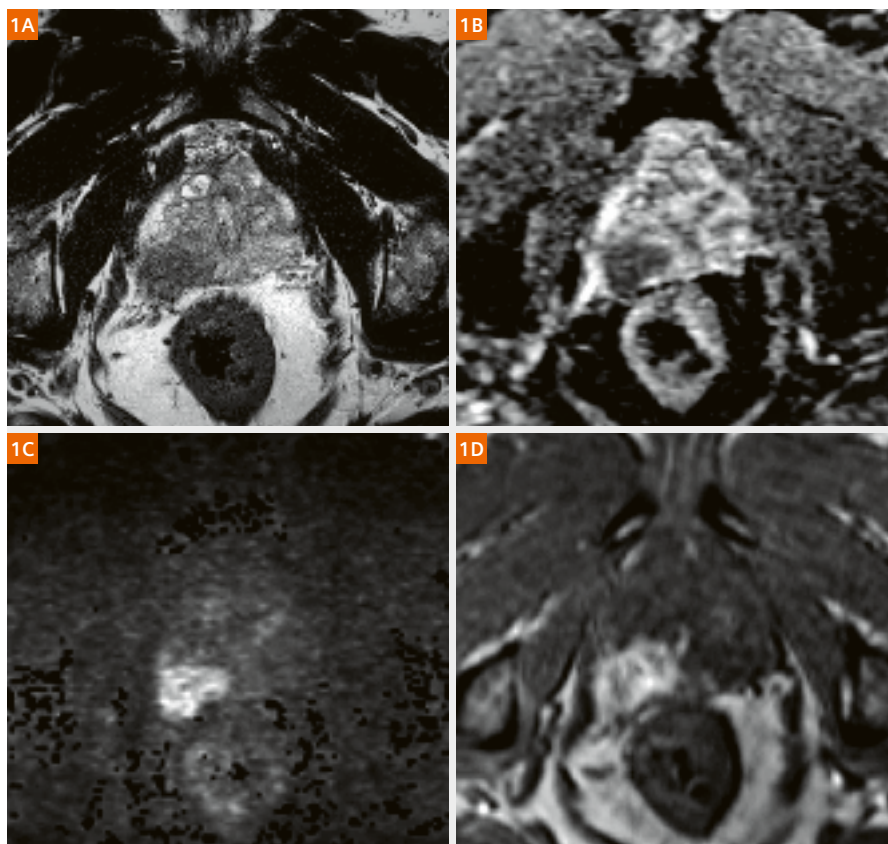
Figure 1:
63-year-old patient with a PSA increase from 5.6 ng/ml to 11.8 ng/ml over a 6-month period. Multiparametric MRI at 3 Tesla (MAGNETOM Skyra). Transverse T2-weighted TSE sequence **(1A)**, diffusion-weighted EPI sequence (ADC map) **(1B)** and calculated b-value of 1400 mm/s^2 **(1C)**, and dynamic contrast-enhanced sequence (TWIST) **(1D)**.

Focal lesion in the posterolateral peripheral zone on the right-hand side with extraprostatic extension and invasion of the neurovascular bundle (1A); there is corresponding marked diffusion restriction (1B, C) and focal early enhancement following contrast agent administration (1D); PI-RADS 5 (histology: Gleason 4+4=8).

Personal comment

Multiparametric prostate MRI is one of the biggest success stories of radiology in the last decade. While we started using MRI as a problem-solving tool in patients with multiple negative biopsies and to assess whether or not patients had extracapsular extension (with suboptimal results), prostate MRI is clinically used in a much broader scope now. It is no longer questioned whether mpMRI can detect and localize clinically significant PCa and it has been shown that negative MRI findings (in case of high-quality examinations!) allow to safely avoid biopsies and further follow-ups in a significant number of patients. Urologists appreciate the clarity of a PI-RADS report with a standardized prostate pictogram, clearly indicating where to target a biopsy.

On the other hand, however, PI-RADS v2 is reducing our flexibility in imaging interpretation as expert readers, and the recommendations remain vague, for example, with regard to apparent diffusion coefficient (ADC) cutoff values or the assessment of the transition zone. Practical aspects in clinical management of patients such as: "What do we do about mpMRI-negative patients?", "Who should follow up PI-RADS 1-2 patients not undergoing biopsy – what should be the regimen for follow-up?", and "How should we deal with PI-RADS 3 patients?" remain unanswered so far and have to be addressed individually. Hopefully, these issues will be solved in one of the future PI-RADS versions. Therefore, the scientific community is called to action and to address these issues in future studies. Researchers around the globe can contribute and influence the development of future versions of PI-RADS into an even more refined tool in diagnosing and managing prostate cancer.

References

1 Padhani AR, Weinreb J, Barentsz J, et al. Prostate Imaging-Reporting and Data System Steering Committee: PI-RADS v2 Status Update and Future Directions. EUR Urology 2018, https://doi.org/10.1016/j.eururo.2018.05.035.

2 Loeb S, Vellekoop A, Ahmed HU, Catto J, Emberton M, Nam R, et al. Systematic review of complications of prostate biopsy. Eur Urol 2013;64:876–92. doi:10.1016/j.eururo.2013.05.049.

3 Ilic D, Neuberger MM, Djulbegovic M, Dahm P. Screening for prostate cancer. In: Ilic D, editor. Cochrane Database Syst. Rev., Chichester, UK: John Wiley & Sons, Ltd; 2013, p. 78. doi:10.1002/14651858.CD004720.pub3.

4 Ahmed HU, El-Shater Boaily A, Brown LC et al., the PROMIS study group. Diagnostic accuracy of multi-parametric MRI and TRUS biopsy in prostate cancer (PROMIS): a paired validating confirmatory study. Lancet. 2017. doi.org/10.1016/S0140-6736(16)32401-1.

5 Kasivisvanathan V, Rannikko AS, Borghi M, et al. MRI-targeted or standard biopsy for prostate-cancer diagnosis. N Engl J Med 2018;378:1767–77. doi: 10.1056/NEJMoa1801993.

PI-RADS 2 Standardized Prostate MRI Reporting
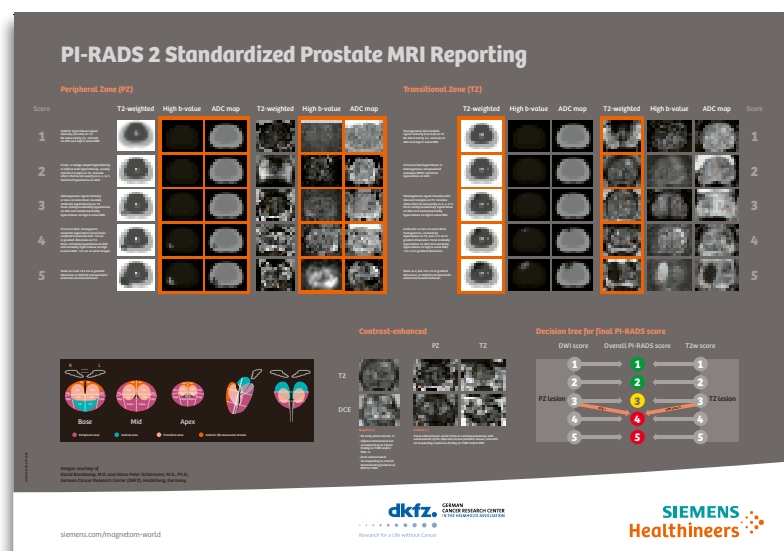
MAGNETOM Altea at 1.5T and MAGNETOM Lumina[1] at 3T are the new 70 cm Open Bore systems that provide full confidence to deliver the productivity, reproducibility, and patient satisfaction that is demanded in the clinical key areas. Powered by our premium MR technology, MAGNETOM Altea and MAGNETOM Lumina combine our unique BioMatrix technology with the new *syngo* MR XA software platform to fundamentally transform care delivery for the better.

Both systems are designed with productivity written in their DNA. At the core of MAGNETOM Altea's and MAGNETOM Lumina's impressive acquisition speed lies our exclusive Turbo Suite. This package includes trend-setting applications for highly accelerated imaging such as Simultaneous Multi-Slice and CAIPIRINHA SPACE. In order to further reduce the overall patient time slot, MAGNETOM Altea and MAGNETOM Lumina[1] include our proven GO Technologies, support by artificial intelligence (AI), and our innovative BioMatrix Sensors for completely automated respiratory triggering.

MAGNETOM Altea and MAGNETOM Lumina also support superior standards for consistent diagnostic results across institutions. With our 9 unique Dot engines, more than 90% of scan protocols are highly automated and standardized. A great example is the new Whole Body Dot Engine that allows consistent and reproducible response assessment in oncology. In addition, the innovative BioMatrix Tuners deliver excellent homogeneity and fat saturation for every patient, every time. As part of the BioMatrix Tuners, CoilShim has integrated shimming elements in the Head/Neck coil to improve B_0 homogeneity, enabling excellent results in the c-spine for all patients.

Designed with the holistic MR experience in mind, MAGNETOM Altea and MAGNETOM Lumina put patients at greater ease. Thanks to Innovision™ – the entertainment solution designed to revolutionize the in-bore experience – patient anxiety is replaced with confidence and comfort. And with our unique patient-centered coil
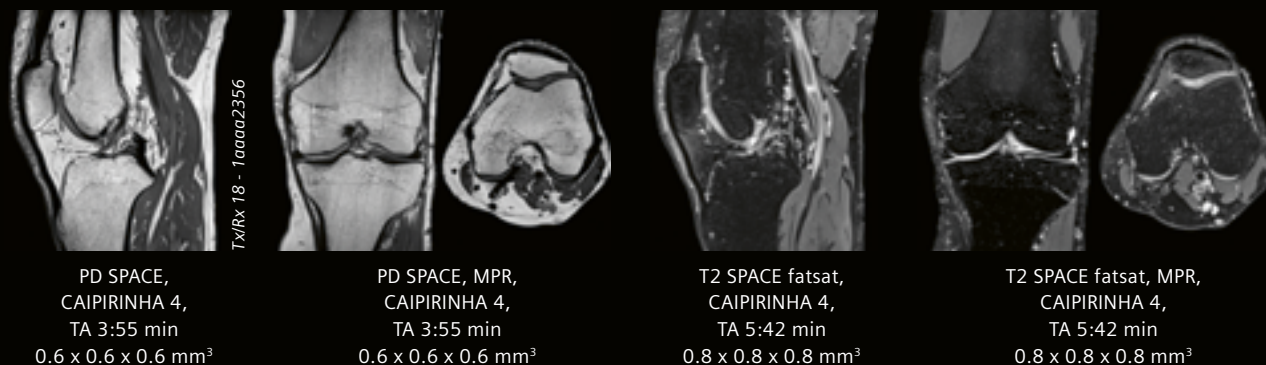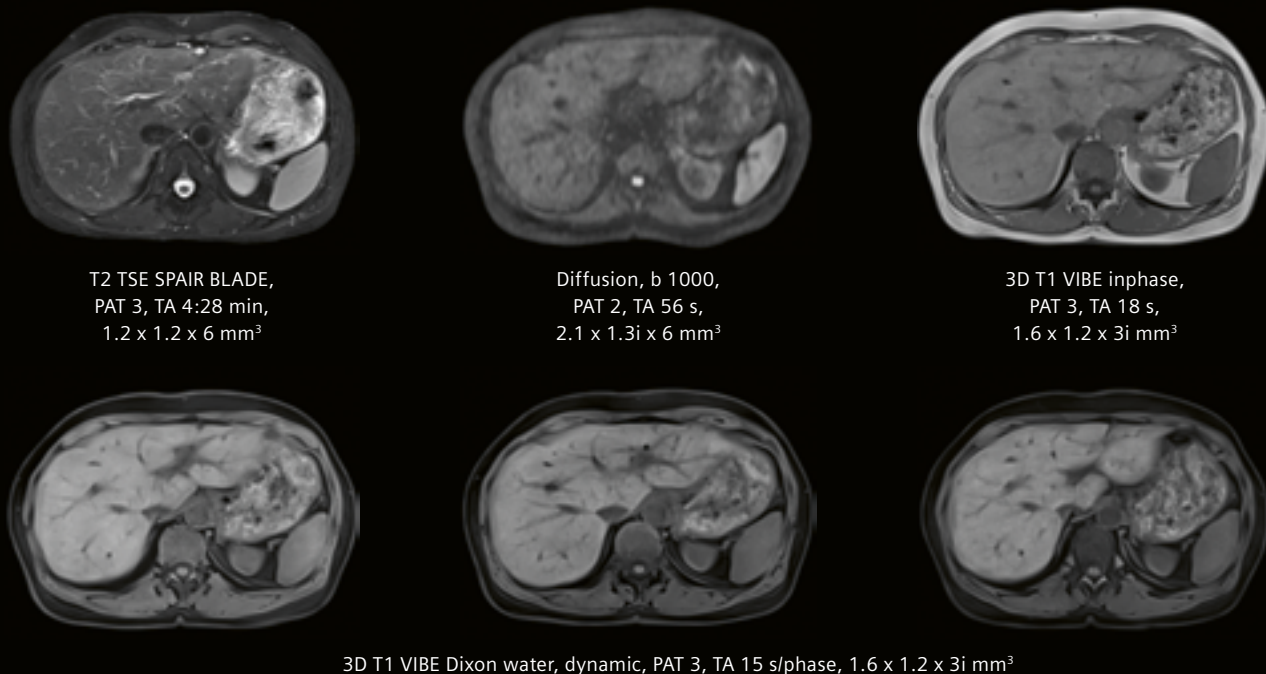

portfolio powered by BioMatrix and Tim 4G technology, preparation and scanning are considerably simplified and shortened. For example, with the ultra-flexible 18-channel surface coils and the new 3T magnet with a 55 x 55 x 50 cm FOV, off-center elbow exams can be performed routinely with improved patient comfort.
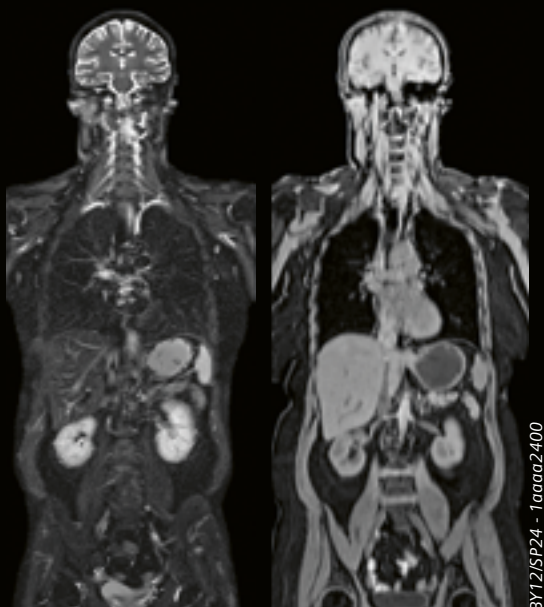
[1]*510(k) pending. The product is not commercially available. Future availability cannot be ensured.*

GO Protocols

HN16 - 2aaaa1259

T1 FLASH, PAT 2,
TA 44.5 s,
0.9 x 0.9 x 4 mm³

T2 TSE,
TA 38 s,
0.9 x 0.9 x 5 mm³

Dark Fluid,
TA 56 s,
0.9 x 0.9 x 5.0 mm³

Diffusion, b 1000,
TA 1:06 min,
1.4 x 1.4 x 5 mm³

T2 FLASH hemo,
PAT 2, TA 56 s,
1.2 x 1 x 5 mm³
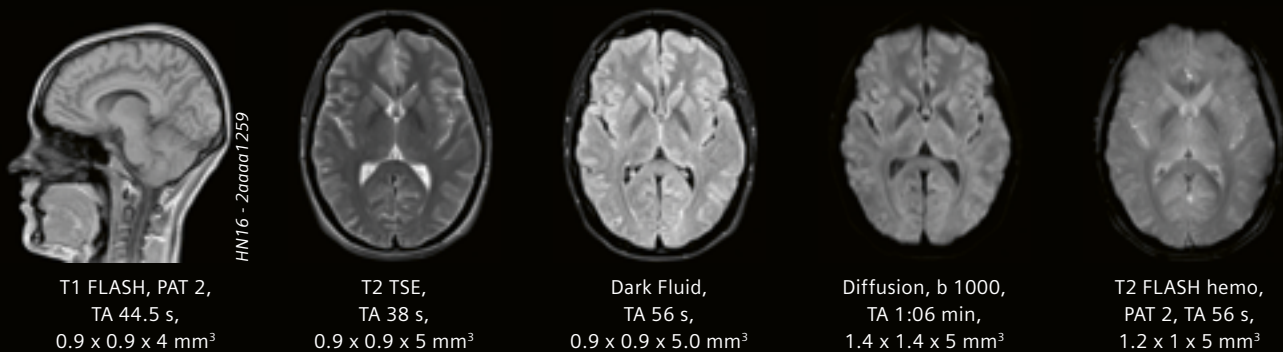
GOLiver (MAGNETOM Lumina): incl. AutoAlign Localizer – Examination time: 12 min

T2 TSE SPAIR BLADE,
PAT 3, TA 4:28 min,
1.2 x 1.2 x 6 mm³

Diffusion, b 1000,
PAT 2, TA 56 s,
2.1 x 1.3i x 6 mm³

3D T1 VIBE inphase,
PAT 3, TA 18 s,
1.6 x 1.2 x 3i mm³

3D T1 VIBE Dixon water, dynamic, PAT 3, TA 15 s/phase, 1.6 x 1.2 x 3i mm³

Tx/Rx 18 - 1aaaa2356

PD SPACE,
CAIPIRINHA 4,
TA 3:55 min
0.6 x 0.6 x 0.6 mm³

PD SPACE, MPR,
CAIPIRINHA 4,
TA 3:55 min
0.6 x 0.6 x 0.6 mm³

T2 SPACE fatsat,
CAIPIRINHA 4,
TA 5:42 min
0.8 x 0.8 x 0.8 mm³

T2 SPACE fatsat, MPR,
CAIPIRINHA 4,
TA 5:42 min
0.8 x 0.8 x 0.8 mm³

BY12/SP24 - 1aaaa2400

T2 HASTE IR, PAT 3,
3 steps, TA 3 x 1.32 min,
0.7 x 0.6 x 6 mm³

3D VIBE DW, PAT 4,
4 steps, TA 4 x 10 s,
2.8 x 2.1 x 1.8i mm³

BY12/SP24 - 1aaaa2400
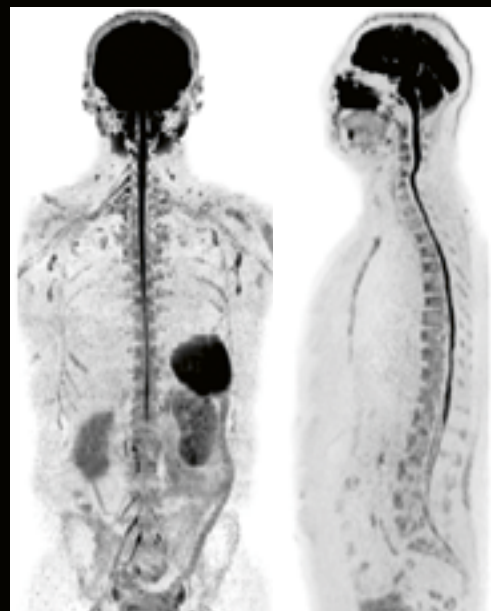
Diffusion, b 800, MIP, PAT 2,
4 steps, TA 4 x 2:42 min,
1.6 x 1.6 x 5 mm³

BY12/SP24 - 1aaaa2371
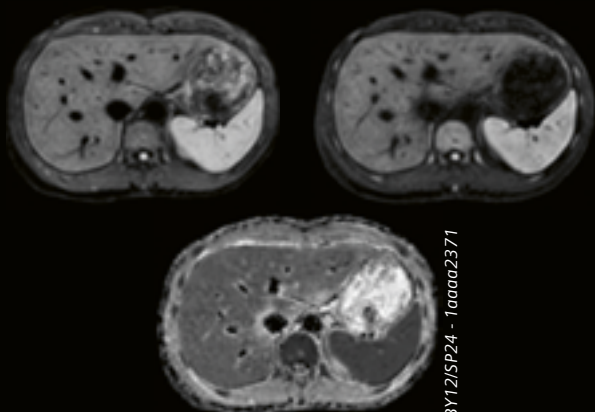
Diffusion, Resp. Sensor, b 50, 800, and ADC map,
PAT 2, SL 6 mm, TA 1:41 min, 1.4 x 1.4 x 6 mm³

BY12/SP24 - 1aaaa2371

NATIVE, 3D TrueFISP, VRT, Resp. Trigg., PAT 2,
TA 4:26 min, 1.2 x 1.2 x 1.2i mm³
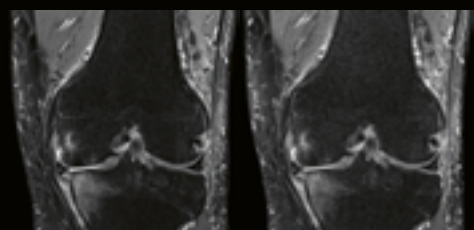
UFL18 - 1aaaa2257

PD TSE fatsat,
PAT 2,
TA 3:54 min,
0.6 x 0.4 x 3 mm³

PD TSE fatsat,
PAT 2 & SMS 2,
TA 2:03 min,
0.6 x 0.4 x 3 mm³

FA16 - 1aaaa2210

PD TSE fatsat,
PAT 2 & SMS 2,
TA 2 min,
0.6 x 0.4 x 3 mm³

UFS18 - 1aaaa2468
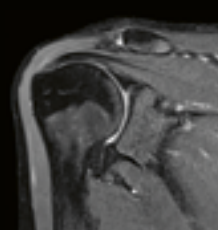
PD TSE fatsat,
PAT 2 & SMS 2,
TA 1:52 min,
0.7 x 0.4 x 3 mm³
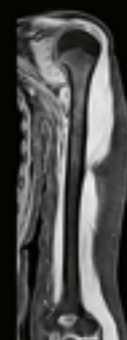
BY12 - 1aaaa2376

3D VIBE DW,
FOV 450 mm, PAT 2,
TA 3:46 min,
1 x 0.7 x 4 mm³
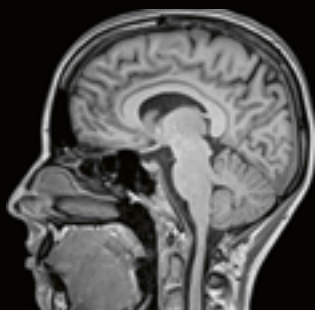
HN16 - 2aaaa1272

3D T1 MPRAGE, PAT 2,
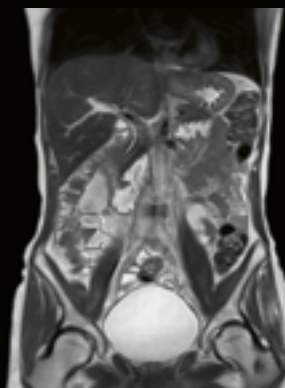TA 4:13 min,
1 x 0.9 x 0.9 mm³
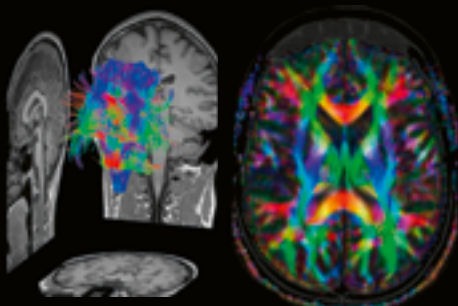
HN20 - 2aaaa1266

Diffusion, DTI, 64 directions, Fibertracking,
and FA map, PAT 2 & SMS 2,
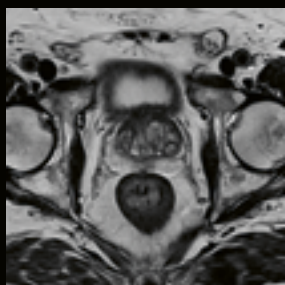TA 7:41 min, 1.7 x 1.7 x 4 mm³
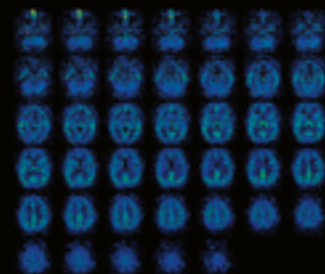
HN16 - 2aaaa1341

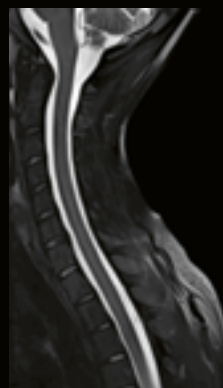Perfusion, 3D PCASL, PAT 2,
TA 4:47 min,
1.6 x 1.6 x 3 mm³

BY12/SP24 - 2aaaa1272

T2 HASTE, FOV 500 mm,
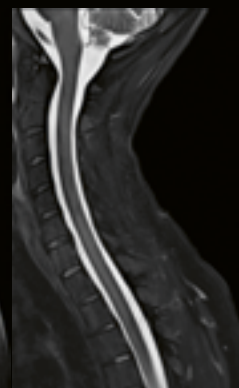PAT 3, TA 1:08 min,
1.3 x 1 x 5 mm³

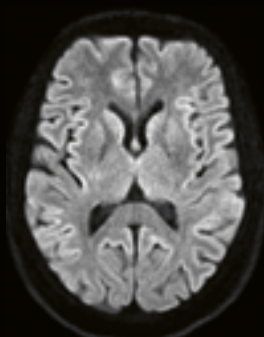BY12/SP24 - 2aaaa1268

T2 TSE,TA 3:14 min,
0.6 x 0.5 x 3 mm³

HN20/SP24 - 2aaaa1257

Conventional T2 TSE
fatsat,
TA 3:08 min,
0.9 x 0.7 x 3 mm³

T2 TSE fatsat,
with CoilShim,
TA 3:08 min,
0.9 x 0.7 x 3 mm³

HN20

RESOLVE, b 1000,
PAT 2 & SMS 2,
TA 2:42 min,
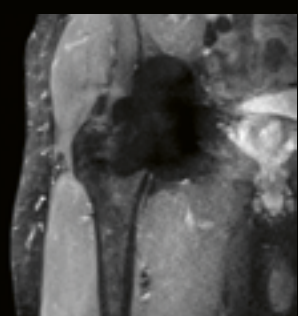1.2 x 1.2 x 4 mm³

HN20

3D FLASH TOF, CS, MIP,
TA 1:58 min,
0.4 x 0.4i x 0.4i mm³

BO18/SP32

3D T2 SPACE SPAIR, CS, MIP,
TA 1:26 min,
0.5 x 0.5i x 1i mm³

BO18

T2 TIRM, SEMAC, CS,
TA 5:30 min,
1.4 x 1.1 x 3 mm³

*CS TOF, CS SEMAC, CS SPACE and SMS RESOLVE are currently under development for MAGNETOM Lumina and Altea.
These features are planned for MAGNETOM Lumina and Altea with XA20 software, future availability cannot be guaranteed.*

*²GOBrain protocols can be downloaded from www.siemens.com/magnetom-world > Clinical Corner > Protocols.
 They are not included in software version VA11B.*

Siemens Healthineers: Our brand name embodies the pioneering spirit and engineering expertise that is unique in the healthcare industry. The people working for Siemens Healthineers are totally committed to the company they work for, and are passionate about their technology. In this section we introduce you to colleagues from all over the world – people who put their hearts into what they do.

Chicago, USA

Ning Jin

got her bachelor's degree in Biomedical Engineering from Zhejiang University in Hangzhou, China, in 2006. She then moved to Chicago, IL, USA, to study for her Ph.D. at Northwestern University, focusing on the research of functional MRI in liver. After graduation in 2011, she joined Siemens as a scientist in the US MR Cardiac Collaboration team, working closely with research partners and the R&D team at the Siemens Healthineers headquarter. She has participated in the predevelopments of several flow-related projects. Recently, she developed a compressed sensing 4D flow prototype that facilitates the use of 4D flow in clinical settings.

How did you first come into contact with MRI?
When I moved to the US to start my doctorate in 2006, I was looking for a research assistant position in bio-medical engineering. Dr. Andy Larson introduced me to the exciting field of MR imaging of the abdomen. I still remember when he took me to the MR scanner to scan a volunteer together right after I joined his lab. I was fascinated by the images popping up on the screen, depicting all the tiny details of the human anatomy.

What fascinates you most about MRI?
MRI is a powerful and versatile diagnostic tool. It plays a critical role in disease diagnosis and management by providing not only anatomical, but also functional information, such as tissue relaxation time, diffusion, flow etc. It allows us to design advanced pulse sequences, image reconstruction, and post processing techniques to explore all the possibilities. That really fascinates me.

As a collaboration scientist in the R&D team, I feel very privileged to work in a research environment with close interaction with our leading research and clinical partners. I am really excited to serve as a bridge between academia and industry by participating in cutting-edge research and translating the results directly into our products and clinical routine. This will hopefully benefit the wider population and make a difference to various clinical practices.

What do you think are the most important developments in MRI?
In MRI, reducing scan time is one of the biggest challenges. Advanced acceleration techniques, such as simultaneous multi-slice imaging and compressed sensing, will have a major impact on clinical throughput and outcomes. Using these innovative techniques, scan times can be significantly shortened while still achieving high-quality images. Fast scans can reduce the need to rescan patients due to motion artifacts, allow the acquisition of additional sequences (such as 4D Flow 😊) to provide valuable diagnostic information, and potentially increase patient daily throughput.

What would you do if you could spend a month doing whatever you wanted?
Professionally, I would like to spend the month participating in a hardware designing project with the hardware team in the factory, to have a deeper understanding of how different parts of the MR system work.

Outside of work, I would like to travel through China with my husband and two kids. Both my daughters were born in the U.S. and have not had a chance to live in their parents' motherland. There are so many fun things we could do. We could visit the Forbidden City, climb the Great Wall in Beijing, see the Terracotta Army in Xi'an, hug the giant panda in Chengdu, stroll the romantic West Lake in Hangzhou, and, most importantly, taste the most authentic Chinese food.

Christoph Forman

is a Computer Science graduate from the Friedrich-Alexander-University in Erlangen and completed a doctorate on the topic of iterative reconstruction methods for whole-heart MRI. During his Ph.D. research, he worked in close collaboration with the cardiovascular MR team at Siemens. In the process, he learned a great deal about MRI, including the programming of pulse sequences and image reconstruction on an MR scanner. In 2014, Christoph joined Siemens Healthineers where he has been able to continue his work with the cardiovascular team. He led the integration of compressed sensing in the MAGNETOM scanners and was also part of the team to develop the first products to apply this technology in clinical MRI.

Erlangen, Germany

How did you first come into contact with MRI?

My very first contact with MRI was as a limping patient. My pain turned out to be nothing serious, fortunately, just an over-stressed knee joint after too many intensive training sessions for the 100 m sprint – my hobby at the time. Professionally, I had my first contact with MRI shortly afterwards when I joined a research team at Stanford University to work on my diploma thesis. My project involved the development of an optical marker and tracking software for a prospective head motion-correction system for brain MRI, using an in-bore camera. I still remember the excitement when I tested my software for the first time in a real-world situation on the scanner. During this time, I developed a real passion for MRI. I was eager to learn more about this fascinating imaging modality and, subsequently, decided to take my interest further by starting a doctorate in this exciting field.

What fascinates you most about MRI?

As a student, I was motivated by the possibility to take images of the human body without the need for contrast agent or ionizing radiation. Being able to apply and test my ideas and software in real clinical contexts added meaning to my work, and felt much better than developing software for more abstract applications. While studying MRI in greater detail during my doctorate, I was fascinated by the vast array of contrasts and imaging capabilities that it offers to visualize anatomy and function. Given the huge range of possibilities, there is also plenty of potential to improve on established methods, discover new ones, and to break with existing imaging constraints. We've seen this very recently in the field of accelerated MR imaging. All this is possible thanks to the vibrant international and interdisciplinary MRI community that works together to constantly push the boundaries in research and everyday clinical routine.

What do you think are the most important developments in MRI?

After improvements to the scanner hardware, the increase in computing performance is becoming more and more important in MRI and healthcare in general. Most recently, computing performance was, in fact, key to developing new technologies and transitioning innovations into clinical routine. For instance, it would be impossible to accelerate data acquisition using compressed sensing without the superior computing performance necessary to reconstruct the highly under-sampled data. Another field that clearly benefits from improved computational power is artificial intelligence (AI), which is currently attracting growing attention. With this technology, high performance computers are needed to train the algorithms to combine and analyze huge amounts of data. Utilizing all this information, AI has the potential to go beyond simple diagnoses by providing more insights into diseases and support their early detection.

What would you do if you could spend a month doing whatever you wanted?

I would like to travel around the world to visit our customers and learn about the challenges they face in their everyday clinical routine. While each setting and workflow is unique to different hospitals or practices, such visits and the face-to-face discussions would provide a great opportunity to develop new ideas and solutions. However, I would relax my schedule if I did take such a trip, leaving room to learn more about the places, people, and their culture as well as to explore the local nature. I think I would start my trip in South America since I haven't been to this continent yet. From what I hear, there are many exciting places to discover.

The entire editorial staff at Case Western Reserve University and University Hospitals, and at Siemens Healthineers extends their appreciation to all the radiologists, technologists, physicists, experts, and scholars who donate their time and energy – without payment – in order to share their expertise with the readers of MAGNETOM Flash.

Note in accordance with § 33 Para.1 of the German Federal Data Protection Law: Despatch is made using an address file which is maintained with the aid of an automated data processing system.

MAGNETOM Flash is sent free of charge to Siemens Healthineers MR customers, qualified physicians, technologists, physicists and radiology departments throughout the world. It includes reports in the English language on magnetic resonance: diagnostic and therapeutic methods and their application as well as results and experience gained with corresponding systems and solutions. It introduces from case to case new principles and procedures and discusses their clinical potential. The statements and views of the authors in the individual contributions do not necessarily reflect the opinion of the publisher.

The information presented in these articles and case reports is for illustration only and is not intended to be relied upon by the reader for instruction as to the practice of medicine. Any health care practitioner reading this information is reminded that they must use their own learning, training and expertise in dealing with their individual patients. This material does not substitute for that duty and is not intended by Siemens Healthcare to be used for any purpose in that regard. The drugs and doses mentioned herein are consistent with the approval labeling for uses and/or indications of the drug. The treating physician bears the sole responsibility for the diagnosis and treatment of patients, including drugs and doses prescribed in connection with such use. The Operating Instructions must always be strictly followed when operating the MR system. The sources for the technical data are the corresponding data sheets. Results may vary.

Partial reproduction in printed form of individual contributions is permitted, provided the customary bibliographical data such as author's name and title of the contribution as well as year, issue number and pages of MAGNETOM Flash are named, but the editors request that two copies be sent to them. The written consent of the authors and publisher is required for the complete reprinting of an article.

We welcome your questions and comments about the editorial content of MAGNETOM Flash. Please contact us at magnetomworld.team@siemens-healthineers.com

Manuscripts as well as suggestions, proposals and information are always welcome; they are carefully examined and submitted to the editorial board for attention. MAGNETOM Flash is not responsible for loss, damage, or any other injury to unsolicited manuscripts or other materials. We reserve the right to edit for clarity, accuracy, and space. Include your name, address, and phone number and send to the editors, address above.

Not for distribution in the US

On account of certain regional limitations of sales rights and service availability, we cannot guarantee that all products included in this brochure are available through the Siemens sales organization worldwide. Availability and packaging may vary by country and is subject to change without prior notice. Some/All of the features and products described herein may not be available in the United States.

The information in this document contains general technical descriptions of specifications and options as well as standard and optional features which do not always have to be present in individual cases, and which

may not be commercially available in all countries. Due to regulatory reasons their future availability cannot be guaranteed. Please contact your local Siemens organization for further details.

Siemens reserves the right to modify the design, packaging, specifications, and options described herein without prior notice. Please contact your local Siemens sales representative for the most current information.

Note: Any technical data contained in this document may vary within defined tolerances. Original images always lose a certain amount of detail when reproduced.